UNIVERSITY OF Southampton

University of Southampton Research Repository

Copyright © and Moral Rights for this thesis and, where applicable, any accompanying data are retained by the author and/or other copyright owners. A copy can be downloaded for personal non-commercial research or study, without prior permission or charge. This thesis and the accompanying data cannot be reproduced or quoted extensively from without first obtaining permission in writing from the copyright holder/s. The content of the thesis and accompanying research data (where applicable) must not be changed in any way or sold commercially in any format or medium without the formal permission of the copyright holder/s.

When referring to this thesis and any accompanying data, full bibliographic details must be given, e.g.

Thesis: Author (Year of Submission) "Full thesis title", University of Southampton, name of the University Faculty or School or Department, PhD Thesis, pagination.

Data: Author (Year) Title. URI [dataset]

UNIVERSITY OF SOUTHAMPTON

FACULTY OF ENGINEERING AND PHYSICAL SCIENCES

Engineering Sciences – Mechatronics Group

Novel strategies for controlled acoustic lateral force fields in planar resonators for biomedical applications

by

WALID MESSAOUDI

Thesis for the degree of Doctor of Philosophy

December 2018

UNIVERSITY OF SOUTHAMPTON

ABSTRACT

FACULTY OF ENGINEERING AND PHYSICAL SCIENCES

Engineering Sciences – Mechatronics Group

Doctor of Philosophy

Novel strategies for controlled acoustic lateral force fields in planar resonators for biomedical applications

By Walid MESSAOUDI

The levitation and manipulation of small particles has attracted much interest, especially for lab-on-a-chip devices and the possibilities of controlling the position of human cells, bacteria, and microbeads. Latterly, the use of acoustic radiation as a way to levitate particles in small channels has encountered plentiful success for many applications including sorting, aggregating and multiple other biomedical operations. Most devices used for these applications used static acoustic radiation force patterns inducing non-configurable trapping positions. Recent years have seen the emergence of dynamic trapping in micro channel which is necessary to widen the range or possible application for such techniques including transport and rotation of single particles and aggregates.

This thesis investigates novel ways of structuring static force fields in planar resonators, and also creating dynamic levitation techniques especially design for biomedical related projects. Several possible approaches are explored all using planar resonators as a basis. Initially the lateral forces in a standard planar resonator are explored, assessing the impact of design parameters on the 'naturally occurring' lateral force components. Secondly, novel devices which add an extra control layer to direct the acoustic excitation of the fluid layer are explored. The third approach consists of having this intermediate control layer be formed of a channel with a two phase flow. The droplet movement in this control layer changes the structure of the acoustic radiation field, which dynamically following the droplet.

The thesis concludes with the design of a planar resonator with strong lateral force components for the culture of discoid-shaped liver cancer cell aggregates. The resulting aggregates are cultured and studied, demonstrating that they present characteristics and functional protein expression that more closely matches *in-vivo* cells and hence could provide a better model for drug screening applications.

Acknowledgements

There is no such thing as a self-made man. I would like to thank the people that supported me during this thesis and congratulate them as this is their achievement as much as mine.

First I would like to thank my wife who supported me with her love and care during the good and the bad days of the thesis, an necessary and inexhaustible source of joy, As well as my parents who cultivated my curiosity, fill our house with kindness since I was a young child, To my siblings who created a fun environment to grow up. To my friends who were always there to crack some jokes.

I could not do it without the superb supervising team I had, Peter Glynne-Jones and Martyn Hill who were always there for support and guidance. More than supervisors, they were mentors. The whole group was an incredible place to work within, I would like to thank Umesh, Zaid, Bjorn, Filip, JunJun and Anthony for their advices and small chats.

The office, laboratory and workshops were marvellous places to work as it was always crowded with smiling faces and kind words. I would like to thank them all, I prefer to not cite their names in order to avoid forgetting some.

Thank God for my life and the people in it!

Table of Contents

Table of Figures

To quantify and compare both structures two performance variables are introduced - firstly, the energy density in the active area of the fluid chamber, which is the sum of the kinetic energy and the potential energy divided by the surface of interest. The second performance metric is the quotient of the energy density in the active area and the energy density in the passive area, which gives a ratio describing the localisation of the energy, hereafter called

Academic Thesis: Declaration of Authorship

I, ...Walid Messaoudi

declare that this thesis and the work presented in it are my own and has been generated by me as the result of my own original research.

Novel strategies for controlled lateral force fields in planar resonators for biomedical applications .....

.....

I confirm that:

1. This work was done wholly or mainly while in candidature for a research degree at this University;
2. Where any part of this thesis has previously been submitted for a degree or any other qualification at this University or any other institution, this has been clearly stated;
3. Where I have consulted the published work of others, this is always clearly attributed;
4. Where I have quoted from the work of others, the source is always given. With the exception of such quotations, this thesis is entirely my own work;
5. I have acknowledged all main sources of help;
6. Where the thesis is based on work done by myself jointly with others, I have made clear exactly what was done by others and what I have contributed myself;
7. None of this work has been published before submission

Signed: .....

Date: .....

Chapter 1: Introduction

1.1 Introduction

This thesis investigates novel techniques of dexterous and controlled manipulation of particles in levitation (*dynamic levitation*) and their application to cell biology. Numerous approaches concerning dynamic levitation exist already; the number of techniques available for similar or identical purposes compels us to look carefully at advantages and disadvantages of each in order to design useful systems for specific applications. The manipulation of small particles can be achieved by the use of dielectrophoretic forces [1], optical forces [2], magnetic forces [3] or acoustic forces [4], which are the subject of this thesis.

Acoustic forces have the significant advantage of being gentle to biological particles like cells [5, 6]. In contrast, magnetic manipulation requires the special preparation of cells to incorporate ferrous elements detrimental for cell viability. Optical forces require a more complex set-up, are typically limited to operating on smaller numbers of cells, and often necessitate the heating of cells at comparable force levels. Manipulation techniques involving the use of dielectrophoretic effects can be of comparable force to those in acoustic systems, but usually operate over shorter ranges and depend on the dielectric properties of the host solution. In addition to the aforementioned benefits, acoustic manipulation has a secondary component called the *Bjerknes force* which brings particles within a levitation plane together into aggregates [7], which can be highly useful for cell aggregation. The main disadvantage of this technique is that acoustic waves are more challenging to precisely control compared to other techniques because of the complex interdependence of the acoustic field and device geometry, and the longer wavelength compared to optical trapping.

Two techniques of acoustic manipulation have been previously demonstrated. SAW (Surface Acoustic Wave) based systems use IDT (Integrated Device Technology) to create acoustic waves propagating on a substrate before being released in a fluid chamber [5]. It allows fine control, but IDTs require precise fabrication and can only

operate a set number of frequencies, making this technology costly and lacking in versatility.

BAW (Bulk acoustic wave) based devices use a transducer axially coupled to a fluid chamber, forming a structure called a planar resonator. This arrangement is cheaper to fabricate and more versatile because Piezo-ceramic transducers can operate in a wide range of frequencies. One of the main drawback to this technology is that planar resonators activate lateral-mode acoustic effects which are difficult to predict and depend on the specific lateral geometry of the device.

Planar resonators are the centre of interest of this thesis, which aims to address this disadvantage via a multiphysics and multi-properties finite element analysis (FEA) of the lateral gradient of the acoustic radiation force field in the chamber of a planar resonator. Novel techniques to dictate the lateral force field will be introduced by adding an extra layer to control the maximum of acoustic energy and therefore the trap points. Finally, the knowledge acquired in this simulation will be used to produce a bioreactor culturing *Huh7* (human liver cell line) discoids and a study comparing huh7 discoids obtained using acoustic trapping in planar resonator to other conventional techniques of cell culturing will be performed in order to validate this technique for drug screening.

The next section present each body of work presented in this thesis.

1.2 Thesis outline

This thesis explores novel techniques for the acoustic control of particles and applications in cell biology.

Chapter 2 introduces theory on acoustic and other forces that contribute to the motion of particles in a planar resonator. It also reviews existing literature, including a discussion of devices that aim to control the acoustic lateral force field using bulk and surface acoustic waves. A short review of the application of acoustic forces to cell culture is included along with introducing the main functions of liver cells to support the cell culture application described in chapter 6.

Chapter 3 introduces the impedance transfer model (one-dimensional) and the finite element model (two-dimension) that will be used throughout the thesis.

A comparison of these two different models is performed using the same example device structure and similar results acquired.

Chapter 4 investigates the lateral components of acoustic modes in a standard planar resonator and their sensitivity to design parameters using finite element modelling. The conclusions obtained by this modelling work are verified by fabricating planar resonators with different design parameters and studying their force fields using fluorescent tracer beads. Predicting the lateral structure of the acoustic radiation force is showed to be hard. Chapter 6 shows that It is possible to a certain extent, indeed the knowledge acquired in the chapter is used to design and fabricate a bioreactor. Chapter 5 introduce static and dynamic innovative techniques to control finely this force field.

Chapter 5 proposes two novel strategies to control the acoustic lateral force field in a planar resonator by adding either an extra static or dynamic control layer that directs the excitation of the fluid layer in the manipulation cavity. Both concepts are modelled, fabricated, tested and characterised.

In chapter 6, the experience gained in previous chapters is used to direct the design of a bioreactor system for creating discoid-shaped cell aggregates, and explores the functional properties of human liver cell (hu7) aggregates in comparison to other culture techniques. Moreover, the response of these discoids to an anti-cancer drug is investigated and compared to responses from cells cultured in conventional 2D and pellet culture.

1.3 Main contribution

The main contributions that this research has achieved are listed below:

- I presented an in-depth investigation into the complex relationship between design parameters and the strength and structure of lateral components of acoustic modes in planar resonators. I used FEA to show that the even small changes in geometry can have large effects on the magnitudes and structure of these acoustic forces. This finding was subsequently confirmed experimentally by changing

transducer position and width and characterising the change in acoustic field over a range of positions and sizes. (Chapter 4)

- I developed and investigated two novel strategies to control the acoustic radiation lateral force field in a planar resonator. Devices were designed, modelled, fabricated and characterized. In both case the design principle was to introduce a structured layer between the transducer and the carrier. In the first strategy this structure is composed of static pillars, where levitation occurs above the pillar. In the second, this layer is instead composed of a channel filled with two immiscible fluids, which when pumped through the channel permit particle transport. (Chapter 5)

- I designed a bioreactor with modes having strong lateral components in order to produce multiple huh7 discoids. The resulting discoids are compared to cell aggregates formed by 2D monoculture (petri dish) and pellet culture (centrifuge). Discoids formed in acoustic bioreactor proved suitable as a model for drug toxicity and screening. (Chapter 6)

Chapter 2: Theory and state of the art

2.1 Physics and theory

Acoustic radiation force is a nonlinear acoustic effect caused by the transfer of wave momentum to absorbing or scattering objects. This force can be gentle and non-invasive and thus has received great interest for biomaterial contactless manipulation. In comparison to other methods of micro-particle contactless manipulation, like the optical levitation, it is more stable than aerodynamic levitation and unlike magnetic or electric levitation the particles don't have to be dipoles or magnetically active to levitate [8]. This is the reason why acoustic levitation technique is used in many applications, especially for bio-related contactless manipulation [9, 10][11]. When talking about acoustic radiation forces, two of them are differentiated. The primary radiation force which is the force on a single particle created by an incident sound field, and the secondary radiation force, or Bjerknes force, which describes particle-particle interaction resulting from acoustic fields scattered by one particle impinging on another.

2.1.1 Primary radiation force

Kundt demonstrated the effect that acoustic wave have on particles by trapping dust particles in a tube using an acoustic standing wave [12] , then Rayleigh studied this event and completed a theory for it including it in his classical theory of sound [13], however King was the first to present the full derivation for acoustic radiation force in 1934 [14]. Yosioka and Kawasima in 1955 included the effect of compressibility of particles [15], this later equation was simplified and generalized is 1962 by Gor'kov [16, 17]. Finally Doinikov added the effect of viscosity and temperature in 1994 [18].

This primary radiation force is defined as the force that a particle encounter

when scattering an acoustic wave. We introduce and later model the radiation force using the simplified and generalized formula given by Gor'kov in 1962. The particle is considered small compared to the wavelength and the surrounding field is considered as inviscid fluid. This force depends on the gradient of pressure and velocity energy densities in the region around the particle. It is given by:

$$F^{Rad} = -\nabla U \tag{1}$$

Where U is the potential energy of the particle:

$$U = V\left(f_1 E_{pot} - \frac{3}{2} f_2 E_{kin}\right) \tag{2}$$

U is derived from the velocity potential, *V* is the volume of the particle. The E_{pot} and E_{kin} are time averaged potential and kinetic energy densities at a special location into the fluid.

$$E_{pot} = \frac{\overline{p^2}}{2\rho_0 c_0^2} \tag{3}$$

$$E_{kin} = \frac{\rho_0 \overline{v^2}}{2} \tag{4}$$

Where *p* is the acoustic pressure, ρ_0 is the fluid mass density, c_0 is the speed of sound in the surrounding fluid, v is the velocity of the field, the $\overline{\ }$ sign shows that this value is time averaged. f_1 and f_2 are two coeficients given by :

$$f_1 = 1 - \frac{\rho_0 c_o^2}{\rho_p c_p^2} \tag{5}$$

$$f_2 = \frac{2(\rho_p - \rho_o)}{2\rho_p + \rho_0} \tag{6}$$

Where ρ_p is the mass density of the particle and c_p is the speed of sound in the particle. The primary radiation's force is directed to the pressure node or antinode of the standing wave where there is the maximum energy potential. We define $\Phi = f_1 + \frac{3}{2} f_2$, the acoustophoretic contrast factor. In a 1D standing wave

(where pressure and velocity are out of phase with each other), if Φ is negative, particles would be pushed to the pressure antinodes via radiation force and for Φ psitive, they would be pushed to the pressure nodes [19].

2.1.2 Axial and lateral radiation force

In a complex three dimensions (3D) structure such as the planar resonator, which will be used throughout this thesis, the acoustic field can be multidirectional. Indeed the resonance does not occur just in the thickness direction but in all direction forming complex, all-directional acoustic radiation force field, in chapter 4 this effect will be described and studied using FEA models.

This more complex force field, which depends on the lateral architecture and composition of the planar resonator is then responsible for the final position of particle aggregate in this field. Indeed acoustic waves are scattered in all direction when encountering a change in acoustic impedance [20], this creating a multidirectional acoustic field.

For some applications this effect can be maximised as a way to produce rapidly many smaller aggregates, for the mass production of cell 3D aggregate for drug screening for example, indeed this lateral radiation force is then used to determine the size and the 3-D shape of aggregates in a planar resonator. For some other applications the lateral of the force field defined by the structure is suffered as a non-wanted and non-controlled detrimental force, for example for fine manipulation of particle, or contactless production of wider cell sheet in levitation.

2.1.3 Secondary radiation force or Bjerknes force

Particles scatter the acoustic wave in their vicinity, if there are many particles in the fluid, the scattered pressure off one create radiation forces for the others and vice versa. A simplified expression of this particle to particle force is this one [21].

$$F_b(x) = 4\pi a^6 \left[\frac{(\rho_p - \rho_0)^2 (3cos^2\theta - 1)}{6\rho_f d^4} v_{in}^2(x) - \frac{\omega^2 \rho_f}{9d^2}\left(\frac{1}{\rho_p c_p^2} - \frac{1}{\rho_0 c_0^2}\right)^2 P_{in}^2(x)\right] \quad (7)$$

Where a is the radius of the particle, d the distance between the particles and θ is the angle between the central line of the particles and the propagation's direction of the incident acoustic wave. $v_{in}\ and\ P_{in}$ are respectively the amplitude of particle's velocity and the pressure amplitude. If the force is positive, it is attractive for the particles, if it is negative the force tends to repulse them to each other [22]. This force is usually smaller than the primary one, however if the term "d", distance between particles, is small enough this force becomes relevant. It is particularly important during the process of aggregation and sedimentation. We can typically see its effect in regions where the radiation force is lower, i.e. the node of the standing wave, where the primary force is at its minimum.

2.1.4 Steaming induced force

The circulatory motion of the fluid induced by a sound wave propagating in the fluid is called acoustic streaming. Acoustic streaming can be classified by their generative mechanism. The classification has been reviewed and studied by Boluriaan and Morris [23], and recently by Wiklund et al.[24]. The main types can be defined as: boundary-driven streaming, jet driven streaming, Gedeon streaming and Eckart streaming [25].

Boundary-driven streaming is composed of outer streaming (also called Rayleigh streaming) [26] and inner streaming (or Schlichting streaming). It is called "boundary-driven" because it is generated by viscous stresses at the liquid-solid interface created by the relative motion between the acoustic movements of the boundary and fluid.

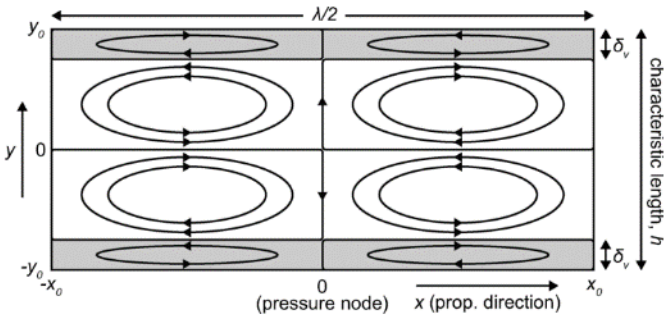

Figure 1- Figure taken from Wiklund et al paper [24] : A system of inner (Schlichting) streaming within the viscous boundary layer (grey areas) and outer (Rayleigh) streaming vortices in a channel with a standing wave propagating along x. The pressure node is located at x= 0 (trapping positon)

Jet driven streaming, is the streaming coming from the ejection or suction of fluid by an orifice. It is linked to the geometric configuration of the cavity compared to the orifice. The streaming patterns are different if the hole is used as a suction orifice or an ejection one [27].

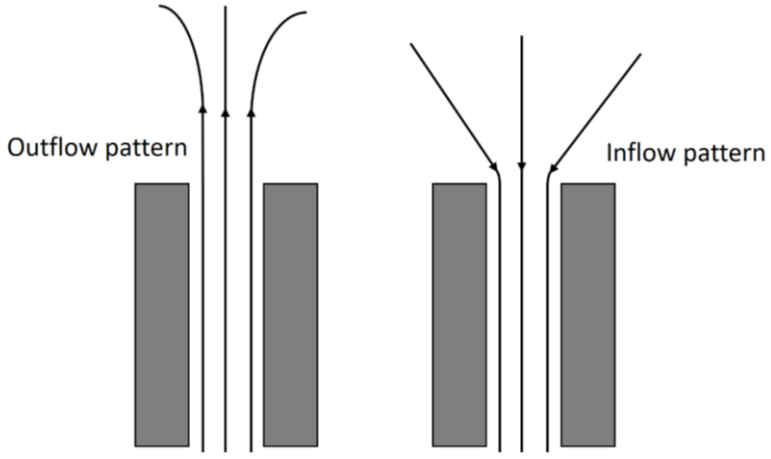

Figure 2- Figure showing different pattern for jet driven streaming depending of the flow, outflow pattern follow the direction of the flow then spread out, whereas inflow pattern take the direction of the flow in the cavity and not before

Eckhart streaming [25] is caused by the absorption of the acoustic wave during the propagation of the wave through a cavity. the Stokes law [28] shows that the

absorption and therefore the streaming induced by it is higher for high frequency. Which is the case for ultrasonic manipulation.

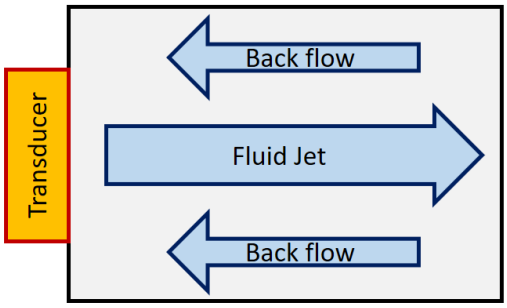

Figure 3- A typical Eckart streaming flow including a backflow that arises due to the confined region. The fluid jet is more pronounced if the opposite wall of the chamber is acoustically absorbent and if the dimension of the fluid chamber parallel to the fluid jet is comparable or greater than the acoustic attenuation length

Spengler et al. [30] prove using 25μm and 1μm white latex particle that streaming affect small particles behaviour and have negligible effect on larger particles. Indeed the drag force is proportional to the particle radius whereas the radiation force is proportional to the particle volume. Making this later force dominating the particle behaviour for particle larger than 10μm [31].

The focus of this thesis being the architecture and magnitude of acoustic radiation force in a planar resonator, particle of 10um will be used to reduce the effect of streaming induced drag force on particles.

2.1.5 Cavitation

Cavitation if the formation of gas cavities in a fluid environment under acoustic excitation. In this case the bubble would expand. A periodic movement of the bubble happened as the bubble expand or contract depending if the inner pressure is respectively lower or higher than the surrounding pressure. This would create acoustic shockwave, and if the contraction and extension in size of the

bubble exceed what the bubble surface can handle it results in the collapse of the bubble, creating a massive acoustic shockwave, and associated jets [32].

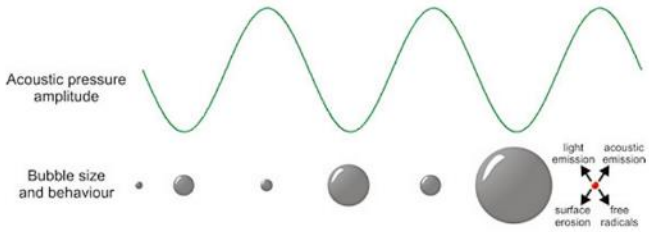

Figure 4 - bubble size and behaviour in response to acoustic pressure

Cavitation is usually divided into two classes of behaviour: inertial (or transient) cavitation and non-inertial cavitation. In the first case the bubble collapses quickly in the fluid. In the non-inertial cavitation, the bubble in the fluid moves, expands and shrinks because of a moving pressure field, and finally collapses when the surface tension fail to maintain the void. It is the most encounter case working with acoustic radiation force [33].

When the bubble collapse and release this rapid and powerful shockwave, the whole force field in the liquid cavity is disturbed, because the pressure field change and therefore the force field. In most application of acoustic manipulation, cavitation is a disruptive effect, which is the case in this this project. In order to avoid any creation of void or bubble in the fluid, the pressure gradient have to be high enough to manipulate particle but low enough to avoid this harmful effect. To do so the temperature have to be controlled as well because of the link the pressure and the temperature have [34].

Some application use acoustically induced cavitation, for example in the case of the sonochemistry, indeed when the bubble is collapsing high pressure and temperatures are created, which can start or enhance chemical reactions [35].

In the case of this thesis, cavitation is seen as a detrimental effect that can disturb the force field. Temperature rise have been kept below 3°C and pressure magnitude have been kept under 1,2 MPa avoiding any creating of bubble in the fluid.

2.2 Device for acoustic manipulation of particle

This part will discuss controlled static and dynamic force field devices. Controlled dynamic force field means that the force field within the cavity change over time and can be predicted and controlled in magnitude and position. A recent review of many papers in this field was recently published by Drinkwater [36].

A wide range of techniques have been studied to give a dynamic reconfigurability of the force field, and this area has shown to interest academics for its important application potential, mainly bio related [37]. Indeed, particles dynamic manipulation can be used to sort cells out, carry them throughout different chemicals, and stack different kind of particles to create composite structure [38, 39]. The state of art of application for biological matter using sound will be discussed into detail in the final part of this literature review.

To do so two techniques are mainly used, called BAW (Bulk acoustic wave) and SAW (Surface acoustic wave). The difference being the nature of acoustic wave, in the first one the waves are propagating through the bulk of the material where the trapping occurs, the second one the waves propagate on the surface of a substrate before leaking in the bulk fluid layer where the particle are manipulated. Recent advancement in SAW acoustophoresis have been reviewed by Lin et al. in 2012 [40].

SAW devices uses IDT (interdigitated transducers) scored on transducer as an emitter. The frequencies excitable by IDTs depends on their fabrication as the main frequency harmonic has its wavelength being equal to the distance between adjacent branches of an IDT. It has been shown that SAW device are able to mix the fluid in a droplet [41], and even move the whole droplet [42]. Furthermore this technique is effective to arrange particles in lines or cluster [43] using phase control or two IDT being place facing the other. More recently fine control over particles trajectory in a flow environment is achieved using the same method [44]. In 2012 Ding et al. shows that by using four IDTs placed on the vertexes of a square it is possible to finely move a single particle in a fluid environment [45].

The difference between SAW and BAW results in the method of acoustic wave emission, SAW usually operate at higher frequency (~5 MHz) whereas BAW operate at lower (<2 MHz). For BAW device for a set transducer size the frequency can be

tuned next to the resonance frequency. In the case of SAW the frequencies usable a tightly linked to the IDT architecture, although harmonics are usable.

BAW planar resonator is much easier to produce than SAW device, plus it can be used to levitate larger object and it is easy to change the plan of levitation height without adding any level of complexity in the device (as shown in next section). All of this making it a natural competitor technique to the dynamic SAW field. Although SAW acoustic device have shown to be particularly good for lateral control over particle in a fluid environment. The next section will explore the state of the art for BAW manipulation techniques, then this thesis will investigate novel techniques for lateral control using a planar resonator.

2.2.1 Bulk acoustic wave planar resonator (BAW)

A bulk acoustic wave of BAW is an acoustic wave that travels through a piezoelectric material into a fluid or a material. Also known as volume acoustic wave.

This report will explore ways to bring lateral control over the planar resonator technique introduced here. It permits by itself control over the thickness direction [46] by clever switching on existing thickness modes. The initialstructure consists of a stacks of planar materials. These simple structures have found a wide-spread application in Lab-On-a-Chip (LOC) applications, including filtration, washing, separation, sensing, sonoperation and more, see review by Glynne-Jones et al [47].

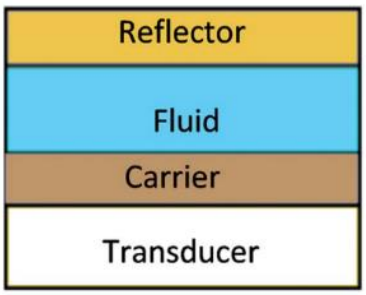

Figure 5- Layered components of a planar resonator.

The main advantage of this structure is its simplicity, formed by a transducer which is glued to a carrier then the fluid layer and finally the reflector, with reflector and carrier having high acoustic impedance relative to the fluid layer. All planar resonators, independently of layer thickness, resonate a certain frequency. However certain thickness combinations induce much stronger resonances within the fluid layer than others, therefore choosing carefully the thickness in this structure is critical for its efficiency, the best case being when most of the acoustic energy is located in the fluid layer. The best thicknesses depends of the acoustic properties of materials used for the different layers.

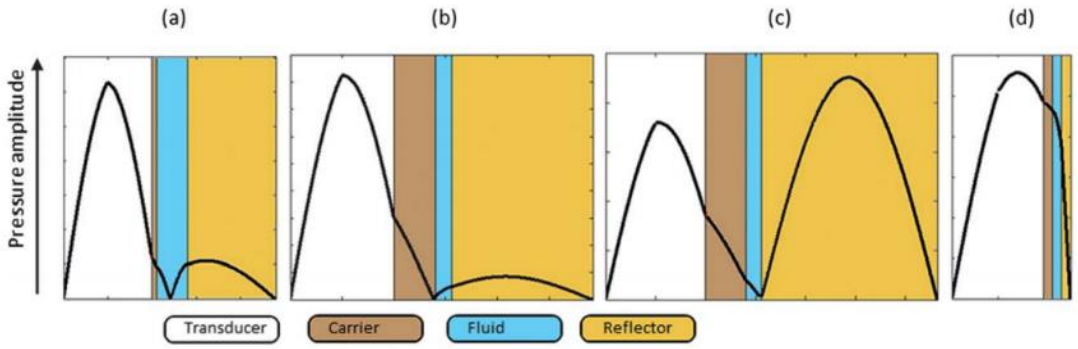

Figure 6- Figure from Peter-Glynne Jones review [47]: Typical pressure amplitude distribution in (a) half-wave, (b) inverted quarter-wave, (c) quarter-wave, (d) thin-reflector resonators. The differing positions of the pressure nodes yield various behaviours.

Moreover, different “modes” are possible depending of the thickness of the layers and the chosen resonance frequency. The word “mode” means the pressure amplitude distribution within the fluid layer in the case of a resonance. Indeed, the pressure amplitude distribution determines the force field, and therefore the particle trapping points. We can differentiate four main type of distribution; - (a) The half-wave, the minimum pressure amplitude is in the centre of the fluid layer, therefore the particles are pushed to the middle plan of it; - (b-c) The quarter-wave, the force field push the particles to the carrier (or the reflector); - (d) The thin, where the minimum pressure amplitude is on the carrier layer (or the reflector) layer. In this particular case -reflector mode, where the pressure minimum is at the extreme end of the device, at the interface of the reflector and the air; - Finally another mode, would be close in the definition from the first half wave, with a fluid

layer thickness “N” half wave(s) wider, in this case the fluid layer would have N+1 trap plan in the fluid layer, we will call it multiple nodes mode.

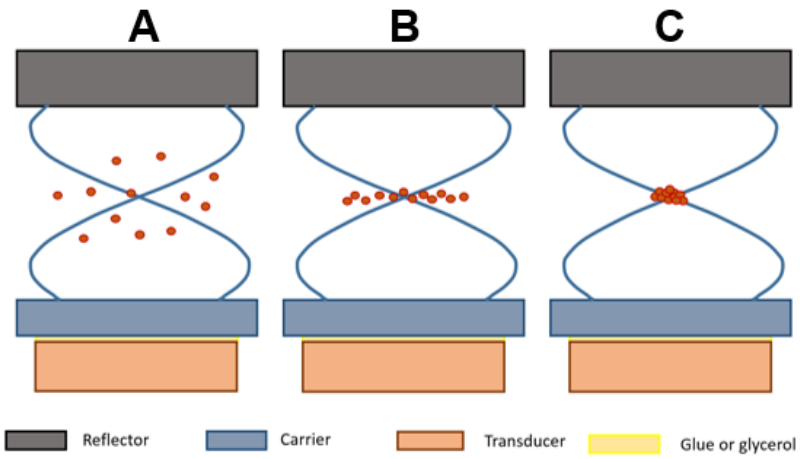

Figure 7- Picture taken from Yongqiang Qiu paper [48], Scheme showing a classic bulk acoustic standing wave device with three node within the fluid layer- a) before the transducer is powered, - b) when the transducer is powered, - c) after a certain amount of time cell aggregate by radiation force and bjerknes force (time depending of the device and the input voltage)

In all the sections of this report this technique is used in a half-wave mode although the findings of chapter 4 and 5 can be transposed of other acoustic modes, chapter 6 can be transposed in the multiple node mode but not in the others.

2.2.1.1 Control of array structures

Once we note that the maximum kinetic energy (trap position) in typically directly axially above the transducer in planar BAW devices, the most intuitive way to control the radial position of this trap over time would be to control the position of the transducer itself over time. However it is tricky to do so, indeed, to carry the acoustic power into the fluid layer the transducer have to be stiffly coupled to the carrier layer, thus is it impossible to move it without high friction increasing heat and reducing durability. One of the strategy that will be modelled and

experiment in this thesis is the addition of a liquid coupling layer juxtaposing the transducer to activate or deactivate certain resonance position, in chapter 5.

Therefore another way to use this idea is to elaborate a way to power just one part of the piezo-electric material having the levitation occurring above this section, by switching on the part next to it, the trap point would move accordingly.

The first paper that introduced this concept was written by Kozuka et al. in 1996 [49], it showed that this technique can be effective. The 40mm transducer electrode has been scratch-diced in 15 smaller 2mm electrodes apart from each other by a .5mm gap. The point being to power up few (or one) grouped electrodes, and disconnect them while connecting some other in the direction wanted for the trap to move in the direction wanted by the operator.

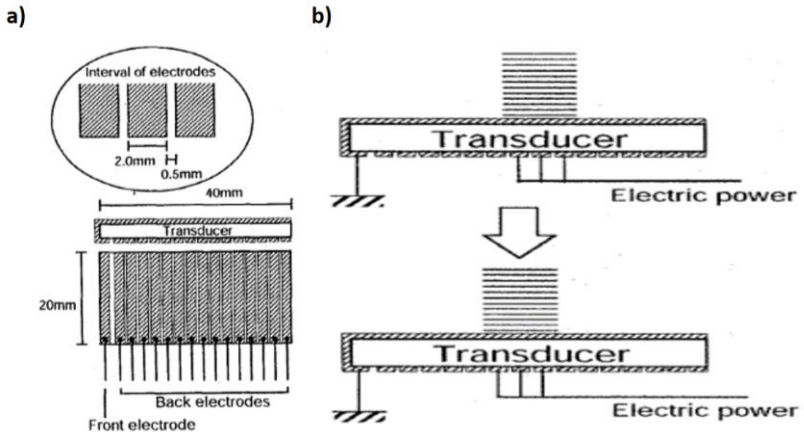

Figure 8- Picture taken from Kozuka et al. paper [49], a) Transducer fabrication, with diced electrode, the left electrode is connected to the other side of the transducer, this one is always powered, b) Effect expected by changing the connected electrodes, in this example the electrodes are excited by group of three

An extensive part of this paper treat the searching or the ideal number of electrodes excited at the same time and the way of deactivating the extreme ones in the direction unwanted and activate the ones in the direction wanted to carry the aggregate . Thus, it showed that powering them one by one is not the most effective, indeed, because the electrode are comparably far away one from each other, some particles are not attracted by next step trap, they are “lost”. In another way, group of five electrodes or more show some displacement but the overall radial displacement by step is lower than what we could expect (2.5mm). The best

number of electrodes powered at the same time in this system was between two and four.

Glynne-Jones et al. addressed this technique more recently, in 2012 [50], the main difference was the scale of the device, whereas the previous work was working with a fluid layer of 30mm and design to carry micro aluminium particle using relatively big resolution (2.5mm), this latter paper work at a smaller scale, the cavity is only 300um thick. The obvious objective is to demonstrate that this technology can be used for micro-particles and thus biological matter.

This article is divided in two main parts, the first one showing a 1D and 2D model of this technique, and the next part is the actual device made with 12 diced electrodes coming from the same 4mm transducer that have a width of 500um. The transducer width is critical as it determines the step size of the moving agglomerations of particle along the channel. Effective particle movement of 10μm polystyrene beads is achieved following a step size of 500μm, as expected. Finer fabrication technique would allow finer control.

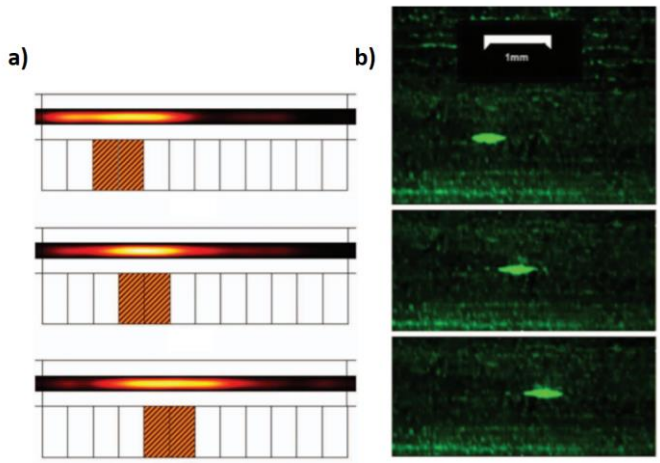

Figure 9- Picture taken from Peter Glynne-jones paper [50]. ,a) 2D modelling showing potential energy on top, and moving kinetic energy depending on which electrode are excited, b) Picture taken with 10um fluorescent beads within the device, the resolution equal the width of the electrodes

These two papers show that this technique is effective and could have an even lower resolution that would be define by minimum width with which we can scratch the electrode of the transducer. The piezo electric material have the same mechanical properties of ceramic, score it in a precise way can be tricky. The

downside of this technique Is the fabrication technique of the scored transducer which is intricate due to the mechanical property of this piezo ceramic.

2.2.1.2 Phase shift

Phase shifting is another method used in the literature to control the position of the node and antinode of the pressure standing wave, and therefore the force field in the cavity. The method uses the fact that a standing wave can be created by an incoming wave and its counter-propagating reflection, which would have been reflected by the reflector for the previous cases. But this counter-propagating wave can also be created by another transducer parallel to the first one. In this last case if the frequencies of both waves are identical the position of the node in the standing wave is related to the phase shift there is between both waves. Courtney et al [51], recently published an article concerning a device using this technique.

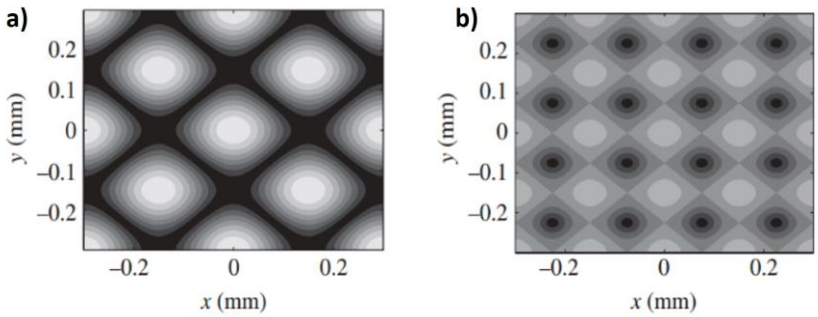

Figure 10- Taken from [51],graph using the equation obtained after summing both incident and counter-propagating wave with and without phase shift, using only two opposing transducers with reflection coefficient, R-0.2. a) without any phase shift. b) With a phase shift of π/4 on the counter propagating wave. Black is low level pressure and white high level of pressure.

To make sure both waves creating the standing wave are the ones phase-shift controlled, and not the reflection of one or the other, the reflection have to be reduce at its minimum. To do so the design of the device was made in such way for the pairs of parallel transducer to be matched to each other and to the fluid.

Finally behind the transducers absorbing elements are added to reduce the internal reflection to its minimum. In this device four transducers allows a 2D control of the nodes, and a fifth transducer at the bottom of the structure vibrates at a standard multi-node resonance frequency to maintain the particles in levitation.

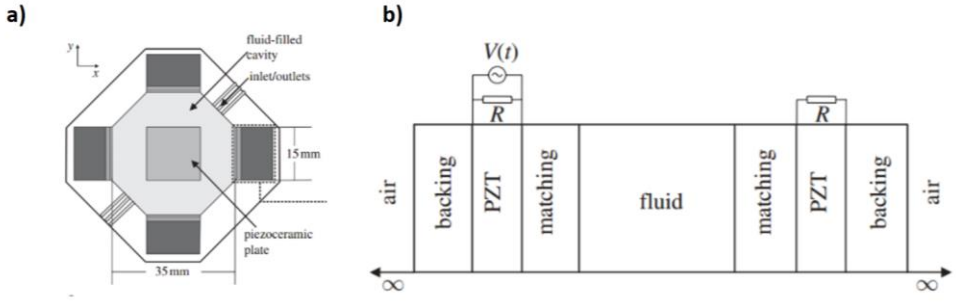

Figure 11- Taken from [51], a) structure of the whole device, showing the four transducers mounted in pairs of parallel transducers, b) typical structure of a pair of transducer, showing the different layer necessary to avoid, as much as possible, unwanted reflection.

The results of this device are promising, indeed, the experimental works showed particle movement similar to what is modelled. 10 um polystyrene beads, used in this experiment, are distributed in grid of particles, going where the node are, and the node positions can be changed by changing the relative phase of the two opposite transducers. This device is capable of controlling the position of small particle aggregates or silne particle with an accuracy in the order of the micrometre. The drawback of this device and this technique would be the complexity of the design and fabrication phase.

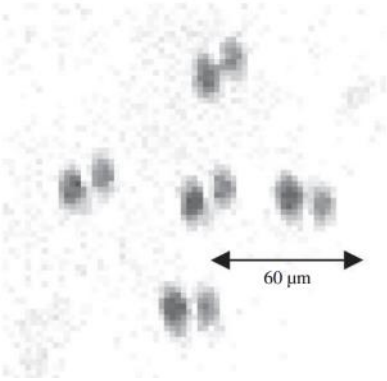

Figure 12- Taken from [51], showing a stack of five images showing a pair of particle changing position depending of the phase shift. The centre one is

without any shift, then the other position are with the pair of transducer affiliated shifted from ± π/2.

Courtney et al. used the same technique in another publication [52], the point of this paper is to show how to manipulate a Bessel function acoustic field to control the node/trap position. The design geometry is different, indeed the transducer are in piezoceramic ring (PZ27) forming a circle of 5.59 mm of radius. It is backed with an absorbing backing layer of epoxy with 60% by weight alumina added, this backing is used as an absorbing thickness, same as before, the goal here is to reduce, as much as possible, the effect of wave reflection. In this case the node is in the middle of the chamber if the phase differences are null (two by two diametrically opposed). However this ring does not create any kind of pressure gradient in height direction, therefore another transducer is added in the bottom of the structure and a reflector at the top of it to induce a half wave and make the particles levitate.

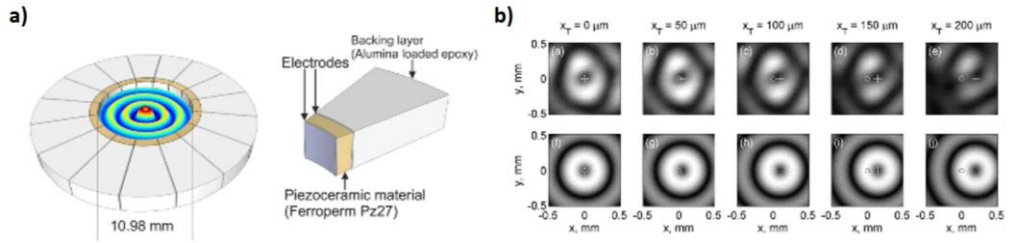

Figure 13 - taken from [52], a), scheme of the 16-element circular array and expected Bessel Function. B), Image of pressure field (Black is zero pressure, White is maximum pressure) while moving the trap position 200um to the right. Up row is the actual experiment the bottom row is the same calculated using a Huygens Model while ignoring boundary effect but including reflection.

The Bessel functions are the radial part of the modes of vibration in a cylindrical cavity, in this particular case the Bessel functions give a zero amplitude at the middle of the cavity if all the excitation are in phase (two by two diametrically opposed). Meaning a small trap point would be situated in the middle of the cavity, and then other trapping 'circle' would be arround it, several of them are posible,

always in a concentric ways. With this radius and the frequency used of 2.35 MHz, five concentric rings are visible.

An extensive numerical study of this Bessel function problem induced by discrete amount of exciting transducers has been made by Grinenko et al [53], it shows that the maximum position for the centre of the concentric trapping rings can be moved by 0.88λ, where λ is the wavelength at this frequency. In this case the maximum distance the middle point of can browse is theoretically 560um. The experiments showed that the trapping position can be controlled within 200 um of the original centre. The difference between this latest number and the theoretical one comes from the non-perfection of the device, the reflection, the boundary effect etc.

This device shows good results preciseness wise, however the maximum magnitude over the position control is low (200 um) and every imperfectness in the complex fabrication process is vastly detrimental for the performances.

Bernassau et al. introduced in 2011 another technique to manipulate particle using phase shift [54], the structure is a heptagon with 0.5mm thick transducer attached to each face of this heptagon. No transducer is facing another, therefore this technique does not rely on standing waves coming from reflection nor facing transducers. In his device the standing waves patterns are created by the activation of two or three transducers from the seven that counts this technique. The transducer are excited at a frequency of aroung 4 MHz with a voltage of 8 V.

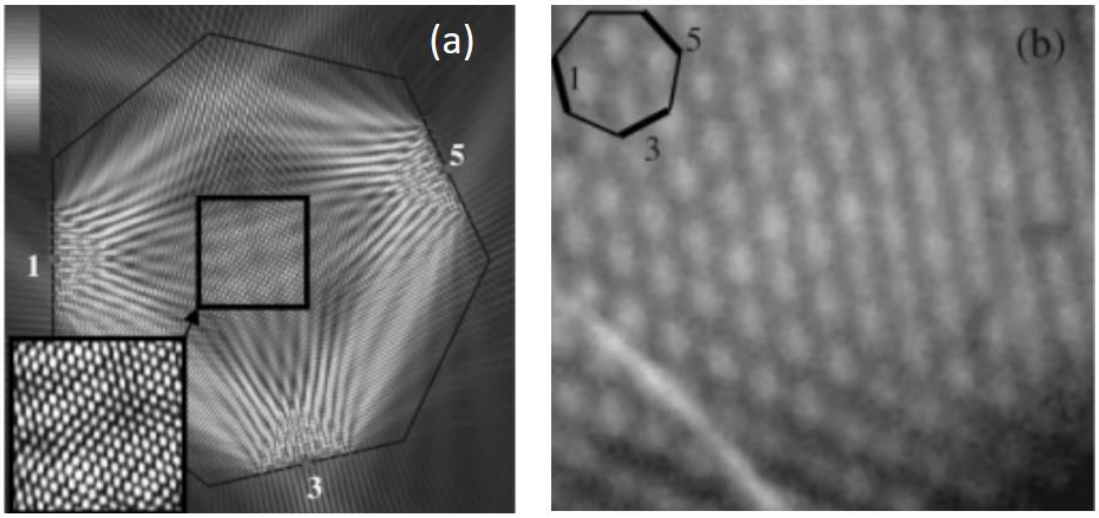

Figure 14 –Taken from [54] (a) Nodes and antinodes created by three excited transducers the configuration 1–3–5 (b) Schlieren image of the acoustic beam pattern in configuration 1–3–5.

Figure 14 shows a Huygens' model based on Huygens' principle, it is used to simulate the acoustic pressure distribution within the chamber with one or more active transducer, in this particular case the transducer 1-3-5 are activated. This modelling shows promising pressure field structure in the middle of the cavity. The device is fabricated using flex circuit, PMMA and a rigid PCB to allow simple connection to each transducer elements. It shows similar results as the simulated ones as shown in Figure 14-b using the Schlieren imaging technique.

This device shows how a heptagon shape can effectively acoid reflections and hence minimizing standing waves. Using shapes having no parrallele sides will be investigate in the case of a planar resonator in chapter 4. In this device activating non-adjacent transducer is the most effective way to have controlled trapping, and in this case changing the phase shift between each transducers results in a change on position of the 10 μm beads.

2.2.1.3 Frequency shift and amplitude modulation

All the techniques reviewed so far are related to trap position manipulation within a middle plane in the cavity, so it is a 2D manipulation, where the radial

force field can be changed but not the axial one. Frequency shift or mode hopping is a technique used to change this so called “plan of manipulation”.

For a planar resonator, as explained above several modes are possible, half wave, thin reflector or quarter wave, with different position of the trap in each of these configuration of the pressure field.

In 2010 a technique to dexterously manipulate this plan of levitation using a rapid switching between the half-wave mode and the quarter-wave mode is experimented [46]. This paper introduce the possibility to have an equilibrium height in the cavity which would be in-between the half wave equilibrium height (middle plan of the cavity) and the quarter wave (next to the reflector) by switching between these two modes rapidly. The paper define α as the ratio of quarter-wave mode time compare to the whole cycle time, which is composed by quarter-wave mode and half wave mode. Three forces are encountered by the beads then, the radiation force coming from the half-wave mode, the radiation force coming from the quarter wave and finally the gravity force which is steady in time. Changing this ratio α would change the equilibrium height of this plane of manipulation.

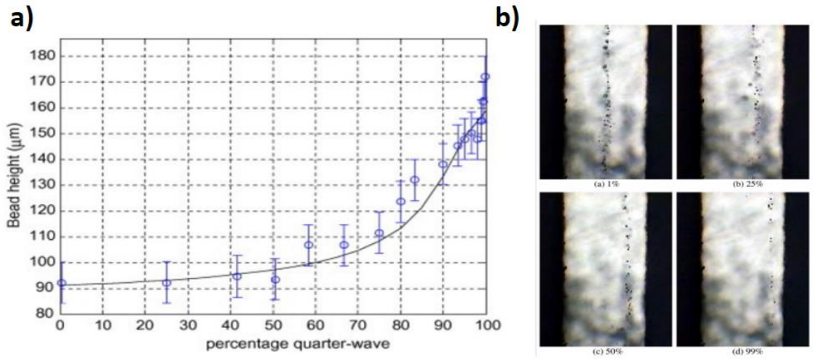

Figure 15- Taken from [46], a) Agglomeration height vs α (steady line is calculated, blue dot is measured) b) Picture of beads levitation plans according to α

It has been shown that it is possible to change the height of the agglomeration plane with a resolution in the order of 10um and predictably via mode switching. This technique has its default, indeed the force linked to each mode can vary overtime depending of the exact geometry of the device which can change over time due to heat, and if the force decreases it would change the ratio effect on the trap position

This section has shown the BAW planar resonators could control the height and lateral position of sole and clusters of aggregates. Moreover acoustic manipulation have shown to be gentle on cells [55, 56] making planar resonator a natural application cell aggregation and 3D tissue culturing. The next section will introduce quickly the benefits of 3D structure of cell aggregates, the advantages of scaffold-free technique. The advantage of acoustic manipulation compared to other kind of technology, finally it will detail acoustic cell manipulation application present in the literature.

2.3 3D cell culturing using acoustophoresis

This section introduces the reason why cell culture using acoustophoresis has attracted a lot of interest in recent years. First the reason why 3D cell culturing is preferred will be exposed, then why scaffold-free technique are favoured and why acoustic seem to be ideal to manipulate particle compared to other type of technology. At the end of the section few recent application for 3D cell culture using acoustic will be detailed

2.3.1 3D cell culturing

Cell culture in two dimensions (2D) has been performed for the past four decades, for all these years this main criticism on this technique was that it assumed that human physiology can be reproduced using cellular monolayer without being able to prove it. In 2015 Ravi et al. reviewed the advantage of using 3D cell structure instead of 2D monolayer [67]. There is now evidence saying that 3D cell culture are closer to in vivo model in many aspect. They offer biologically superior structure [68], better gene/protein expression [69], differentiation [70] and drug susceptibility [71]. Making 3D cell culture ideal for many applications such as drug discovery, pharmacological studies, understanding cell physiology and tissue engineering.

2.3.2 Techniques of 3D cell culturing

Clinical test of a new drug is a long and expensive process, the first step being the in vitro trial of the drug on cell tissue. For step, biologist are particularly keen to produce close to in-vivo tissue as it gives stronger evidence of the non-toxicity and effectiveness of the drug for later commercialisation. To do so 3D cell culture have been extensively used in the past 10 years, with a focus on two mains techniques.

The first one being scaffold and matrix technique [72] is composed of a support that mimic in vivo, some might even incorporate growth factors [73]. It allows very controllable aggregate is size and structure. However this technique is very expensive for large-scale production and there is difficulty in retrieving cells from the structure after the formation.

Forced-floating or agitation-based approaches [74] uses stirring, gravity or centrifugal force couple to a round shape vial to create 3D spheroids. This technique is inexpensive and the aggregate are easy to retrieve. However it is labour intensive and there is no clear control over the structure and size of the cell aggregate, moreover the principle induce heavy shear stress on the cells, which can damage them [75].

Therefore three is a demand for a quick, inexpensive and undemanding technique of tissue engineering to create size/structure controlled tissue. Magnetic and acoustic technique have been the recent candidate. In 2010 Souza et al. published a paper on 3D tissue cultured based on magnetic levitation [76], this paper attracted a lot of attention as it seemed like it was answering all the biologist requests. However it necessitate to incorporate magnetic iron oxide nanoparticles to the cells in order to make them react to the magnetic fields. This taking this cells further apart from in vivo. Chen et al. in 2016 revealed their innovative technique of cell culture using acoustophoresis [77], its SAW based produce high-throughput continuous fabrication of 150 size-controllable cell aggregate. This paper will be detailed in the next section as it represent a compelling technique of cell tissue. Acoustophoresis has been described as being particularly good as it allows good synergy with scaffold-based technique for the creation or complex multi-type aggregates [78].

2.3.3 Applications of 3D cell culturing using acoustophoresis

The major advantages of our acoustic levitated cell culture techniques are that they are label-free and non-invasive , they are gel free and avoid “artificial” matrices influencing cell behaviours, all of which making them good for tissue engineering among other applications drug screening and aggregate physiology studies etc.

In this section two recent applications using acoustic cell aggregation are explored.

2.3.3.1 SAW 3D spheroids production

Chen et al. explore the possibility for the technique introduced in section 2.3.2 to produce cell spheroids [77]. The SAW travel on the surface of the substrate and radiate in the fluid cavity placed on this substrate. The radiation force push the particle laterally, and is coupled with microstreaming forming to levitate cells in the vertical direction as shown in .

The device is 2 mm x 2 mm PDMS micro chamber bonded to a $LiNbO_3$ piezoelectric substrate. Four IDTs are deposited on each side of the chamber. This IDT have 40 pairs of electrodes with inter branch width of 75 μm. The method of fabrication is detailed in a previous paper [81].

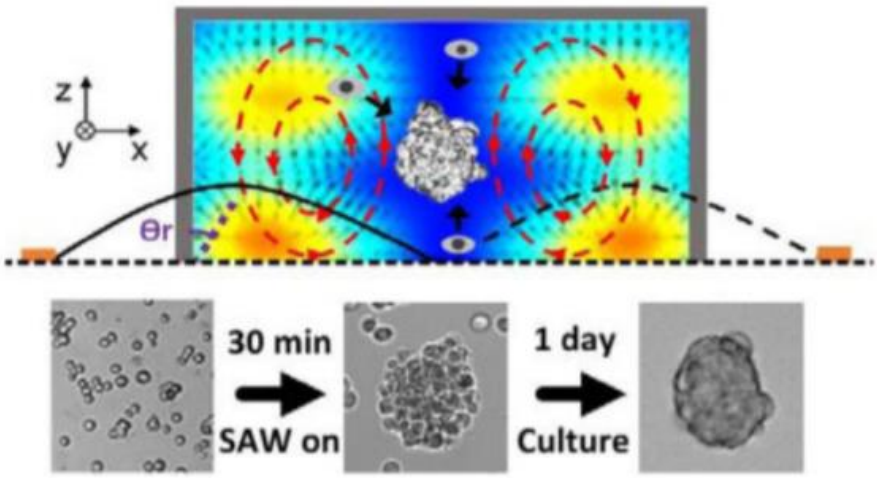

Figure 16 – diagram for the cell culture technique using SAW for cell spheroids production taken from [77]

This device is able to control the size of the spheroid by changing cell concentration in the PDMS chamber, the show successful aggregation of 30 to 90 μm diameter cell spheroid with input cell concentration of respectively of 2 and 17 × 10^6. The cell aggregation process took 30min and after up to 7 days more than 95% of the cells were alive, independently of the aggregate size.

Aggregates produce this way would be ideal for drug screening, to prove it the authors tested their aggregate with anti-cancer drug 5-fluorouracil and showed significant difference between the spheroids and 2D culture for different drug concentrations. *$p < 0.01$.

This paper attracted a lot of attention from biologist as it represent a quick and relatively inexpensive way to produce cell tissue for drug screening, moreover it opens possibilities for more complex bio-printing [78].

A potential downside of such technique is that it relates on microstreaming to levitate cells making the levitation height dependent of the aggregate size. Moreover the fabrication process is complex and necessitate high grade equipment. This is why is this thesis BAW approach is preferred.

2.3.3.2 The Production of cartilage tissue using BAW planar resonator

Jonnalagadda et al. developed in 2018 a BAW planar resonator bioreactor for multiple cell aggregation in parallel [82]. I took part in the designing and the fabrication of this bioreactor. The bioreactor fabricated in this paper is comparable in many aspect with the one introduce in chapter 6 of this thesis.

An open layered resonator configuration is adopted as is allows free gas exchange with the fluid, avoiding bubble cavitation within the resonator. There are excited by a PZ26 transducer at a half-wave mode frequency of 1.5 MHz. A swept frequency is used around this half-wave mode frequency. Depending on the range and the frequency of this sweep, different drag force is applied by the surrounding fluid on the aggregate. It comes from the different lateral modes findable around the main half-wave frequency. Therefore the aggregates are shaken as different frequency are activated.

The bioreactor consist of four planar resonator maintains in one sealed chamber with a fluid exchanger for long-time cell culture under levitation. Four resonators are used in order to increase the parallel production of cell aggregates.

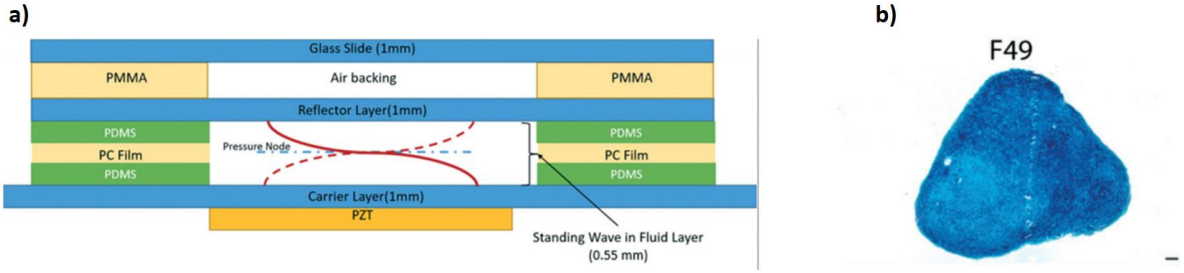

Figure 17 – taken from [82] a) Schematic diagram detailing resonator design and the dimensions of each layer, b) Cartilage example after 21 days of acoustic levitated culture

Previously the author demonstrated that this device gives robust cells viability [83]. The focal interest of this paper is to prove that BAW planar resonator can effectively mechanically stimulate human articular chondrocytes (human bone) but this is the case for any of cell types. This is achieved without adding any level of complexity to the device, just by sweeping the excited frequency.

2.4 Conclusion on literature review

This literature review showed that [83]acoustic has been successfully used in the past to configure or manipulate micro particles. While SAW seems to have the favour of the scientific community for now. BAW-based planar resonator is appealing due to its low-tech aspect, inexpensiveness and its possibility to finely control the height of the particle. However SAW based device seems to have the upper hand on lateral configuration of particles. This thesis will explore the reason why lateral manipulation in a planar resonator is challenging and how to reduce this inconvenience, then this device will introduce a new and compelling way to configure and manipulate particles aggregate on a BAW-based planar resonator.

In addition this literature review showed that particle manipulation is particularly of interest for biologist, and that recently acoustic have attracted a lot of interest by them. SAW-based bioreactor are on the verge of being widely used for tissue engineering and drug screening. But BAW-based bioreactor are usable to study the mechanical stimulation. This thesis will use the knowledge and technique developed to control the lateral radiation force field in a planar resonator to produce a bioreactor designed to produce cell aggregate for drug screening. The size and shape of such aggregate will be studied, in addition with a comparison with 2D monolayer and pellet culture reactor to anti-cancer drug among other aspects.

In order to understand the mechanism behind the structure of the acoustic radiation force field two type of modelling are introduced, the 1D modelling to study the thickness acoustic mode, and 2D and 3D modelling to have an understanding of the lateral acoustic mode. They are introduced in next chapter before being used in chapter 4.

Chapter 3: Planar resonator modelling

Modelling deeply changed the designing part of any research or industrial projects since a couple of decades. It is now essential when trying out some configuration or properties of a device without having to build it. In addition, it saves time on the fabrication and allows to change parameters one by one, to tell their effects. Different techniques of modelling have been used during this project: one and two-dimensional modelling. The second one grants more precision and the visualisation of the lateral effects, which will be explained in a latter chapter.

In this chapter the modelling tools used in subsequent chapters are introduced. In this thesis, modelling is used to draw conclusions about the sensitivity of trapping forces to device parameters (chapters 4), and also as an aid to designing practical devices (chapter 6). The tools include both analytical 1D models and finite element models (1D and 2D).

The analytical 1D model is easy to use, required low computing power and time and gives reasonably estimates for the thickness mode of a planar resonator. The finite element models are more demanding in computing power and time, and are harder to set-up, however, they allow quantification of the lateral effects that form a major part of this thesis.

3.1 KLM - Impedance transfer model (one-dimensional)

The goal of the impedance transfer model is to model a planar resonator as introduced in section 2.2.1. This method was first used to model this structure by Hill et al. in 2000 [84] [85], a Matlab code using this method was produced my Hill et al. in 2002 [86] and he kindly provided it to us.t.

At this stage the planar resonator is considerate to have laterally infinite layer, therefore the pressure field is only 1D, on the vertical direction. Thus, the force vectors are directed in 1D as well, up or down.

The impedance transfer method has been developed where the properties of the acoustic field are given by electrical equivalent, added with force transfer equations and impedance. This method is good enough to visualize general behaviours, pressure amplitude, structures, and force potential depending of the particles' properties. However because of its unidimensionality, Finite element analysis (FEA) will be used later to model lateral component of the acoustic field.

The pressure versus voltage characteristics of any piezoelectric transducer can be understood based on the circuit model developed by Krimholtz, Leedom, and Matthaei in 1970 known as the KLM model [87]. A diagram illustrating this model is shown below

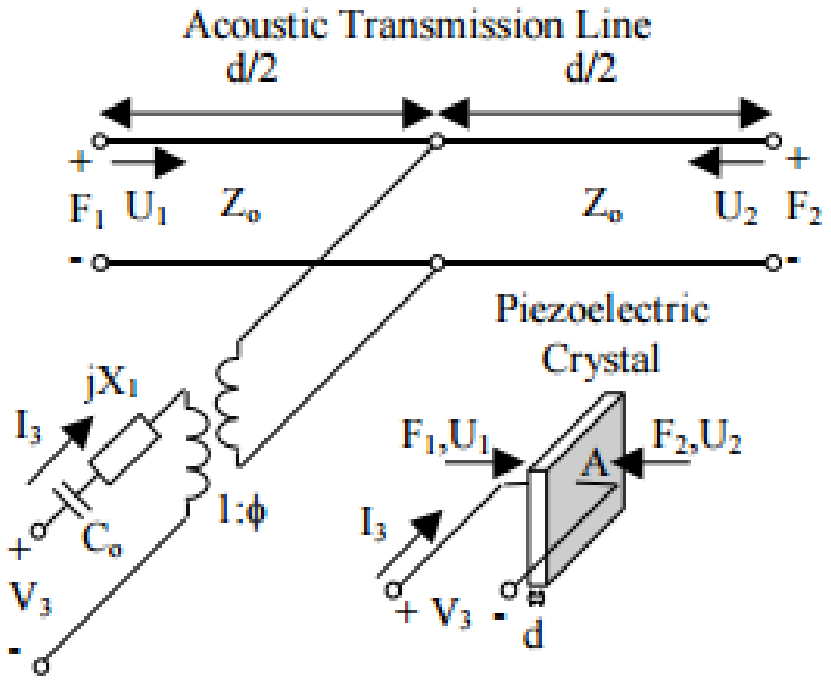

Figure 18- The KLM model of a piezoelectric transducer, picture taken from [87].

The 'electric' part is composed of clamped capacitance, *C0*, and a second reactive term *jX1*. The 'mechanical' part of the KLM circuit is equivalent to a lossy acoustical transmission line, and *Φ* is the transformer ratio of electric voltage to mechanical force. Equivalent KLM network of a thickness- mode piezoelectric transducer, with thickness '*d*'. The circuit parameters of the piezoelectric material are defined as follows: once the piezo ceramic transducer model has been

implemented, acoustical layers must be considered, they represent the stacks of layer forming the layered resonator. The carrier, the fluid layer and the reflector.

In the code provided by Prof. Hill [86] the inputs are the thickness, the density, the speed of sound and Q factor of all layers. In addition the transducer voltage, the dielectric loss, the piezo constant 'h', the permittivity of the transducer are required, all of which can be find in material datasheets.

The outputs are three graphs, the performance number vs frequency, the performance number is defined by Groschl et al. in 1998 as a resonator efficiency number [89], the impedance of the planar resonator vs the frequency, and finally the acoustic energy density vs the frequency, this latest graph is the one used the most to find the frequency resonance which relate to the maximum of acoustic energy density in the fluid layer. At this frequency the pressure structure throughout the planar resonator can be displayed. Inputs and outputs are shown in Figure 19

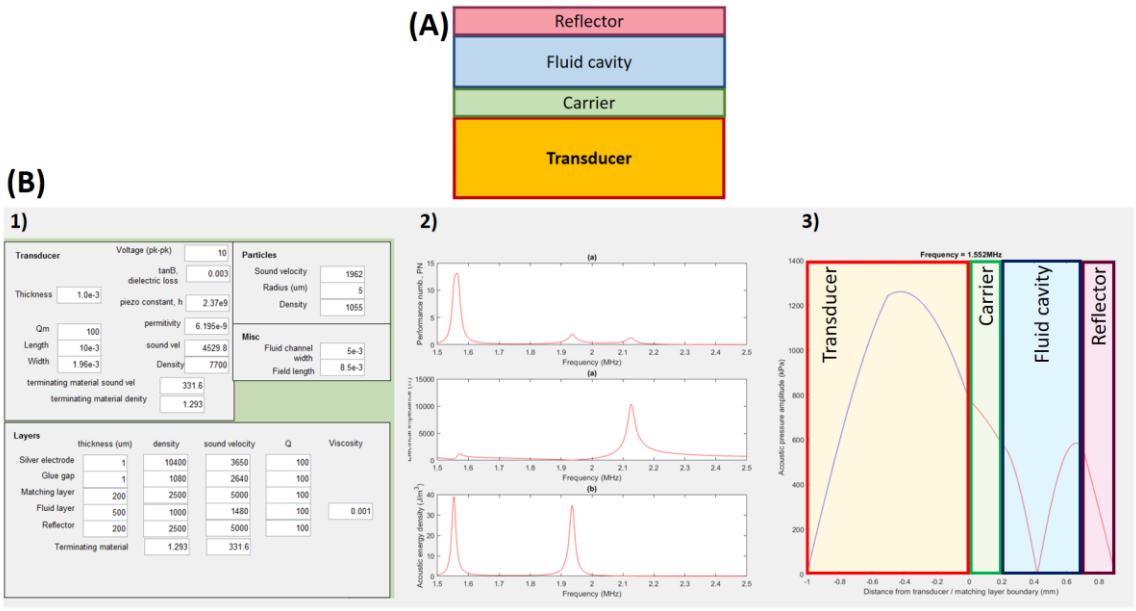

Figure 19- (A) schematic of a typical planar resonator, (B)1) Input window, the planar resonator modelled is the following, Transducer (PZ26): 1 mm, Carrier (Glass):0.2 mm, Fluid cavity (Water); 0.5 mm, Reflector (Glass): 0.2 mm, (B)2) output graphs a) performance number vs frequency, b) the impedance of the planar resonator vs the frequency, c) acoustic energy density vs the frequency. (B)3) present the pressure depending on the position on the acoustic resonator, the blue line represents pressure magnitude in the

transducer whereas the red line represents the pressure magnitude in the other layers. (B)2) & (B)3) have been obtained with the inputs of (B)1).

This KLM – 1 dimensional modelling is used in the early process of planar resonator design. It is quick and easy to use, it is cheap in computing power. It permits to know before fabrication if a thickness combination of layers would give effective acoustic modes and the expected frequencies of this acoustic modes.

However to observe and quantify the lateral effect that can be expected in a planar resonator 2D finite element analysis modelling has to be used.

3.2 Multiphysics finite element modelling (two-dimensional)

COMSOL multiphysics is a finite element analysis solver and simulation software. Finite element method, or FEM, is a numeral technique for finding approximate solution to a complex problem with partial differential equations. The technique used is to subdivide the whole field in smaller parts and to solve the subdomains one by one. The accuracy of the results varies with the subdomains' size: the smaller they are, the smaller the final error would be, however the calculus time would increase as the domain size decreases

Comsol multiphysics is mainly used for physics and engineering application, the main asset of this software is that it models multiphysics or coupled phenomena, in our case, piezoelectric (PZT), Mechanics (PZT, and pressure potentially) and fluid mechanics (for the fluid pressure field). The software allows adding equation to its already exhaustive package, in our case the potential energy density, the kinetic energy density, and the primary radiation force are added, equation (1) to (6) in section 2.1.1

3.3 Radiation force from energy

In physics, potential energy is the energy that an object has due to its position in a force field or that a system has due to the configuration of its parts. For the acoustic potential energy, the force field concerned is the radiation force one, which is related to the gradient of pressure.

The kinetic energy of an object is the energy that it possesses due to its motion. It is defined as the work needed to accelerate a body of a given mass from rest to its stated velocity. In our fluid layer, the velocity of the fluid is greater at the low-pressure points, so at the pressure node. Indeed, the velocity of the fluid v, is given by this formula, which comes from Bernoulli's equation: $v = \sqrt{\frac{2q}{\rho}}$, with q the dynamic pressure and ρ is the fluid density. The dynamic pressure or velocity pressure is the increase in a moving fluid's pressure over its static value due to its motion. In the case of our device, at the resonance frequency, $q = P_{node} - P_{antinode}$.

In a planar resonator the acoustic radiation force is expected to dominate the total force field (which consists of radiation force field, drag-force, Bjerknes force, see section 2.2), radiation force field equations (1) to (6) showed that in the case of particles are denser and less compressible that the fluid in which they suspend (which is the case for the case studied in this report), the kinetic energy is a attracting energy and whereas the potential is repulsive one. It means that in two dimensional modelling, the particles are expected to be attracted to the maximum of E_{kin} or the minimum of E_{pot}

3.4 Two-dimensional model hypothesis

A planar resonator is a complex multiphysics device, using COMSOL multiphysics, the transducer is modelled as a 'Electrostatics' and a 'Solid mechanics' layer, the glass reflector and carrier are modelled as 'Solid mechanics' layers, the fluid cavity is modelled as 'Pressure acoustics layer', some less important layer are not modelled to simplify the model and decrease simulation time, the coupling between transducer and carrier (glue or glycerol), the side wall

of the channel, the fluidic connection set up, the typical planar resonator 2D physics and material is shown in Figure 20-a)

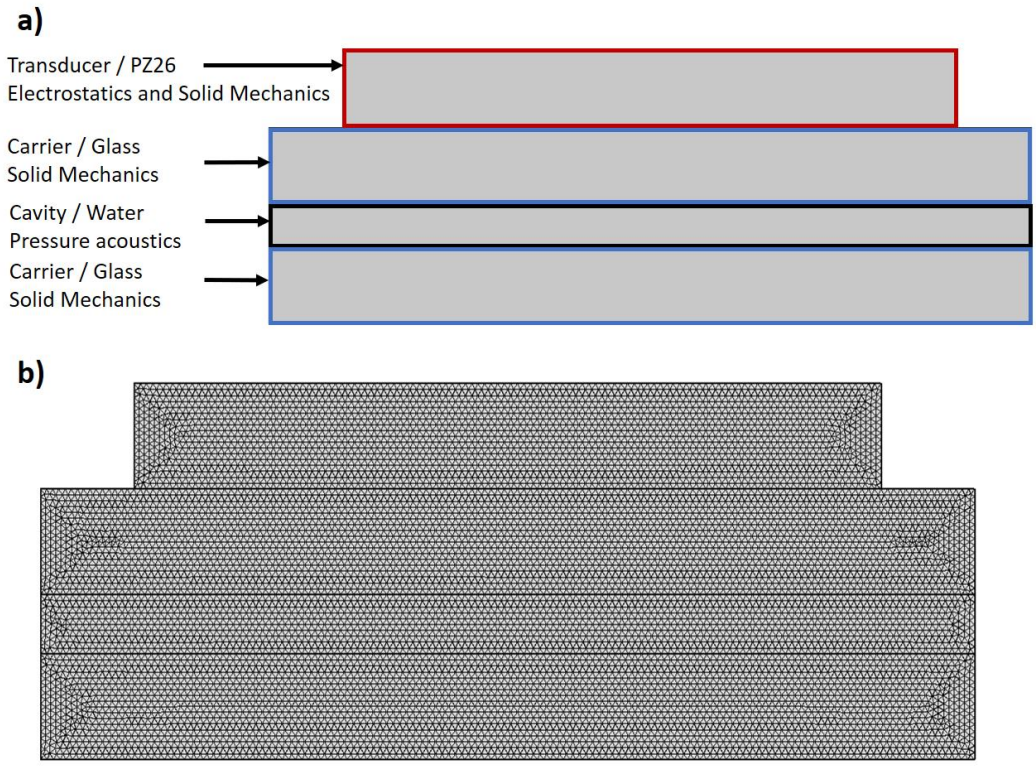

Figure 20- a) Modelled layers with their 'physics' modelled in COMSOL and their material, b) mesh for at λ/16

The mesh size is chosen to be equal to λ/16, this being chose after the investigation of colleagues on the effect of mesh size 2D modelling results for planar resonator[90] [91], where λ is the wave length in the fluid modelled in the cavity, which is water in all cases in this report, as shown in Figure 20-b)

The boundary condition of the mechanical part are modelled as free surface which is sensible as the planar resonator would perform in air.

The boundary condition of the fluid cavity is 'acoustic hard boundary' which means that all waves would reflect back to the fluid. In actual planar resonator it would depend on the acoustic and mechanics properties of the material chosen to form the cavity, a part would be absorbed, transmitted, refracted and diffracted, the different behaviour of incident sound wave hitting an interface with different acoustic impedance is showed in Figure 21. It is sensible because, although some part would be transmitted to the material, this material would have a final interface

with air which have widely different acoustic impedance than water or tape (most of the device that will be presented in this report use tape to form the different cavities), making it an excellent reflector. It has been decided to not model the tape and the glycerol/epoxy layer that couple the transducer to the carrier glass in order to simplify an already complex system. Moreover the silicone-based tape used as separator has comparable acoustic impedence with water making it an almost transparent material acoustic wise. As it will be demonstrated in section 5.4.1.1.

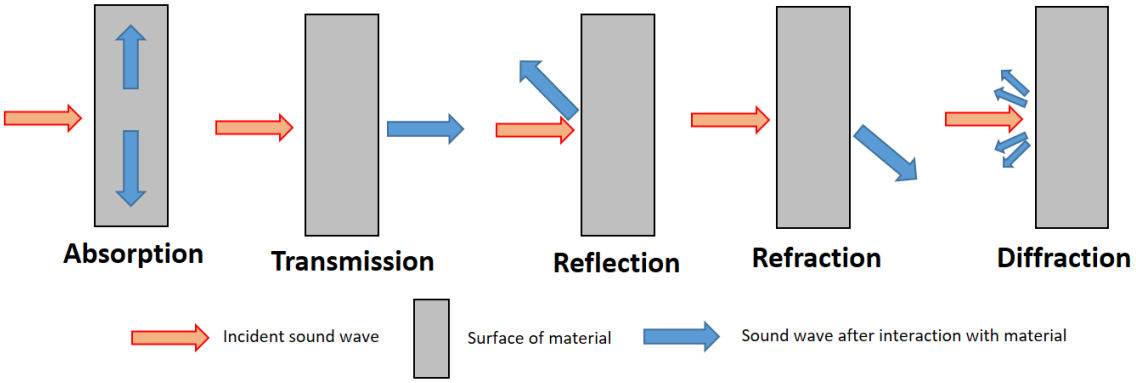

Figure 21 - Sound wave interactions with material

The different boundary condition are showed in Figure 22

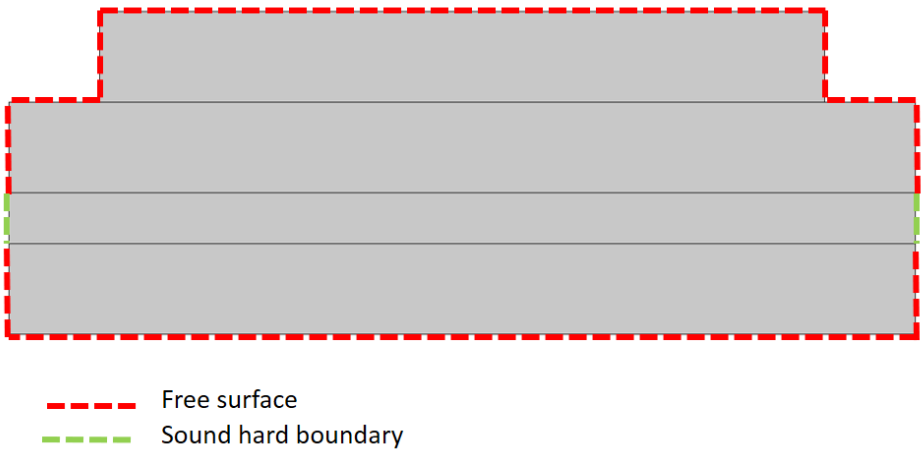

Figure 22 –Boundary condition of planar resonator modelled using COMSOL multiphysics

To have a model with results closer to reality a mechanical Rayleigh damping has been added to the PZT, the carrier, and the reflector.

Rayleigh damping is viscous damping that is proportional to a linear combination of mass and stiffness. The damping matrix *C* is given by $C = \mu M + \lambda K$ where *M*, *K* are the mass and stiffness matrices respectively and μ, λ are constants of proportionality.

Rayleigh damping does afford certain mathematical conveniences and is widely used to model internal structural damping [93]. One of the less attractive features of Rayleigh damping is that the achieved damping ratio varies as response frequency varies. The stiffness proportional term contributes damping that is linearly proportional to response frequency and the mass proportional term contributes damping that is inversely proportional to response frequency. Mathematically, these frequency dependencies can be seen in the formula for damping ratio $\xi = \pi (\mu/f + \lambda f)$ where f is the response frequency.

3.5 Modelling of infinite planar resonator in 2D and comparison with 1D model.

Both models are useful for different investigation, the 1D model or KLM model is useful because quick and easy to set up. Whereas 2D modelling is useful to model the lateral effect linked to lateral configuration of device, for instance the lateral component of a complex multidirectional acoustic radiation force field due to axial non-symmetry or lateral gradient of the pressure field in the fluid cavity. Which is always the case in real device. The design process is using both 1D and 2D modelling, the first step being to model in 1D the planar resonator with each thickness to check to strength and configuration we could expect for the acoustic standing wave.

The second step is to design a 2D model using COMSOL, this time the lateral effect would be modelled. To check to credibility of our 2D model, a comparison with 1D model is undertaken. The structure used is strictly the same in both case. A 1.03mm thick PZT (h=2.37e9, c=4529 $m.s^{-1}$, $\rho = 7700$ $kg.m^{-3}$) on top of a 0.17mm glass (c=5510$m.s^{-1}$, ρ = 2540 $kg.m^{-3}$) above a water layer of 0.45mm thick (c= 1480$m.s^{-1}$, ρ= 1000 $kg.m^{-3)}$, finally the same thin carrier glass is used as a reflector.

To be able to compare a 1D model and a 2D model, this one must be defined as an infinite planar resonator, meaning that the lateral border of the PZT, the glass and the fluid cavity must have a symmetric periodic condition, to avoid any lateral effect. No lateral gradient of the kinetic energy is achieved as shown in Figure 23.

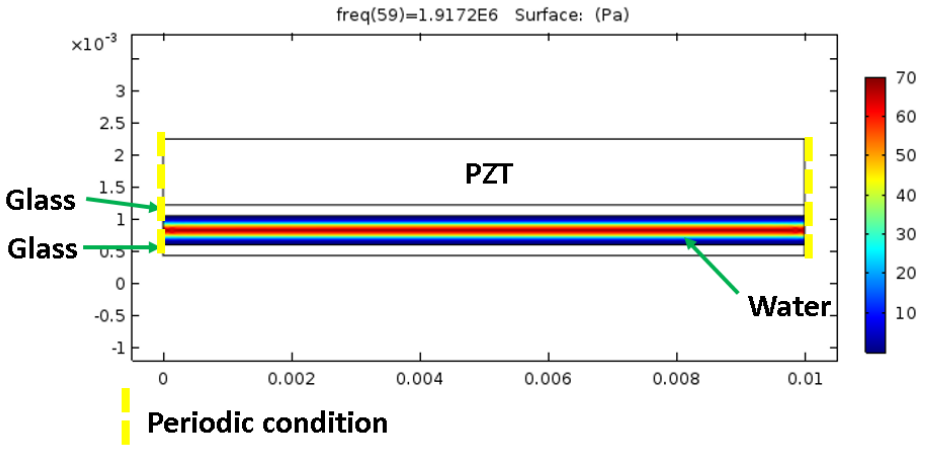

Figure 23- Kinetic Energy graph in an infinite planar resonator driven at the resonance frequency, symmetric periodic conditions have been included at all lateral end interface.

The 2D model of the lateral resonator is acting like a perfect planar resonator driven at a half wave frequency. The kinetic energy maximum position represents the trapping position in the manipulation chamber. Thereafter the objective is to compare this latest result to the one obtained with a 1D model using the same properties, the purpose is to validate our 2D model by correlation with an already verified one. The two plots are visible in Figure 24.

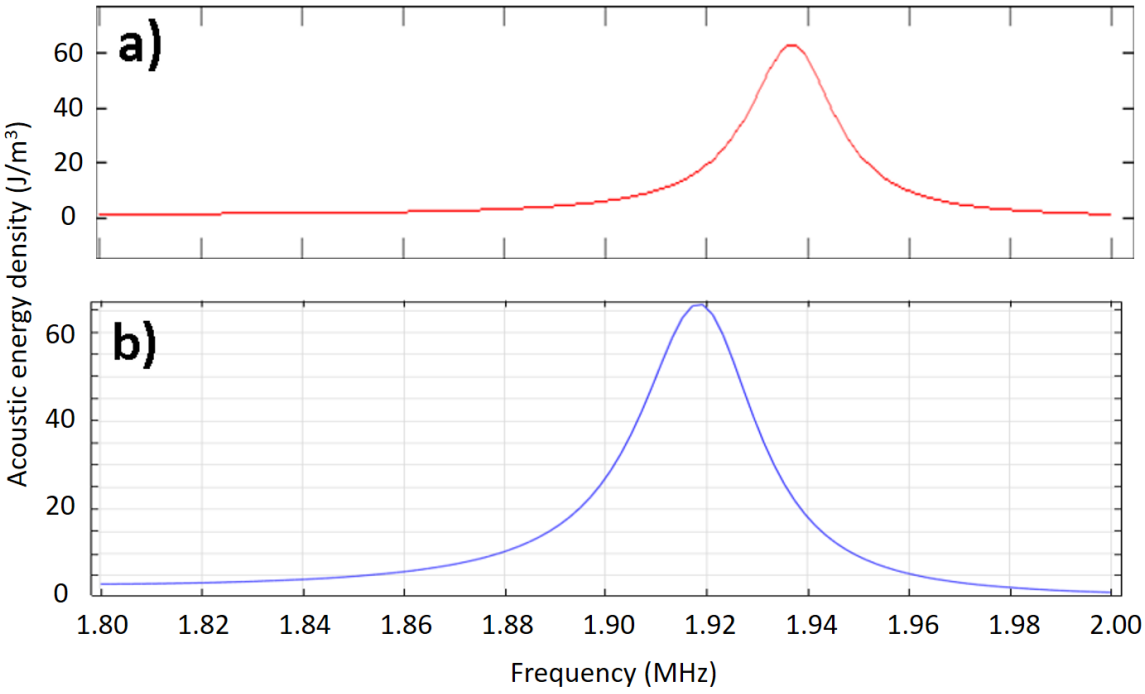

Figure 24 – Energy density in the manipulation cavity depending of the frequency; (a) 1D model, (b) 2D model.

The energy density plots are identical from value perspective (65 J.m^{-3} for 1D and 65 for 2D) and close from a frequency perspective (1.937 MHz for 1D 1.917 MHz for 2D, 1% difference), which is a good hint showing both 1D and 2D models as viable model. To prove furthermore their likelihood a plot of the pressure field throughout the whole device axially is done in both 1D and 2D, at their resonance frequencies. In the fluid cavity the acoustic pressure is displayed, in the solid areas the normal stress is displayed both is Pascal as displayed in Figure 25.

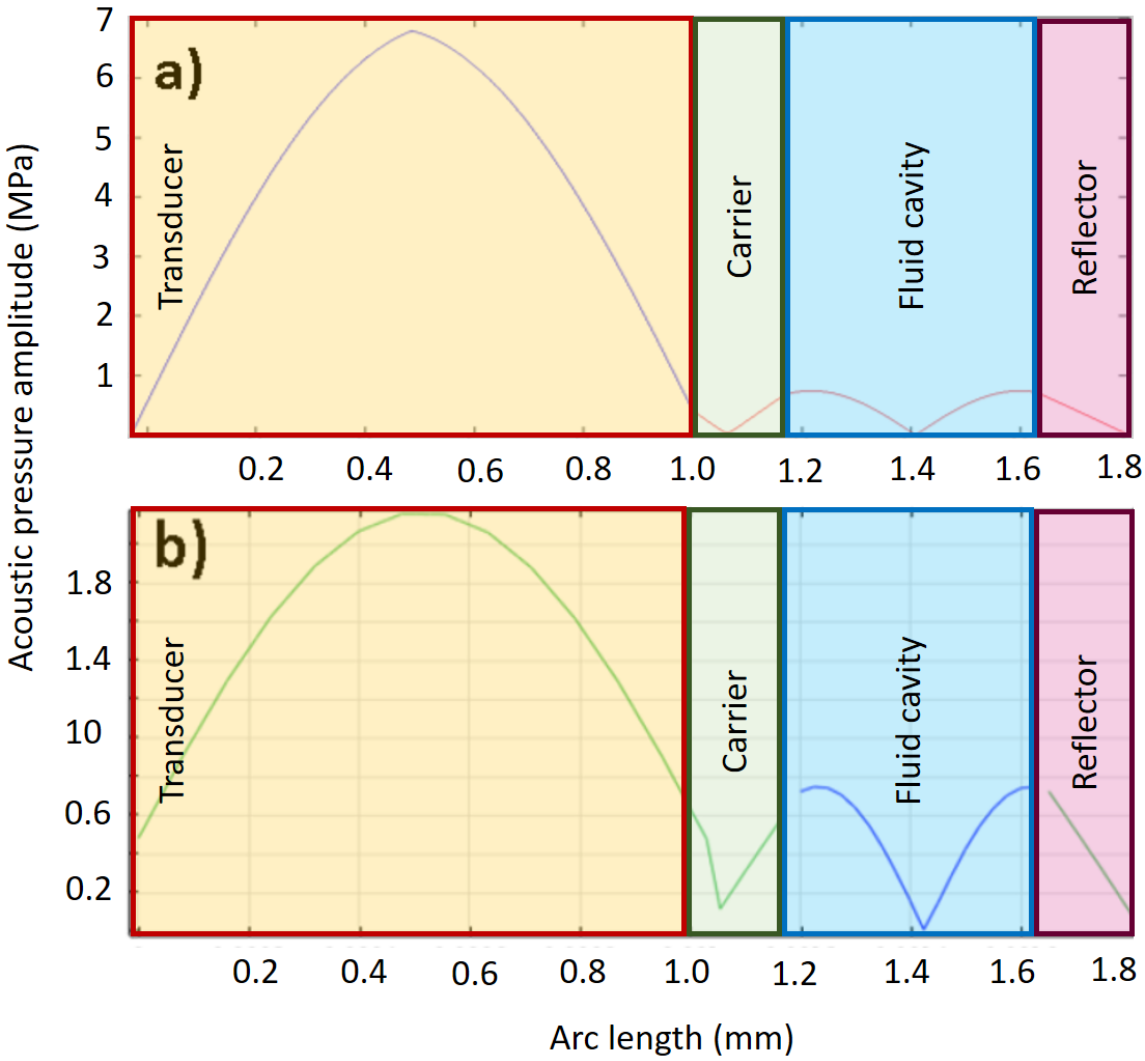

Figure 25- Pressure value throughout the device at the half-wave mode frequency, top to bottom, transducer to reflector; (a) 1D model at 1.937 MHz, (b) 2D model at 1.917 MHz, the green line represent normal stress in solids, and the blue line represent acoustic pressure in fluid.

We can note that the results are similar but shows differences, in value for the pressure plot (especially in the PZT) and in frequency in the energy density plot. It can be explained by the meshing coarseness or a Multiphysics effect showing in 2D and not in 1D. Nevertheless, they are highly comparable therefore both usable for latter investigation.

In the next chapter the lateral component of acoustic mode will be investigated using the FEA modelling using the boundary condition introduced in section 3.4

3.6 Summary

In this chapter, the two modelling techniques used in this thesis have been carefully described, including the underlying hypothesis and approximations. The comparison between both simulation techniques on a 1D model gave us similar results, giving confidence that they are accurately formulated. If we are interested in the thickness mode of a planar resonator (i.e. where lateral modes are not significant), the impedance transfer model is sufficient, and much quicker to set up and to run. However, as the next chapter shows, it is hard to predict *a priori* when lateral modes are going to be significant, and two dimensional models will generally be required, although the 1D models remain useful as practical design tools for choosing layer thicknesses and understanding how to create effective half-wave resonators.

In the next chapter this two type of modelling introduced here are used to model planar resonator, with a focus on the lateral configuration of the radiation force field in the fluid layer.

Chapter 4: Investigation of lateral resonances in planar resonators, and their sensitivity to design parameters

In simple 1D models resonances in planar resonators form trapping plane at the pressure node. However, in real devices the resonances frequently have significant variations in the lateral directions, giving rise to forces in those directions which tend to create trapping into lines and agglomerates. There has been little previous work investigating these features and how to either supress them or intentionally direct them. This chapter explores how sensitive these lateral resonances are to geometrical parameters of the device design.

Initially 2D models are used to examine the effect of transducer width, transducer position compared to the cavity, the transducer side angle and the cavity width. The effect of the shape of both the transducer and the cavity is then studied using a 3D model.

Finally, experiments using particle tracking are presented for a range of device shapes and sizes in order to confirm the findings.

4.1 Introduction

Because the planar resonator is a 3D structure that vibrate in all direction, in some case, the acoustic mode desired (half-wave for example) excite a complex three dimensional mode having strong lateral component [95, 96]. This can be detrimental for fine control using planar resonator, or the production of large cell sheet under levitation, but can be used for the production of numerous 3D smaller particle aggregates, as shown in chapter 6 of this report. Figure 26 shows an example where the final position of particles is dictate by the lateral component of the half-wave acoustic mode. This picture is a top view of a planar resonator drove

at 1.72 MHz at 8 Vpp after 1 min with the fluid layer filled with a solution of water and 10 μm polystyrene beads with a concentration of $5x10^5$ particles/mL. The picture is taken on the direct transducer axis, the transducer is coupled to the carrier situated on the bottom of the fluid layer. This picture shows line arrangement of the particle dictated by the lateral force field, in the case the non-controlled lateral force field was cancelled out, we would see an even distribution of particle in the field of view.

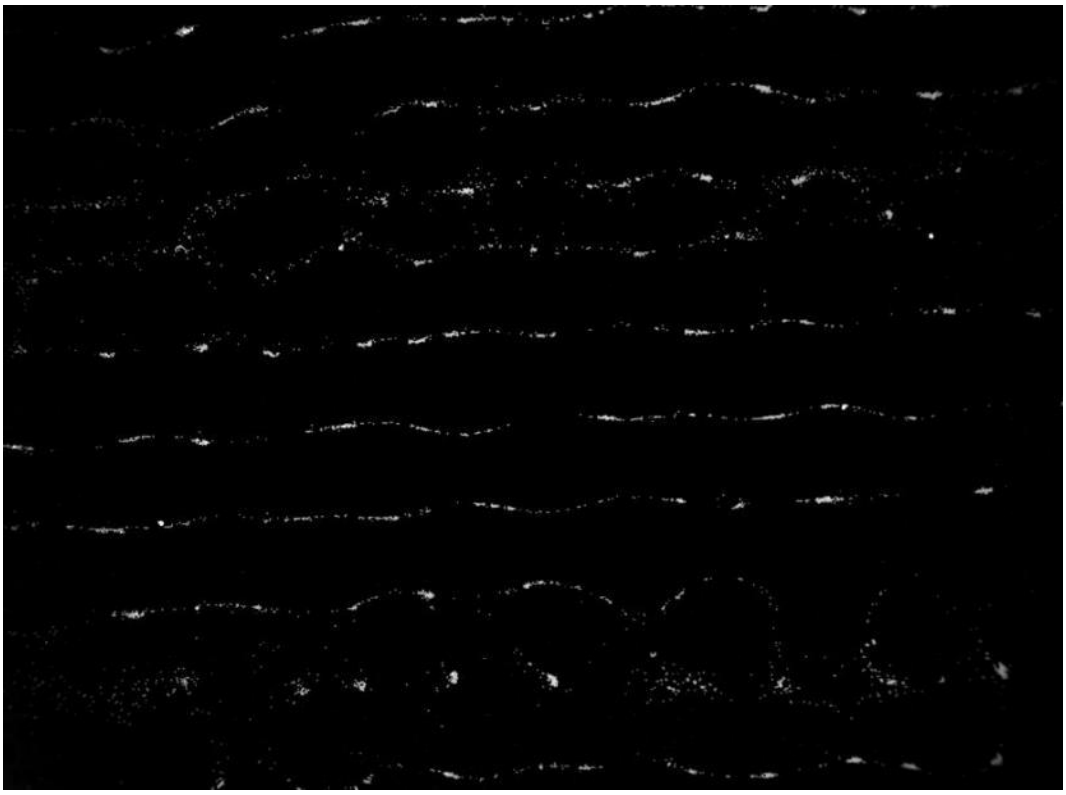

Figure 26- Example of particle final position in a planar resonator being driven at half-wave mode frequency. The half wave mode is disrupt by a non-controlled lateral cavity mode, dominating the final configuration of particles. (Particles are 10 um polyester beads, cavity of 420 um filled with water, driven at 1.72 MHz)

In this chapter, this effect is investigated. First a 1D modelling will be performed to show what acoustic pressure and nominal stress configuration to be expected in a planar resonator that is possible to replicate in laboratory, and to locate coarsely the axial resonance frequency. The 2D modelling is used to compare the effect of potential and kinetic energy in the structure of the acoustic radiation force field. The plane of levitation is then studied more into detail.

Then the flatness of this levitation plane and the strength of the force field associated with it will be compared with one another while changing some characteristic of the planar resonator design. The design parameters studied using this 2D finite element analysis model are; total width of cavity, width of piezo transducer, angle of transducer sides, and position of the transducer compared to the fluid filled cavity. Finally, a shape study of the cavity and the transducer is carried out using a 3D FEA model of the same planar resonator thickness characteristics. Two shapes of interest are compared, the rectangular parallelepiped and an asymmetric shape. As for the 2D model, the qualitative comparison is followed by a quantitative analysis investigating the flatness of the resonance plane, and the magnitude of lateral force.

Finally, experiments confirm the conclusion extracted from the model and their analysis, this experiment are performed using a set of planar resonators with different design fabricated for this purpose, using laser cutter, silicone tape, glass and piezo ceramic transducer. The acoustic radiation force field in the fluid cavity is extracted by studying the movement of particle in the fluid chamber employing particle image velocimetry.

4.2 Design and Modelling

4.2.1 Device configuration

As introduced in section 2.2.1 the planar resonator can excite a wide range of thickness mode, in this report, the half-wave mode is studied but the reasoning and the conclusions can be transposed to other acoustic mode. Because we want to confirm the conclusion induced by the finite element analysis modelling, the thickness chosen in the model work is chosen using the thickness material at disposal it allows us to later produce device modelled.

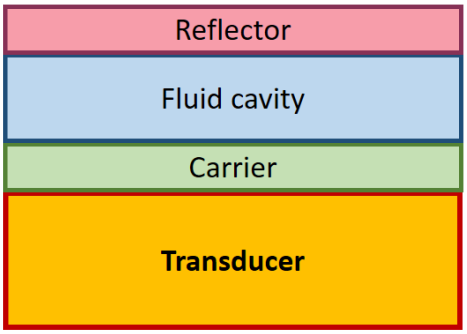

Figure 27 - Layered components of a planar resonator.

The carrier and the reflector will be made using usual 25x75x0.17mm thin glass slide, the tape forms the cavity between both and therefore the cavity is necessary smaller than 25x75mm, a cavity of 15x45 mm is chosen arbitrarily. This cavity is formed by stacking three layers of 0.14mm 3M 9731silicone adhesive tape (3M, St. Paul, MN, US) for a total thickness of 0.42mm, this tape is laser cut beforehand. The carrier and reflector are made of a 0.17 0-CON 161 thick glass (Logitech, Old Kilpatrick, Glasgow, UK). The PZ26 piezoelectric transducer (Ferroperm piezoceramics, Kvistgaard, Denmark) has a thickness of 1mm and is coupled to the glass carrier using 15 mL glycerol, this volume is chosen because it is found empirically to be the perfect amount of “wetting” to have strong surface adhesion between the transducer and the carrier. It allows the coupling to be non-permanent and therefore the piezo to be reusable, plus the adhesion is so strong the transducer does not move. This set-up in cheap and easily reproducible.

4.2.2 One dimensional modelling.

A one-dimensional equivalent-circuit transducer model coupled with an acoustic impedance transfer model [97] is used to estimate promising thickness combinations and their associated resonance frequencies for planar resonators. This modelling method approximates the structure as an infinite planar structure with plane waves traveling only in the axial direction (transducer to reflector). Even though it is does not model lateral component of the acoustic modes, it was useful to explore promising combinations of layer thickness. To model precisely the

planar resonator, the material chosen have to have known properties. Properties used are presented in Table1, they come from datasheet provided by suppliers.

Table 1- Modelled properties and layer dimensions

Layer	Material	Density (kg.m^{-3})	Speed of soud (m/s)	Thickness (µm)
Transducer	PZT (PZ26)	7700	4530	1000
Carrier	Glass	2500	5000	170
Fluid	Water	1000	1480	420
Particle	Polystere	1055	1962	Diameter 10
Reflector	Glass	2500	5000	170

In Figure 28 the pressure plot is shown, and we see that a half wave mode is excited in the levitation cavity, indeed the pressure minimum is in the cavity and situated 180 um from interface between the carrier layer and the cavity layer, the place of minimum pressure coincide with the place of maximum velocity, hence the trap point. This strong resonance is predicted at 1.77 MHz.

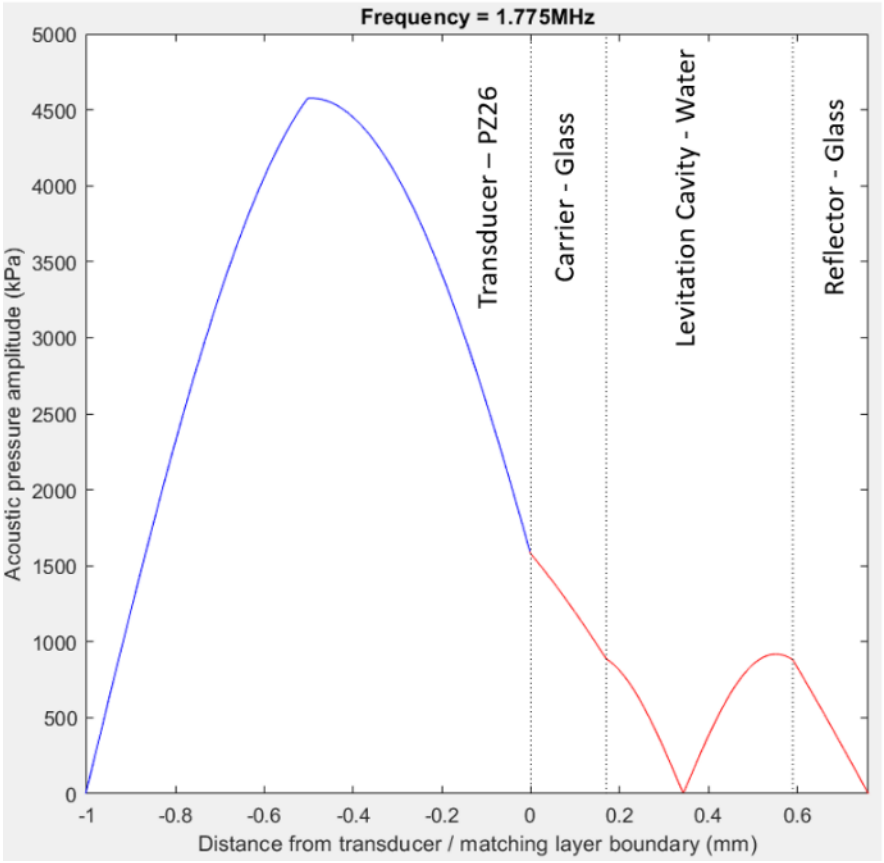

Figure 28 –Pressure distribution through the thickness of the modelled planar resonator from the 1D simulation at F= 1.775 MHz with the characteristic presented in table 1.

4.2.3 Two dimensional Finite Element Analysis

In order to model the lateral acoustic field, the planar resonator introduced above is modelled using 2D finite element analysis (FEA; Comsol multiphysics, Comsol Ltd, Hertfordshire, UK). The mesh, hypothesis and boundary conditions are introduced in section 3.5. The properties and thickness of this model are as described in table 1.

The initial model introduced here is shown in Figure 29-a) has a cavity width of 15mm, carrier and a reflector width of 15mm fitting the cavity and a transducer of 12mm nearly in the middle of cavity,0.05mm to the right of the exact middle. This is because perfect symmetry can induce non-observable aberration. The lateral wall of the cavity, the carrier and the transducer are vertical, since most transducers are sold as rectangular parallelepiped, and most cavities fabrication techniques (see section 4.6.1) give orthogonal walls compare to the carrier planes. A Q-factors of 100 is applied to all solid materials in this model, which is an arbitrary value taken because it is the transduce Q-factor from datasheet. The results in this section do not depend on the Q-factor – varying it over a plausible range tends to change the absolute amplitude, but preserves the geometric distribution of forces and relative amplitudes of forces. Rayleigh damping is modelled in the transducer, carrier and reflector with a coefficient-β of 9.10^{-10}, this value is obtained using the formula for a Q-factor of 100 and a frequency of 1.77 MHz, close to where we expect the half-wave thickness mode to occurs, from the 1D modelling. Attenuation is modelled in water with a coefficient of 4 dB/m, this is typical attenuation for water at ambient temperature, this property have almost no impact in microscale device.

The computer used to solve the previous 2D models has an Intel Xeon CPU E5-2630 2.3GHz processor and a 64GB of memory RAM installed. Using this mesh density, the time to compute the harmonic analysis of the device is 5sec/freq. At least a hundred frequencies are necessary to be sure to “hit” the half wave resonance frequency, indeed the 1-D modelling gave us an expected frequency of this mode, but this model being more complex by implementing another dimension, and having another mesh, the resonance frequency can be slightly different. In our case, the model is simulated from 1.7 MHz to 1.8 MHz. Then the

energy density in the cavity is plotted by summing the kinetic and the potential energy and divide it by the area of interest (fluid layer in our case). A graph of the total energy density in the cavity is then available to know the resonance frequency of the modelled device, which is the frequency with the highest energy density in the fluid cavity.

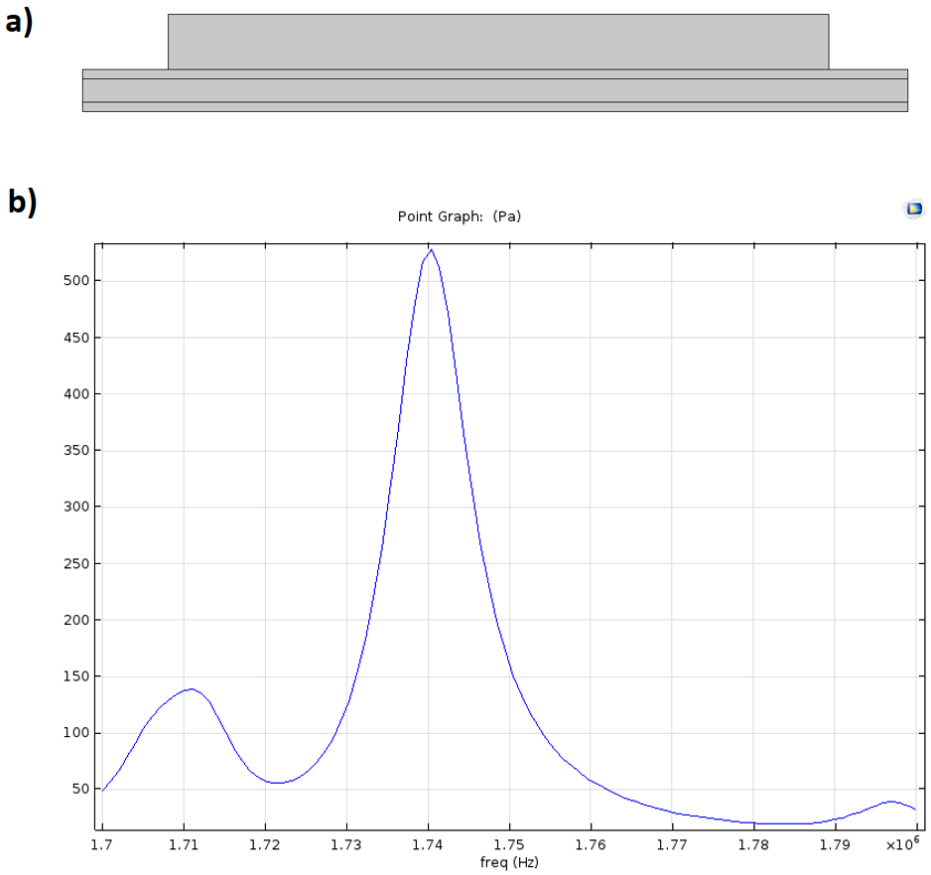

Figure 29- (a) Typical modelled planar resonator using FEA, with a cavity width of 15mm, carrier and a reflector width of 15mm fitting the cavity and a transducer of 12mm nearly in the middle of cavity, (b) Energy density in the manipulation cavity depending on the frequency of excitation of the transducer, the resonance frequency is correlated to the energy peak at 1.74 MHz.

The frequency of resonance in the case of our planar resonator is 1.74 MHz, it is the maximum of energy density which can be seen in Figure 29-b). The resonance frequency of the 2D model is close to the one found in the 1D model (1.77 MHz).

4.2.4 Method of analysis

The trap position is localised at kinetic energy local maxima in this report, indeed in the case where the particle compressibility is higher than the one of the surrounding fluid and the particle density is higher than the surrounding fluid, the kinetic energy attract the particle, see equation (5) and (6). It is the case in this report the particle used are polyester fluorescent beads (Fluoresbrite Fluorescent Microspheres 10.0µm). The time after which the particle would rest at their final levitation position depends on many factors including: the compressibility of the particle compared to the fluids, the density and compressibility of the particle compared to the fluids, the input power of the transducer, the Q factor of each part of the device, the level of acoustic induced streaming and finally the level of lateral force field compared to the axial force field. This part use FEA modelling to locate the trapping position in a planar resonator.

In this method section two different planar resonator designs are introduced, which both have the same materials and layer thickness. The only changing characteristic is the transducer width. One excites an apparently simple half-wave thickness mode that would induce a flat levitation plane Figure 30-a), the other one excites a more complex cavity mode with strong impact of lateral resonance Figure 30-b). Both architecture were found using a mono-parameter study on the transducer width, which will be presented in section 4.3.3. The flat levitation surface one have a transducer width of 12.091mm, the other high lateral force magnitude one have a transducer width of 10.545mm. The first model excites a half wave mode, with a flat pressure node and low lateral component on its force field. The other produces a corrugated pressure nodal plane, with higher level of lateral force magnitude, along the nodal plane.

Potential energy is deducted from the pressure and displayed in Figure 30.

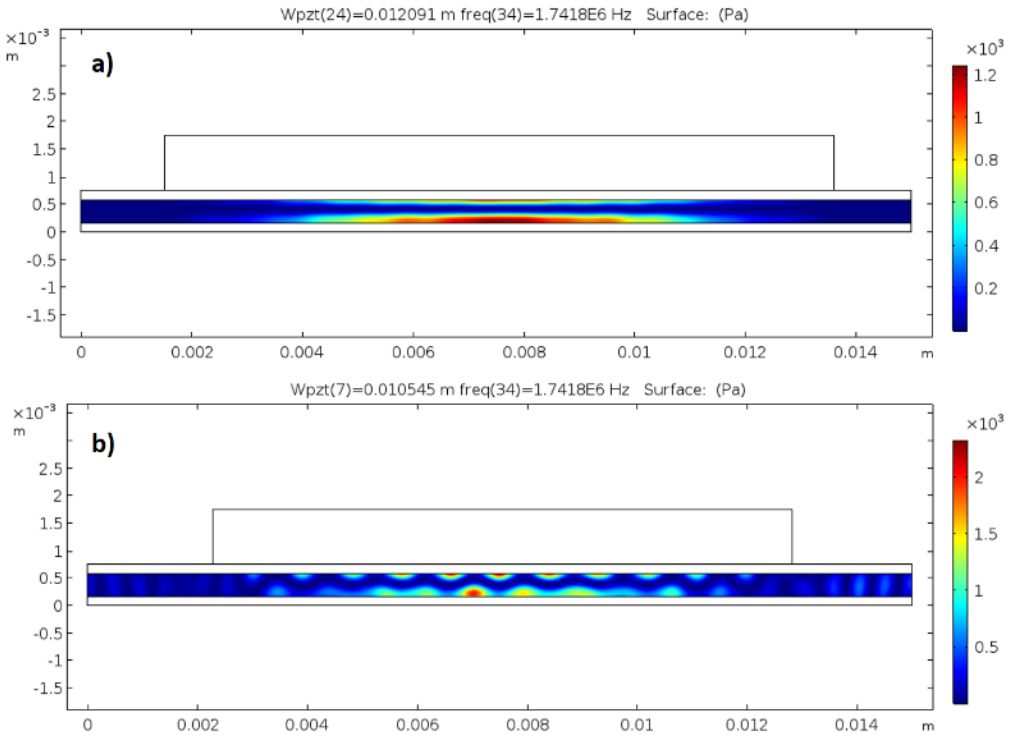

Figure 30 - a) Potential energy structure in a planar resonator exiting a half wave mode with a flat plane of levitation, Transducer width of 12.091 mm, b) Device with different transducer width: potential energy structure in a planar resonator exciting a half wave mode with strong lateral gradient, Transducer width = 10.545 mm.

The second form of energy carried by acoustic wave is kinetic energy. Kinetic energy is deduced from it and displayed in Figure 31. The kinetic energy is the energy coming from the fluid velocity fluid.

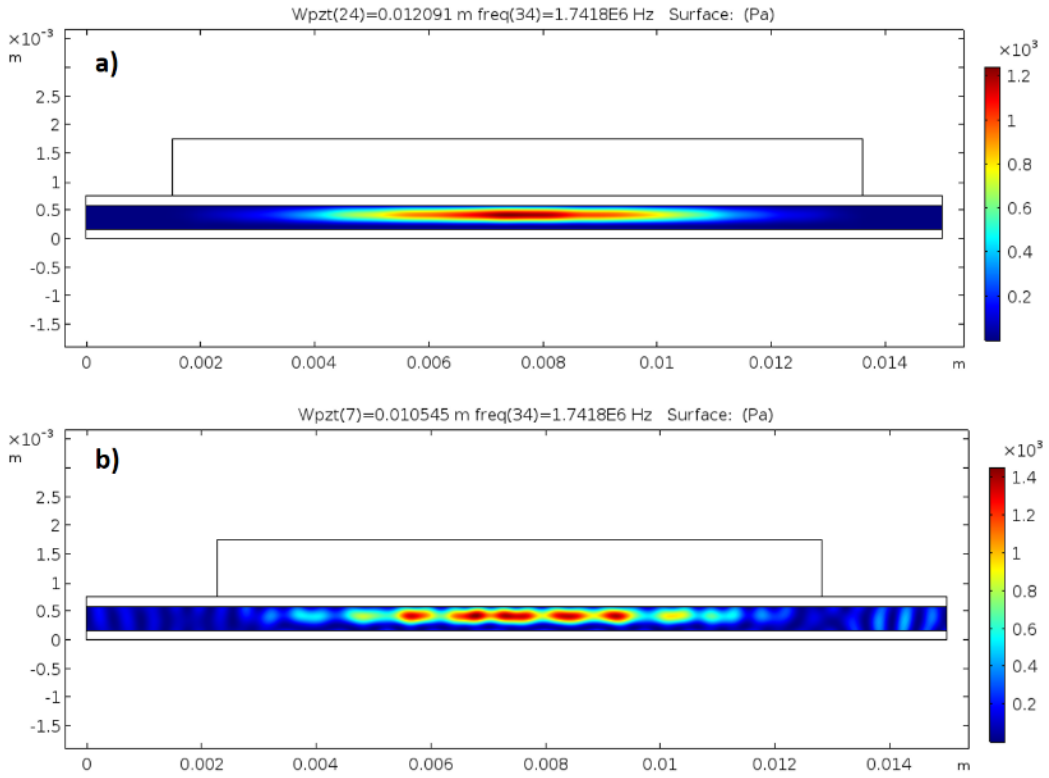

Figure 31 - a) Kinetic energy structure in a planar resonator exiting a half wave mode with a flat plane of levitation, this would create a uniform sheet of particle, Transducer width of 12.091 mm b) Kinetic energy structure in a planar resonator exiting a half wave mode with a flat plane of levitation, this would create uneven lines of particles Transducer width of 10.545 mm.

It is interesting to note that the higher level of lateral acoustic energy variation seems to be related to the increased amount of flexural waves seen in the thin reflector layer as shown in Figure 32. This flexural waves are modelled by modelling the mechanical movement, and by exaggerate the movement by 50000.

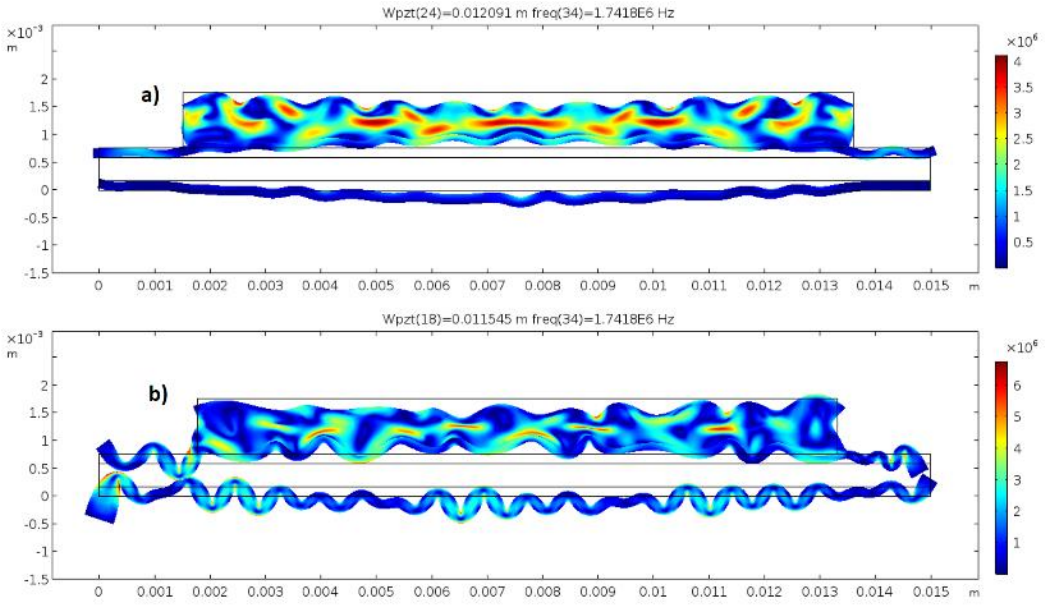

Figure 32 - Deformation of solid layers, transducer, carrier and reflector while exciting a half wave mode, transducer width of 12.091 mm. a) With a flat plane of levitation in the fluid cavity, b) wavy plane of levitation in the fluid cavity, transducer width of 10.545 mm. Deformation exaggerated by a scale factor of 50000.

The radiation force on a particle is defined as the Laplacian of the total Gor'kov radiation force potential. Because at this stage of the simulation, the kinetic energy density and the potential energy density are known, the radiation force potential is computable, as shown in Figure 33.

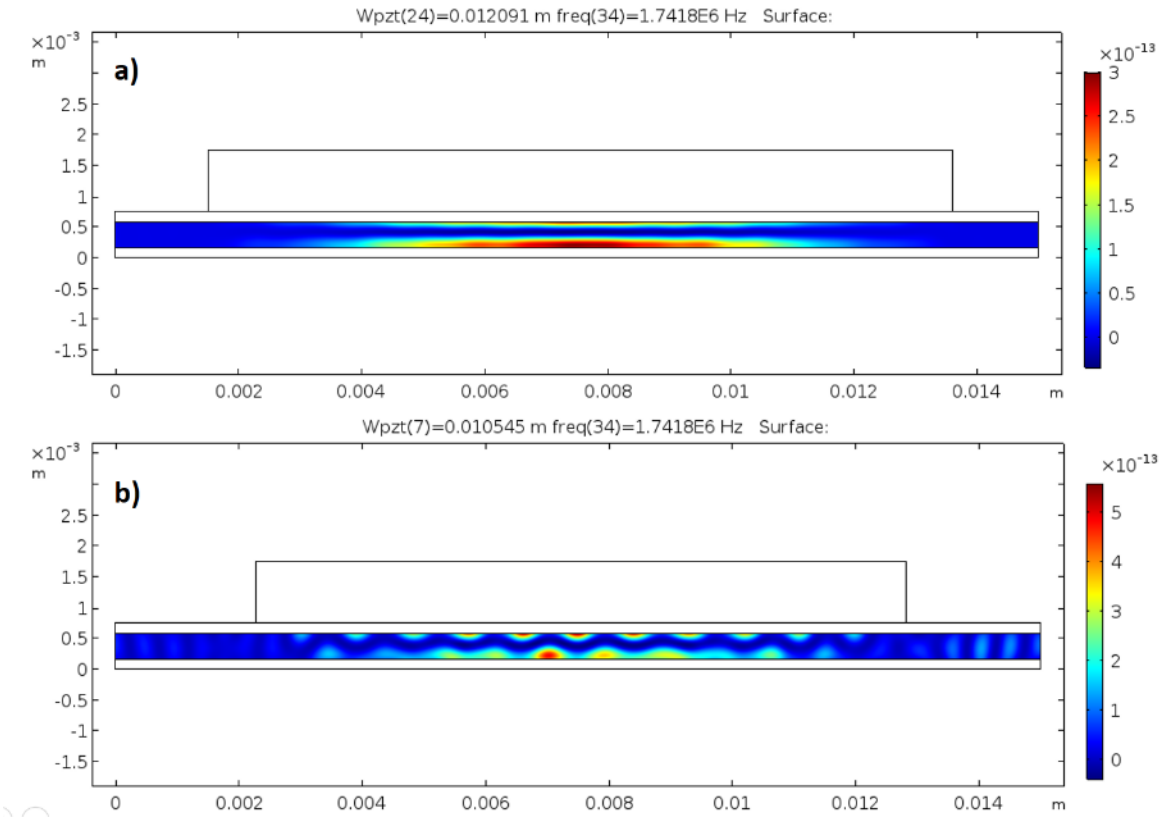

Figure 33 - a) Radiation force potential structure in a planar resonator exiting a half wave mode with a flat plane of levitation, b) Radiation force potential structure in a planar resonator exiting a half wave mode with a flat plane of levitation.

This figure shows that the force potential field is largely dominated by the potential energy density and not the kinetic energy density. It is expected, indeed, many experiments have been carried out for planar resonator it is usual. In the radiation force field, the larger axial force tend to bring particles close to the levitation plane with lateral movements into lines, small aggregate, or larger aggregates seen subsequently. For typical particles with material properties like polystyrene beads, the contribution from the potential energy density is often around ten times greater than the part deduced from the kinetic energy density. We are particularly interested in the lateral force field which determines the structure of the final position of such particles aggregate(s). We can decouple both part of the radiation force equation. The radiation force is a Laplacian of a sum of energy density, which means that it is a sum of Laplacian of energy density as well.

$$F^{Rad} = -\nabla\left(V\left(f_1 E_{pot} - \frac{3}{2} f_2 E_{kin}\right)\right) \quad (8)$$

Or,

$$F^{Rad} = -\nabla\left(V\left(f_1 E_{pot}\right)\right) + \nabla\left(V\left(\frac{3}{2} f_2 E_{kin}\right)\right) \quad (9)$$

The area of kinetic energy domination is introduced as the spaces where the force potential deduced from the kinetic energy density is stronger than the force potential deduced from the potential energy density. That is to say where;

$$\frac{3}{2} f_2 E_{kin} > f_1 E_{pot} \quad (10)$$

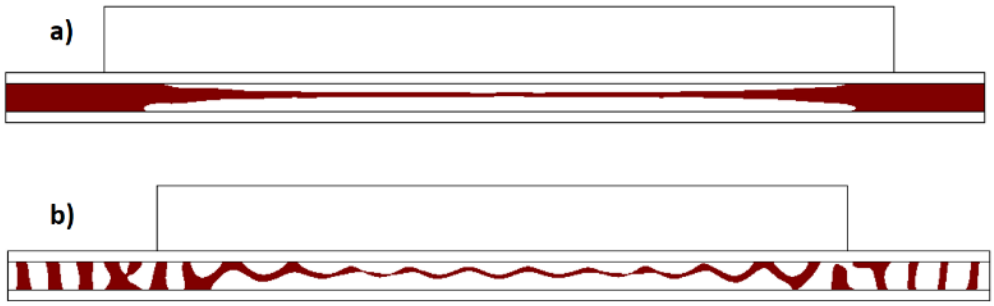

Figure 34 a) Design giving a flat area of particle structuring with a transducer width of 12.09mm, b) design giving a wavy area of particle structuring with a transducer width of 10.545mm. Red region indicates area of kinetic energy domination where $\frac{3}{2} f_2 E_{kin} > f_1 E_{pot}$

The results are processed to show just the parts of the fluid cavity where the kinetic energy part in radiation force potential is greater than the potential energy part. This is shown in Figure 34. The smaller transducer design gave the wavier plane of levitation. It is interesting to know that for both structure, the levitation plane is focused only where the transducer is. As the extremities of the device, where the transducer is not, the kinetic energy is dominant in most of the areas. Levitation would not occur there.

The kinetic energy density maximum is related to the strongest force of attraction in the levitation plane. To have a clear vision of where the aggregate would go if encountering the force present in this field for long enough time, the kinetic energy part of the radiation force filtered by the plane of levitation is

displayed in Figure 35. This give the position of maximum force attraction and the magnitude of such force.

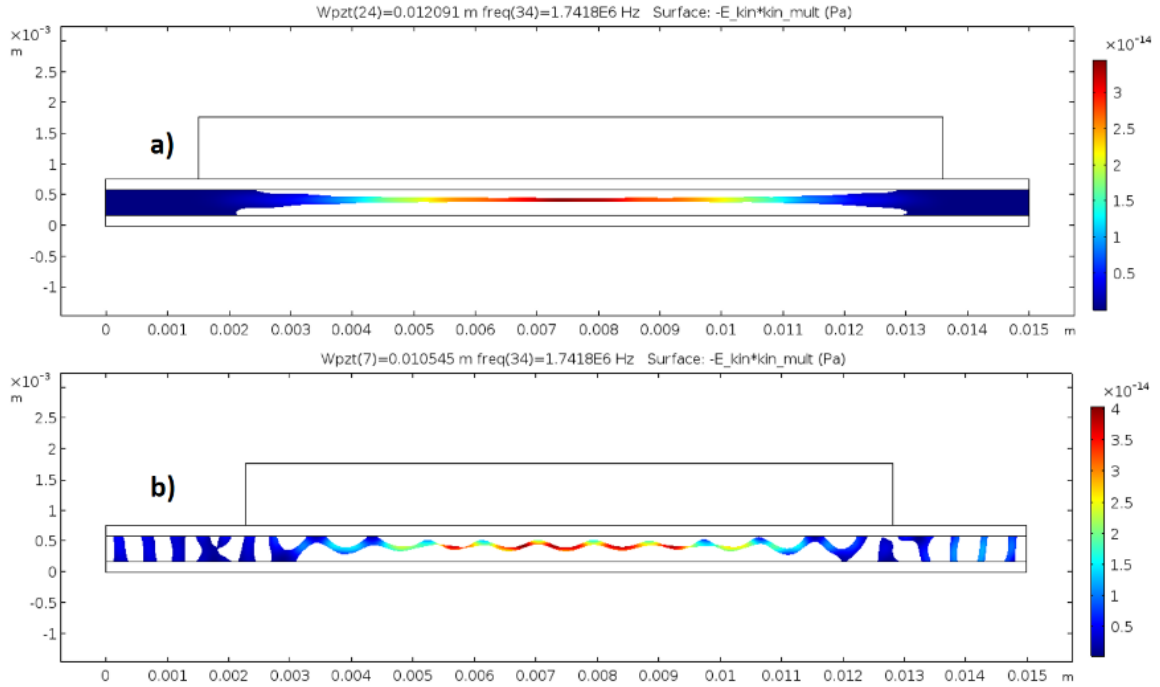

Figure 35 - Kinetic energy induced radiation force potential filtered by the levitation plane. a) In the case of a low lateral force field planar resonator with flat levitation surface, b)) In the case of a high lateral force field planar resonator with wavy levitation surface

. In the case of Figure 35, a particle would be pushed mainly orthogonally to the levitation plane, because of the radiation force induced by the potential energy density is dominant (go up or down depending on the position of this particle). Once in the plane of levitation, the particle would go to the closer local maxima of kinetic energy or kinetic energy induced potential radiation force. In the case of Figure 35-a) particles would all gather at the middle of cavity, where the maximum is (red area), as shown in Figure 36-a), in the case of Figure 35-b), the particle would go to its local maxima. Many are visible a displayed in Figure 36-b).

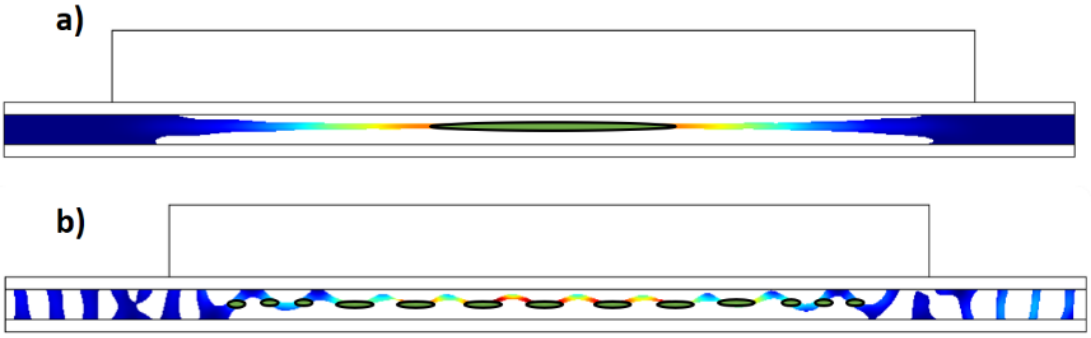

Figure 36- Estimation of aggregates final position and shape if particles were evenly spread throughout the fluid channel before the activation of the half wave mode, a) in the case of a laterally non-resonant device, b) in the case of a more complex cavity mode with lateral resonance

It is interesting to note that the spacing between two smaller aggregate in Figure 36 is 0.45mm which is the spacing shown in Figure 26, this picture being taken with the same device as the one modelled, the measurement is made using the measurement tool of COMSOL. Moreover, the spacing between particle aggregates is close to the half wave length, or full wave length, at this frequency in this fluid, indeed nominal wavelength at this frequency is the quotient between the speed of sound in water and the value of the resonance frequency, $\lambda = \frac{c}{f} = \frac{1480\ m/s}{1.741 \times 10^6 Hz} = 850.1\ \mu m.$

It is important to remind here that the radiation force is not the only force affecting a particle in an acoustically exited fluid. Indeed, several other forces come into play. The Bjerknes force (Inter-particle force) and drag forces (fluid-particle force) are the main ones. These two forces are not simulated in this thesis. Therefore, the magnitude of lateral force compared to these is important to be sure that the radiation force is the dominant factor in determining the final position of aggregates. This is the case for particle larger than 6 μm and with a relatively low concentration, see section 2.1.

Because the objective of this chapter is to explore the effect of transducer width, cavity width, transducer position and transducer shape on the magnitude and structure of the force field in a planar resonator, quantitative measures have to be introduced to assess the differences. These quantitative measure are then used to compare which design factors are the most significant in changing the lateral force field in the fluid channel.

4.2.5 Quantitative measures of field uniformity

To quantify the level of undulation, the standard deviation of the z values of the area of kinetic energy dominance (equation (10)) is calculated. As seen in Figure 34 the plane of levitation is clearly defined in the middle of the cavity, below the transducer, but it becomes more spread out when leaving the range of action of the piezo ceramic material (corresponding to a weaker acoustic field). Because of this, the measurement is carried out in just the middle third of the cavity, as shown in Figure 37.

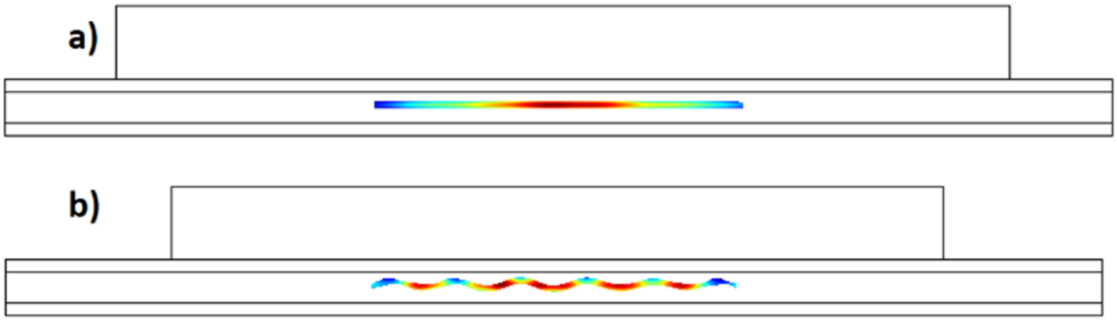

Figure 37 - Middle third of the cavity. Active area of interest for quantitative measures.

The standard deviation calculated by listing all the modelling points in the fluid layer that follows equation (10), the z-position of each of them the standard deviation of the heigh of each point is then calculated. In our case it gives 46.1 μm for Figure 37-B), the wavy plane of levitation case, and 34.3 μm for the Figure 37-A), the flat plane of levitation case. As expected the more undulated the plane of levitation is the greatest the standard deviation of the Z-value in the filtered area is. 34 μm is likely to be close to the minimum value for the standard deviation; indeed, the levitation plane is nearly perfectly flat, this value only represent the thickness of the levitation plane. The variable just introduced will be referred as $SD_{Waviness}$ for short.

For a measure of the strength of the agglomerating forces, the magnitude of the (x-directed) lateral forces can be calculated from equation (1)

$$F^{Lat\_Rad} = \frac{d(-V\frac{3}{2}f_2 E_{kin})}{dx} \quad (11)$$

Figure 38 shows this for our example devices.

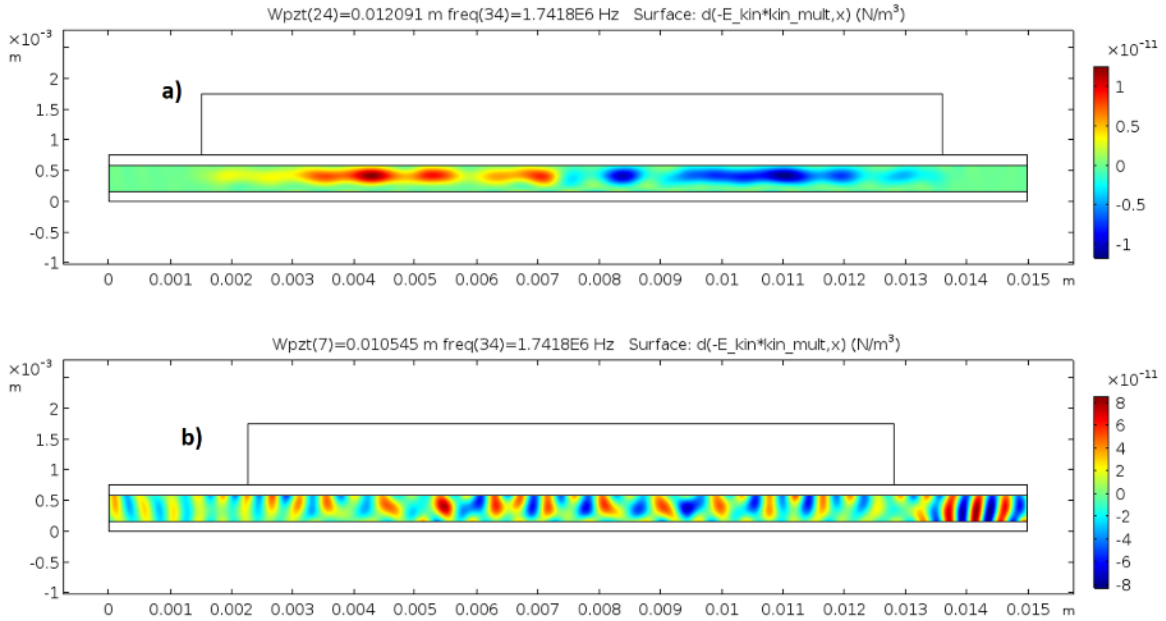

Figure 38 – Lateral radiation force in the fluid cavity in Newton, for a half wave mode excitation at the resonance frequency F=1.418 MHz. Reds means positive value, the particle in this field would be pushed to the right, blue means negative value, the particle in this field would be pushed to the left. a) The case of a flat levitation plane, b) case of an undulated levitation plane.

To quantify the lateral force field, its absolute value is averaged on the totality of the fluid cavity. It could have been conceived to take into account only the plane of levitation, however because it is already accounted for in the waviness standard deviation calculation, adding it here could only add uncertainty because the area of interest delimited by the plane of levitation can differ slightly from design to design.

Some planar resonators are more resonant than others, meaning that for the voltage amplitude applied to the transducer, more or less energy will be transformed into acoustic energy in the cavity fluid, depending on the efficiency of the coupling to the resonance of the device. To normalize the acoustic lateral force

field to the acoustic energy in the fluid, the average lateral radiation force magnitude is divided by the averaged kinetic energy in the fluid at the same frequency (Figure 31). This value is given in N/J, or in m^{-1} (SI, reciprocal length). This value will be referred as $F^{Rad\_lat\_norm}$ for short and are compared later with others coming from different planar resonator layout. The highest the value the stronger the lateral force field is compared to the axial force field.

In the case of the wavy levitation surface case, the $F^{Rad\_lat\_norm}$ is equal to $7.04x10^{-14}$ m^{-1}, in the case of the flat levitation surface case, the $F^{Rad\_lat\_norm}$ is equal to $0.97x10^{-14}$ m^{-1}, the device with the more complex cavity mode, have stronger relative lateral force coming from its lateral resonance component.

In section 4.3, properties of the planar resonator are changed while exciting the half wave thickness mode with the same thickness, the properties changed are the following, cavity width, transducer position, transducer width and fianally the side angle of the transducer. The goal here is to see which design architectural properties influence the most the lateral force strength at the plane of levitation. Comparisons are made using the two variables introduced in this part.

4.3 Effect of geometry of the planar resonator on lateral forces

In this chapter, the resonator geometry is varied to explore its effect on the strength of lateral cavity modes; parameters include cavity width, transducer width, transducer side angle and finally transducer position compared to the cavity. These changes in the planar resonator layout are then compared to one another using the two references values introduced earlier, the standard deviation of in Z values of the plane of levitation ($SD_{Waviness}$), as a measure of its waviness, and the normalized lateral radiation force magnitude in the field ($F^{Rad\_lat\_norm}$).

4.3.1 Effect cavity width

To test the effect of cavity width on lateral forces, the total width of the cavity is changed from 15 mm to 18 mm, as shown in Figure 39. While changing this dimension, the width of the carrier and the reflector are also modified to be equal to the width of the manipulation chamber, while the transducer width is kept constant. A range of 34 different widths are modelled. Each simulation identifies the varying half wave resonance frequency by modelling frequencies from 1.7 MHz to 1.8 MHz.

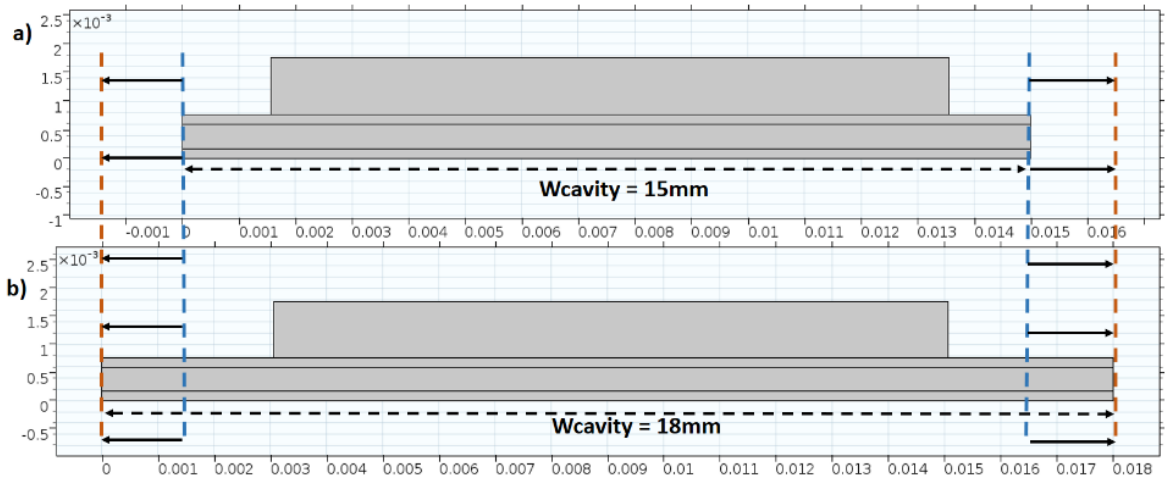

Figure 39 - Diagram of the planar resonator with a cavity total widths of a) 15 mm, b) 18mm. Arrows show that the size is expanding in both direction. All the other characteristic of the model are introduced in section 4.2.3.

The standard deviation of in Z values of the plane of levitation ($SD_{Waviness}$) and the normalized lateral radiation force magnitude in the field ($F^{Rad\_lat\_norm}$) are calculated and reported in Figure 40.

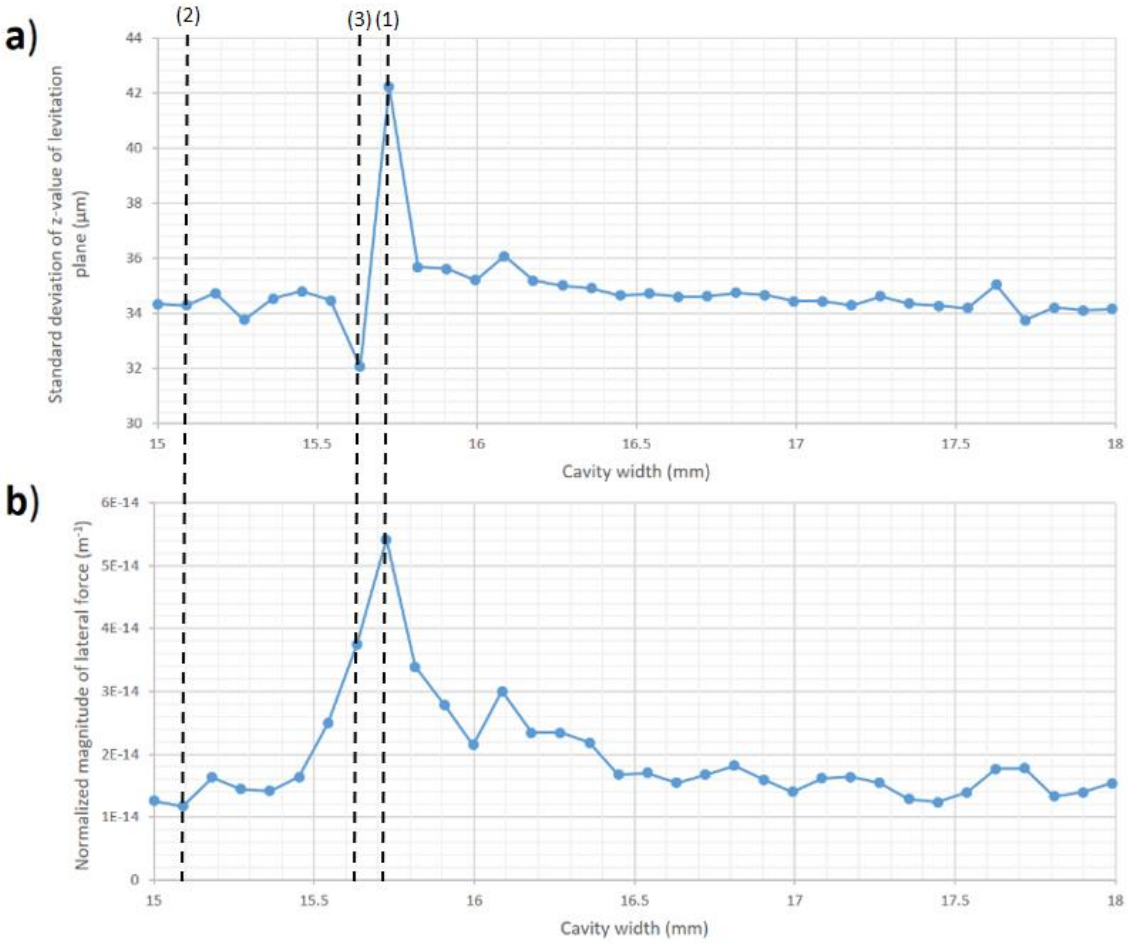

Figure 40 – Effect of changes of the cavity width on; a) the standard deviation of the z-value of levitation plane (in µm). Larger values indicate a more corrugated levitation plane. b) Normalized magnitude of lateral force in the fluid layer.

This design property have an impact on the magnitude of lateral force and the waviness of the plane of levitation, this effect is not linear nor periodic. We see that the trend of $SD_{Waviness}$ is correlated with the trend of $F^{Rad\_lat\_norm}$. The maximum of both variable is for a cavity width of 15.73 mm with $SD_{Wavines}$ = 42 µm and $F^{Rad\_lat\_norm}$ = $5.4x10^{-14}$ m^{-1} (or $N.J^{-1}$), point marked (1) on the graph. However, minima are not related to the same cavity width, the minimum of $F^{Rad\_lat\_norm}$ is $1.2 x10^{-14}$ m^{-1} for cavity width of 15.09mm, point marked (2) on the graph, and the minimum of $SD_{Wavines}$ is 32 µm for a cavity width of 15.63mm, point marked (3) on the graph. In contrast to other widths that tend to create a series of lateral trapping positions, this latter width creates a lateral force gathering the particle into one large flat aggregate.

This confirms that the cavity width affects the acoustic radiation force field in planar resonator, the next section study the effect of the transducer position, in section 4.3.5.

4.3.2 Effect of transducer position

In many applications, the lateral transducer position is not well defined, this design choice can have an effect on the lateral radiation force. This effect is studied in this section by changing the position of the transducer without changing any other aspect of the design. A 15mm wide transducer is modelled in a range of positions up to with up to 1.2 mm in each direction. The central position of the range is slightly off centre (0.05mm to the right) to avoid the non-physical results that occurs when the device has perfect symmetry Figure 41 illustrates this.

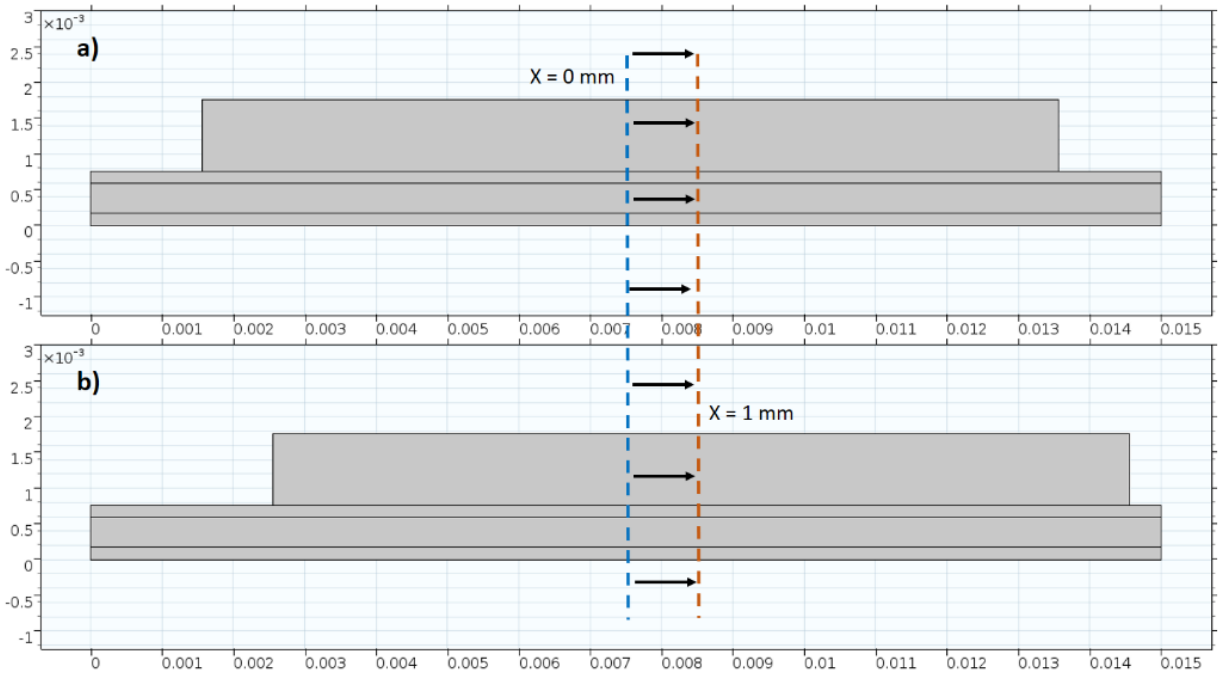

Figure 41 - Diagram of the planar resonator with the transducer (a) in the centre of the carrier and b) with the transducer moved 1 mm to the right. When the displacement is positive it is on the right of the middle position, when it is negative it is on the left. All the other characteristic of the model are introduced in section 4.2.3.

Here again the two introduced variables are used to have a quantitative measure of the waviness of the plane of levitation and the normalized lateral radiation force field in the water filled cavity, these graph are shown in Figure 42.

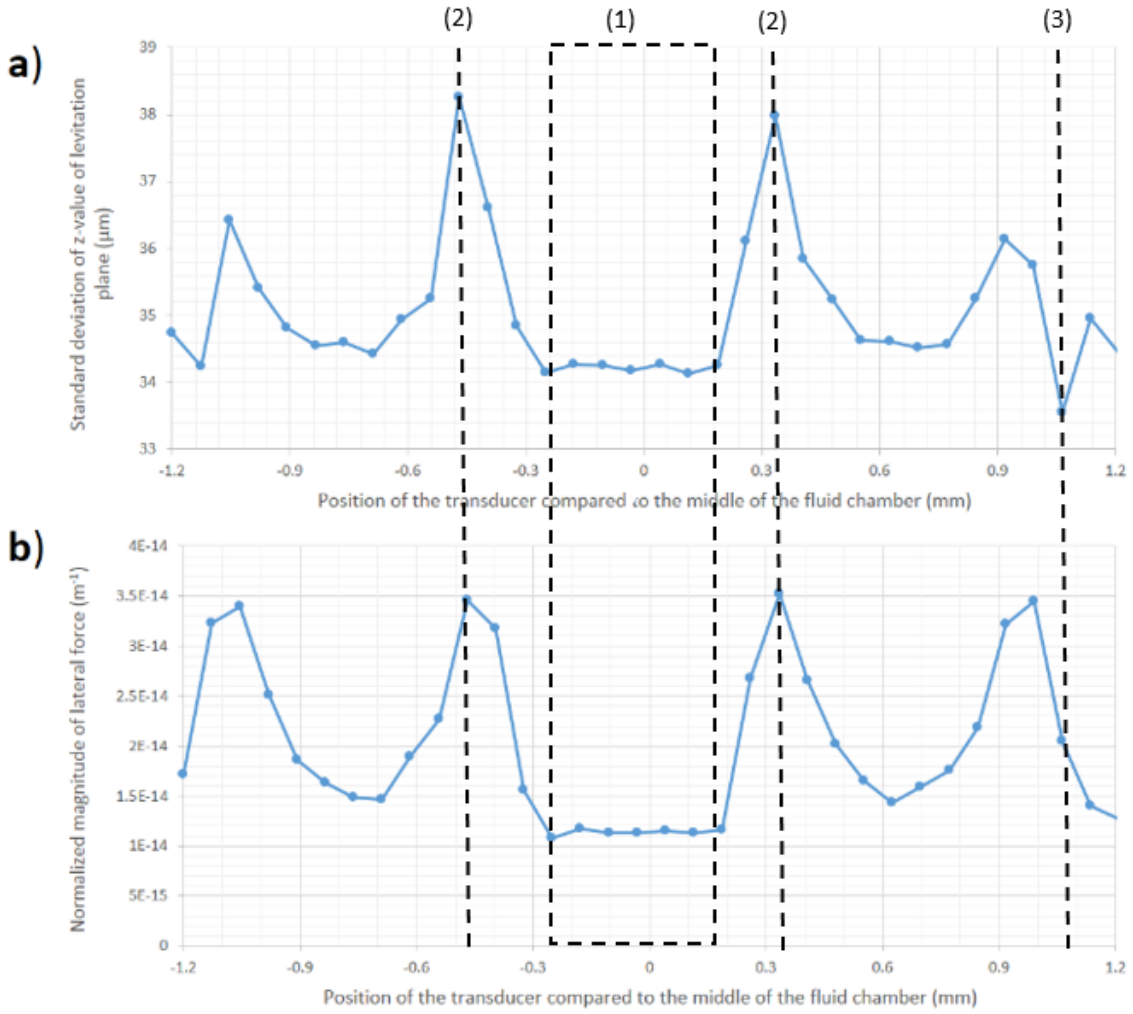

Figure 42 - Effect of changes of the transducer position compared to the cavity on; a) The standard deviation of the z-value of levitation plane (in µm), b) Normalized magnitude of lateral force in the fluid layer (in m^{-1}).

There is a clear relationship between the waviness of the plane of levitation and the magnitude of lateral radiation force, with more corrugated resonances having larger lateral radiation forces. As expected, the trend or graph is symmetric; indeed, all layers are simulated as symmetric piece of glass, fluid and piezo ceramics. The point of symmetry is off at 0.05mm because of the asymmetry introduced in section 4.2.3 to avoid modelling aberration due to perfect symmetry.

The positions near the centre line of the cavity gather the lowest values for the normalized lateral force magnitude, 1.08 x10^{-14} m^{-1}, zone marked (1) on the graph. The maximum of $F^{Rad\_lat\_norm}$ is found at 0.34mm and -0.48 mm from the middle, for a value of 3.50 x10^{-14} m^{-1}, this point being the maximum of $SD_{Waviness}$ as well, with a value of 38 μm, point marked (2) on the graph. However, the minimum of $SD_{Waviness}$ break the apparent coherence in curvature found between $SD_{Waviness}$ and $F^{Rad\_lat\_norm}$, by being apart from the minimum of $F^{Rad\_lat\_norm}$, it is found 1.06mm to the right to the modelled middle position, for a corresponding value of 33.5 μm, point marked (3) on the graph.

This confirms that the transducer position affects the acoustic radiation force field in planar resonator, the next section study the effect of the transducer position, in section 4.3.5.

4.3.3 Effect of transducer width

The transducer width effect on the level of lateral radiation force in the levitation plane is studied here. Only the transducer width is changed gradually with 34 values linearly distributed from 10mm to 13mm, as shown in Figure 43. All other design choice are kept identical, see section 4.2.3.

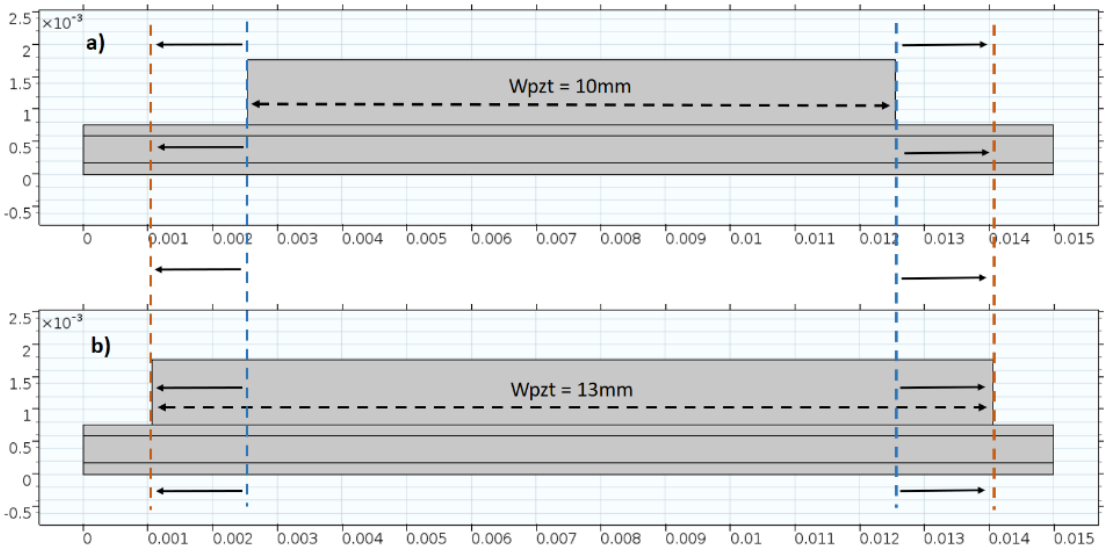

Figure 43 – a) Diagram of the planar resonator with a transducer width of 10 mm, b) Diagram of the planar resonator with a transducer width of 13 mm.

Arrows show that the symmetrical increase in transducer width over the modelled range. All the other characteristic of the model are introduced in section 4.2.3.

To quantitatively observe the lateral cavity mode change depending on the transducer width, a $SD_{Waviness}$ and $F^{Rad\_lat\_norm}$ versus transducer width is represented as a graph and displayed below in Figure 44.

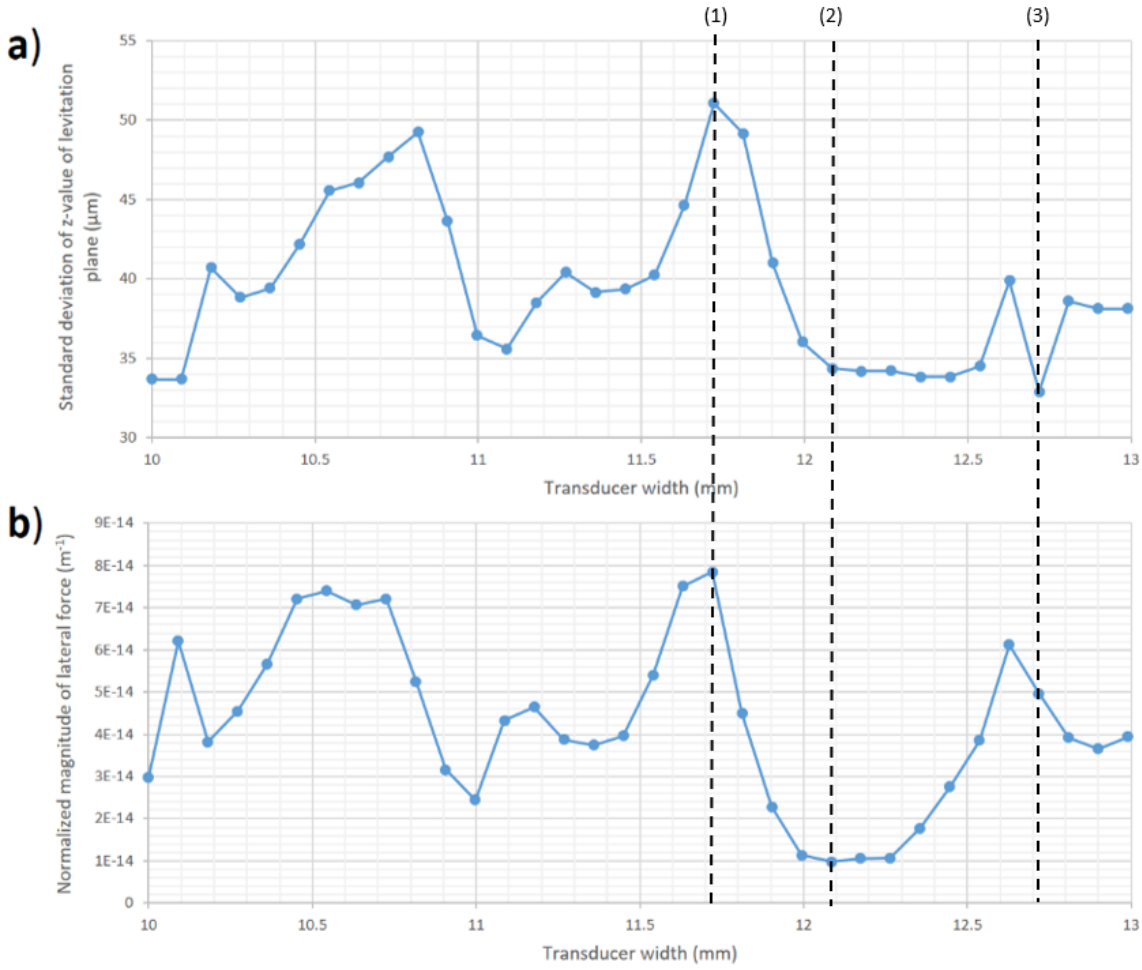

Figure 44 - Effect of changes of the transducer width; a) The standard deviation of the z-value of levitation plane (in µm), b) Normalized magnitude of lateral force in the fluid layer

Here again, the trend of both curves Figure 44-a) and Figure 44-b) look similar. The transducer width of 11.72 mm is particularly interesting because it is

related to the maximum of both $SD_{Wavines}$ and $F^{Rad\_lat\_norm}$, respectively 51 μm and $7.8x10^{-14}$ m^{-1}, point marked (1) on the graph. Here again the minimum of normalized force is not given by the same planar resonator design as the minimum of waviness. The minimum of $F^{Rad\_lat\_norm}$ is 0.97 $x10^{-14}$ $m^{-1}$and is established for a transducer width of 12.1mm, point marked (2) on the graph, the minimum of $SD_{Wavines}$ is 32.9 μm and is associated with a transducer width of 12.7mm, point marked (3) on the graph. This later point in the graph break the apparent alikeness of both variable when compared to the transducer width.

This confirms that the transducer width affects the acoustic radiation force field in planar resonator, the next section study the effect of the transducer position, in section 4.3.5.

4.3.4 Effect of a transducer side angle

Previous parts showed the importance of the transducer width in the level of lateral radiation force in the fluid chamber. Reducing the lateral component of displacement and stress in the transducer might alter the lateral component of the acoustic radiation force field in the cavity. The easiest one being to reduce the possibility for lateral resonance by changing the parallelism of the side edges. The angle ϑ is introduced as the angle between the vertical or axial axis and the side angle of the trapezoid transducer as shown in Figure 45.

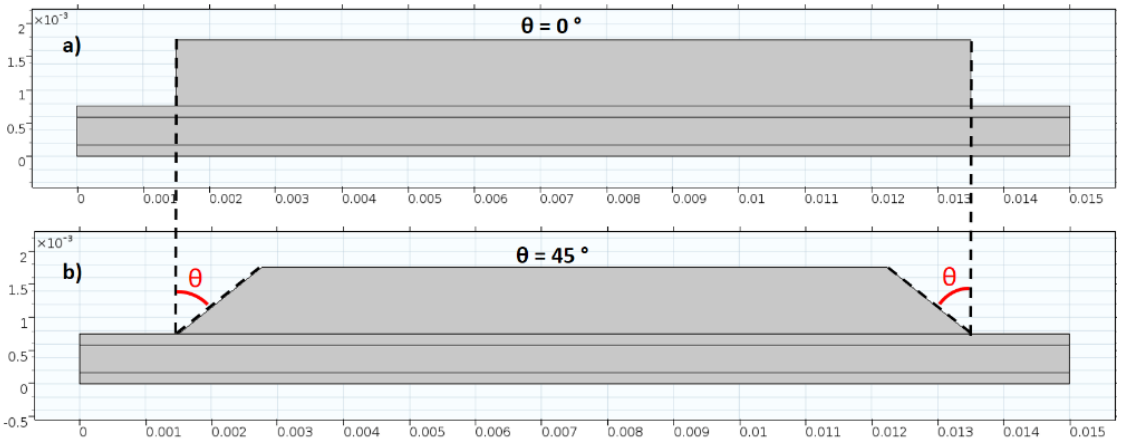

Figure 45 - a) Diagram of the planar resonator with a side angle of 0 degree, b) Diagram of the planar resonator with a side chamfer angle of 45 degree. All the other characteristic of the model are introduced in section 4.2.3.

To quantitatively observe the lateral cavity mode change depending on the transducer side angle,a $SD_{Waviness}$ and $F^{Rad\_lat\_norm}$ vs transducer side angle is respresented as a graph and displayed below in Figure 46.

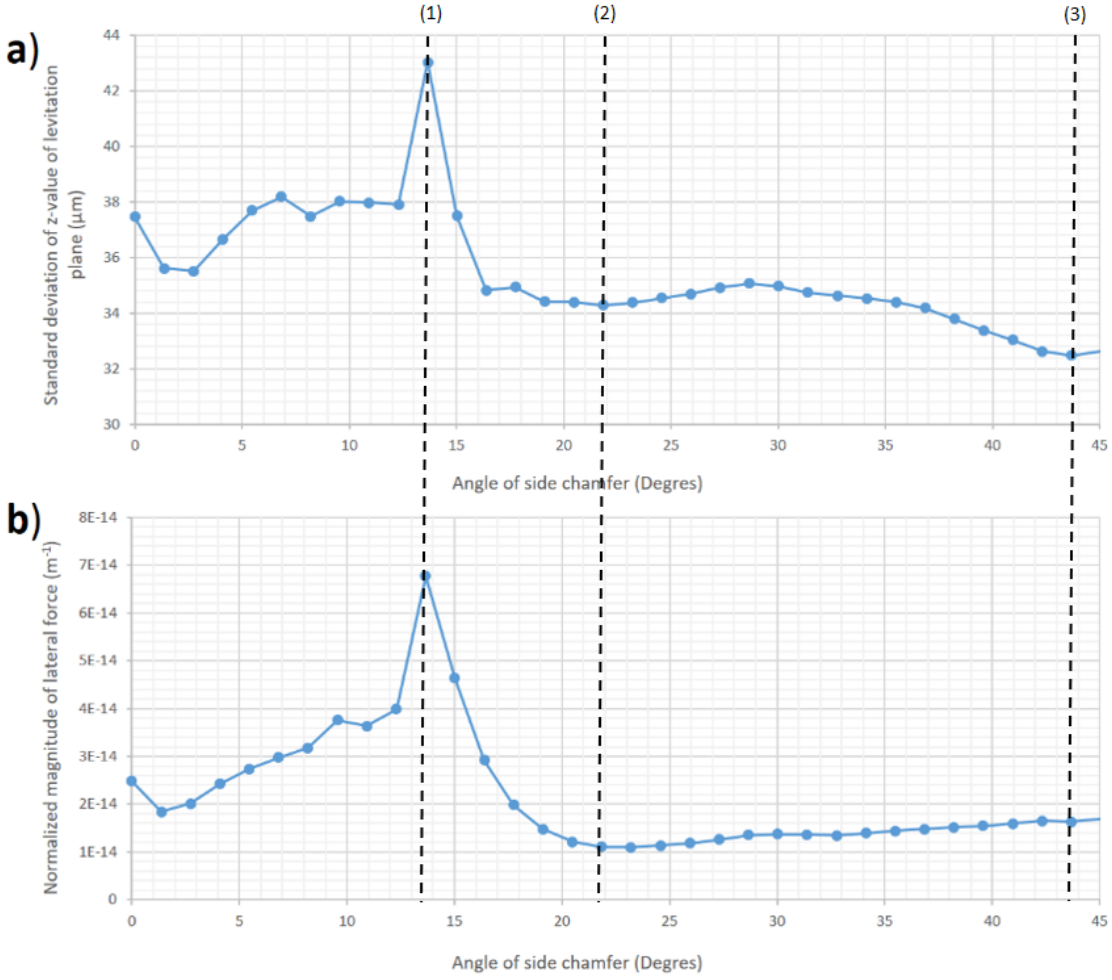

Figure 46 - Effect of changes of the side angle of the transducer on; a) The standard deviation of the z-value of levitation plane (in µm), b) Normalized magnitude of lateral force in the fluid layer

Once more, trends of both curves Figure 46-a) and Figure 46-b) are comparable, the side angle of 13.65˚ is particularly interesting because it is related to the maximum of both $SD_{Wavines}$ and $F^{Rad\_lat\_norm}$, respectively 43 µm and $6.8x10^{-14}$ m^{-1}, point marked (1) on the graph. Here again the minimum of normalized force is not given by the same planar resonator design as the minimum of waviness. The minimum of $F^{Rad\_lat\_norm}$ is 1.1 $x10^{-14}$ $m^{-1}$and is established for a transducer side angle of 21.84˚, point marked (2) on the graph. The minimum of $SD_{Wavines}$ is 32.4 µm and is associated with a transducer width of 43.60˚, point marked (3) on the graph.

This confirms that the transducer side angle affects the acoustic radiation force field in planar resonator, the next section study the effect of the transducer position, in section 4.3.5.

4.3.5 Discussion of 2D parameter study

The distribution of energy in any given mode is a complex arrangement of electrostatics in the transducer, solid mechanics for the transducer and chamber walls (which can include flexural modes) and the acoustic field in the fluid. In this model, the planar resonator has been simplified, by removing the glue or glycerol layer between the transducer and the carrier glass needed in real device. A free surface replaced the necessary spacer that form the cavity. Studying design choice in 2D and not in 3D have been made to simplify the model as well. Even though, this model remain a complex one and each design choice change affect the whole structure of the planar resonator. For example, changing the width of the transducer, change the spacing there is between the transducer and the glass free surface, and so on.

Four design parameters have been explored in this section. These four characteristics are chosen because we have good control over them during the fabrication process of a planar resonator. These design features are cavity width, transducer position, transducer width and transducer side angle. All simulations were made across a range of values. Changing specifically each property while not changing the others. The two variables used to quantify the level of lateral force magnitude and waviness are shown below in the same graph for comparison. Figure 47 represent the effect of all design characteristics changes on the $SD_{Waviness}$, Figure 48 display their effect on $F^{Rad\_lat\_norm}$

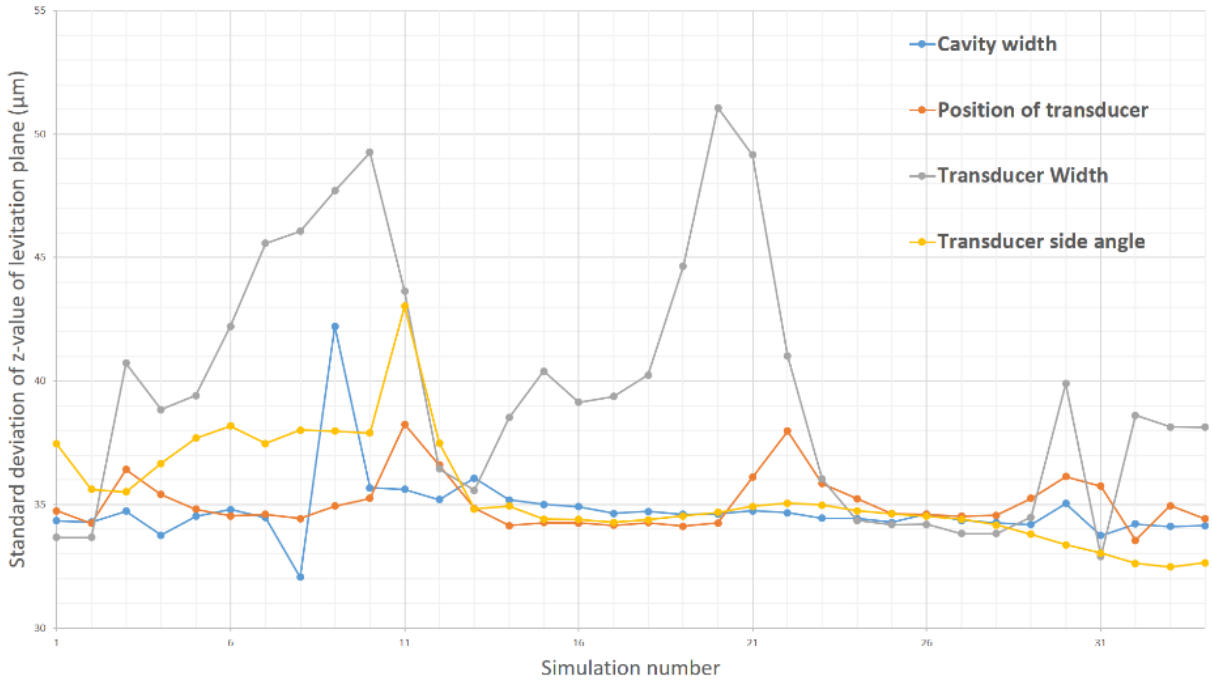

Figure 47 – Effect of changes of various design properties on the standard deviation of the z-value of levitation plane (in µm)

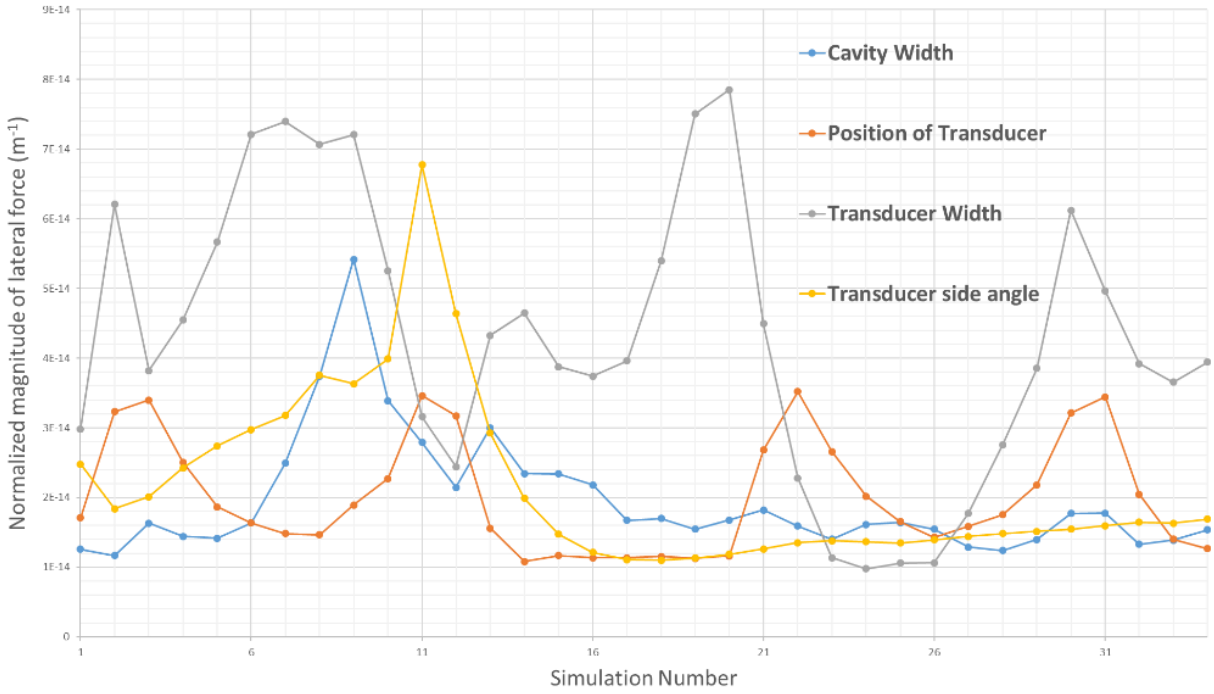

Figure 48 - Effect of changes of various design properties on the normalized magnitude of lateral force in the fluid layer

Both Figure 47 and Figure 48 are useful as they allow visualization of the difference in magnitude of $SD_{Waviness}$ and $F^{Rad\_lat\_norm}$. We see that curves are dominated by the transducer width curve. This property seem to have the most effect on the

level of lateral radiation force magnitude and the way the force field is structured in the fluid layer. At the opposite, the transducer position is exhibited as relatively flat curve compared to the other; we conclude that this design characteristic has the less effect on the final level of $SD_{Waviness}$ and $F^{Rad\_lat\_norm}$.

To be able to compare clearly the effect of each and every of these design characteristics, we introduce two ratios, equal to the fraction of the highest value and the lowest value throughout the values studied; the $SD_{Waviness}$ ratio and the $F^{Rad\_lat\_norm}$ ratio. The ratio is the quotient of the maximum value and minimum value of the variable for a design characteristic studied. All maximum and minimum have been discussed in earlier parts of this chapter. Table 2 gives the results for comparison for each design architecture studied.

Table 2- Comparison of properties change effect on force level using the effect ratio introduced in this chapter

	$SD_{Waviness}$ ratio	$F_{Rad\_lat\_norm}$ ratio
Cavity Width	1.31	4.66
Transducer position	1.12	3.26
Transducer width	1.55	8.08
Transducer side angle	1.32	6

It is interesting to note that high $SD_{Waviness}$ ratio and $F^{Rad\_lat\_norm}$ ratio are correlated. We see in this table that each design property has its importance in regards to the lateral radiation force field in the fluid layer. The most critical characteristic seem to be the transducer width, followed by the transducer side angle, the cavity width have less effect and finally the transducer position have the least effect.

It is difficult in such a large parameter space (which also includes different later thicknesses) to explore the effects of all combinations of design parameters variations in detail. However, the work here does provide guidance as to which parameters are more significant and worthy of attention when creating a new design, and also provides information about the level of sensitivity that a particular design may have to manufacturing variations.

To go further in our study, a 3D model is examined in the next section to see the effect of transducer and cavity shape on the level of lateral component of the acoustic mode.

In order to confirm with stronger confidence the results obtained in this section, later work using more computing power would be necessary.

4.4 Three dimensional Finite Element Analysis

The aim of this section is to study qualitatively and quantitatively the effect of transducer's and fluid cavity's shape on the strength of the lateral strength of acoustic mode in the levitation plane. The 2D modelling allows a limited range of shape change for the each layer as it is considered infinite in the out of plane lateral direction. 3D model is therefore use to give a more details picture of the effect of transducer and cavity shape on lateral radiation forces. Two different shapes are introduced, the parallelepiped rectangle, which is commonly the shape used in planar resonators, and an asymmetric shape inspired by a US Patent o Larson et al [98]. This shape is a non-rectangular and irregular polygon, chosen because no sides are parallel to others. This could limit the possibility for lateral resonance effect. Both symmetric and asymmetric transducer and cavity are modelled. Four different structures are studied, symmetric transducer with symmetric cavity (SS for short), symmetric transducer with asymmetric cavity (SA), asymmetric transducer with symmetric cavity (AS) and finally asymmetric transducer and asymmetric cavity (AA). The 2D modelling results showed that the size of the transducer is critical, therefore many sizes are simulated to confirm the sensitivity of the shape change associated with the size. One of the focus of interests here is to confirm or refute the hypothesis regarding the importance of the transducers size and shape in 3D.

The computer used to solve the previous 2D models has an Intel Xeon CPU E5-2630 2.3GHz processor and a 64GB of memory RAM installed, which solved each frequency step in around 18 min for with fine mesh and 4.5 min for coarse mesh. However, 3D models consume more computing power than to 2D models. Therefore, the size of the model and the mesh density have to be thought carefully to be able to solve the model to limit the amount of memory to prevent COMSOL

aborting a simulation for low memory. After many trials, a compromise, presented in section 4.4.1, is chosen between size and mesh density.

4.4.1 3D model, design, mesh and approximation

4.4.1.1 Symmetric transducer and cavity

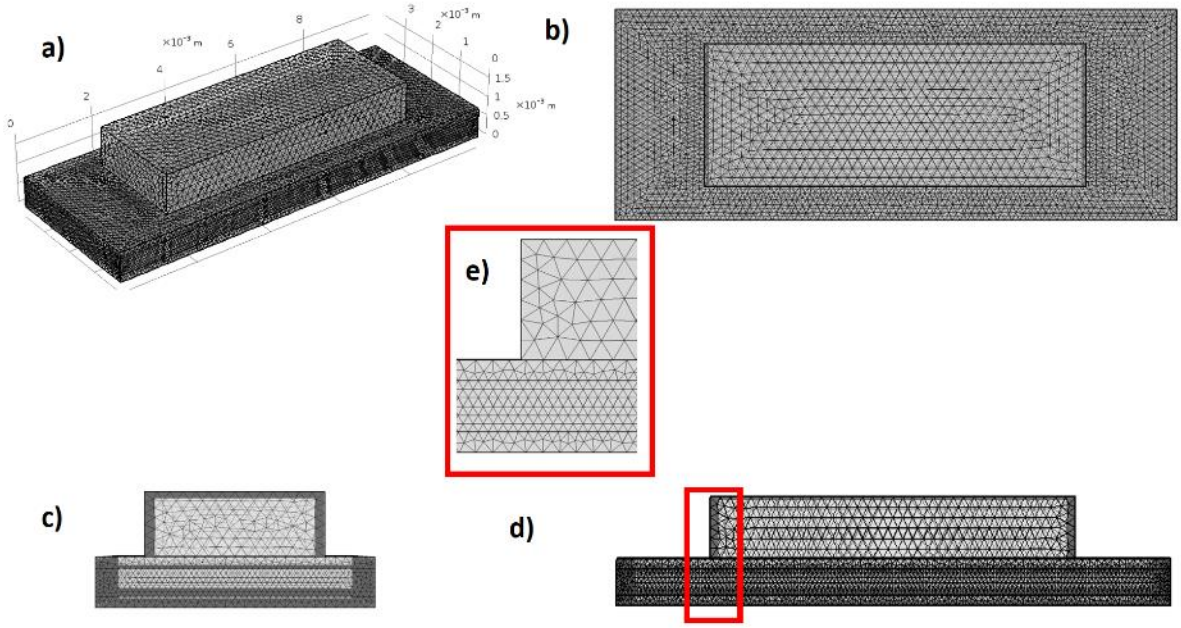

Figure 49- Mesh of symmetric transducer and symmetric cavity. a) Isometric view, b) top view, c) side view, d) front view, e) zoom on mesh with front view. Parameters: The levitation cavity is a 10x3.7 mm rectangular parallelepiped formed by a 0.42mm water chamber sandwiched between two 0.17mm glass slides of the same size. On top of one of the glass slide, the carrier, a rectangular parallelepiped transducer of 6.67x2.5 mm is laid. The characteristics of all the layers are introduced in table 1.

This section present the symmetric cavity and symmetric transducer that will be used in the case SS / SA and AS. The levitation cavity is a 10x3.7 mm rectangular parallelepiped formed by a 0.42mm water chamber sandwiched between two 0.17mm glass slides of the same size. On top of one of the glass slide, the carrier,

a rectangular parallelepiped transducer of 6.67x2.5 mm is laid. The material and material properties are identical as the ones introduced in the previous 2D simulations (See table 1), namely, water for the levitation cavity, glass for the carrier and reflector and finally PZT for the transducer. The sides of the water-filled chamber are modelled as a sound hard-boundary to maximise the lateral effects. All other external sides are modelled as free surface, representing the low acoustic impedance of an air boundary. The mesh sizes of the PZT transducer, the glass carrier and reflector and the water cavity are 0.18 mm, 0.13 mm and 0.07 mm respectively. Finer mesh cannot be achieve, except at the expense of the size of the model. We want to keep the size in the same order of magnitude as the size introduced in section 4.3. The final rendering of the mesh is displayed is Figure 49.

4.4.1.2 Asymmetric transducer and cavity

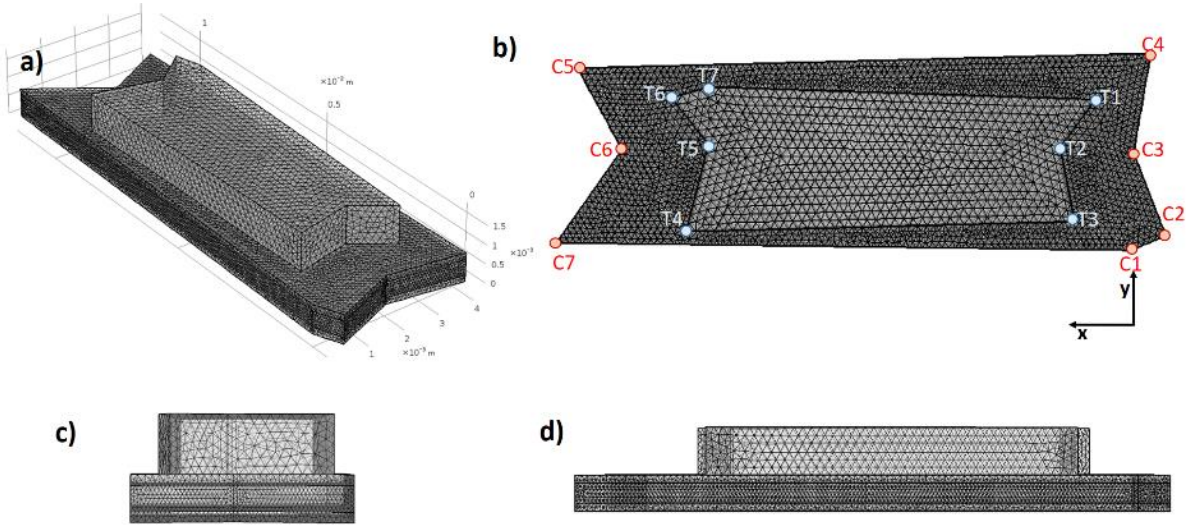

Point of polygone	Position in X-axis (mm)	Position in Y-axis (mm)
T1	0.6	1.2
T2	2.1	1.5
T3	3.05	0.8
T4	3.3	8.55
T5	3.1	9.3
T6	2.16	8.5
T7	0.4	9

Point of polygone	Position in X-axis (mm)	Position in Y-axis (mm)
C1	0	0
C2	0.3	-0.7
C3	2	-0.05
C4	4	-0.4
C5	3.7	11.25
C6	2.06	10.35
C7	0.15	11.7

Figure 50 - Mesh of asymmetric transducer and asymmetric cavity. a) Isometric view, b) top view, containing notation of all point forming both asymmetric cavity and transducer, c) side view, d) front view.
Blue Table – Points position of the polygon forming the basis of the asymmetric transducer, x and y-axis from the model.
Orange Table – Points position of the polygon forming the basis of the asymmetric cavity, x and y-axis from the model.

The inspiration for the design of this asymmetric layer came from a US patent developed by Larson, III et al.[98]. The shape consist of an irregular polygon composed of seven segments, with none of the sides parallel to each other. The patent is used as guideline more than as an absolute reference, indeed, the design is loosely followed, the main reason being that our piezo is more longitudinal than the patent design; furthermore in later control experiment it is impossible, with tools available in our lab, to cut precisely a transducer to fit exactly the patent design. The conclusion that can be drawn in this section are about a non-symmetric device and not the patent itself.

The design of both asymmetric transducer and cavity are presented in Figure 50. This figure presents the asymmetric transducer and cavity from various point of view. The mesh size is the same as the one introduced earlier for the symmetric 3D modelling. Below the meshed view are two tables giving the position of the points delimiting both asymmetric polygons forming the basis of the cavity and the transducer. These polygons are extruded to match the thicknesses used in the 2D modelling, that is to say, 1mm for the transducer, 0.42mm for the cavity, and 0.17mm for the carrier and the reflector.

4.4.2 Method

In this part, the method to get to the lateral force data is described; this process is divided in several part, and follow what was done for the 2D modelling:

In the following pages the configuration with the symmetric transducer on top of a symmetric levitation chamber (SS) is explored in detail then results for other configurations presented later.

Analogous to the method used experimentally, the half wave resonance of a given configuration is found by having a frequency sweep and take the frequency giving the higher acoustic energy density in the fluid cavity. The 1D modelling is used to check what frequency is to be expected for a half-wave mode, the value is 1.78 MHz. The energy density in the water filled levitation chamber is calculate for each frequency. Because of computing limitation, the mesh for this step is two times coarser than the one introduced in chapter 3. Both example of such energy density graph vs frequencies are showed in Figure 51. The half wave resonance at the frequency of maximum energy density, which is 1.824 MHz in the SS case. Acoustic mode frequencies are a complex function of the whole system, in all direction, and therefore it is influenced by any change of shape or size, even if not in the height (z) direction.

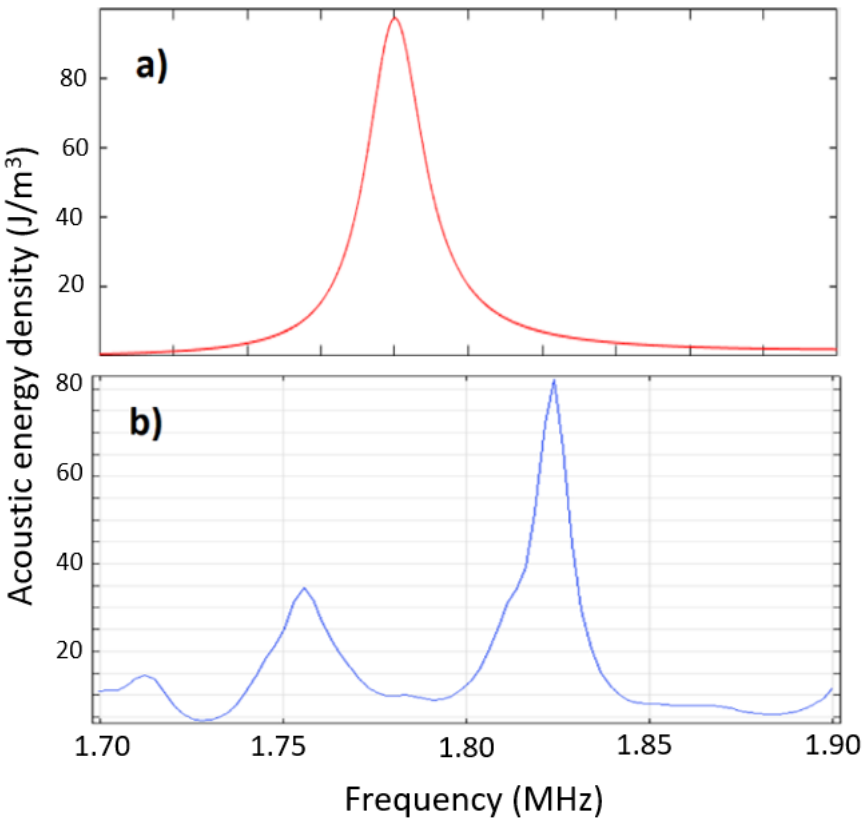

Figure 51- Graph of Acoustic energy density vs frequencies from 1.7 MHz to 1.9 MHz a) 1D modelling, transfer impedance, KLM, b) 3D modelling, finite element analysis

Once the resonance frequency is found, a finer meshed simulation (as introduced earlier) is required to model the reaction of the planar resonator to this

particular excitation. The plane of levitation is located by filtering using equation (10). The geometry of this plane of levitation is important as for the final configuration of particle in this acoustic radiation force field. If the energy density has a single peak, the particle would be attracted in a single discoid like aggregate, on the contrary if it has multiple turning points, multiple discoid or lines of trapped particles (depending on the structure) would be created, as seen in Figure 26. Out of the range of the transducer, the plane of levitation with the definition express earlier is not clearly define, as shown in section 4.2.4, therefore we are only interested in part visible under the transducer as shown in Figure 52.

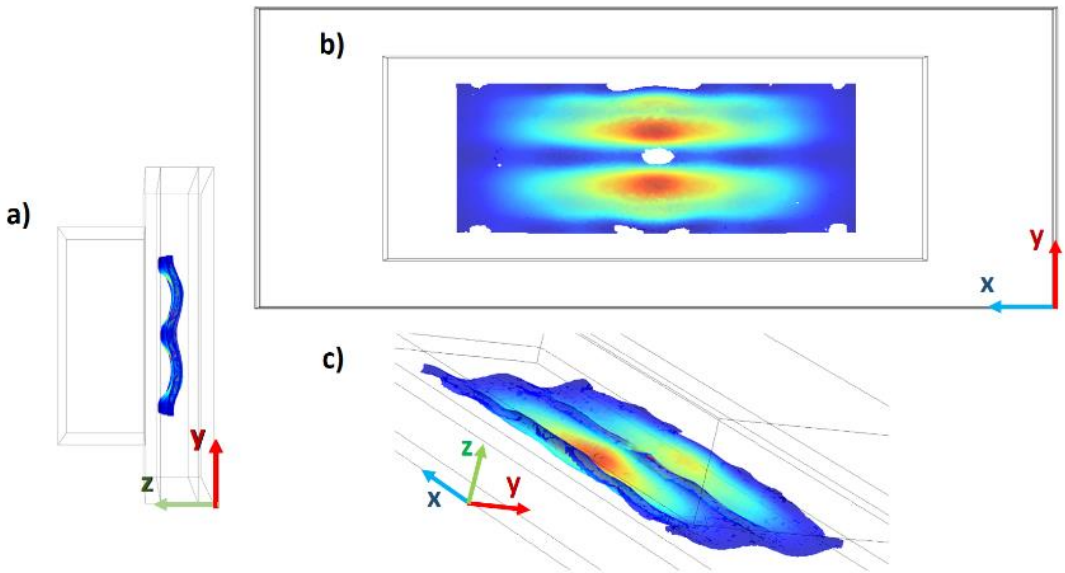

Figure 52 – Plane of levitation displayed by filtering the area below the margin of transducer (1/8th of PZT width and length), and filtering area where the force potential induced by the potential energy density is stronger that the kinetic energy density one. a) Side view of the planar resonator b) Top view of the planar resonator, c) isometric view of the planar resonator.

Once the plane of levitation is known, we can calculate the $SD_{waviness}$ as introduced earlier. It is the standard deviation of the Z-position of points showed in Figure 52. The standard deviation is higher as the undulation magnitude of the plane of levitation is greater. This number is used as a way of quantifying and compare plane of levitation planarity. To have a more complete view of the radiation force field in the fluid layer, we are interested in the force potential related to the kinetic energy density (which gives the lateral forces within the levitation place). A variable is introduced as a way of measuring and comparing the strength

of the lateral force field, its formula is comparable to equation (11) and is defined as such:

$$F^{3D\_Lat\_Rad} = \sqrt{\frac{d(-V\frac{3}{2}f_2E_{kin})}{dx}^2 + \frac{d(-V\frac{3}{2}f_2E_{kin})}{dy}^2} \quad (12)$$

Similar to the 2D modelling, because each device configuration has varying average energy density, the measure is normalised to average energy density in the fluid layer:

The two values are calculated for this case shown as example (SS), the $F^{3D\_Rad\_lat\_norm}$ is equal to 1.25×10^{-13} m^{-1} and the $SD_{waviness}$ is equal to 69.9 μm.

4.5 Results

4.5.1 Qualitative comparison

The different configuration, SS, SA, AS and AA all have different half wave resonance frequencies, respectively, 1.82 MHz, 1.79Mhz, 1.84Mhz and 1.85Mhz. These are found by exploring the frequencies around the expected resonance frequency which is 1.78Mhz (found by 1D modelling) and finding the maximum average acoustic energy density in the levitation cavity. Because it is known from the 2D modelling that the size of the layers of the planar resonator have a critical importance on performances, the same volume (+/- 5%) is used for both symmetric and asymmetric transducer, and symmetric and asymmetric cavity. Because it has been found in previous section that the level of lateral force depends greatly on many aspect of the design, and due to the large computational time associated with each simulation (18 min per model) only qualitative remarks can be made at this point, other simulation could be performed to be able to conclude

quantitatively on the effect of shape on lateral force field in a planar resonator used as a levitator. A qualitative view of the different planar resonator geometries and kinetic energy density gradient is showed in top view, in order to see how the field is structured, in Figure 53 and in side view to see, how the levitation plane is structured, in Figure 54.

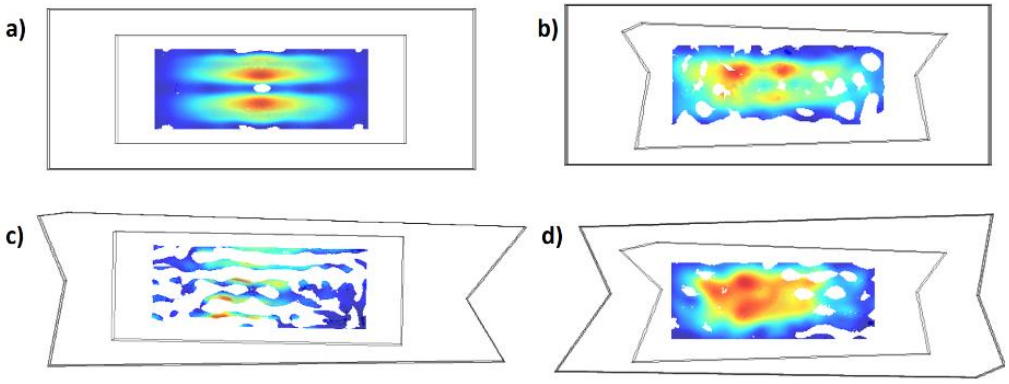

Figure 53 – Kinetic energy gradient filtered laterally to be below the transducer, and filtered axially to be the plane where the force potential is dominated by the kinetic energy term. In top view A) Symmetric/symmetric structure, b) Asymmetric/symmetric structure, c) Symmetric/asymmetric structure, d) Asymmetric/asymmetric structure

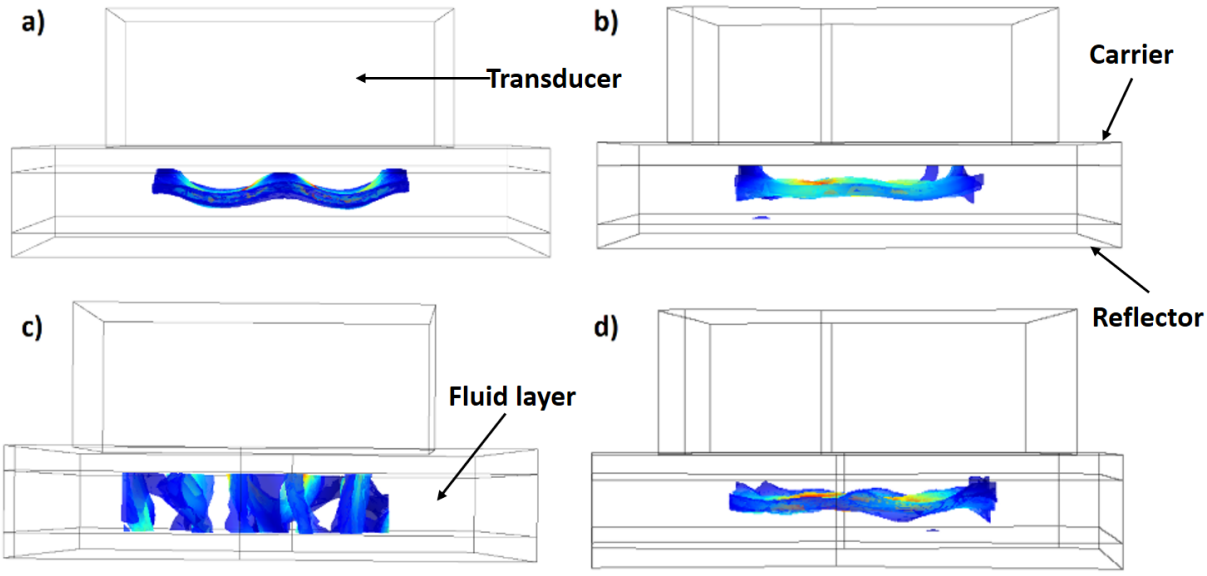

Figure 54 - Kinetic energy gradient filtered laterally to be below the transducer, and filtered axially to be the plane where the force potential is dominated by the kinetic energy term. In side view A) Symmetric/symmetric

structure, b) Asymmetric/symmetric structure, c) Symmetric/asymmetric structure, d) Asymmetric/asymmetric structure

The SS configuration gives a symmetric kinetic energy field as showed in Figure 53-a) and Figure 54-a). This configuration therefore would give a symmetric pattern of aggregate. This particular configuration gives a wavy plane of levitation. $F^{3D\_Rad\_lat\_norm}$ is equal to $1.25x10^{-13}$ m^{-1} and $SD_{waviness}$ is equal to 70 μm, this would give two lines of particles after acoustic excitation at this frequency at 1.82 MHz.

The AS set up results in an asymmetric energy field in the fluid layer as shown in Figure 53-a) and Figure 53-b). It seems that this configuration gives a flatter plane of levitation. $F^{3D\_Rad\_lat\_norm}$ is equal to $1.16x10^{-13}$ m^{-1} and $SD_{waviness}$ is equal to 65 μm.

The SA configuration results in an irregular energy field as seen in Figure 53-c), no clear half-wave resonance is seeing at the stage, as seen in Figure 54-c). Particle in this field would strongly be pushed sideways by the force field, resulting in line of aggregate that would levitate a certain point and fall to the glass reflector at other point. The lateral component of the acoustic mode is completely dominating the half wave mode. $F^{3D\_Rad\_lat\_norm}$ is equal to $1.81x10^{-13}$ m^{-1} and $SD_{waviness}$ is equal to 113 μm.

The AA Configuration results in more uniform kinetic energy field as shown in Figure 53-d) with a flat plane of levitation as shown in Figure 54-d). Particles in this field would be in levitation in a large flat discoid. $F^{3D\_Rad\_lat\_norm}$ is equal to $0.85x10^{-13}$ m^{-1} and $SD_{waviness}$ is equal to 48 μm.

The qualitative studies of kinetic energy density field configuration and plane of levitation geometry, gives some insight into how the force field is structured. First, the pattern of kinetic energy maxima and therefore potential trap position are mainly directed along the x-axis (the length direction) as seen in Figure 53-a) and Figure 53-c). This would tend to create aggregation lines, or long discoid, parallel to the longer sides of layers in a planar resonator. However in some case, the cavity mode is has a complex arrangement, as displayed in Figure 53-b), in this particular case, more circular discoid are expected, as the lateral force field would have both X and the Y components. Furthermore, the more symmetric the device is, the more symmetric the kinetic energy hence the force field seems to be, as

shown in Figure 53-a). For some structure, the lateral component can completely overcome the half wave mode, or levitating field, like in Figure 53-c). Finally, the AA structure seems to be able to give a flat and uniform structure for the half wave mode as shown in Figure 53-d).

Because the sizes, position and all other input of the planar resonator design have been chosen arbitrarily, previous simulation cannot be used for quantitative conclusion. Indeed, as shown using the 2D modelling, the structure and magnitude of lateral force field can change drastically when the planar resonator architecture is changed. To be more confident on the above conclusion, more simulation have to be performed to test the sensitivity of the results to various parameters. The models do, however, give clear example of the kinds of resonant behaviour that can be expected in real devices, including mode shapes that are only seen when the full 3D representation is modelled.

Section 4.3 demonstrated how changing the size of the transducer and the cavity could affect greatly the resulting acoustic radiation force field in the fluid layer at the half-wave frequency, the same study is performed in next section with a3D model. This modelling study has two goals, the first one is to confirm the influence of this two parameters, the second one is to establish if asymmetric or symmetric cavity/transducer have a definite effect on the lateral component of the acoustic radiation force field.

4.5.2 Quantitative comparison

The goal of this section is to establish how changing the shape of a transducer or the cavity affects the lateral forces and the structure of the plane of levitation. Because this is such a complex phenomenon, one simulation is not enough; it could have particularly high, or low, magnitude of lateral force due to special “lucky” or “unlucky” size or position choice. The method used here is to vary parameters other than the shape, and regard any behaviours that are maintained despite this “disturbance” as a trend associated with that shape (which is also less likely to be sensitive to the exact shape). The 2D investigation showed that the most potent aspect of a planar resonator design that affects the level of lateral force in the levitation plane is the width of the transducer. However, because we are in 3D, the

width change is transposed in a surface change. To do so two distinct set of simulations are planned:

The first will be to change the basis area (or contact area) of both symmetric and asymmetric transducers, the second is a change of basis area of both symmetric and asymmetric cavity. The cavity is studied in addition of the transducer for two reason, first, we are interested in the effect of shape of the cavity, secondly we want to confirm or refute the conclusion made using the 2D model, that the transducer shape? is more important than the cavity shape? For determining the type of lateral forces.

The method to quantify the effect of shape difference of transducer is the following; the basis areas for symmetric and asymmetric transducers are changed accordingly, while keeping the same shape ratio for the rectangular parallelepiped or the asymmetric shape. The levitation cavity is a rectangular parallelepiped that keeps a basis area of 37.5mm^2. The position of transducer stay central, 0.05mm off to the top (X-direction), to avoid any nonlinear effect due to perfect symmetry. The properties remain identical for all simulations. The method to extract $F^{3D\_Rad\_lat\_norm}$ and $SD_{waviness}$ is the one demonstrated in the method section of this sub-chapter. The 3D model take longer to compute, and the results get longer to extract than from the 2D model, therefore 7 sizes of transducer and cavity width are studied here.

4.5.2.1 Effect on shape of cavity tested with cavity total area

First, we decide to quantify the effect of cavity width and shape for a fixed transducer. The transducer chosen is the one introduced earlier in the method section, it is symmetric, has a length of 6.66mm and a width of 2.5mm, which results in an face area of 16.65mm^2. Here again the transducer have a thickness of 1mm, which gives a volume of 16.65mm^3. Under this fixed transducer, is place the cavity consisting a water layer sandwiched between two glass layers, the thickness remains the same as previous models. The basis area of the cavity changes with every simulations. Both symmetric and asymmetric cavity presented above had an approximate area of 37.5mm^2, with a thickness of 0.42mm giving a volume of 15.75mm^3. The top face area is shifted gradually and linearly from 30 to 45mm^2 for both symmetric and asymmetric cavity as shown in Figure 55.

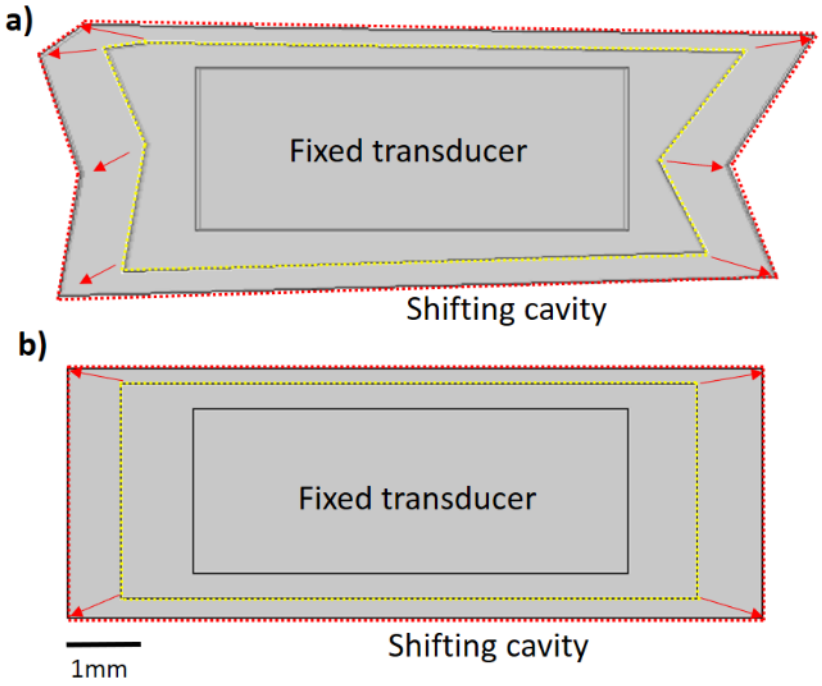

Figure 55 - Drawing showing the extension of basis area of the fluid cavity while having a fixed transducer size. A) in the case of a symmetric transducer coupled with an asymmetric cavity (SA), b) in the case of symmetric transducer coupled with a symmetric cavity (SS)

The goal here is to see of the effect seen of in Figure 65 and Figure 66 or relative sizes in the device. To do so, the quantitative variables, namely $F^{3D\_Rad\_lat\_norm}$ and $SD_{waviness}$, used in throughout this chapter are calculated using the method exposed earlier. This values once calculated are displayed below in Figure 57and Figure 56.

Figure 56 – Standard deviation of z-value of levitation plane, in μm, versus the change in area of the cavity face coupled to the transducer, in mm^2, for both SS and SA structure.

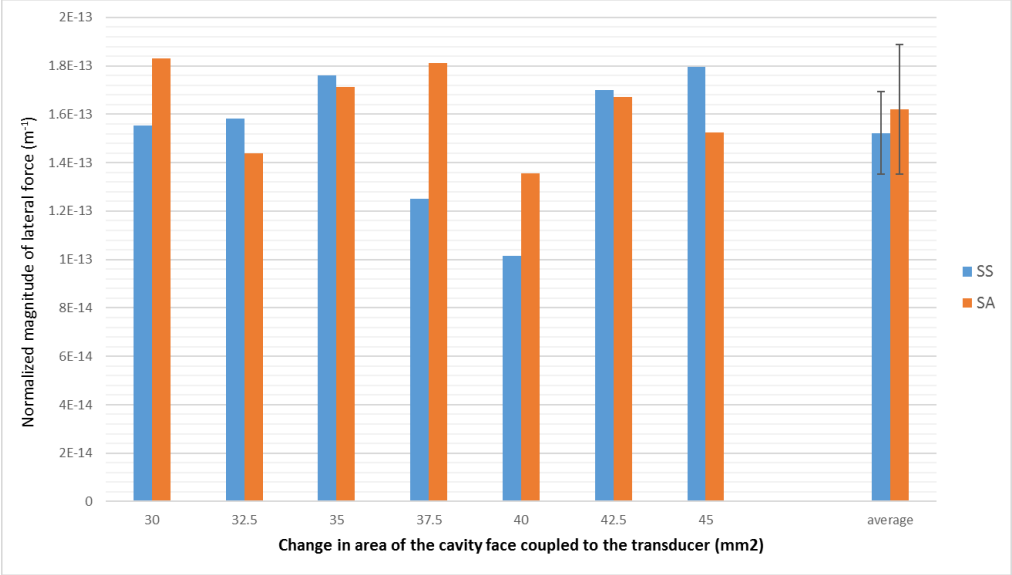

Figure 57 – Normalized magnitude of lateral force in the fluid layer, in m^{-1}, versus the change in area of the cavity face coupled to the transducer, in mm^2, for both SS and SA structure.

An effect of the cavity architecture on the level and structure of the lateral force field in the fluid layer is visible. On average, the SS structure gives flatter plane of levitation than the SA structure. Furthermore, the SS structure gives lower average of lateral radiation force magnitude than the SA structure

It is interesting to note that the average level of waviness and magnitude of lateral force field is high and fluctuates relatively slowly. Furthermore the level of

undulation of the levitation plane fluctuate much more in the case of a SS structure with the size of the cavity than for the case of a SA structure.

In conclusion this section shown that there is no significant correlation between the cavity symmetry and the average properties of the lateral forces found in the chamber. The next section presents a study performed on the effect of the transducer size and symmetry on the acoustic radiation force field structure.

4.5.2.2 Transducer area shift

In this part, the effect of varying transducer width and shape is investigated for a fixed cavity. The cavity chosen is the one introduced earlier in the method section, it is symmetric, has a length of 10mm and a width of 3.75mm, which results in an face area of 37.5mm^2. Here again the fluid cavity have a thickness of 0.42mm, which gives a volume of 15.75mm^3. Above this fixed fluid cavity, sandwiched with the carrier and reflector having the same surface area, is placed the transducer consisting of a piezo ceramic layer. It thickness remains the same as previous models. The basis area of the transducer changes with every simulations. Both symmetric and asymmetric transducer presented above had an approximate area of 16.67mm^2, with a thickness of 1mm giving a volume of 16,67mm^3. The top and bottom faces areas are shifted gradually from 12.04 to 22.04mm^2 for both symmetric and asymmetric transducer as shown in Figure 58.

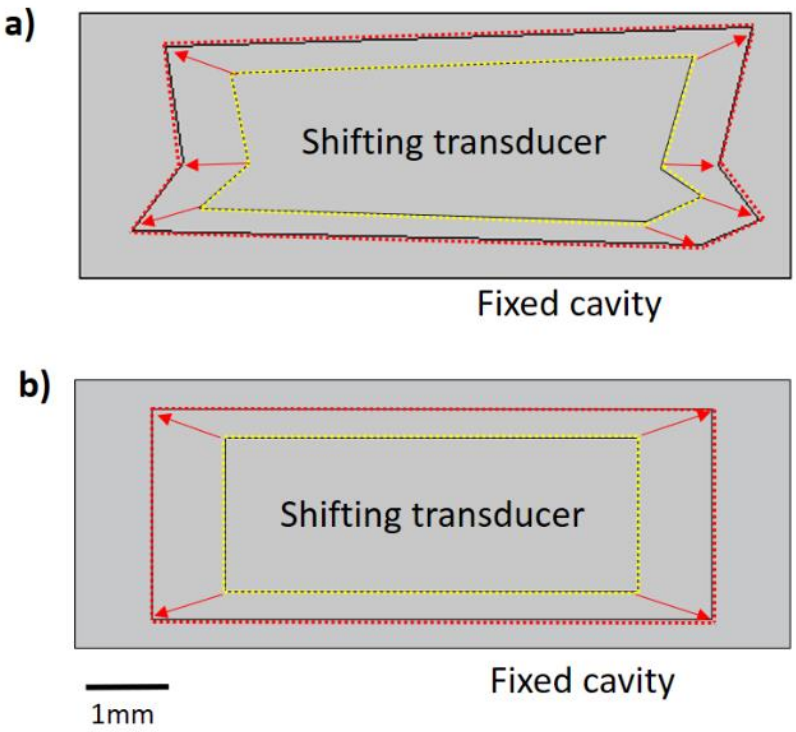

Figure 58 – Drawing showing the extension of basis area of the transducer with a fixed cavity size, a) in the case of an asymmetric transducer coupled with symmetric fluid cavity, b) in the case of symmetric transducer coupled with an asymmetric cavity.

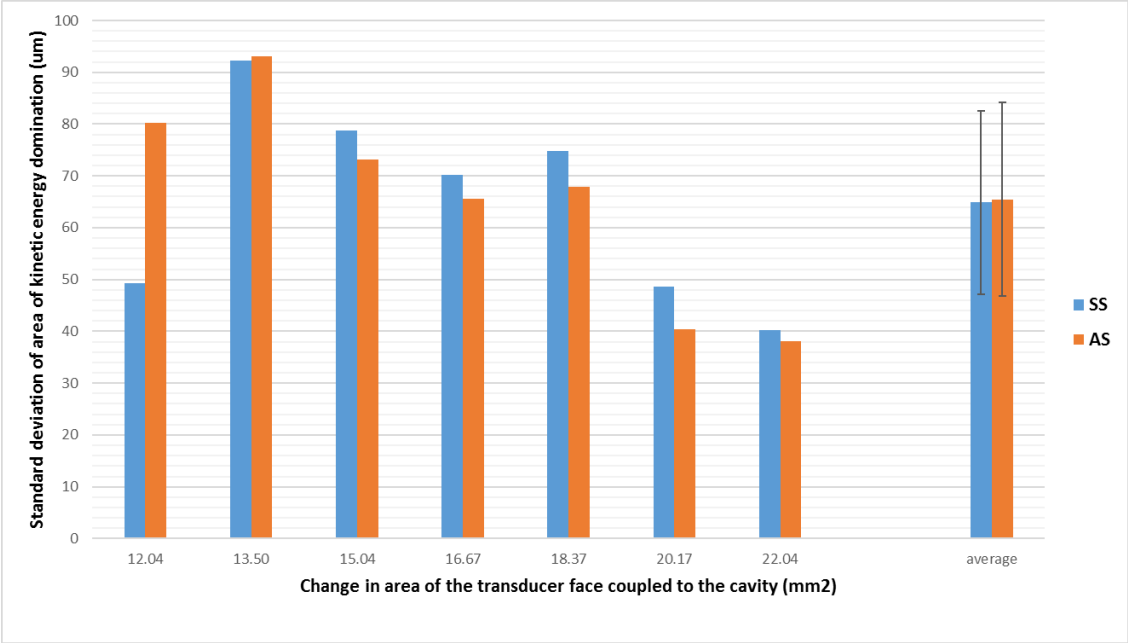

Figure 59 – Standard deviation of the z-value of levitation plane, in μm, versus the change in area of the transducer face coupled to the cavity, in mm^2, for SS and AS structure

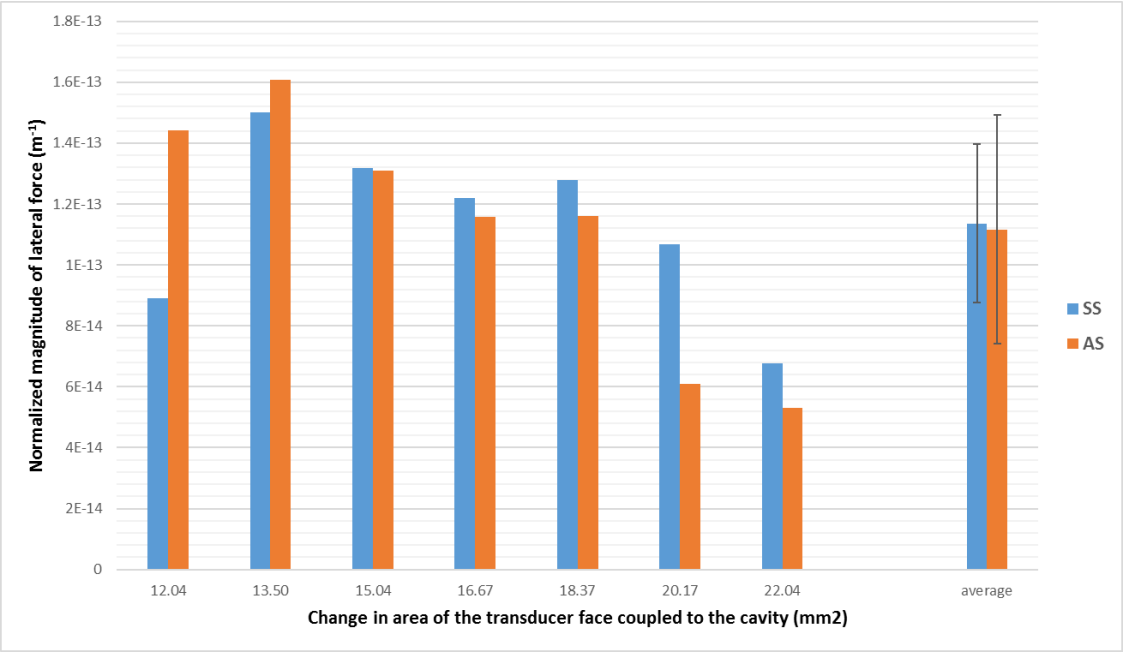

Figure 60 – Normalized magnitude of lateral force, in m^{-1}, versus the change in area of the transducer face coupled to the cavity, in mm^2, for SS and AS Structure.

No clear correlation between the transducer lateral architecture and the strength or structure of the lateral force field in the fluid layer is visible. On average the SS structure gives comparable level of undulation of the plane of levitation than the AS structure. As for the lateral radiation force magnitude, the SS structure gives a comparable average of the AS structure.

It is interesting to note that the average level of waviness and magnitude of lateral force field is comparatively low and fluctuated highly with the transduce size.

Thus, for these dimensions, the lateral shape of the transducer has low to no effect on the magnitude of lateral force field nor the geometry of this field. However, this modelling confirms the sensitivity of the acoustic field to the size of the transducer.

2D and 3D modelling showed a great influence of transducer size on the acoustic radiation force field structure and magnitude. Futhermore, section 4.3 showed an important effect of the transducer position on it. The next section will confirm the above statement by fabricating planar resonators and study particle behaviour in the fluid channel excited at a half-wave frequency.

4.6 Experimental Evaluation

The main conclusion of the modelling work is that the design configuration of the planar resonator has important effect on the magnitude of lateral force in the fluid cavity, and that even small structural changes in the design can have large effects on the lateral component of the acoustic modes. However the inter-dependency of the design parameters and the high computational cost of performing more exhaustive searches of the parameter space make it difficult to have firm conclusion on effect of each parameters.

This part will confirm the influence of design configuration experimentally, particularly transducer position and width. First the layered resonator fabrication is described. Experiments are performed, changing gradually the position and the width of the transducer, and levitation and aggregation processes examined using particle image velocimetry (PIV).

4.6.1 Device fabrication

A half wave resonator is fabricated with transuducer, carrier, fluid and reflector layers. The 0.14mm thick double sided adhesive tape (3M 9731) is stacked three times with itself to have the required thickness of 0.42 mm to form the fluid channel height. Then it is laser cut using the Laserscript LS 6090 to the shape required (50x15mm rectangular shape). Then the double side adhesive with external dimension of 75x25mm is sandwiched between two 75x25x0.17 0-CON 161 glass slide (Logitech, Old Kilpatrick, Glasgow, UK), the second one is drilled to allow fluidic exchange using a 0.6 mm diameter tungsten tile bit. Finally, a laser cut 75x25x10mm piece of acrylic is taped to the pierced glass slide using the same double coated adhesive. This acrylic layer is fabricate for fluidic exchange; two 3mm diameter holes are laser cut in it to allow silicone tubings to fit in it. A large 45x15 mm window is cut as well to grant visual access to the levitation channel. This glass sandwiched laser cut tape form the cavity channel or levitation channel as shown in Figure 61 a) & b).

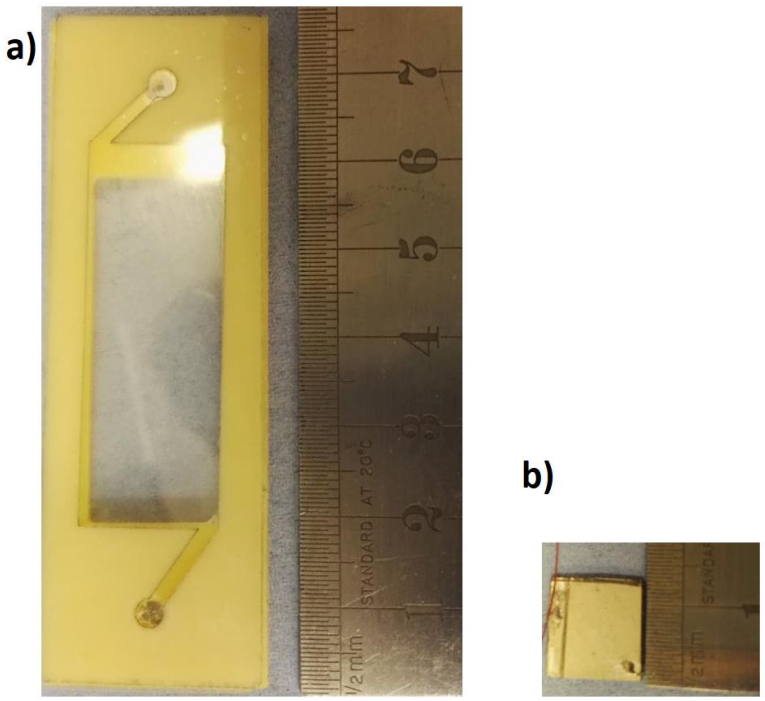

Figure 61 – a) Picture of asymmetric cavity, b) Picture of symmetric cavity, c) Picture of asymmetric transducer, d) Picture of symmetric transducer

The method to fabricate the transducer is the same for all devices. The PZ26 piezoelectric transducer (Ferroperm piezoceramics, Kvistgaard, Denmark) is provided as a 50x25 mm sheet of 1mm thick transducer. The first step is to cut the large sheet into smaller rectangular transducer (12.9x11mm) using a manual tile cutter.

Then, using the tungsten tile bit, the transducers are scored top to bottom on one side (far from the centre) in order to isolate most of the top electrode from the scored side part. Then by using a Silver Conductive Paint (SCP03B, ELECTROLUBE) the scored top part is connected to the bottom part. This allow both live and neutral electric wire input to be soldered on the same surface. Indeed in the case of bulk acoustic wave planar resonator. The quality of the device and therefore resonance is related to the flatness/parallelism of each layer.

In most application the transducer is fixed to the carrier using epoxy, but for our experiment, the transducer have to be removable from one device to be reused, a non-permanent coupling layer was sought. Finally, glycerol is picked as an temporary coupling fluid, it has the advantage of being highly viscous, and therefore the transducer is immobile while performing the experiment. Glycerol has a comparatively high acoustic impedance of 2.4×10^6 Pa s/m (water acoustic impedance: $1{,}5 \times 10^6$ Pa s/m) making it a good acoustic coupler for ceramic and

glass. Finally, it is a harmless chemical compound, which facilitates experiment set-up.

4.6.2 Set-up and method

4.6.2.1 Set-up

The set up consist of a moving holder carrying the planar resonator, the transducer is coupled with the levitation cavity using 15 µL of glycerol, measured with a micropipette. The transducer is positioned above the acrylic optical window randomly. In order to quantify the effect of position. The transducer is plugged via a BNC Male Plug Q9 to Dual Hook Clip Test Probe Cable an amplified signal generator. The amplifier is a ten time gain non-inverting OP-amp. The input signal is an amplified swept frequency sinusoidal, from 1.82 MHz to 1.87 MHz. Because the transducer impedance varies depending on if the resonance frequency is hit or not[97], the amplitude varies accordingly. In this experiment the minimum amplitude applied to the transducer is set to 3Vpp. The resonance frequency is 1.85 MHz but can change slightly with the position or width of the transducer, or the temperature of the device, hence the frequency sweep.

The planar resonator is filled with a solution of water containing Ø 10 µm polystyrene fluorescent microbeads per millilitre (Fluoresbrite Fluorescent Microspheres 10.0 µm). The concentration of this solution is of 4.55×10^5 particles/ml. The fluid channel volume is 250 mm^3 thus the fluidic capacity is 0.25 ml. This fluid is injected in the levitation chamber using a 5mL syringe and silicone tubing fitting the Ø 3mm laser cut hole in the acrylic layer, as shown in Figure 62.

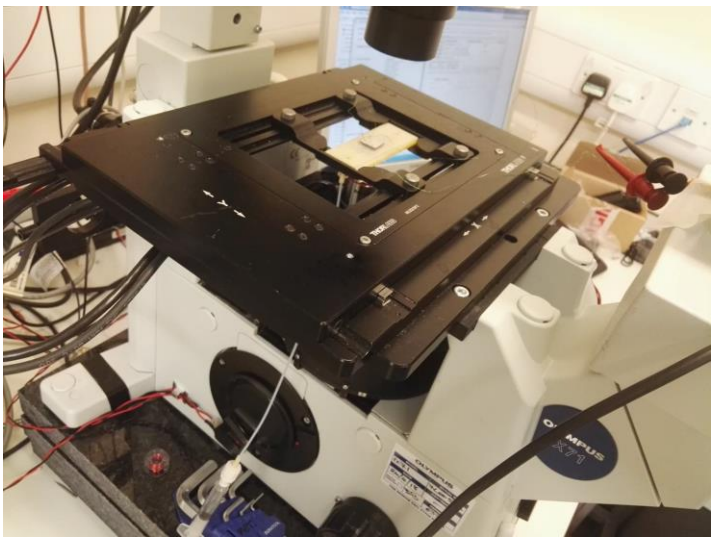

Figure 62 – Planar resonator held by the 2-ayis holder, the transducer is placed faced up and coupled to the carrier using 15mL of Glycerol. The syringe contains a solution of water and 10 μm fluorescent beads, it fills the planar resonator by the bottom. The inverted microscope take image by the bottom. We can see grabber clips on the right of the microscope, this connect the transducer to the amplified wave generator.

4.6.2.2 Experimental method of optical acquisition

The experimental method is kept the same for all following experiments; the fluorescent polystyrene beads are injected in the channel. Then the amplified swept sinusoidal signal is supplied to the ceramic piezoelectric transducer.

As the signal is carried to the transducer and the planar resonator a movie is recorded using Olympus IX81 inverted research microscope which is fitted with a Hamamatsu ORCA-ER black/white digital camera, fitted with blue-light fluorescent filters. The transducer amplitude is 3Vpp, this being chose to avoid any temperature rise, at this amplitude the lateral movement is expected to be slow. Therefore a movie of 1min is taken, with 1s between each image having an exposure time of 50ms.

Movement analysis for quantitative comparison

Once the first minute of movement is recorded, these pictures are processed in a PIV (Particle Image velocimetry) GUI-CODE using Matlab. William Thielicke [99]

wrote this code called PIVlab. This software allow us to extract from a couple of images different output such as the velocity magnitude, velocity vorticity, velocity divergence and others. We are principally interested in velocity magnitude which is proportional to the acoustic forces on the particles This force field is a sum of three distinct forces, the lateral acoustic radiation force, the drag force (resulting from fluid motion from streaming) and the Bjerknes force. Bjerknes force is negligible in comparison of the radiation force because of the relatively low concentration of particles, and the drag force is negligible because of the small velocity of particle compared to the fluid.

The method to extract the velocity in a constant way is presented below:

First, two pictures are loaded in the GUI, the first one is taken at the 10 sec mark, the second one is taken at the 20 sec mark. The first picture taken after 10s in the force field because it is the time the particles to fully overcome any fluid motion resulting from the injection. Moreover this time allow us to be sure than all the particle are rested in the plane of levitation. The second picture is taken after 20 sec to have a difference in position significant enough to have a clear view of the movement, but not too large, indeed large movement of particle can be cause of mistake from the PIV (wrongly associating a particle for another). Moreover the simulation showed us that the force field, tend to diminish when to particle approach their final position. Recording the beginning of the lateral movement is critical.

Secondly, the interrogation area is stipulate, a multipass PIV is chosen, the interrogation area are finer at each pass, 4 passes of interrogation are done subsequently. The first one have an area of 256 pixel, then 128 and 64 pixels.

Then, we calibrate the PIV for a good pixel to mm and step to second association, pictures are a 1024x1024 pixels square, equivalent to a 2.2x2.2mm. The time step between the couple of image is 3 seconds as specified earlier.

Next, PIVlab displays the amplitudes found in a graph showing the V velocity (top to bottom in the movie) in the Y-axis, and the U velocity (left to right in the movie, which is the flow direction as well) in the X-axis. Outlier are therefore clearly visible as they are out of the lump of velocities. These outliers are due to PIV mistaking one particle from another when extrapolating the movement endured between the two pictures. This step is important because few outliers can disturbed averaged absolute value which is the final step.

After that, the amplitude are showed in a picture as arrows, many possibilities of rending are there available. We chose to only show the V velocity (top to bottom) because the U velocity is a mix of lateral radiation induced movement coupled to flow movement due to the possible difference in pressure at the two end of our fluidic connection, and the injection inertia. Moreover, the width of the transducer is changed just in this direction. This arrows and then complement with a colour gradient to be able to see the movement induced by lateral force at first glance.

Finally, these V velocity amplitudes are exported as a text file. These numbers are converted in their absolute values and averaged. Lastly, they are stored for future comparison.

4.6.3 Experimental results

As described earlier, the solution containing the particles is flowed into the channel, then the flow is stopped and the excitation signal is sent to the transducer. At the same moment recording of the one minute video begins. The video is being taken below the middle of the transducer.

After every recording the transducer is translated to another positon. The side of the rectangular shaped transducer is kept parallel to the rectangular shaped cavity underneath. Five random positions are then tested.

After a set of five position, the transducer is removed, and the top side of the transducer is sanded to remove 0.1mm of matter. Then five random position are tested again. A third transducer width is then tested, by removing another 0.1mm of matter to the transducer.

Fifteen video are therefore taken, the first step is to remove the immobile background, formed by sedimented fluorescent particles, and these particles could interfere with the particle analysis later on. To do so, the stack average picture is calculated then subtract from the stack of pictures using imageJ. That way, all immobile light field is removed. Some case of stronger lateral force than others are clearly identifiable at this stage, Figure 63 shows the case of a strong lateral force field and the case of a weak lateral force field.

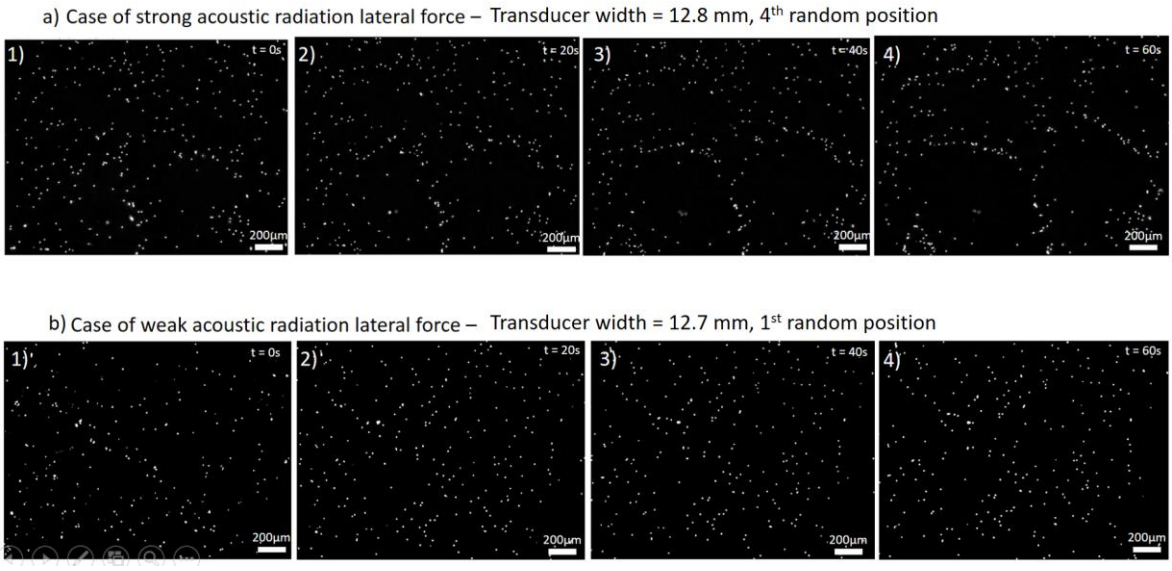

Figure 63 – **a)** Case of strong acoustic radiation lateral force – transducer width of 12.8 mm, 4th random position, 1- at the beginning, 2- after 20s, 3- after 40s, 4- after 60s sound standing wave formation. **b)** Case of weak acoustic radiation lateral force field, transducer width of 12.7mm , 1st random position, 1- at the beginning, 2- after 20s, 3- after 40s, 4- after 60s sound standing wave formation.

Figure 63-a) shows the case of strong lateral resonance. This movie have been taken with a transducer Y-width of 12.8mm, it is the 4th position tested. We see at the beginning (a) an even spread of particle. The lateral acoustic radiation force begin to push particles up or down, thus some areas have less concentration in particle than others (b). After 40 or 60 sec, the particle are clearly forming lines of particles as seen in respectively (c) and (d).

Figure 63-b) we see the case of a weak lateral resonance. This movie have been taken with a transducer Y-width of 12.7mm, it is the 1st position tested. We see no difference between pictures over the global disposition of particle in the fluid, even after one minute in the standing wave force field. To have a fine look over small movement of particle, the MPIV is used. As shown in Fig.85.

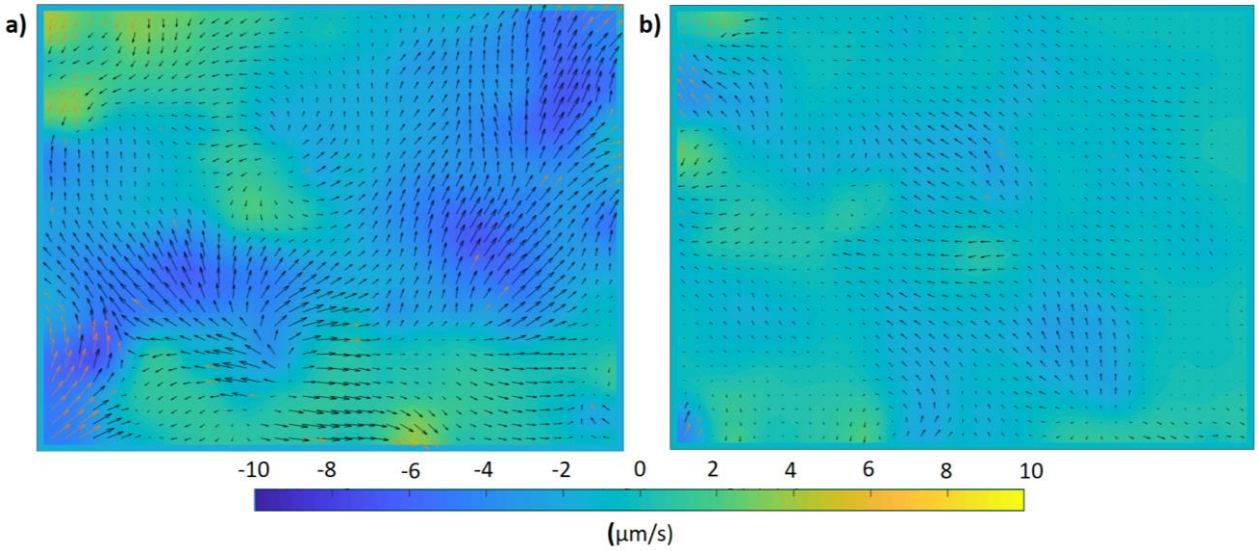

Figure 64 –"v" velocity, velocity in the Y direction, (bottom to top). Blue areas is where the particles are pushed up, yellow areas are where the particles are pushed down. Green areas shows area of little movement. a) transducer 12.8mm Y-width, 4th position, case of strong lateral acoustic radiation force field, b) transducer 12.7mm Y-width, 1st position, case of a weak lateral acoustic radiation force field.

Figure 64 is given as an output of PivLab, a software using a Matlab GUI introduced earlier. After the steps presented before we obtain this graph, showing the lateral velocity, bottom to top.

We are particularly interested in this bottom-up velocity, and not the left to right one, because the width of the cavity is smaller in this direction and 3D modelling showed us that the lateral acoustic radiation force field is oriented to push particle to in the direction of lower width. Moreover this avoid to take account of some residual movement due to injection, which is left to right.

Moreover the position of the transducer is arbitrarily translated in this direction, closer to one "wall" of the cavity, or the other. Also, the sanding of the transducer is made in this direction as well, always the same side (top side) is sanded two times to vary the width of the transducer.

Figure 64-a) shows a stronger y-velocity field compared to Figure 64-b). The velocity field is the derivative of the lateral force field, which is largely dominated by the acoustic radiation force. Therefore comparing the magnitude of the velocity field is relevant to compare the magnitude of force field.

To do so, the absolute value of the Y-velocity (v) is averaged on the totality surface of the levitation plane recorded in the video. This is made for all position, then it is averaged. This last average represent the magnitude of velocity for this transducer width, data calculated this way are represented in Figure 65.

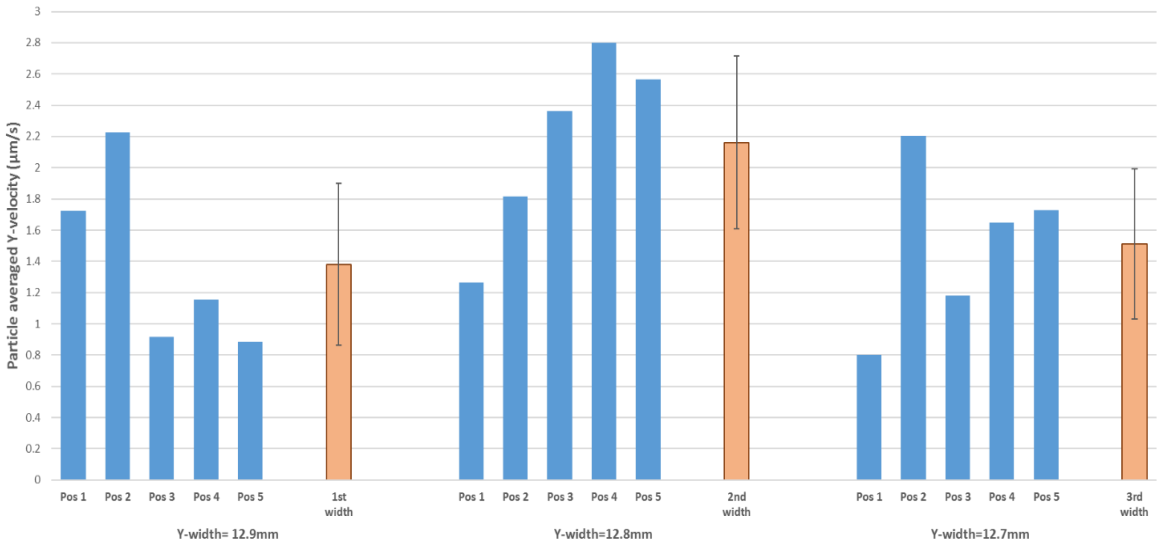

Figure 65 – Average of magnitude of Y-velocity for random position and the three size of transducer studied. The values are retrieve using PIV, on 1 min movie taken after a half-wave frequency excitation of 3 Vpp at 1.85 MHz.

Figure 65 shows that the position have an important effect on the magnitude of acoustic lateral radiation force, a small change in position can change drastically the average value of absolute lateral velocity. Moreover, by averaging them by y-width of transducer, a difference is noticeable, which tend to prove an effect of the width of transducer as well.

The position has an important impact on the magnitude of lateral velocity, this impact make it impossible with this N-number to have a definite conclusion as for the transducer width.

Experiments with higher N-number, and higher possible values as for the transducer width are necessary to have a clear conclusion on the effect of this device property on the lateral force field. However, experimental results showed us that moving slightly the transducer of position, or altering the width of the transducer can have a massive effect on the lateral force field in the fluid chamber.

The problem of such experiment is how complex it is to isolate the effect of modifying one element of the device compared to other. For example, in this experiment one side of the transducer is sanded to remove 0.1mm of material though all the thickness. Because of the technique, the angle of this side might have changed slightly, moreover this change the X-to-Y ratio of the rectangle forming the transducer. It changes the area of the transducer in contact with the glass and so on.

A better way to have more definitive conclusion as for the lateral force field in a planar resonator, would be to do more experiments with random transducer widths and lengths, random positions, random chamber widths, and gather all information and the results associated, process them with statistical analysis to have definitive conclusion.

The next section summarized the insight on acoustic radiation force field lateral structure gave by this modelling and experimental chapter.

4.7 Summary

In this chapter the sensitivity of lateral acoustic radiation forces to device parameters has been explored. These lateral forces are important: In some In this chapter the sensitivity of lateral acoustic radiation forces to device parameters has been explored. These lateral forces are important: In some applications such as imaging cytometery [100], they are unwanted, whereas in the tissue engineering work presented in chapter 6 they are required to form discrete cell agglomerates. Hence being able to remove them or modify their position is useful.

Investigations into varying geometrical parameters and small changes in the shape of both the transducers and cavity have shown a important effect of transducer size and position on the acoustic radiation force field structure and magnitude. Moreover it seems like all planar resonator structural parameters can affect this force field greatly.

This chapter has experimentally confirmed that a simple change of the transducer position or width can drastically change the lateral force field in a planar resonator.

A modelling work based on randomized planar resonator structures, with high N-Number, supported by a strong statistical analyse could give stronger conclusion on the importance of each design property as for the lateral acoustic radiation force in the future.

The hard-to-predict sensitivity of lateral forces to device design, has important implications for the manufacture of planar resonator devices as it shows that without extremely tight tolerances on all parameters, each device from an assembly line is going to behave differently. There are various strategies that might help to work around this sensitivity. These include:

a) Using resonators in ways that are not sensitive to small variations. For example in flow through cytometers [101], the final particle at the device outlet results from the average fielded experiences during its transit.
b) Analogous to the laser trimming of crystal oscillators, these results show that devices can be tuned by small alterations after fabrication.
c) Use planar resonator with very large length and width dimension compared to thickness, to highly dump potential lateral component of the acoustic modes.
d) High-speed lateral movement of the transducer should excite different lateral component of the acoustic modes, if the movement is quick enough they could average and counter-act one another.

The fabrication of simple planar resonator that would give perfectly controlled acoustic radiation force field for a special application is complex. In chapter 6 such device is achieved by trying multiple combination of size and it is used to form Huh7 discoids. However force field obtained this way are still not controlled, in next chapter, two novel ways to control the lateral acoustic force field are introduced by adding an extra layer to the layered resonator.

Chapter 5: Structured excitation for tailored lateral force fields in planar resonators

5.1 Introduction

In this chapter novel strategies are investigated for the creation and control of lateral force distributions in planar resonators. Both static and dynamic strategies are explored. In each case the principle is to introduce a structured layer between the transducer and the fluid chamber that directs the coupling of the acoustic field.

In the case of the static technique, the intermediate layer comprises a 3D-printed part which directs the excitation of the fluid chamber to specific points. In the dynamic technique the intermediate layer is instead composed of a channel filled a two-phase flow having differing acoustic properties. Transport is achieved by using flow to move the acoustically active phase along the channel.

This chapter introduces in detail both concepts, introduces the design procedure followed to achieve the required acoustic structure, and presents experimental investigation of devices using these principles.

5.2 Concept

The concept of this device is to add an extra layer to the layered structure composing a planar resonator. This layer comprises two different materials having different acoustic properties. By tuning the excitation of the transducer to excite a thickness standing wave in one of these materials and not the other, the acoustic field is structured accordingly. Therefore, the configuration of this extra layer drives the configuration of the force field in the fluid, or particle manipulation, layer.

5.2.1 Static two-material intermediate control layer

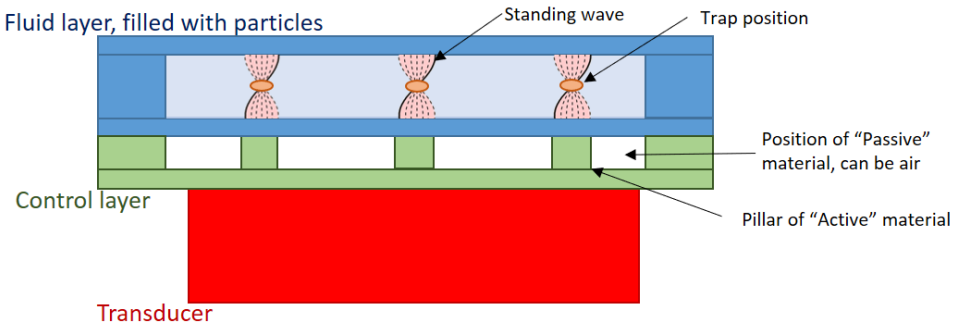

Figure 66 - Schematic of planar resonator with intermediate two-material control layer. The active layer (green) is designed to transmit acoustic radiation force into the fluid layer for particle manipulation, whereas the passive layer (white), which can be a gas, does not. The particle-trapping position happens above the active part of the control layer with the speed of sound fitting the transducer frequency for a given thickness mode.

The static control layer is composed of two materials having different acoustic properties arranged laterally. It is placed in the acoustic path of the thickness acoustic mode, and therefore can be placed between the transducer and the fluid cavity or between the fluid cavity and the air interface. The effect of these two placement options will be studied later. For most applications, having a standing wave transmitted through one of the materials (here called the active material) and not the other (called passive) is sufficient. In this case the passive material can be a weak acoustic transmitter, such as a gas like air. In this case just one resonant frequency exists, and standing waves are excited locally, adjacent to the solid material. In the case of a two-phase solid control layer with two solids having different internal speeds of sound, two different resonance frequencies would exist in the same thickness mode. In this case, changing the transducer frequency from one to the other would change the lateral configuration of the acoustic energy field. In this chapter the case with just one possible active material is studied and the concept is schematised in Figure 66.

This concept allows localization of force fields, and has the comparative advantage of being easy and low-cost to produce. Moreover, different shapes and

sizes are possible for the active area(s) in this extra layer, potentially benefitting a wide range of applications.

5.2.2 Dynamic two phase flow intermediate control layer

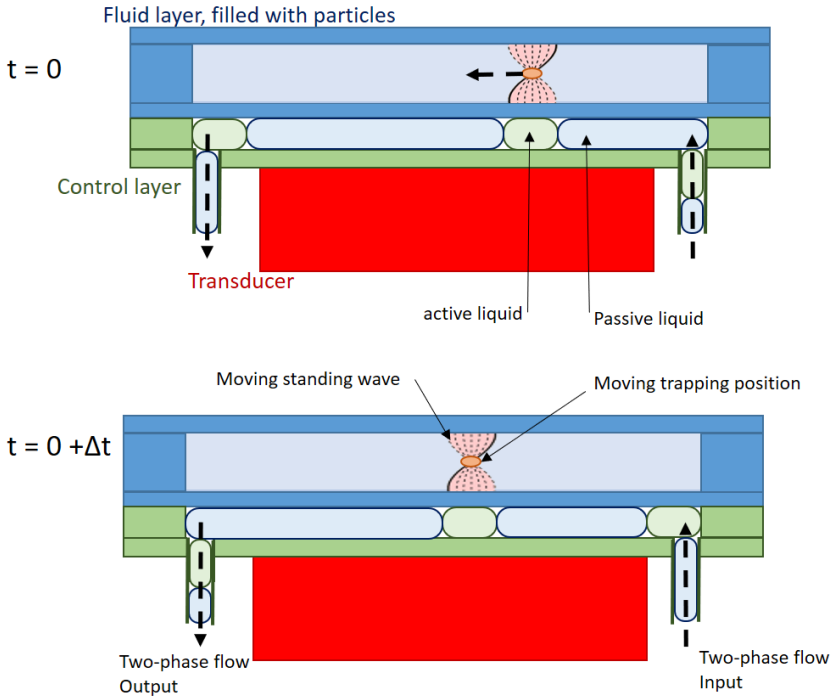

Figure 67 - Schematic of planar resonator with intermediate two-liquid phase layer. Here the active liquid is pale green. The pale blue liquid is passive. The trapping position is above the active liquid, with the speed of sound fitting the transducer frequency for a given thickness mode.

This concept is similar to the one introduced above; the control layer is composed of two different materials having different acoustic properties. This design, however, uses two immiscible fluids pushed through a channel. The transducer is tuned to excite a thickness standing wave though one of the fluids and not the other, as schematize in Figure 67. A combination of liquid and gas is possible and would be effective as they have vastly different acoustic properties, but liquid/liquid combinations are preferred because they are incompressible, facilitating steady and predictable flow in the channel. The particles in the manipulation cavity follow the active liquid along the path formed by the channel.

This design concept allows both localisation and transport of particles in levitation, whilst again being low-cost and easy to fabricate compared to other particle manipulation systems. Since particle trajectories follow the channel path in the control layer, this system is ideal for applications requiring repeatable behaviour, such as bio-printing, cell-cell interaction and others.

5.3 Design choice assisted by two dimensional finite element analysis modelling

Before fabrication of the device, modelling is used to investigate the effect of design configuration on system characteristics and performance. The performance of such a device is related to the acoustic energy localisation in the fluid layer. If most of the energy lateral configuration follows the lateral configuration of the control layer, the device has good performance, and vice versa. Studied below are the effect of control layer position, speed of sound difference between the two materials forming the control layer and the active area width on overall system performance. Analyses are carried out using *Comsol* two-dimensional FEA models introduced in chapter 3. The knowledge acquired here is then used for further modelling and device fabrication.

The models used have a particle or manipulation chamber of 0.42mm thickness, sandwiched between two 0.17mm thick glass layers. The control channel is 0.42mm thick and has a 0.17mm thick glass layer attached to it. The width of the device is 15mm and the transducer width is 12mm, which is chosen arbitrarily to be similar to what is easily producible. The middle of the transducer is always placed slightly off the middle of the cavity axis to avoid any numerical aberration caused by perfect symmetry in the device.

5.3.1 Position of control layer

There are two possible configurations of the position of the fluid control layer within the device - adjacent to the reflector or adjacent to the transducer, as shown in Figure 68. In order to identify the most effective configuration, modelling is used to investigate how the energy field in the manipulation cavity reacts to the change of position of the active fluid within the control channel. For this modelling air and water were respectively used as the passive and active fluids in the control layer due to the significant difference in their acoustic properties. The width of the active area is 2 mm, and it is positioned to the right of the control layer centre, as shown in Figure 68. This width was chosen arbitrarily, and the position also chosen arbitrarily away from the middle of the cavity to avoid any aberration due to symmetry.

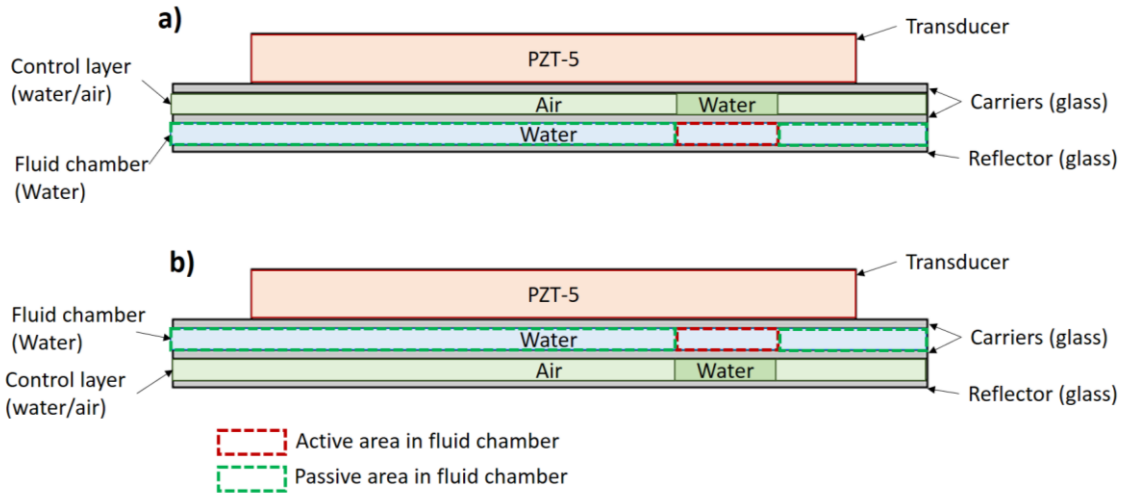

Figure 68 – The two configurations of placement of the control layer within the particle manipulation system described. a) Control layer placed between the transducer and the fluid chamber filled with particles. b) the control layer is placed between the fluid chamber and the reflector.
The active area in the fluid chamber is marked with a red dotted line; passive areas are marked with a green dotted line.

To quantify and compare both structures two performance variables are introduced - firstly, the energy density in the active area of the fluid chamber, which is the sum of the kinetic energy and the potential energy divided by the surface of interest. The second performance metric is the quotient of the energy density in the active area and the energy density in the passive area, which gives a ratio describing the localisation of the energy, hereafter called the localisation ratio. This

metric is more useful than the first, as while the energy density can be increased by increasing the voltage amplitude at the transducer, the localisation ratio is fixed for any structure. The fluid active area and passive areas are shown in Figure 69.

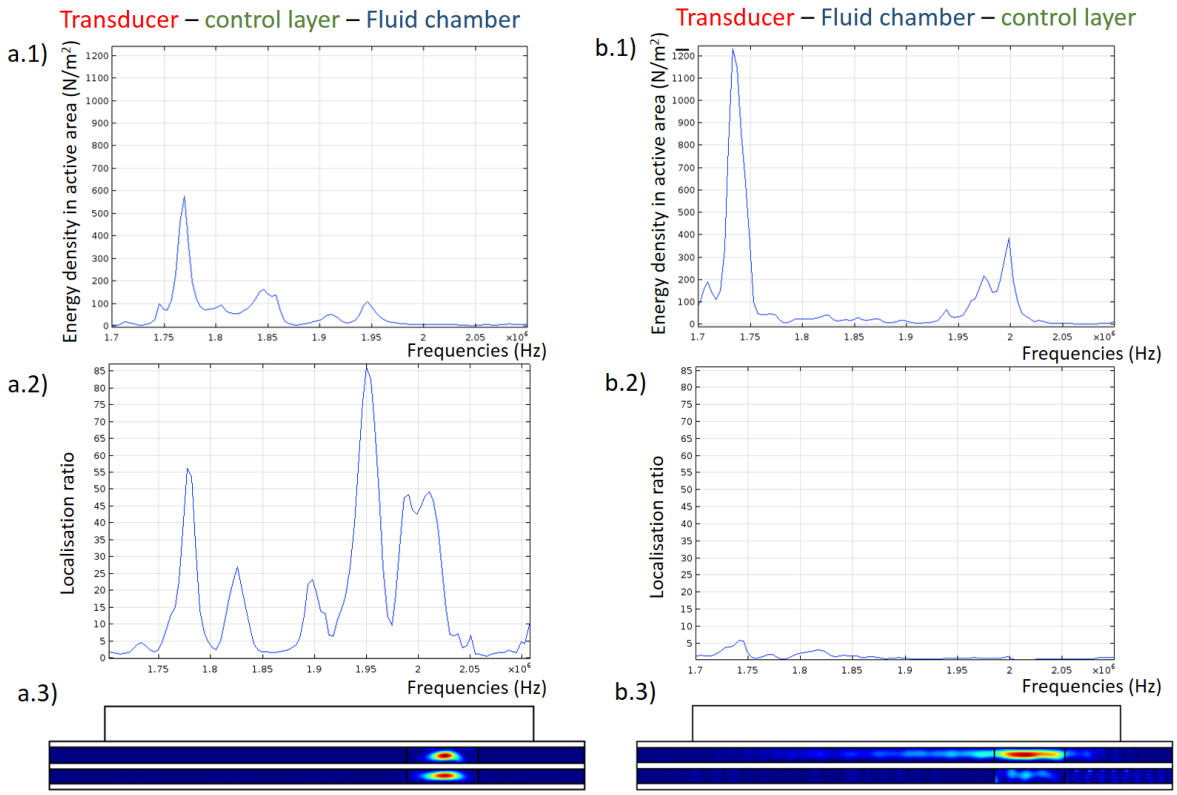

Figure 70 – a) Structure with the control layer adjoining the transducer. 1- Energy density in the active area of the fluid chamber vs transducer frequency, 2- Localisation ratio vs transducer frequency, 3- Energy kinetic gradient at the frequency of maximum localisation ratio (1.95Mhz); b) Structure with the control layer next to the reflector. 1- Energy density in the active area of the fluid chamber vs transducer frequency, 2- Localisation ratio vs transducer frequency, 3- Energy kinetic gradient at the frequency of maximum localisation ratio (1.74Mhz)

In Figure 70, the two system configurations are compared using the two variables introduced earlier. .a-1) and .b-1) demonstrate that the energy density in the active area is greater when the control fluid is next to the reflector, but .a-2) and Fig.95.b-2) show that the localisation ratio is greater in the case where the control layer is next to the transducer. .c-1) and .c-2) show the gradient of kinetic energy for the frequencies associated with the respective maximum localisation ratio for each configuration. The system with the control layer next to the

transducer gives a more focused energy field. Since for our application the focusing is critical, this arrangement is preferred.

5.3.2 Speed of sound difference

The two materials in the control layer must have different speeds of sound for the proposed concept to work. This section investigates the effect on localisation ratio of the magnitude of the speed of sound difference between the active and the passive material. We model the active material as water with a density of 1000 $g.L^{-1}$ and a speed of sound of 1480 $m.s^{-1}$. The passive material is modelled as a liquid which has the same density as water but with a speed of sound that varies over the simulation from 1000 $m.s^{-1}$ to 2000 $m.s^{-1}$. Three cavity and control layers thickness are modelled: 0.38 mm, 0.42 mm and 0.46. The structures modelled have the control layer next to the transducer, with the width of the active material being 2mm. All three models are analysed across frequency ranges between 1.60 MHz and 2.00 MHz. The result of the localisation ratio value against speed of sound difference can be seen in Figure 71. The graph represents the value of maximum localisation ratio for each of the range of frequencies studied.

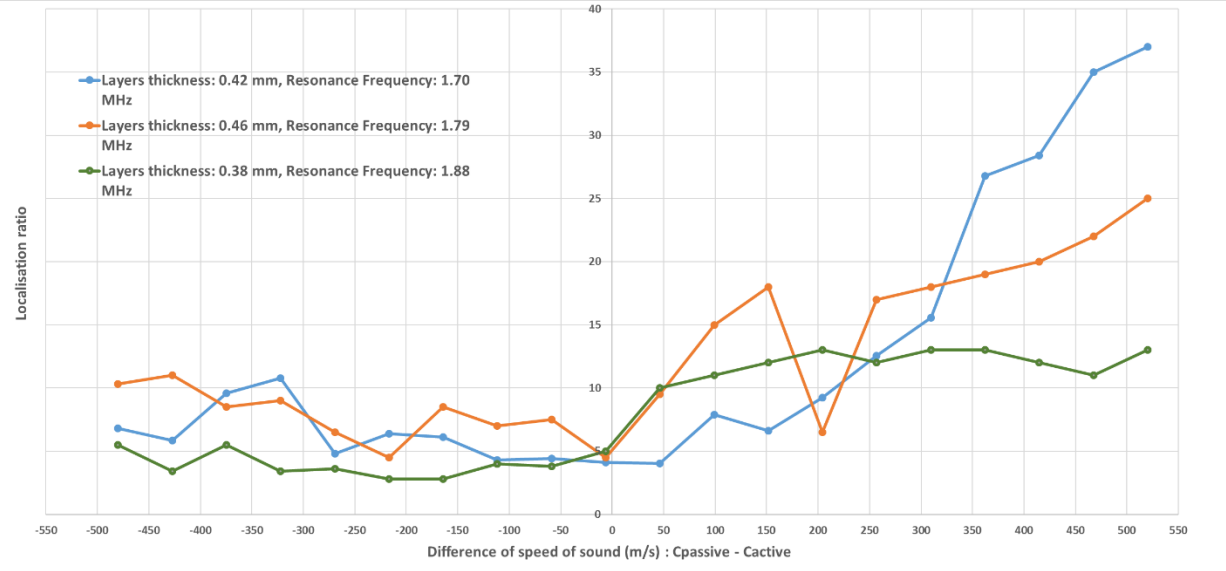

Figure 71—Modelled system localisation ratio against difference of speed of sound between passive and active material in the control layer.

There is an obvious asymmetry to the curve: negative differences in speed of sound ($C_{passive} - C_{active}$) have lower location ratio than positive differences for all cases modelled. This modelling implies that it is preferable to use the material with the lower speed of sound as the active material in cases where the other acoustic properties of both materials are comparable.

Maximum localisation ratio values are found for a passive material speed of sound of 2000 $m.s^{-1}$, meaning that it is preferable to have the highest possible difference of speed of sound between the active and passive material. However it should be noted that good localisation ratios (>10) are obtained from a difference of speed of sound of 250 $m.s^{-1}$ in all three cases modelled. The kinetic gradient in the fluid cavity for the case with maximum localisation ratio is shown in Figure 72 -b).

The minimum localisation ratio is associated with a low difference of speed of sound between the passive and the active material. In this case the control layer merely acts as an extra carrier layer and localisation is almost non-existent. The residual value of localisation ratio (~5) in this case is due to lateral forces that can activate the active area of the chamber. The kinetic energy gradient in the fluid cavity in the case of minimal localisation ratio is shown in Figure 72 -a).

In the modelled case of a device with 0.46 mm layer thickness, a break in continuity is noticeable for an active-passive speed of sound difference of 200 $m.s^{-1}$, which is due to a strong lateral resonance excited at half-wave resonance frequency.

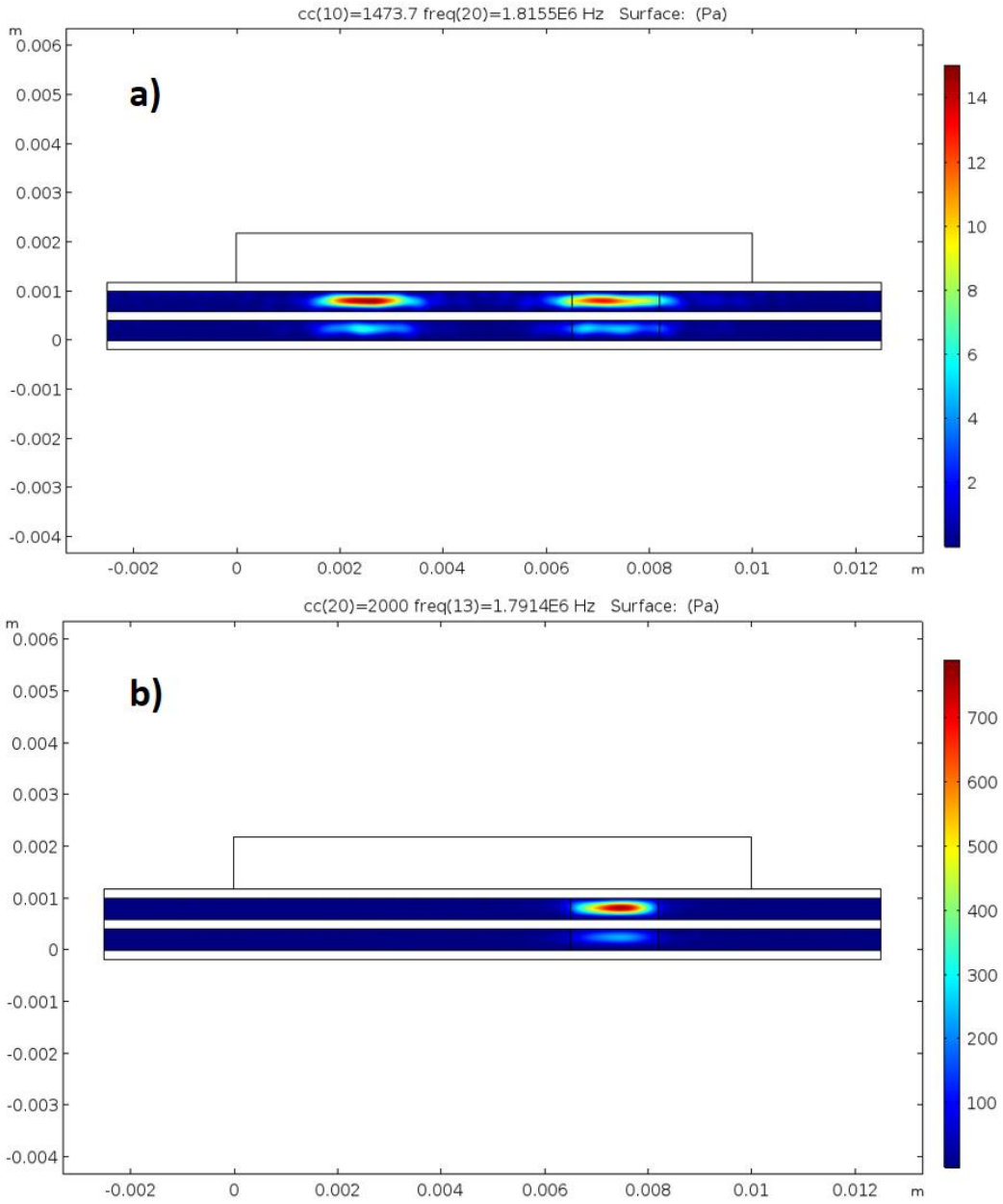

Figure 72 – a) Case of minimal localisation ratio (4.5). Layer thickness: 0.42mm, passive material speed of sound: 1473 $m.s^{-1}$, frequency: 1.82 MHz. b) case of maximal localisation ratio (37). Layer thickness: 0.42, passive material speed of sound: 2000 $m.s^{-1}$, frequency: 1.79 MHz.

The magnitude of localisation ratio found in the different modelled structures suggests that finding a good layer thickness combination is critical for such a device.

5.3.3 Control layer active area width

This section investigates the effect of the control layer active area width on the localisation ratio. This width is important as it is one of the factors that drives the resolution of the manipulation. In the following modelling, air is used as a passive material whereas water remains the active material (to maximize the localisation potential). The width of the active area of the control layer is changed from 0.1mm to 3.0mm, with a step size of 0.1mm.

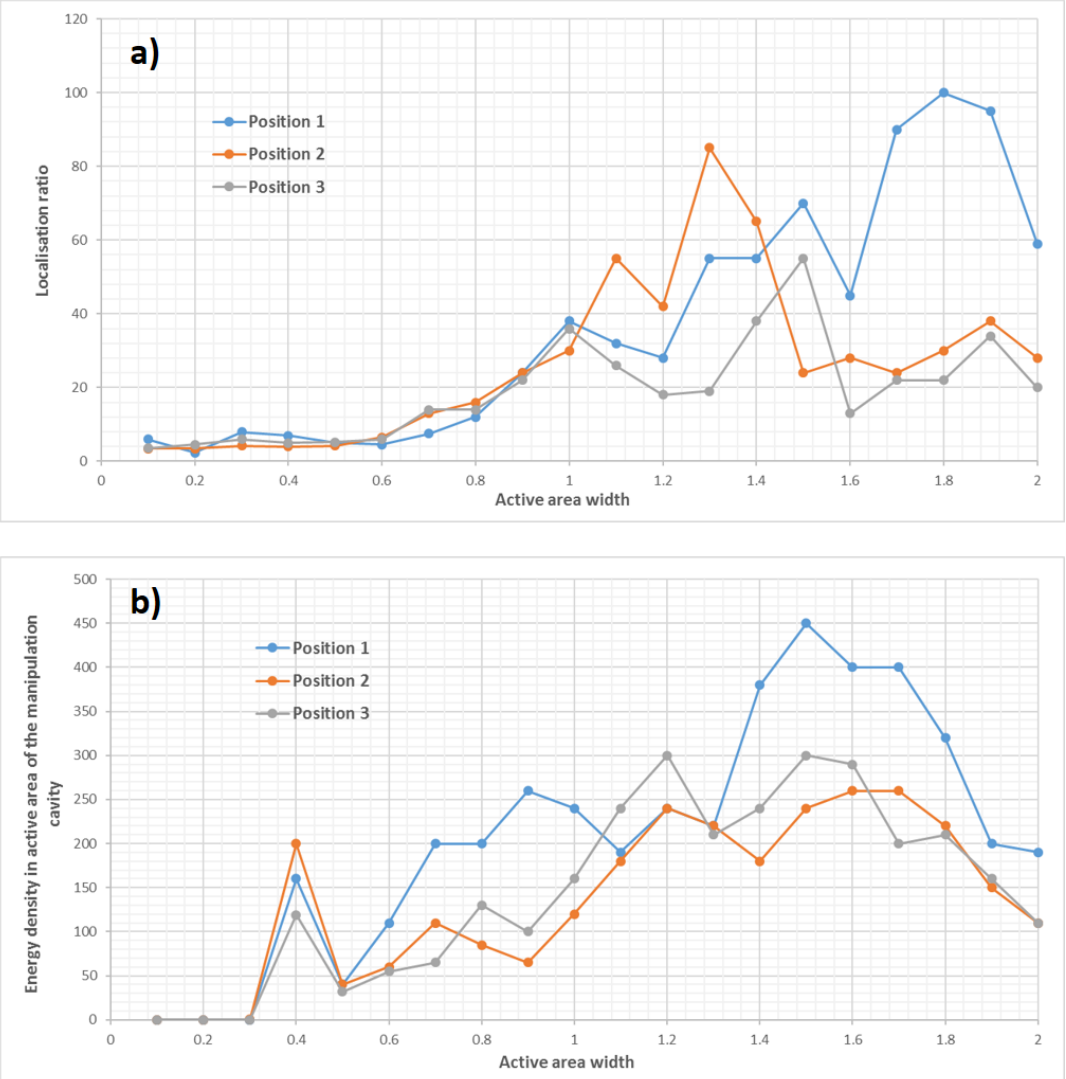

Figure 73 - Control layer active area width (mm) vs localisation ratio

The result of this FEA study is shown in Figure 73, which demonstrates that when the active area is too small, the effect in the fluid chamber is non-existent;

the effect can be measured at widths above 0.7mm, and is substantial at widths greater than 0.8mm. The effect magnitude tends to grow with active area width, then decreases after a maximum between 1.2 and 2, depending on the position of the active area, before increasing again. Figure 85 shows a non-periodic effect of the active material width on the localisation potential.

When lateral components of the acoustic mode are excited, the device's localisation potential is reduced as the energy is scattered throughout the fluid channel. It is possible to relate the non-linear effect seen in Figure 73 with the nonlinearity of the lateral force magnitude depending on the transducer width shown in section 4.3.3. Some active material widths activate lateral components of the acoustic mode, in the same way as some transducer widths, as demonstrated in section 4.3. This reduces the performances of this device, as shown in Figure 74.

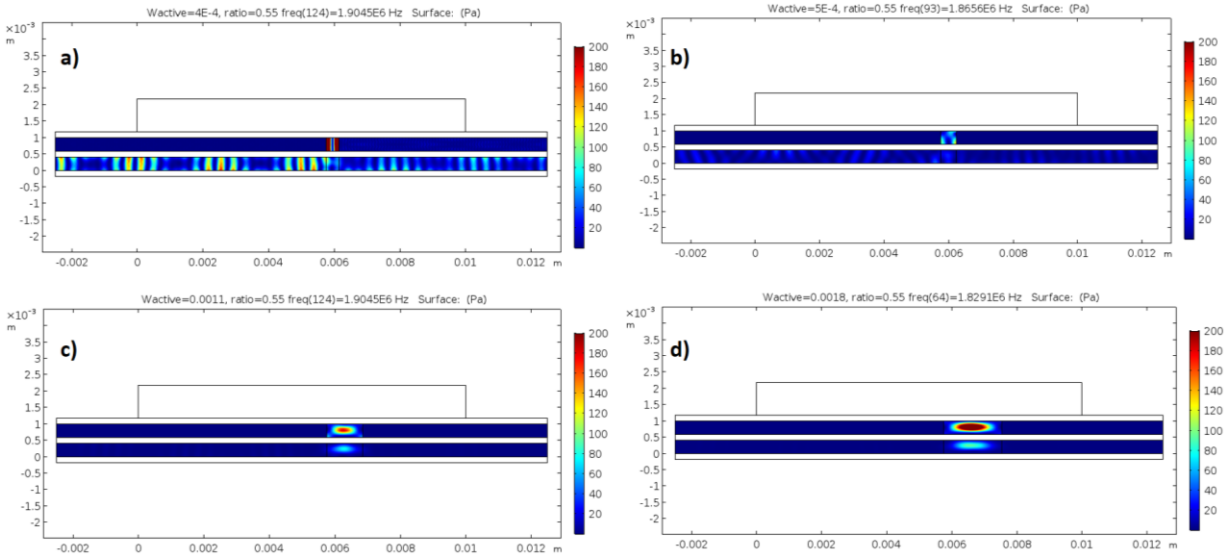

Figure 74 - Kinetic energy gradient in both control and manipulation layer, a) Active width of 0.4 mm, b) Active area of 0.5mm, c) active area of 1.1 mm, d) active area width 1.8mm

5.3.4 Conclusion on design choice for two material control layer planar resonator

This sub-chapter studied the overall design characteristics required to design an effective planar resonator with an extra control layer. The level of

energy localisation, dependent on the structure of the control layer, defines the level of quality of the device.

To have an effective device, the control layer must be placed between the transducer and the fluid chamber. This configuration increases the localisation potential although it decreases the overall energy potential.

The speed of sound difference between the passive and the active material is critical for the localisation potential of devices. Best performances are achieved with a speed of sound lower in the active material than the passive material. Higher difference in speed of sound is preferable but decent localisation ratio are found for a speed of sound difference of 250 $m.s^{-1}$.

The width of the active area in the control layer must be above $\lambda/2$ to have a noticeable effect, and above λ to have a good effect. After this point, the effect increases and decreases at the same rate as the driving wavelength, this effect being related to the effect of transducer width on lateral component of the acoustic mode in a planar resonator. Indeed, lateral components of the acoustic mode decrease the effectiveness of our device.

5.4 Static design for planar resonator with control layer

5.4.1 Material choice and speed of sound

The static design of a two-material control layer planar resonator follows the concept laid out in the introduction. This device would is intended for applications needing static localisation of the acoustic energy in the fluid following the pre-determined structure of the control layer. In this device, the control layer is composed of two static materials, which can be solid, liquid or gaseous. The choice of the material is dictated by the technology used to produce this layer and the comparative speed of sound of both materials.

In our case, many techniques have been studied to produce pillars that are repeatable, with controlled thicknesses. Firstly, we tried tape, but the production using laser cutting is suboptimal as it produces warping that can prevent high-

quality fine (1mm) pillar production. We tried ABS 3D-printed parts made with a *Ultimaker 2+* Fused Deposition Modelling (FDM) printer, but the results were not repeatable between prints: pillar thicknesses were found to differ by up to 20 μm. Moreover, the thickness could differ depending of the position in the hot plate, giving parts with low parallelism.

The fabrication technique ultimately selected was the use of an Object500 Connex3 3D printer, which uses a technology called PolyJet, combining ink jet technology with UV curable material. This technique produces parts with far higher precision than standard FDM. The precision advertised in the datasheet of the machine is 200 microns, which is far superior to the precision of the Ultimaker 2+. The material used here is VeroClear, a proprietary material which is UV curable and is designed to be similar to acrylic plastic (Poly(methyl methacrylate)).

Because the speed of sound of this material is not provided in the datasheet of this material, it has to be measured. Two method are possible to measure the speed of sound of a new material: by measuring the time it take a sound signal to reach a receiver though the material, or by measuring the frequency that excites a particular thickness mode in the material. Both methods are used here to have confidence in the speed of sound found experimentally.

5.4.1.1 Travel time measurement

The method here consists of printing two tubes of different lengths using VeroClear, with sizes chosen arbitrarily (as any size combination is acceptable, providing sample lengths are long enough and different enough). In our case, the shorter tube is 4cm long and the longer is 8cm long, as seen in Figure 75-c). Next, two transducers are attached to each tube's ends using double sided tape, as shown in Figure 75-d) (though any type of attachment is admissible, providing it carries the sound wave). A square pulse is sent to one of the ceramic transducers using a pulse generator, as shown in Figure 75-a). The pulse is received by the second transducer, and both sent and received signals are displayed using an oscilloscope, as shown in Figure 75-b). The time between both signals is measured for both 4cm and 8cm VeroClear tubes; the difference between these values is the time necessary for sound to travel 4cm in the material. The use of two different

tube lengths is necessary as it removes all the time "lost" in the wire, in the transducers and in the tapes.

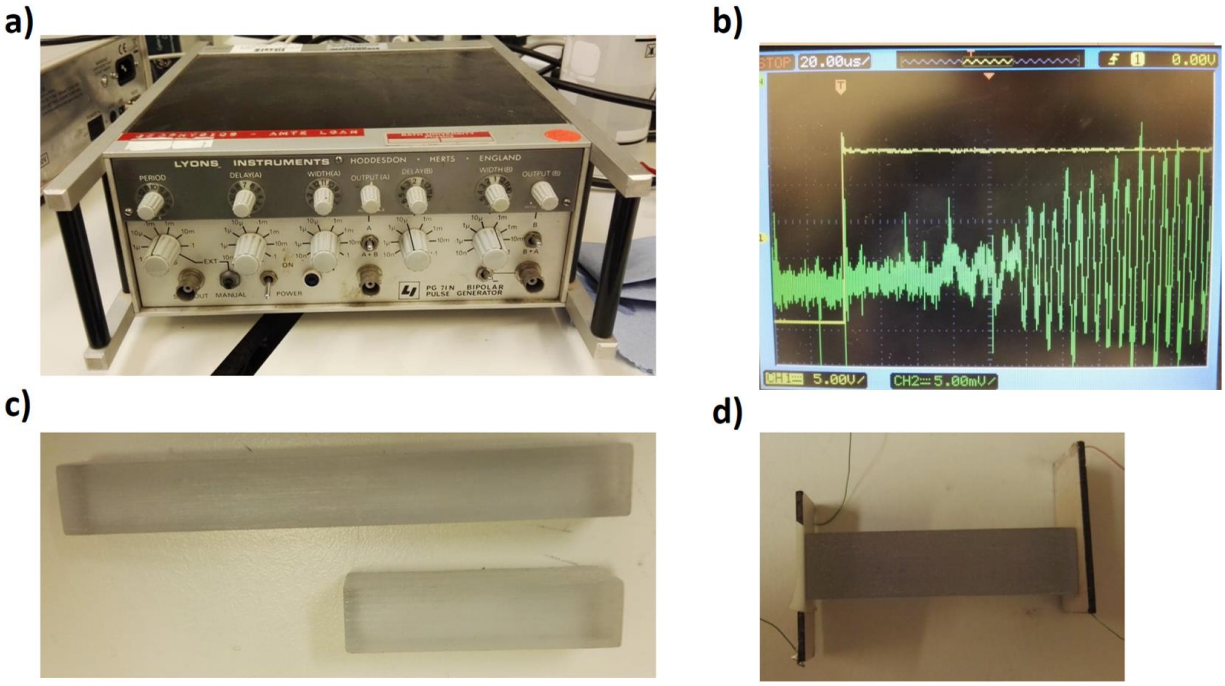

Figure 75 – Set up for time of flight experiment to measure the speed of sound in the VeroClear, a) Pulse generator, b) Oscilloscope, in yellow the sent pulsed signal, in green the received signal, c) two length of VeroClear, 4cm and 8cm, d) Piezo ceramics transducer attached to the veroclear bar using double sided tape.

The travel time measured for the 4cm bar was 51.2 μm; the travel time measured for the 8cm bar was 78.4 μm. Therefore, the travel time through 4cm of VeroClear material is 27.2μm, (+/- 2μm). The uncertainty comes from the noise of the received signal and the resolution of the oscilloscope, which is 0.1 μm. We can therefore conclude that the speed of sound in VeroClear of 1470 $m.s^{-1}$ (+/- 54$m.s^{-1}$). This experimental result can be further improved by using a longer tube of the material of interest; more powerful sending transducer; and a more precise measurement tool attached to the receiving transducer.

The datasheet introduce VeroClear as an "acrylic-like" material. The speed of sound of PMMA acrylic is 2750 $m.s^{-1}$. The speed of sound of VeroClear is widely different than PMMA- it is closer to water (1480 $m.s^{-1}$) or silicone (1485 $m.s^{-1}$)

Because the speed of sound value for this material is critical, and because it varies significantly from what could be expected from reading the datasheet, another speed of sound technique is used to verify this experiment.

5.4.1.2 Conductance test and transfer impedance model

To find the speed of sound using this technique, a thickness mode resonance is found by applying a conductance test on a simple structure that includes the material of interest. Then, following the transfer impedance model method introduced by Martyn et al.[85], the speed of sound of the material of interest is incrementally adjusted until the same resonance frequency is found.

A 750 μm thick VeroClear section is coupled using glycerol to a 980 μm thick PZ26 transducer. A conductance test is applied to this simple structure at a range of frequencies from 1 MHz to 1.8 MHz and is displayed in Figure 76-a). The curve shows many peaks with one being stronger than the rest. The smaller peaks represent lateral component of the acoustic modes of the transducer, this is confirmed by testing the transducer by itself. The impedance test shows the same frequencies (with higher Q factor) as the smaller peaks for the construct showed in Figure 76-a). Therefore a thickness mode is found at 1.45Mhz.

Then, the 1D impedance transfer model is used as a way to find the speed of sound for VeroClear. The method consists of inputting to the model all known information about this structure: thickness; density; speed of sound and piezo constant of PZ26 transducer; density of VeroClear; the speed of sound in VeroClear (set to 1470 $m.s^{-1}$, the speed of sound found in previous section). Then this last value is changed until a resonance frequency at 1.45 MHz is found. A speed of sound of 1450 $m.s^{-1}$ (see -b)) gives a maximum of energy in the structure, resultant of a thickness standing wave, as shown in Figure 76-c).

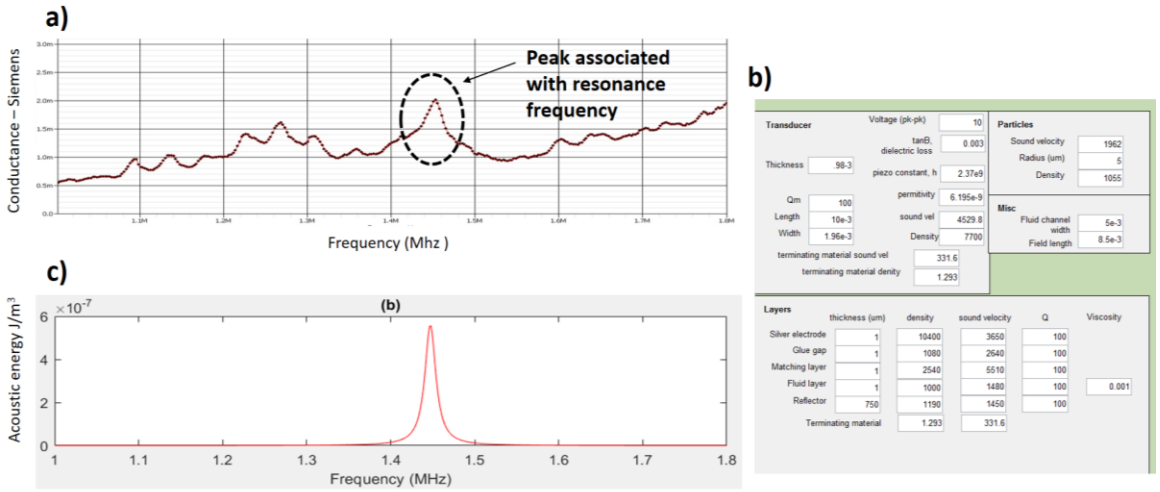

Figure 76 – a) Conductance vs frequency of the simple test structure, given using C60 CypherGraph, b) Value filled in the impedance transfer model conveived by Martyn et.al, c) Acoustic energy vs frequency given for a speed of sound of VeroClear of 1450 $m.s^{-1}$, given by the impedance transfer model.

This technique confirms that the speed of sound of VeroClear is around 1450 $m.s^{-1}$, however this technique has the disadvantage of being dependent on the knowledge of other material properties. In our case the glass speed of sound in estimated with data found online, and the glycerol thickness is not accounted for.

5.4.2 Effective device thickness using modelling

Now that the acoustic and mechanical properties of all the parts composing the complex planar resonator are known, a two-dimensional finite element model is used to determine an effective device.

An static two-material control layer planar resonator is selected for modelling as a device with a high localisation ratio and a strong energy density.

The two materials used in the control layer of our planar resonator are VeroClear and air. Both materials' acoustic properties are known and are widely different, moreover the 3D printing fabrication technique allows the easy production of our control layer using Solidworks as a design software.

The carrier layer attached to the transducer, and the pillar composing the control layer are modelled and fabricated together as one VeroClear part as shown in Figure 77.

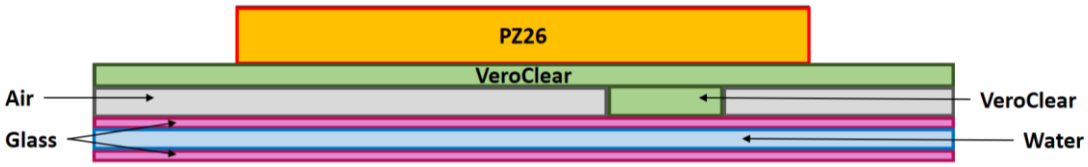

Figure 77 –Schematic of planar resonator with control layer with affiliated material

The VeroClear material has shown to be very flexible for thicknesses below 0.3mm and becomes stiffer with increasing thickness. To ease fabrication, stiff rigid, parts are preferred. The VeroClear carrier layer thickness is set to 0.4mm. The VeroClear pillar thickness is chosen to excite the standing wave thickness half wave mode, resulting in the highest energy magnitude in the water filled cavity.

For this task, one dimensional modelling is used to avoid any lateral resonance as we are only interested in the thickness mode. The most effective thickness mode is found with a pillar thickness of .35mm; with this thickness, two distinct resonance frequencies are found: one at 2.03 MHz and anther at 2.16 MHz, the most effective being the former. Both excite a half wave mode in the cavity. The acoustic energy distribution is dependent on the frequency and the associated pressure throughout as shown in Figure 78.

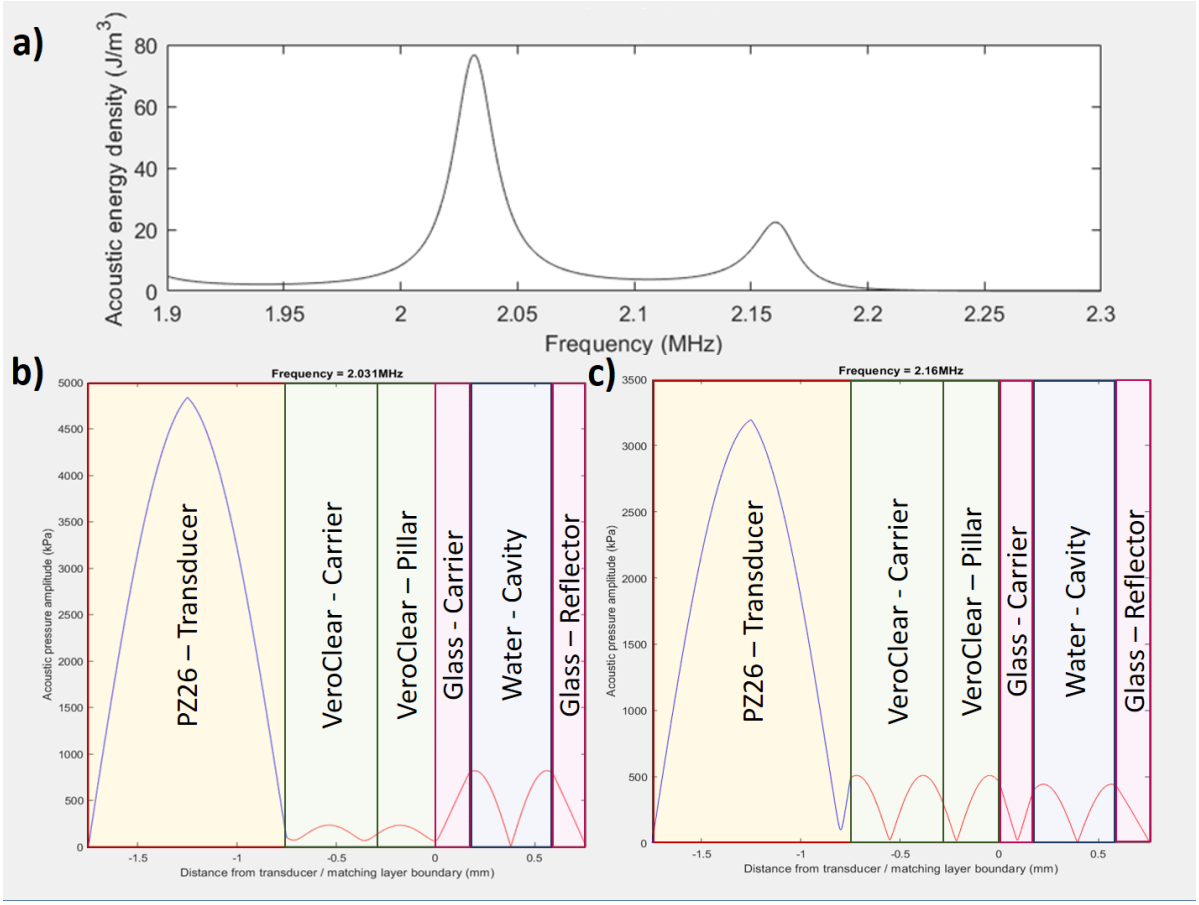

Figure 78 – Results of transfer impedance model. a) Acoustic energy density ($J.m^3$) vs Frequency (Hz), b) Pressure field throughout the planar resonator vs the distance from transducer / matching layer boundary, at resonance frequency 2.03 MHz, c) Pressure field throughout the planar resonator vs the distance from transducer / matching layer boundary, at resonance frequency 2.16 MHz

This thickness configuration offers two resonant frequencies creating a strong acoustic standing wave throughout the planar resonator, with half-wave in the water filled cavity. Having a choice between two frequencies can be useful as one of them could invoke a strong lateral acoustic field, which would be detrimental for this concept.

This thickness configuration is chosen for the fabrication stage.

5.4.3 Unsuccessful static control layer design

The fabrication process that is presented in the next section (5.4.4) followed experience gained after exploring a number of other approaches. While these approaches were not found to be satisfactory, they are presented here in outline to show how the final design evolved, such that others might learn from these failures.

The first method attempted was the use of 3M 9731 double-sided tape to construct the intermediate layer. However, it was not found to be possible to fabricate the small feature sizes required for pillars due to the high temperature of the laser cutting, which caused melting of the tape. Laser cutting was retained for forming the channel outline and intermediate layers design due to its relative speed and simplicity as a fabrication technique.

I also explored printing the intermediate layer using a Ultimaker 2+ 3D printer using a 0.25 mm nozzle for high precision and a low speed of printing of 4 $mm^3.s^{-1}$ with PLA. Once this layer was constructed, it was sandwiched between the cavity layer fabricated with the tape technique introduced in section 4.7 (or using the same method introduced here) and an ethanol-cleaned carrier of 0.17 mm thick glass slide. It was then placed in an oven set at 180 °C for 12 minutes with a weight on top. The result of successful fabrication process is showed in Figure 79.

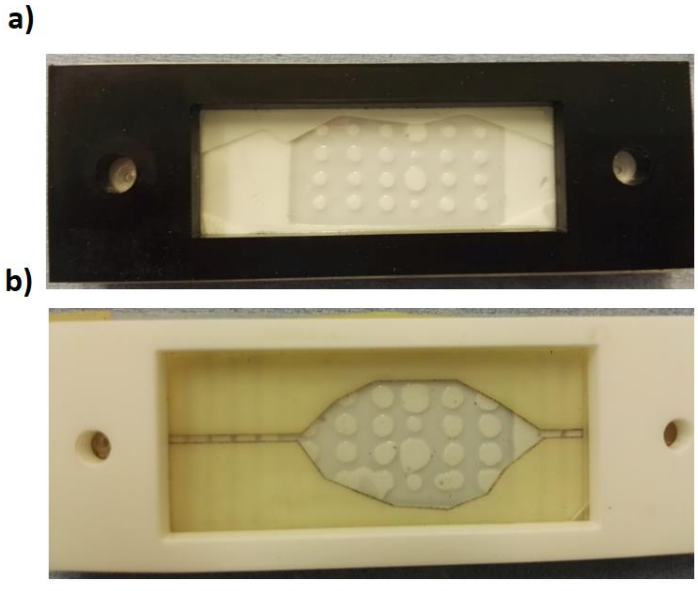

Figure 79 – Example of planar resonator containing a static control layer fabricated using melted 3D printed PLA

This method was promising as it was cheaper and quicker than the fabrication method introduced in the next section, however there were some limitations on device repeatability:

- The Ultimaker 2+ has a datasheet resolution of 20 μm in lateral directions, however our test showed that we could not do better than 40 μm. This is detrimental for device performance especially the in thickness direction, where small changes can disrupt the intended acoustic resonances.
- The thermal bonding technique (which involved melting the PLA) to couple the PLA layer to the glass layers (main carrier and middle carrier) was found to be unreliable. The time window for removing the planar resonator from the oven was very short, resulting in either melting or poor bonding if the incubation time was too long or short respectively. Attempts to optimise this procedure were not successful, and also occasionally showed delamination from the differing thermal expansion coefficients of glass and PLA. In light of this issue combined with poor printing performance, the approach was abandoned in favour of the next method.

The device showed in was carrying the acoustic waves through the pillar, however the pillars were too close to each other, creating strong streaming patterns close to and influencing each other, resulting in chaotic streaming inhibiting any aggregation process.

While ultimately unsatisfactory, it was possible to produce the device shown in Figure 80.

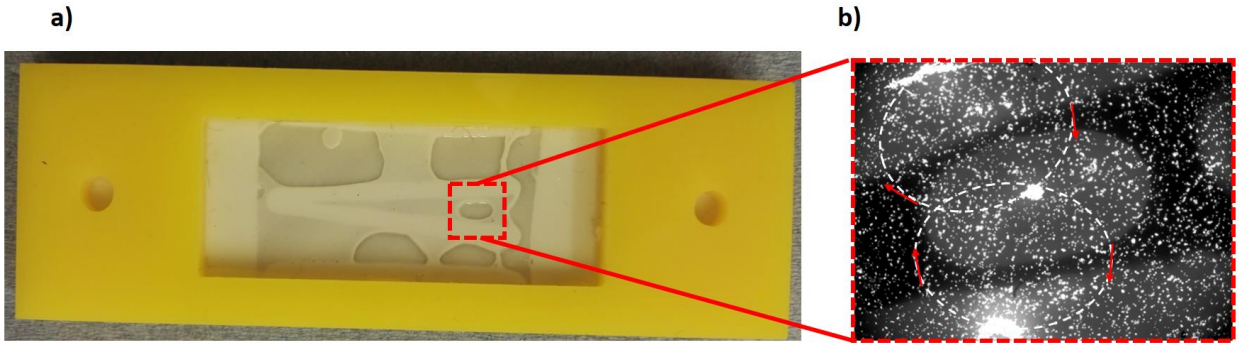

Figure 80 – a) V-shape intermediate layer, control layer thickness of 500 μm, cavity layer thickenss 500 μm. b) Half-wave mode at 1.97 MHz, 28 Vpp, 10 microns fluorescent beads at a concentration of 4.10^5 beads/ml, after 2 sec of

acoustic excitation, with dotted lines representing the streamlines; red arrows represent the streaming direction.

This device tested the feasibility of pushing particles to the centre of the fluid channel under flow using a V-shaped intermediate layer. The particles injected from the right at a uniform spread, were intended to be pushed laterally (up and down) to the centre by the V-shaped configuration as they are carried by pump driven flow from right to left.

However the device was dominated by acoustic streaming which disrupted the intended manipulation. Nevertheless, this device did demonstrate some early potential for the concept of an intermediate layer: at high transducer driving amplitude (28 Vpp), particles aggregated at the positions shown which corresponded to structures in the intermediate layer; an extra trapping position is due to streaming lines touching each other, creating a trap point at a 'passive' area, as shown in Figure 80-b).

5.4.4 Fabrication of static two material control layer planar resonator

The water-filled cavity where the manipulation occurs is formed by stacking three layers of 75x0.14mm 3M 9731silicone adhesive tape (3M, St. Paul, MN, US) for a total thickness of 0.42mm. This piece is laser cut to form a 30x12mm channel.

The channel-shaped, two-sided tape is sandwiched between two 75x25x0.17 mm thin glass slide (161 Logitech, Old Kilpatrick, Glasgow, UK0-CON).

Two holes are drilled in one of the glass slides to allow fluid input. An extra layer is produced by laser cutting a 75x25x0.5mm piece of acrylic PMMA, with two ø3mm holes to allow tubings to fit in, and a 45x15 window in the middle, to allow optic access to the cavity.

The control layer is printed using an Object500 Connex3 3D printer; the design is created using Solidworks 2018, then exported to a STL file usable by the machine.

As shown in section 5.3.2, the diameter of the pillars can have an important effect on the acoustic energy density in the manipulation cavity. To explore the effect of the pillar diameter, three different diameters are fabricated.

The control layer is composed of five cylindrical pillars positioned in the middle of the 73x24 piece. Four pillars are placed on the vertexes of a 10x6mm rectangle, the last pillar is in the middle of this fictitious rectangle. Three different pillar diameters are produced: 1mm, 1.5mm and 2mm. Each of these VeroClear are similar thickness wise, indeed the 3D printer resolution is 30 microns.

On the top, bottom and sides of the pillars, rectangular shapes having the same thickness as the pillar are present. These shapes are used to ensure planarity of the layer above. There is a 1mm gap between each of them, allowing the excess glycerol to fit this gap, keeping the control layer flat and levelled. The water channel and the control layer are shown in Figure 81.

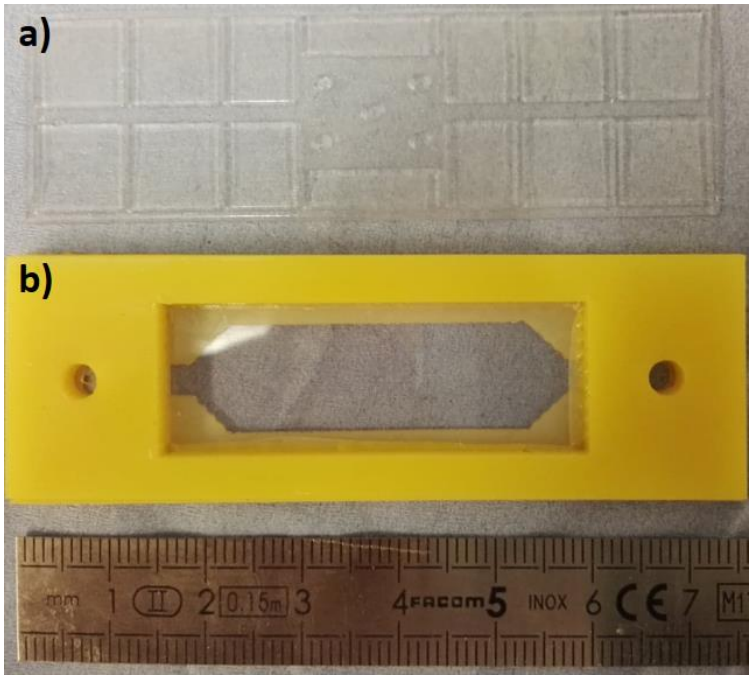

Figure 81 – Pieces composing the planar resonator. a) 3D printed VeroClear part, with a pillar diameter of 1.5mm, b) fluid cavity accompanied by acrylic fluid exchanger.

To couple the fluid cavity and the control layer, glycerol is used as a coupling fluid. 50mL of glycerol are poured on the carrier glass of the cavity. A piece of

tissue paper is then used to spread the glycerol over all the glass slide surface, additionally removing any excess glycerol.

Next, the control layer is pressed to the wet carrier glass slide and is moved laterally to remove any fluid excess, which would fill the gaps present in the control layer structure. Once this is done, the control layer is secured to the fluid cavity by surface tension.

Finally a 13x9mm transducer, prepared beforehand by scoring it and using silver paint to connect top and bottom electrodes together as explained in section 4.7.1.1, is placed on the flat surface of the control layer. It is placed to cover all pillars.

The frequency response of the planar resonator is tested using Cypher Graph. Two frequency sweeps are carried out from 1.9 MHz to 2.2 MHz, one with the fluid cavity empty and one filled with water. The conductance response is saved as graph and displayed in Fig.82. .

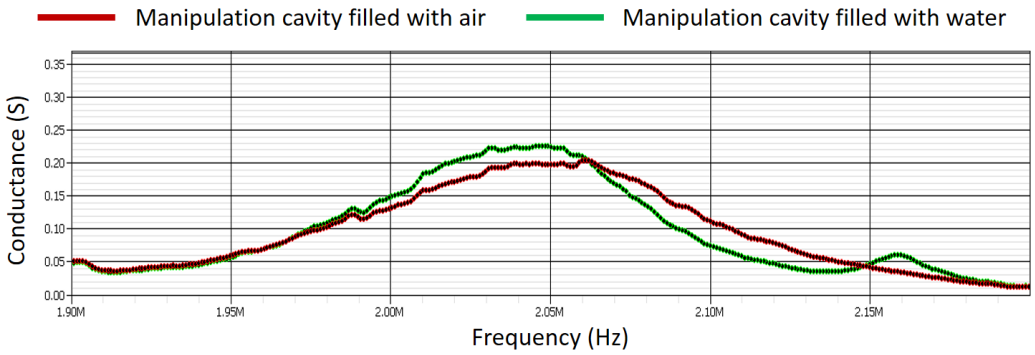

Figure 82 – Conductance (S) vs Frequency (Hz) for static two-material planar resonator. Red: fluid cavity filled with air; Green: fluid cavity filled with water.

The conductance test carried out with fluid cavity filled with water shows two distinct peaks: the first at 2.04 MHz and the second at 2.16 MHz. Conductance peaks relate to maximum acoustic energy in the planar resonator as established in section 3.1. This gives comparable results as the impedance transfer modelling performed earlier. However, the curve with the fluid cavity filled with air gives a peak at 2.05 MHz, which might mean that in the case of the first resonance frequency, the acoustic energy is localised in the solid parts of the planar resonator, rather than in the fluid cavity.

5.4.5 Experimental method and results

The device is placed on an Olympus IX81 inverted research microscope which is fitted with a Hamamatsu ORCA-ER monochrome digital camera, fitted with blue-light fluorescent filters. A mixture of water and 10 μm fluorescent microspheres (Fluoresbrite YG 10 μm, polysciences), with a concentration of 3.10^5 beads/ml is injected to the fluid cavity.

The optical set up is the same as that introduced in section 4.7.2.2; the planar resonator is put on Olympus IX81 inverted research microscope which is fitted with a Hamamatsu ORCA-ER black/white digital camera, fitted with blue-light fluorescent filters.

The two potential resonance frequencies given by the conductance measurement are tested. 2.04 MHz does not affect the particle behaviour, while 2.16 MHz clearly affects the particles. As a result, 2.16MHz will be used during the rest of the chapter.

Modelling showed that we expect aggregation in levitation at the position of the pillars. When a low voltage is applied to the transducer (3Vpp) the dominating effect is acoustic streaming, typically creating a pair of vortices in the plane of the transducer above each pillar. At higher amplitudes (above 8Vpp), some particles begin to converge and rapidly accumulate additional particles, beginning to produce particle aggregates above the pillars. The streaming is still present and strong, ultimately preventing the stable formation of aggregate. The streaming patterns and the aggregation process is showed using long exposure pictures in Figure 83.

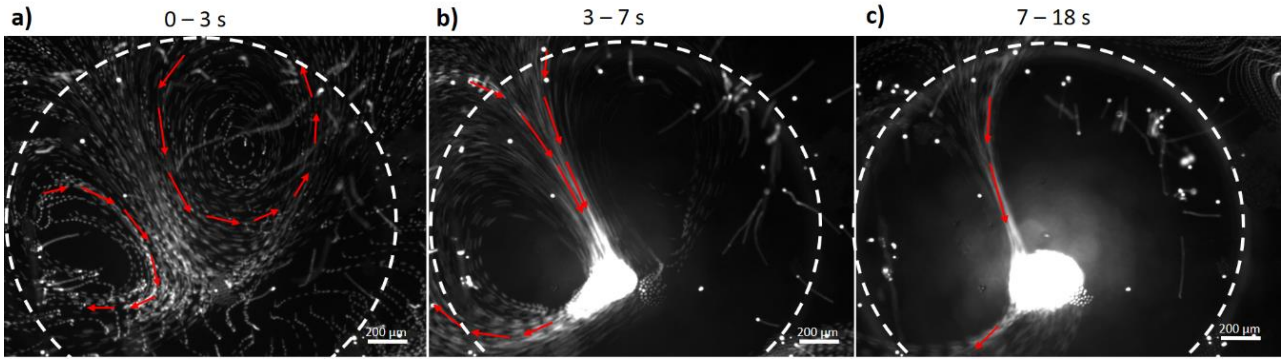

Figure 83 – Video taken with a pillar diameter of 2mm and transducer amplitude 8Vpp: a) Streaming pattern above a pillar at the beginning of the acoustic levitation process before aggregation. b) Aggregation process, following the first small aggregate after 3s of acoustic standing wave activation in the fluid layer. c) Critical size obtained after 7s under levitation; some particles aggregate from the top and some leave from the bottom left. Red arrows shows cell movement direction and white doted circle shows the pillar position

The pillar width greatly affects the acoustic energy in the fluid layer; to quantify both this and the transducer amplitude effects, an experimental method is designed.

Each of the five pillars of each control layer are tested with three different transducer driving amplitudes: 3Vpp, 8Vpp and 16Vpp. At each amplitude a 10s movie is taken at a rate of 10 Hz during the levitation, streaming and potential aggregation process.

In Figure 83-a) in the early phase of the acoustic excitation, acoustic streaming is induced. After 3 seconds the first aggregate is formed (-b) which attracts more and more particles, increasing the size of the aggregate. After 7s, a critical aggregate size is attained and many beads simultaneously disband from the aggregate while new particles join - Figure 83-c).

The particle velocities are measured after 0.5s of levitation using the same method as introduced in section 4.7.2.2. The measurement is carried out at the beginning of the process to avoid aggregation disturbing the streaming pattern and velocity field (b and c). Five measurements are taken for each pair of pillar width and driving amplitude; they are averaged and shown in Figure 84.

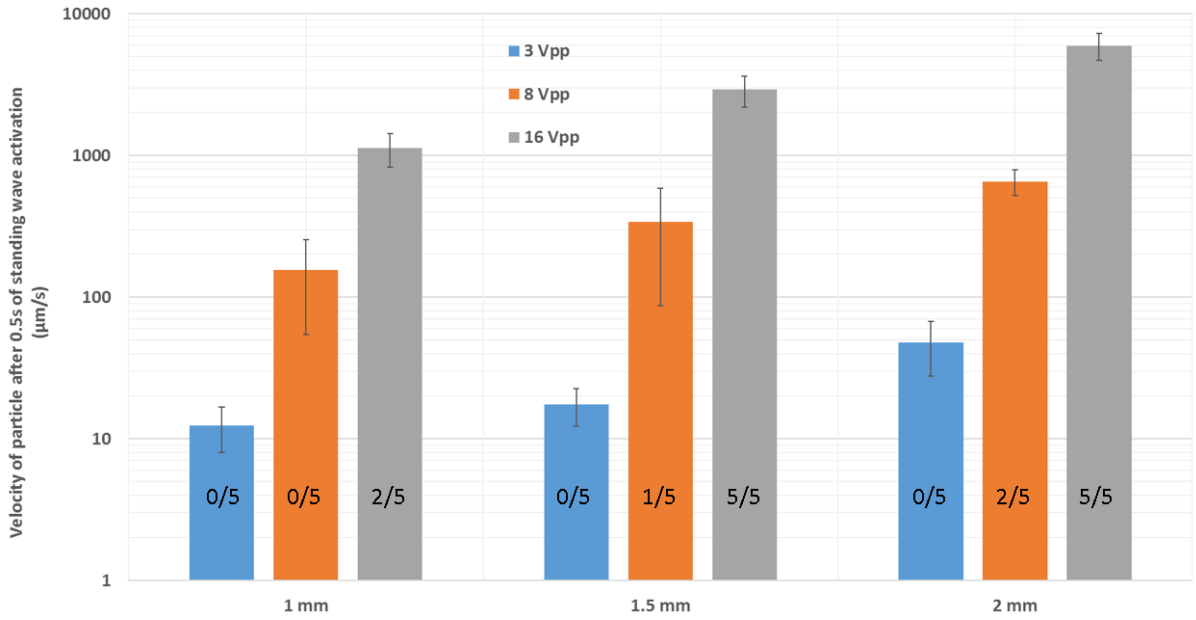

Figure 84 – Particle average velocity above the pillar after 0.5s of acoustic excitation is shown y-axis is a log scale. The numbers inside the bars show the respective success rate of agglomeration for each experimental set-up.

The data collected and displayed in Figure 84 shows that aggregation happens above an acoustic energy threshold related to a particle velocity of 500 $\mu m.s^{-1}$. Below this threshold, particles follow the streaming lines, forming a pair of vortices (.a). The particles' velocity in the fluid depends of the amplitude applied to the transistor and the width of the pillar.

A pillar with of 2 mm is associated with higher acoustic energy; 1.5 mm pillar width is associated with lower acoustic energy and 1 mm pillar width is associated with the lowest measured acoustic energy in the fluid.

The transducer amplitude additionally has an important influence on the acoustic energy: the velocity field evolves non linearly with the amplitude applied to transistor.

While it has been shown that the velocity field is rather repeatable, in the case of aggregation, the size and the position of aggregates are not easily predicted. They depend of the time of aggregation and vary between trials; two examples are shown in Figure 85, both with a pillar diameter of 1.5 mm and 16 Vpp at the transducer.

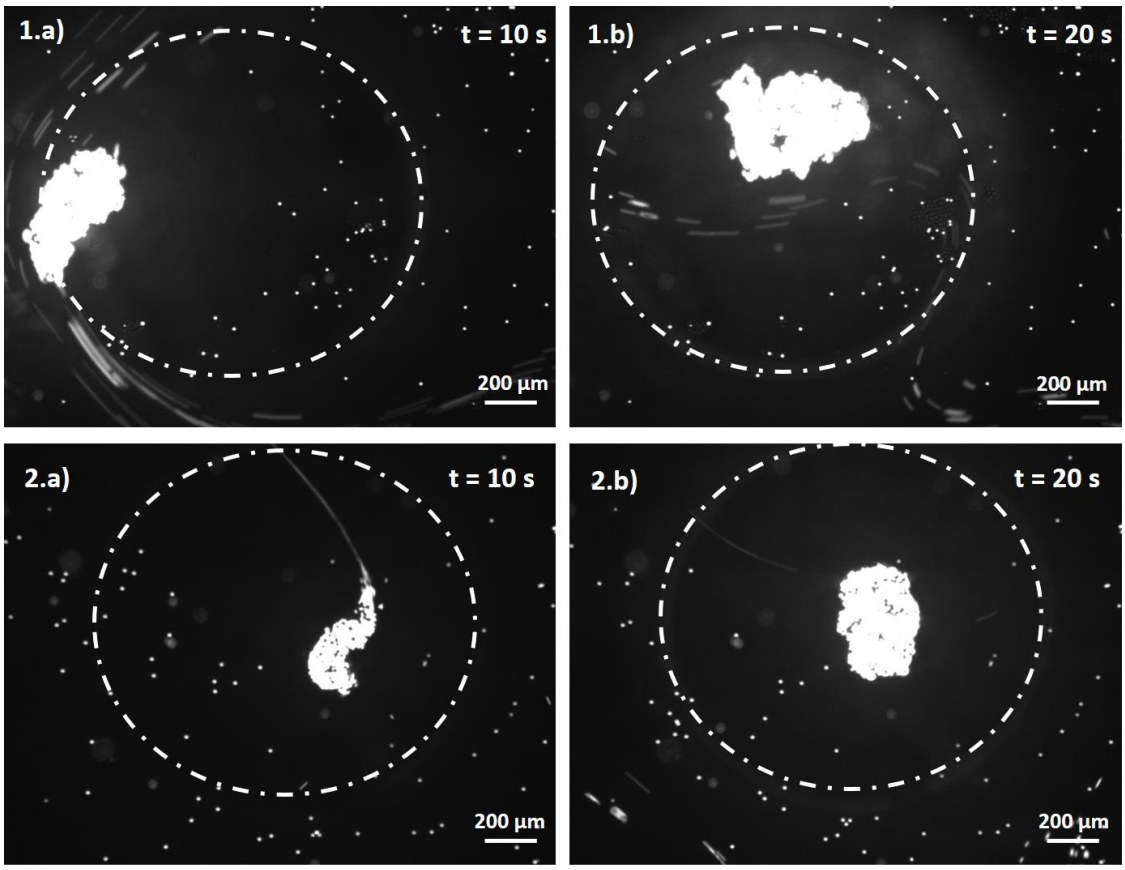

Figure 85 – Transducer driving amplitude: 16Vpp, pillar diameter: 1.5mm. 1.a) First pillar after 10 seconds of acoustic excitation. 1.b) First pillar after 20 seconds of acoustic excitation. 2.a) Second pillar after 10 seconds of acoustic excitation. 2.b) Second pillar after 20 seconds of acoustic excitation.

In Figure 85.1.a) aggregation is seen to occur in the upper left side of the pillar; in Figure 85.1.b) the aggregate size increases as additional particles are attracted to it and are pushed by the strong fluid velocity field to another quasi-stable position above the top part of the pillar. We observe that the streaming streamlines change radically after the change of position of the aggregate. The other pillar show different behaviour: in Figure 85.2.a) the aggregate is formed above the near-centre of the pillar and grew over time without changing position as shown in Figure 85.2.b).

The experienced radiation force evolves with particle volume and the drag forces evolve with the diameter. Therefore, bigger particles experience more radiation force compared to the drag force induced by streaming. Clearly, aggregation should occur more easily for larger particles. This is investigated using 20 µm diameter, non-fluorescent beads mixed in water at a concentration of 1.10^5 beads/mL, using the same cavity coupled to the 2 mm diameter pillar control layer.

Images show that the drag force has a lesser influence on the beads and bead aggregation behaviour. Streaming patterns are still visible but aggregation occurs at lower transducer amplitudes (above 4 Vpp) with a related bead velocity of 70 $\mu m.s^{-1}$. Moreover the drag force does not disturb the aggregate position or width by removing matter during the agglomeration process. Stable aggregate production using the 2 mm pillar at 16 Vpp is shown in Fig.86.

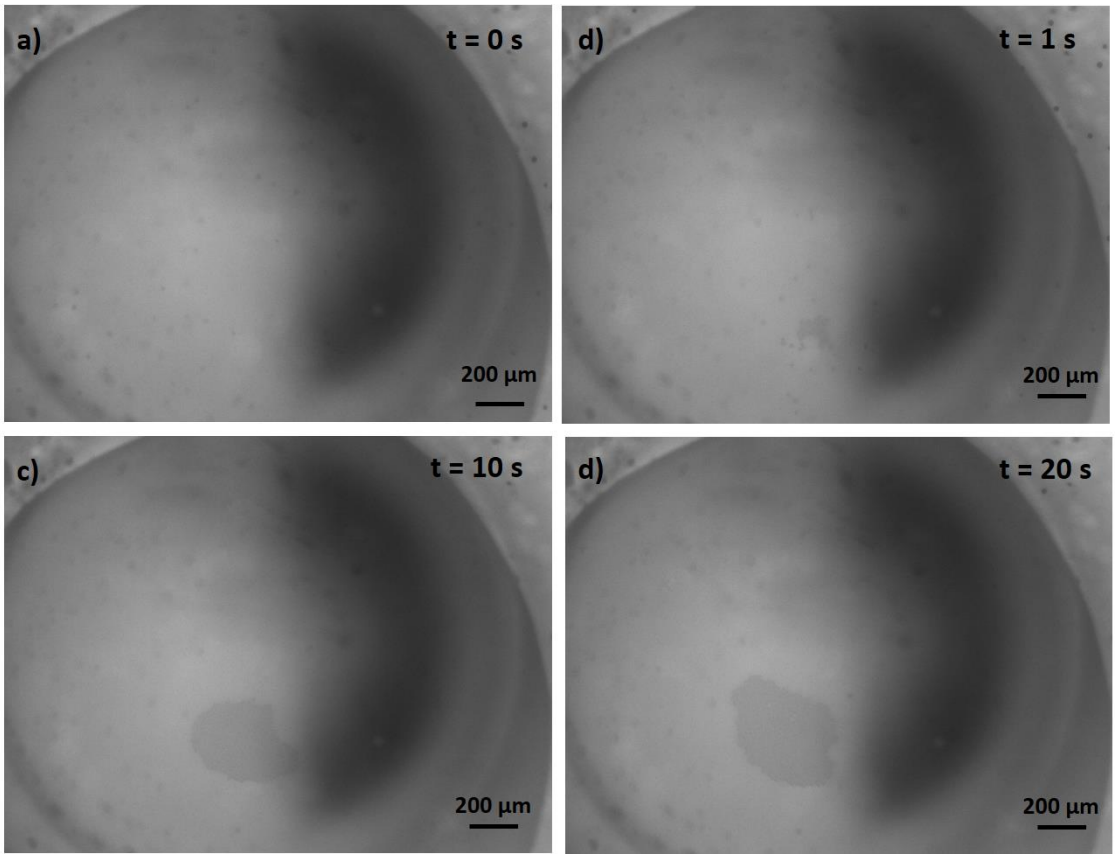

Figure 86 – Aggregation process with ø 20 µm polystyrene beads and control layer pillar width ø 2 mm. Transducer is driven at 16 Vpp. a) Beads are evenly distributed at the beginning of the acoustic excitation. b) 1s after acoustic levitation commencement, particles begin to aggregate in the central lower part of the device. c) Aggregation after 10 seconds. d) Aggregation after 20 seconds.

.a) shows the bead distribution before the beginning of the acoustic excitation; no aggregates are present. An aggregate is rapidly formed after only 1 second of acoustic excitation as shown in Figure 86.b). The aggregate grow in size by attracting all surrounding beads but remains in the same position, and no

beads escape the aggregate once trapped in it, as shown in Figure 86.c) and Figure 86.d)

5.5 Dynamic design for planar resonator with two-material control layer

This concept is similar to that introduced above in that the control layer is composed of two different material with different acoustic properties. In the dynamic design, however, the control layer is formed of two immiscible fluids pushed through a channel. The transducer is tuned to excite a thickness standing wave though one of the fluids and not the other as schematized in Figure 67. The combination of liquid and gas is possible and would be effective as they have vastly different acoustic properties, but liquid/liquid combination are preferred because they are incompressible, thus facilitating steady and predictable flow in the channel. The particles in the manipulation cavity should levitate above the active liquid, following the path formed by the channel.

5.5.1 Material choice and speed of sound measurement

Suitable fluids must be immiscible and have a large speed of sound difference; the two fluids investigated here are Silicone oil and water. These fluids are immiscible and the silicone oil has a speed of sound range between 1000 $m.s^{-1}$ to 1200 $m.s^{-1}$, with the water having a speed of sound 1480 $m.s^{-1}$.

The control channel is formed by a third material, in the case of this device it is made of *3M 9731* silicone acrylic based double sided adhesive tape (3M, St. Paul, MN, US) which has proven to be a robust, quick and repeatable way of creating precise separators and channels when laser cut.

The goal of this chapter is to investigate the speed of sound of both silicone oil and tape.

For the silicone oil, the acoustic wave travel time technique is used as introduced in section 5.4.1; the set up is comparable as used for the VeroClear, however because the material to be investigated is a liquid and not a solid, a hydrophone is used as an acoustic emitter instead of a piezo ceramic material. The set-up is shown in Figure 87.

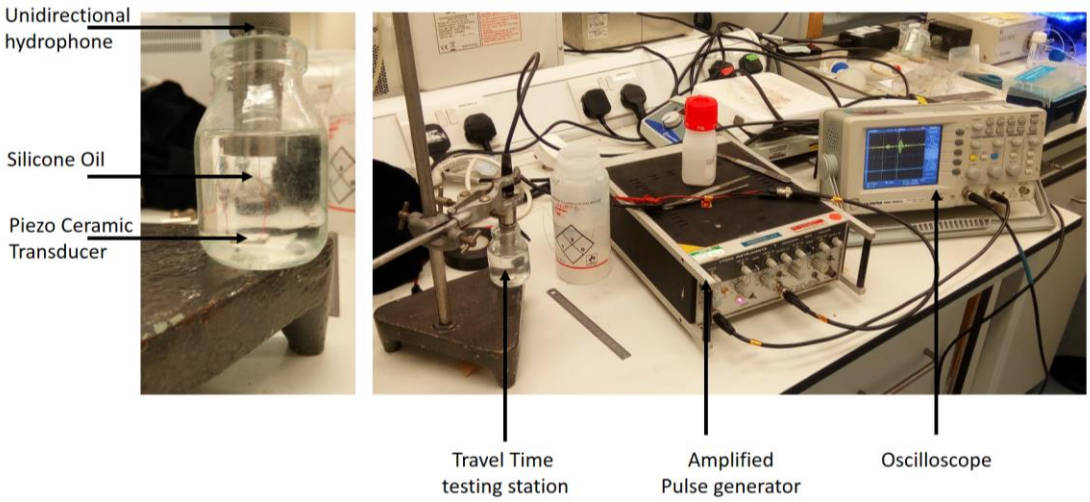

Figure 87 – Silicone oil travel time measurement set-up

A piezo ceramic transducer is taped to the bottom of a vial filled with silicone oil, and the hydrophone is held 3 cm above the piezo ceramic transducer, submerged in the fluid using a clamp. A pulsed signal is sent by the hydrophone using the amplified pulse generator and received to the piezo ceramic transducer. The travel time is measured and repeated with an increased separation distance of 6 cm. As in section 5.4.1, two measurements are sufficient to calculate the speed of sound of silicone oil at 1050 $m.s^{-1}$ (+/- 54 $m.s^{-1}$); the measurement of speed of sound in Vero Clear having confirmed the robustness of this method even with such small separation distances.

To calculate the speed of sound of tape, the method of Conductance test and transfer impedance model is used as previously introduced in section 5.4.1. The result given by the 1D impedance transfer model gave a speed of sound in tape of 1330 $m.s^{-1}$.

5.5.2 Modelling

The modelling results described here are for the final device described below, however this method holds valid for the intermediate design iterations described in the next section, 5.2.3.

One-dimensional impedance transfer modelling is used to find effective layer thickness combinations of water or silicone oil. As investigated in section 5.5.1 better performances have to be expected with the material having the lowest speed of sound of both. In the case of this experiment, the Silicone Oil, with a speed of sound of 1050 $m.s^{-1}$. Double coated precision tape has been found to be a useful tool for quick and precise prototyping for complex shapes when cut with a laser cutter. After several trials using the different possible combinations possible with a 140 μm thick tape as separator, the most effective planar resonator is found with a water, silicone oil or tape filled control layer of 420 μm thickness. A water filled manipulation cavity of 420 μm thick. The glass transducer carrier, cavity carrier and reflector are modelled as 170 μm thick layers. Because the control layer will be filled with three materials; water, silicone oil and tape, it is important that their respective thickness resonance frequencies are distinct enough to permit the excitation of a thickness mode in one material and not the others. The energy density using the acoustic properties found experimentally for the three materials are shown in Figure 88 for a range of frequencies from 1.6 MHz to 2.4 MHz.

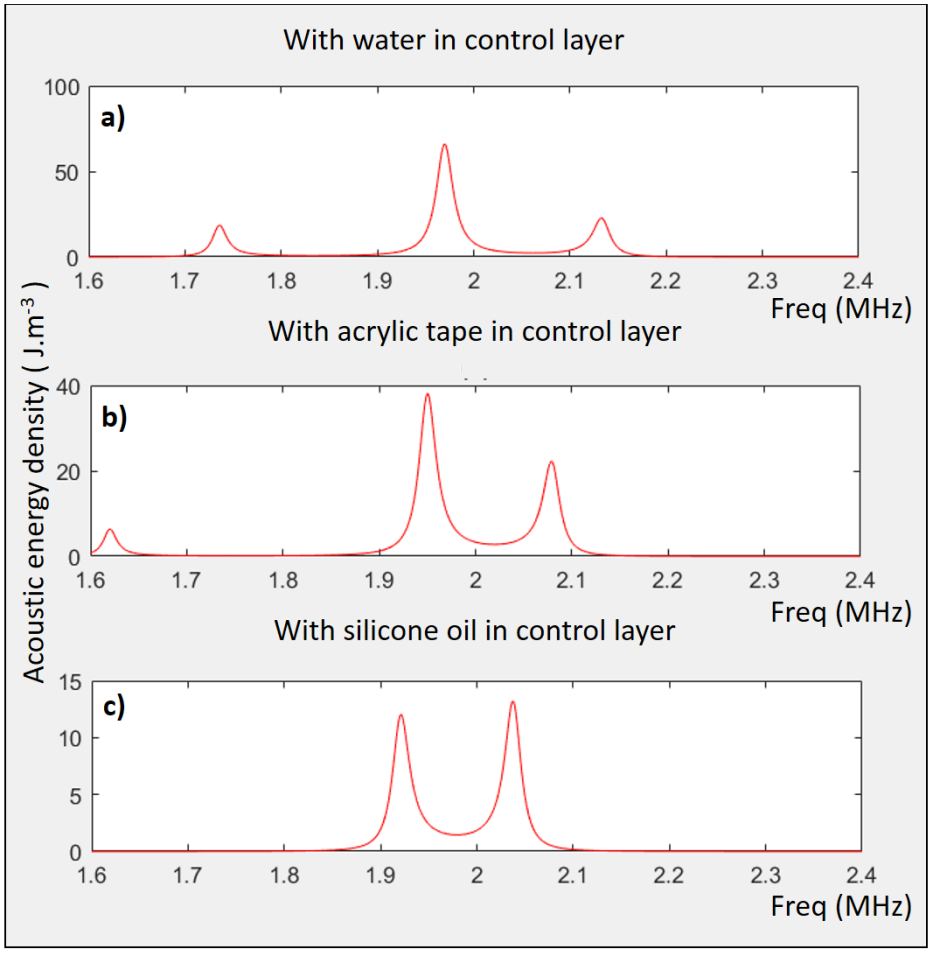

Figure 88 - Acoustic energy density in the fluid layer vs frequencies, a) in the case of water in the control layer, b) in the case of of acrylic in control layer, c) in the case of silicone oil in the control layer.

A control layer of 420 µm is thick enough to have clear variation in resonance frequency all three materials composing the control layer. A resonance frequency of 2.04 MHz have been found for silicone oil in the control layer, 1.97 MHz for water and 1.95 MHz for the acrylic tape. The energy density is higher with water in the control layer than for other materials. The structure of both potential active fluid, meaning Water and Silicone oil are shown in Figure 89.

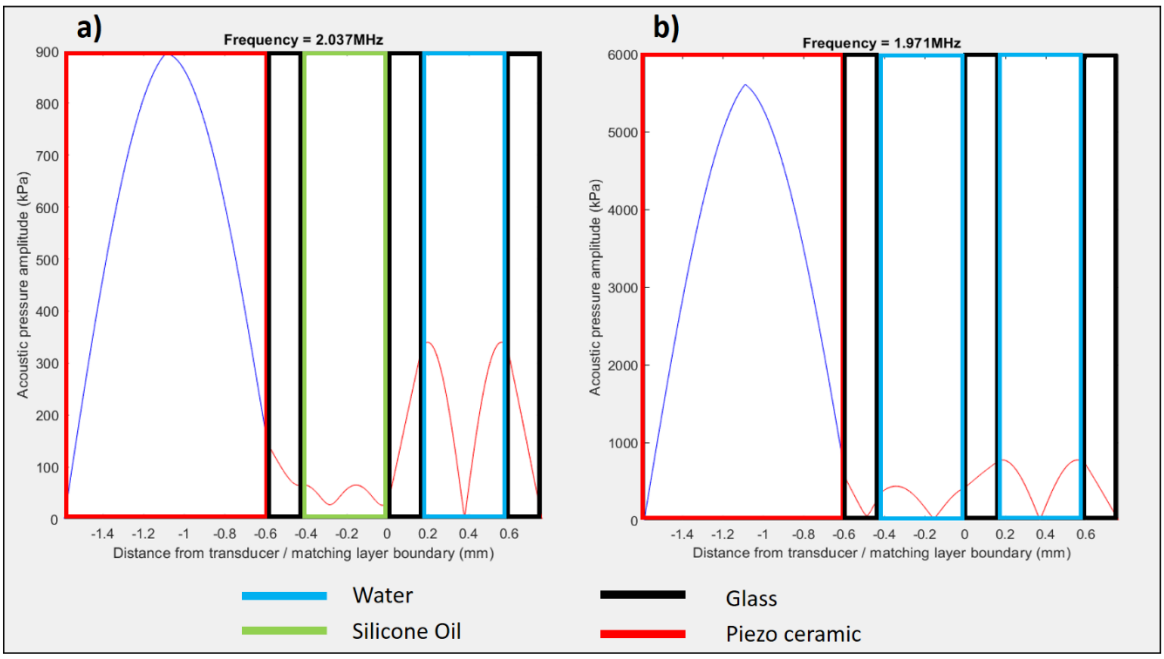

Figure 89 – Acoustic pressure structure, a) in the case of water in the control layer, b) in the case of silicone oil in the control layer.

Both water and silicone oil give a half-wave mode in the manipulation cavity, this confirm the usability of this thickness combination.

In the control layer all three material will be in contact of each other of all time, the localisation ratios of all combination matters for the performance of the device. To study it a 2D modelling is used, the model used in comparable as the one introduced in section 3.2. The mesh size is λ/16, the width of the active material is 2 mm as is showed the best result in the statically controlled planar resonator. The thickness and the acoustic follows what was introduced earlier in the 1D modelling. The kinetic energy gradient in the manipulation cavity are shown in Figure 90 for the case of the third position.

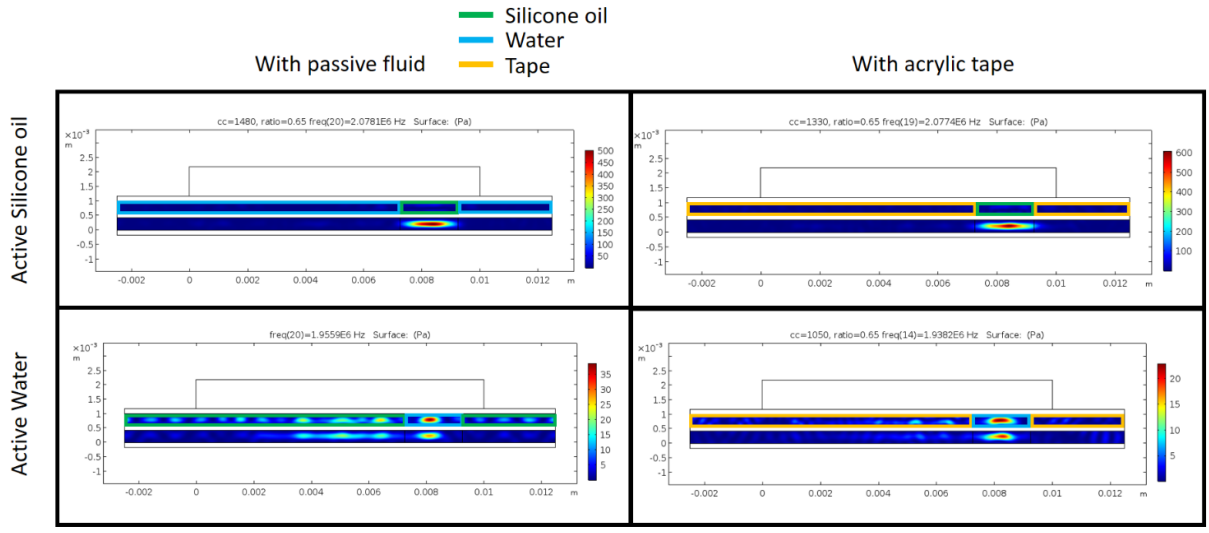

Figure 90 – Kinetic energy gradient at maximum location ratio half-wave frequency in the manipulation layer. For different material composition.

As expected 5.3.2 the location ratio is better in the case active silicone oil, it is because lower speed of sound material are better active material in the case where the speed of sound difference is relatively small.

Although it has been showed that, for the same active width, the model could react differently for different positions. In order to confirm that the difference in localisation ratio are not due to aberration link to the position, three positions are simulated, respectively 1.75 mm, 2.5 mm and 3.25 mm to the right, compared to the centre of the manipulation cavity. The localisation ratio resulting from these simulation are averaged and shown in Figure 91.

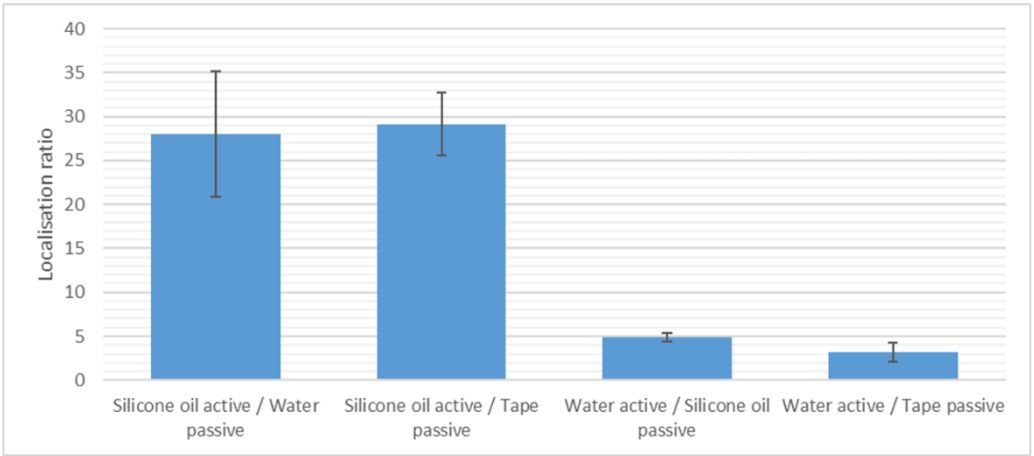

Figure 91 – averaged maximum localisation ratio resulting from a half-wave frequency excitation. For different material composition.

Finally the two dimensional modelling confirm the potential performance of this structure. Even though the three materials composing the dynamic control layer have close acoustic properties, the device should give good localisation ratio and descent acoustic energy when excited at the silicone oil half-wave mode frequency. However, water as active material should not give good localisation ratio or acoustic energy density.

5.5.3 Unsuccessful dynamic control layer design

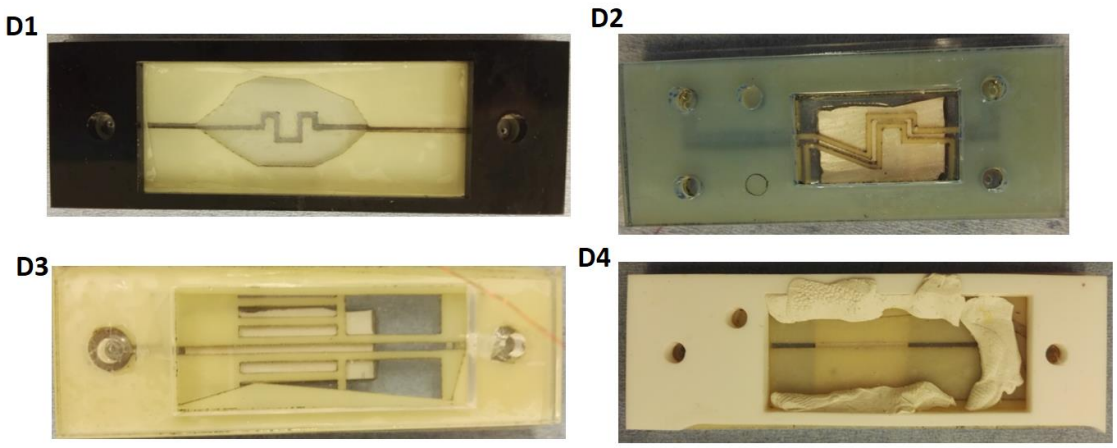

Figure 92 – Pictures showing four unsuccessful devices

Before arriving at the final design that is introduced in next section, a number of before arriving at the final design that is introduced in next section, a number of intermediate designs were modelled and fabricated. Unfortunately none of these provided the controlled lateral forces that were required, however, the process led to insight into the important factors used in the final design. The intermediate designs are label D1 to D4, and shown in Figure 92.

Design D1 was fabricated using double sided tape following the same method introduced in section 4.8. The thickness of the control and manipulation layer is respectively 0.14 mm and 0.42 mm, the channel had a width of 1.5 mm, the shape of the channel was chosen to show lateral movement of particles, to validate that

it comes from the channel architecture and not due to injection parameters or pressure difference between the two ends of the manipulation cavity. The two phase flow was made by rapidly switching a manual valve prior to the injection in the layer.

The Two-phase flow was successfully developed although the droplet lengths were irregular. However no localisation in the acoustic regions of the channel was obtained. Aggregation happened at high amplitude above the tape.

It was hypothesised that it didn't work because the tape acoustic properties were too close to water and silicone oil. (and thus did not provide the acoustic isolation that was desired). Indeed, the silicone oil, water and tape speed of sound are respectively 1050 $m.s^{-1}$, 1480 $m.s^{1}$ and 1330 $m.s^{-1}$. The speed of sound of tape is between the value for oil and water making it a poor choice for this concept.

In order to overcome this issue design D2 was fabricated, using the least amount of tape possible to form the channel walls. The tape width was 1.5 mm as it is the minimum obtainable with laser cutting because of the melting described in section. 5.4.3. The channel path was intricate for the same reason as before, however this time the two phase flow was formed using a junction mixer in the channel. The structure thickness was identical as D1.

The two phase flow droplet lengths were more repeatable using the mixer in the channel. However, unwanted acoustic transmission through the tape layer continued despite the reduced width of the tape channel walls. It was also hypothesised at this stage that a thicker control layer might allow for more response to the differing acoustic properties of the materials it comprised (either transmitting energy or not, respectively).

Thus device D3 was fabricated with a thicker control layer of 0.56 mm, and a channel width of 2.5 mm. In addition an asymmetrical cavity was introduced, at this stage as it was thought to lessen unwanted lateral acoustic radiation forces from interactions with fluid channel walls (this device was created before the results were known from the modelling study described in section 4.5). To speed device evaluation droplet mixing was again temporarily performed outside the device.

However, with the thicker control layer, issues now arose around the stability of the two-phase flow. In some places the two phases became overlaid vertically, rather than being sequentially present as the flow progressed. This

made effective control not possible. It was seen that the control layer channel was too thick and too wide for the required control flow to be stable.

Thus device D4 was created with a control channel thickness of 0.42 mm and a channel width of 1.5 mm. This gave promising results with properly structured two-phase flow. For the first time, acoustic energy was successfully found to be localised in the area of the channel. However, the acoustic energy maxima were sometime above the tape near the channel. In addition the droplet length was not completely repeatable.

It was hypothesised that the control layer width was not optimum; as shown in section 5.3.3, the width has significant effect on the localisation ratio.

In order to overcome the issue raised above, in the next section the channel width is changed to 2 mm and the droplet mixer changed to a V-shape to provide more repeatable droplet formation.

5.5.4 Fabrication of successful dynamic design

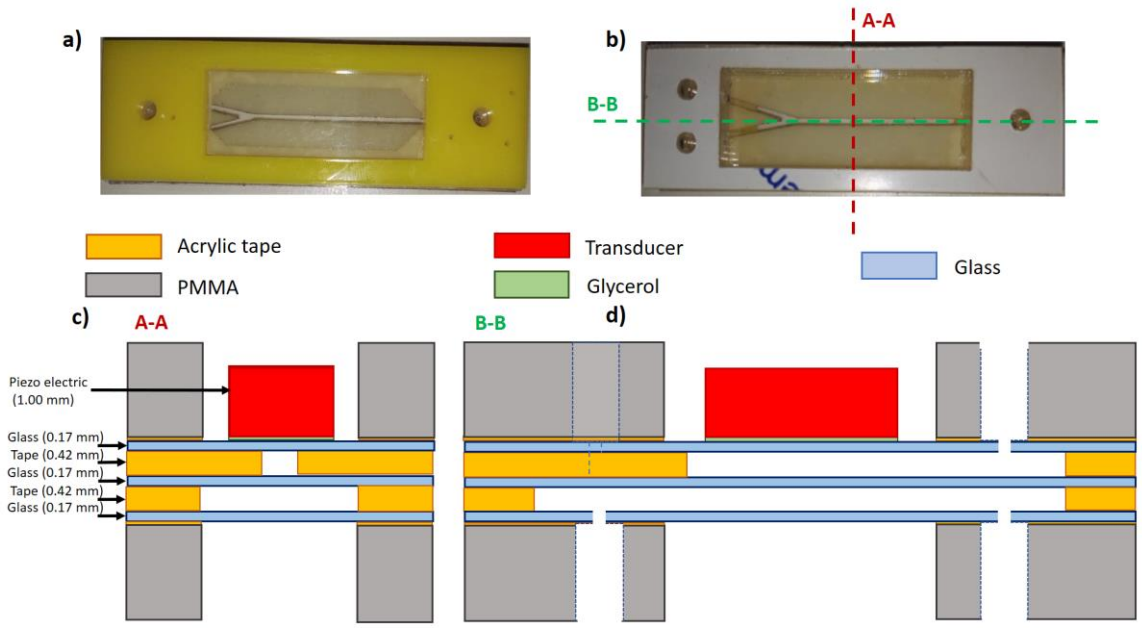

Figure 93 – a) Manipulation side of the planar resonator, b) Channel side of the planar resonator, c) A-A schematic cut-view, d) B-B schematic cut-view

The fabrication of the manipulation cavity follows the same process a discussed in section 4.8.1.1. The cavity consist of a 12x30 mm cavity with V-shape opening at the right and left side of it allowing easy complete filling. As shown in Figure 93.a).

The fabrication of the control layer follows here again the same process as discussed in section 4.8.1.1. The channel is a 2 mm width Y-shape, with two flow inputs and one flow output. Two different fluid are injected in the two inputs. The flow inputs and output are connected to syringes using a PMMA layer laser cut with circular hole to allow fitting tubings and a window for optical access, as shown in Figure 93.b).

Two cut schematics are presented in Figure 93.c) and Figure 93.d). This structure has the advantage to be low-cost and quick to fabricate.

5.5.5 Experimental method

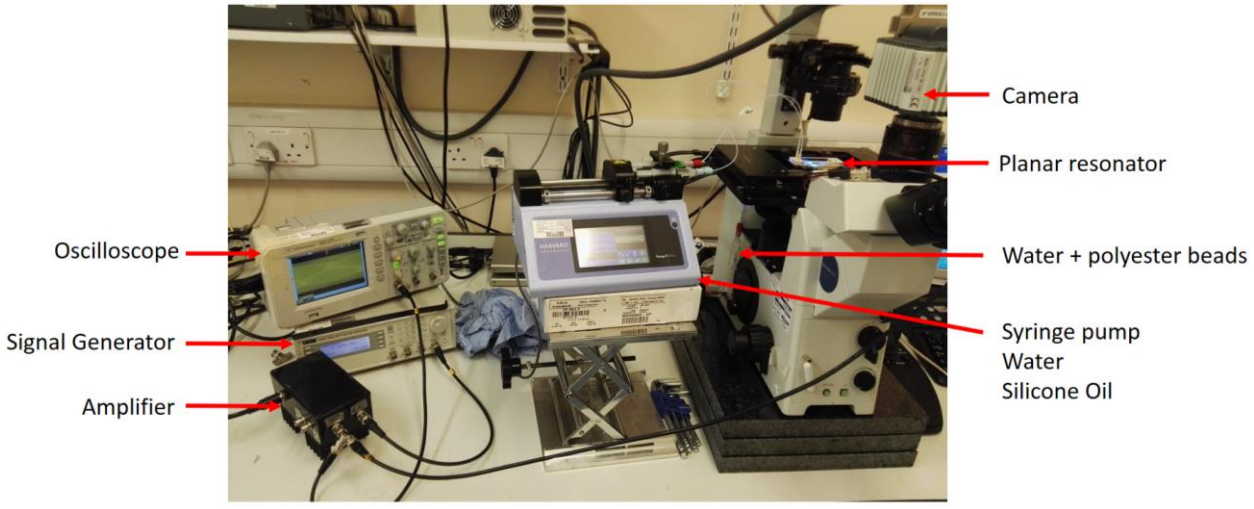

Figure 94 – Experimental set-up for transport experiment using a two-phase fluid control layer

The experimental method is comparable to the one discussed in section 5.4.4. Few differences exists between both set-ups. The mixture of water and 10 μm fluorescent microspheres (Fluoresbrite YG 10 μm, polysciences) injected in the manipulation cavity, have a concentration of 2.10^5 beads/ml.

A syringe pump is added to the set-p to inject the two-phase flow in the Y-shape channel control layer, as shown in Figure 94. Water is mixed dark green food colouring to distinguish it from the colourless silicone oil in the channel. The two fluid are pushed at a rate of 0.25 μL each. In the channel two phase flow advance at a steady rate of 0.6 $mm.s^{-1}$ as a slug flow. The droplets length are almost repeatable with a droplet length going from 4 to 7 mm with this pump set-up.

The conductance test using cypher graph helped us estimate the resonance frequency with silicone oil in the channel, which is 2.03 MHz and the one with water, which is 1.99 MHz. It is close that what the 2D modelling gave as result as shown in section 5.5.2.

The transducer used is a 9x12 mm transducer prepared as described in section 4.8.1.

5.5.6 Experimental results

The half-wave thickness resonance with water, with a frequency of 1.99 MHz, give noticeable effect above 13 Vpp at the transducer. At this amplitude there is levitation but no clear localisation in the channel, particles levitate everywhere in the cavity, above silicone oil, water and tape. There is complex streaming pattern and acoustic radiation force, changing over time as the two-phase flow progress in the underneath Y-shape channel. No transport or stable aggregation occurs at this frequency.

The half-wave thickness resonance with silicone oil, with a frequency of 2.03 MHz, give noticeable effect above 8 Vpp at the transducer. Above the silicone oil droplets acoustic radiation force and multiple pairs of streaming patterns are apparent.

A transport experiment is carried out using the syringe pump to make the fluids flow through the channel at a steady speed of 0.6 $mm.s^{-1}$. At this rate particle

transport is achieve following the centre of the channel, and the direction of the underneath flow as shown in Figure 95.

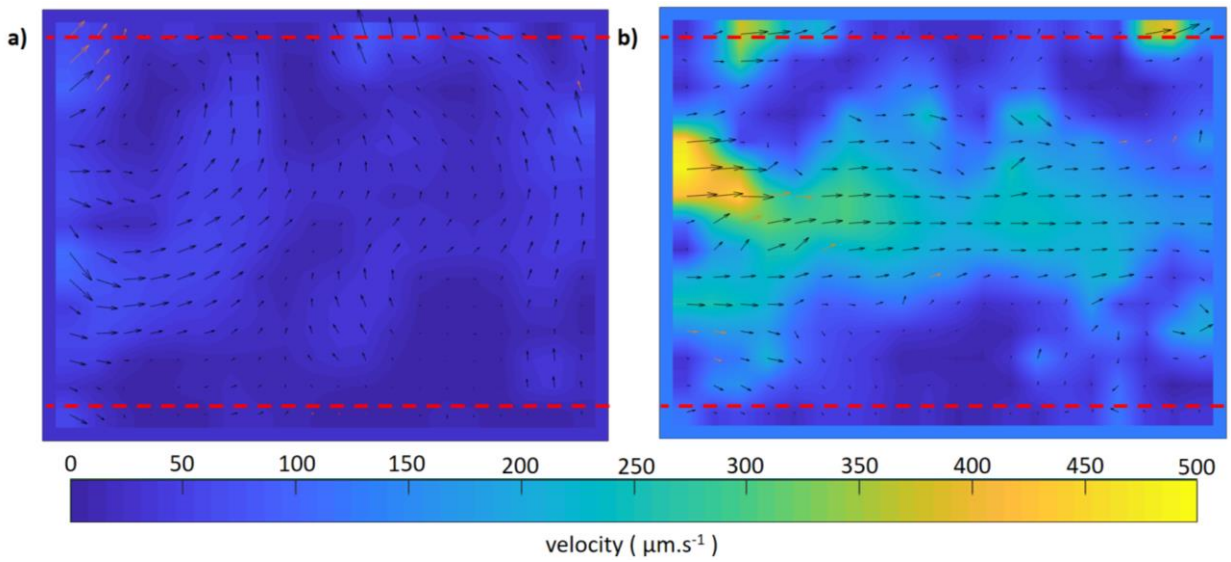

Figure 95 – a) PIV as water flows in the underneath channel, b) PIV as the silicone oil flows in the underneath channel. The colour gradient represent the velocity magnitude, the arrows show the direction. Red dotted line represent the position of the channel's borders.

In Figure 95, the arrows show the particles movement directions, the colour gradient represent the velocity magnitude.

When the water flows in the underneath channel, the particles are pushed by drag force coming from strong streaming. The movement direction varies over time. The magnitude is relatively low. The average magnitude is 29 $\mu m.s^{-1}$, the average lateral magnitude (following the channel direction) is 17 $\mu m.s^{-1}$.

When the silicone oil flows in the underneath channel, the particles are transported to the right, following the flow direction in the channel. The particle are directed toward the middle of the channel, few particles escape from the channel pushed by the drag force coming from the important streaming. The particles in the middle of the channel are pushed to the right at a non-uniform magnitude up to 490 $\mu m.s^{-1}$ as shown in Figure 95.a). The average magnitude in the whole window is 140 $\mu m.s^{-1}$, for a lateral average magnitude of 113 $\mu m.s^{-1}$. This suggest a non-uniform acoustic energy field moving to the right following the

silicone oil in the channel below. If the acoustic energy field was static, some particle would be pushed to the left.

This experiment proved that this strategy can result in a dynamic acoustic force field, driven by the two-phase flow in the control channel. This open to a wide range of possible applications.

5.5.7 Discussion

The dynamically controlled planar resonator presented above have been found after extensive search. Indeed, several aspect of the design have to be carefully thought out for optimal performances.

The first aspect is the choice of material, choosing a two-phase flow composed of gas/liquid can be tempting because of their widely different acoustic properties but since gas is compressible, the flow in the channel is hardly controllable. A Fluid/fluid two-phase flow in the channel is preferable, however they have comparable acoustic properties.

Because of their relative similarity in acoustic properties, the thickness of the control channel is critical. If it is too small the relative wave phase between the active and the passive material would small, resulting in poor localisation ratio. If it is too thick, the two phase flow disposition change, the fluid with the lower density flows above the one with the higher one and not one after the other, this being inappropriate for this concept. In the case of silicone oil and water, in channel thicker than 0.5mm the fluid tend to arrange themselves one on top of each other, hence the 0.42 mm thickness in the control layer presented above.

The channel width is an important aspect, if the channel width is too small the localisation ratio is low as investigated in section 5.3.3. In the case of silicone oil and water and a channel thickness of 0.42 mm, the localisation ratio and the acoustic energy density were decent for droplet wider than 1.5 mm, and better for a droplet width of 2 mm. If the channel is wider than 2.5 mm the two fluid arrange themselves side to side and not one after the other. Hence the channel width of 2 mm.

Practical difficulties were found around maintaining and controlling the two phase flow, which were largely solved through a trade-off between channel aspect ratio, and the width required to give sufficient acoustic coupling through the layer.

This two techniques could be use in the future in many applications, especially for contactless tissue engineering [77]. In planar resonators the expected force field is 10 time stronger in the height direction than in the side direction. (See section chapter 4 or [90]) This would result in discoid shaped aggregates. Before using this two techniques to create size controlled aggregates, and being able to transport them, it is sensible to confirm the metabolic viability of such cell aggregates.

In next chapter, a bioreactor is designed and fabricated to produce cell discoids using the knowledge obtained in chapter 4. The goal is to confirm that this shape is relevant for tissue engineering for drug screening, opening the possibility to use the novel techniques introduced in this chapter for future tissue engineering application.

5.6 Summary

In the chapter, two novel strategies to create and control lateral force fields in planar resonators have been investigated.

The first method consisted of placing a static intermediate layer formed with two different material in the acoustic path of a standing wave. This layer structure directed the acoustic field structure in the cavity and therefore the trapping positions.

Modelling showed that the control layer was most effective when placed between the transducer and the cavity. By putting the control layer next to the reflector, the energy density in the cavity is greater but the energy contrast is lower. Modelling (and experiments) also showed that the pillar width should be greater than the wavelength in the active material of then control layer. Finally modelling showed that the difference of speed of sound of both material is critical, in the case where both material have similar speed of sound; the active material should have the lowest speed of sound for better energy contrast ratio.

The device gave convincing results aggregating particles above the pillars at rates of up to 6 $mm.s^{-1}$. Acoustic streaming was also present, typically creating a pair of vortices in the plane of the transducer above each pillar. The streaming often disrupted the intended agglomeration, interacting in a complex manner with the aggregate in ways that depended on aggregate size. To make practical use of this system further work to reduce or control the streaming flows would be necessary.

The dynamically controlled device consisted of a planar resonator with a controllable two phase flow channel to direct the trapping position. Practical difficulties were found around maintaining and controlling the two phase flow, which were largely solved through a trade-off between channel aspect ratio, and the width required to give sufficient acoustic coupling through the layer. Careful choice of the two different phases was also required to give sufficient acoustic difference between them, with a combination of silicone oil and water proving useful (and also acoustically different from the bordering channel walls). Results demonstrate a device effectively dynamically control the acoustic energy field in

response to the pumped flow of the control layer channel. Moreover particles transportation have been accomplished. This open to a wide range of possible applications, such as dynamic aggregation and transport, size sorting and others.

Chapter 6: Investigating lateral trapping for hepatocyte cell culture and tissue engineering

In this chapter, a bioreactor system has been designed and used to grow in levitation Human hepatoma (liver) cell (huh7) discoids. The huh7 discoids were assessed for viability, their functional activity and their response to 5- fluorouracil (5FU), an anti-cancer drug. The responses are compared to conventional 2D cell models, with an aim to showing that this cell model is a useful approach to creating an effective drug toxicity and screening model. Throughout the chapter, the system is referred to as the *AFB* (AcoustoFluidic Bioreactor).

The work in this chapter has been carried out in collaboration with Mogib El-Rahman Khedr (Academic Unit of Clinical and Experimental Sciences group, Southampton General Hospital) and Umesh Jonnalagadda. I worked jointly with Umesh on device design (leading on the finite element analysis), fabrication, electronics fabrication and optimisation. I developed protocols for loading cells into the device, jointly worked on optimising cell loading parameters, development of the culture strategy (Mogib carried out the majority of actual cultures once we had together carried out initial experiments to find the best strategy). The viability, E-cadherin and functionality assays were carried out by Mogib, and we jointly analysed the data and wrote the paper.

6.1 Bioreactor modelling

The lateral acoustic resonance is used to produce cell discoid without scaffold, in levitation. As investigated in chapter 4, a simple planar resonator can strongly resonate laterally, changing the force field accordingly. In this case, many trap points are available. Because the axial radiation force field is ten times stronger than the lateral radiation force field, we expect the creation of cell discoid.

Modelling is performed as a first step to design a good planar resonator, with strong lateral resonance. One-dimensional impedance transfer model is used to find a suitable thickness combination, with materials available for fabrication. The cavity have to be thick enough to welcome the tip of a flexible pipette to inject cell directly in the cavity. A structure fitting the requirement described earlier consist of a cavity thickness of 0.56 mm sandwiched between a 1 mm thick glass carrier and a glass reflector, and next to the carrier, a 1 mm transducer. From the modelling, this structure excites a half-wave thickness mode at a frequency of 1.468 MHz, its pressure structure is shown in Figure 96

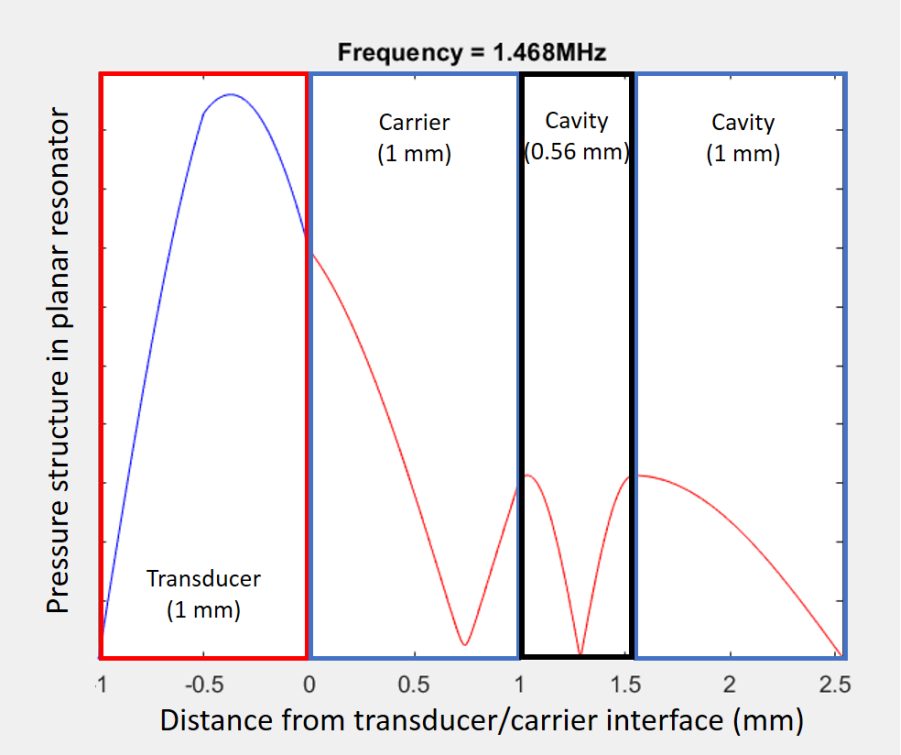

Figure 96 – Pressure structure in the planar resonator

To create cell discoids, many trap positions or local kinetic energy maxima have to be present, to visualize the number and shape of trap positions in such planar resonator a FEA two-dimensional modelling is used. The model is similar as the one introduce in Chapter 3, the mesh size is set as λ/16, where λ is the longitudinal acoustic wavelength in water, the lateral wall of the water cavity are modelled as acoustic hard boundary, reflecting all the wave back to the fluid, maximizing lateral resonance potential. The carrier and the reflector are modelled as glass, and the transducer is modelled as PZ-26.

A device creating multiple trap positions is found and its kinetic energy gradient in the fluid layer in displayed in Figure 97.

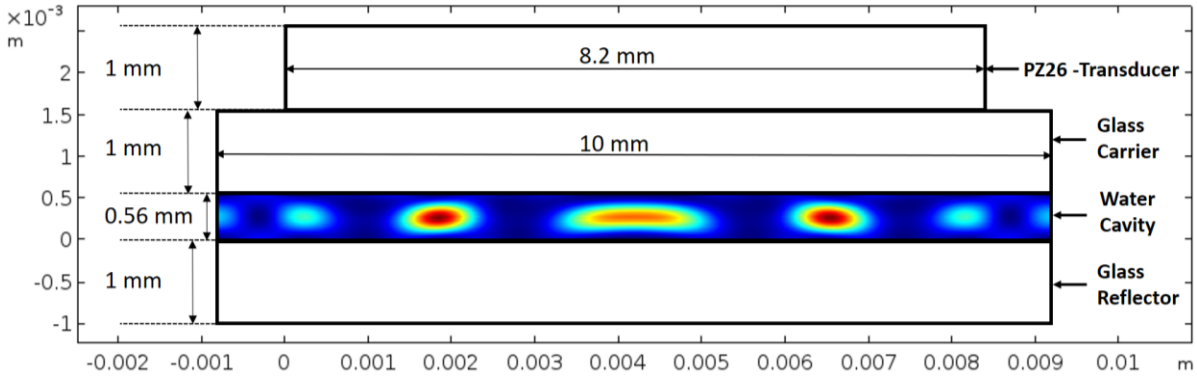

Figure 97 – Kinetic gradient of planar resonator in the case of strong lateral force creating multiple trap positions in levitation.

Figure 97, shows 5 clear trap positions. The transducer width is 8.2 mm, the cavity, carrier and reflector width is 10 mm.

In this thickness structure, most of the width composition showed lateral component in the force field, a flat and unique aggregate is exceptional. The architecture showed in Figure 97 gave particularly strong lateral resonance but imperfection in the production of this planar resonator should give lateral component fluid acoustic force field.

6.2 Bioreactor fabrication

6.2.1 Bioreactor design

The planar resonator modelled earlier is used to produce cell aggregates in levitation, lateral resonance actuated at the half-wave thickness frequency is used to produce a multitude of aggregates per planar resonator.

The planar resonator has to be open to allow the cell media in. Thus it is conceived as an open-sided cavity as shown in Figure 98.

In a bioreactor the planar resonator would be submerged in cell media in order to avoid frequent change of media. However, the difference of acoustic impedance between glass and cell media is lower than the difference of acoustic impedance between glass and air. Therefore, submerging the planar resonator could lower its performance as part of the acoustic energy would be transmitted to the cell media around. To maximise its performance an air backing layer is added to the planar resonator using 0.14 mm tape and 0.17 mm as a seal. The planar resonator and air backing is schematize in Figure 98.

In order to increase the number of experiment achievable in the same time, four of these planar resonators are place in each planar resonator. The carrier of each planar resonator is the same glass piece of 75x50x1 mm. Separators, reflector, air backing separator and air backing glass seal are individuals for each planar resonator.

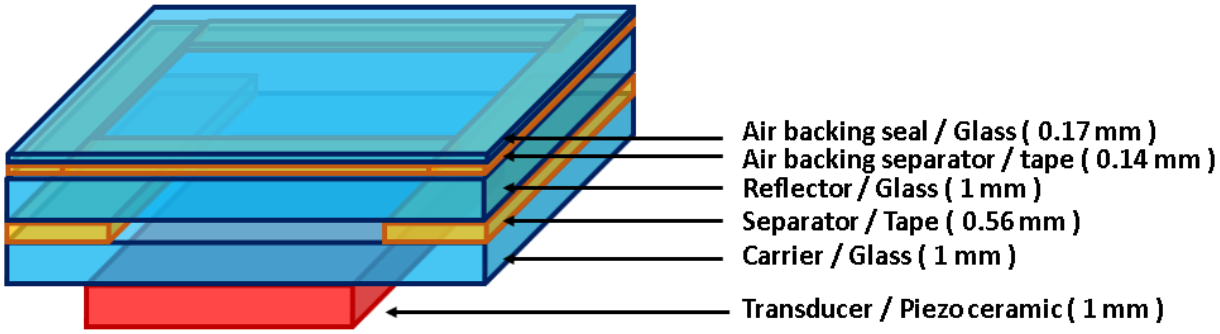

Figure 98 - Schematic of planar resonator and air backing

The aim for having four planar resonators in the same bioreactor is to be able to make several experiments in parallel, using the same device. To do so, each planar resonators have to be placed in independent wells as the cell media can be studied for its proteins mix and concentration, and can interact with cells.

10 mm thick four wells grid made of PMMA is attached to the glass carrier and form the four wells, the planar resonators are fabricated inside this tructures as schematized in Figure 99.

It shows schematize top view of the bioreactor without air backing for clarity.

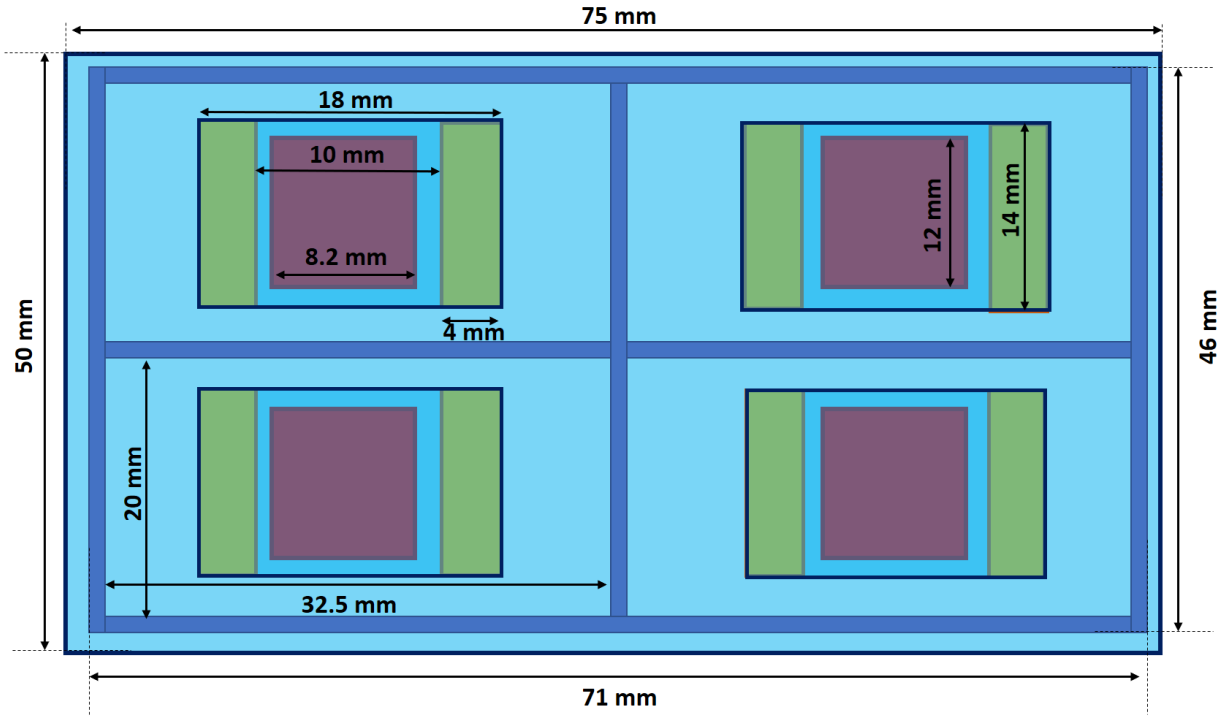

Figure 99 – Schematic of bioreactor with four planar resonator, common carrier and individuals separators, reflector and wells. Top view without air backing for clarity.

An extra 75x50x1 mm glass slide is added on top of the four well bioreactor to permeably close the wells, it is done to avoid quick evaporation of the cell media.

6.2.2 Bioreactor fabrication process

To fabricate the resonators, double width glass slides (Corning, 75 × 50 × 1 mm) and standard microscope slides (Corning, 75 x 25 x 1 mm) are cleaned using ethanol. Four transducers (Ferroperm PZ26, Kvistgaard, Denmark; 8.2 × 12 × 1 mm) were prepared using the same method as in section 4.8. They are glued to the double width glass slides using epoxy (Epoxy 353, Epotek, Billerica, MA, USA) according to the position showed in Figure 99 and cured at 80 ˚C for 1 hour. Standard slides were cut to a 14 x 18 mm rectangles using glass tile cutter. The 75x0.14mm 3M 9731silicone adhesive tape (3M, St. Paul, MN, US) are stacked four times on themselves for a total thickness of 0.56 mm, and cut to 4 x 14 mm rectangles. The cut standard glass are taped to the double width glass slides using

the pre-cut stacked tapes. On top of the 14 x 18 mm glass slide rectangle, a 14 x 18 mm double coated tape is placed, then a 9 x 12 mm rectangle is cut on top of the transducer using a scalpel and removed, finally a thin glass is placed on the cut tape to close the air backing layer.

An acrylic plastic (PMMA) is cut to obtain four windows of 32.5 x 20 x 1 mm, as shown in Figure 99. It is stick to the double width glass slide using PDMS, curing it for two hours at 65 °C. Finally another double width glass close the four wells permeably.

The fabricated bioreactor is shown in Figure 100.

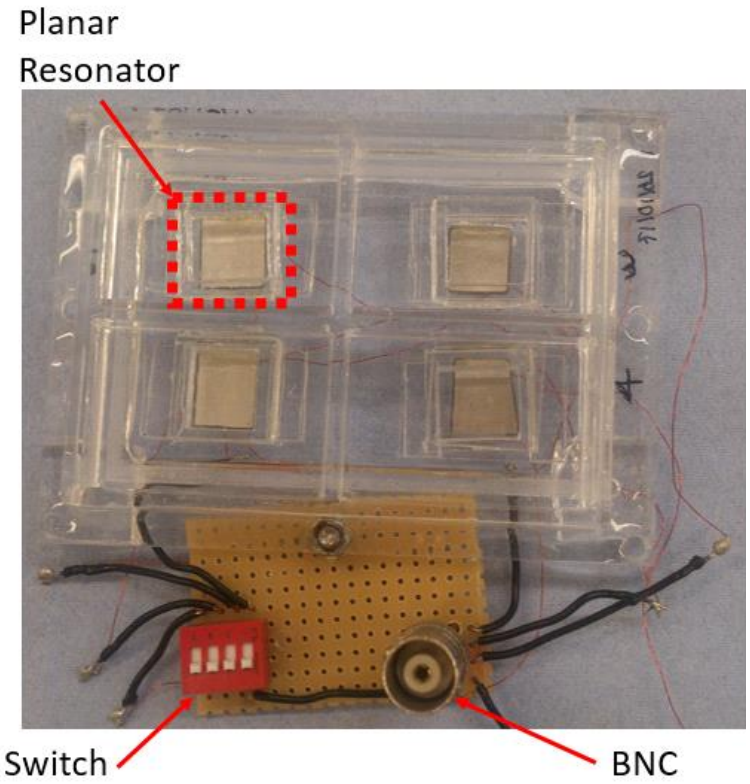

Figure 100 – Bioreactor containing four wells and four planar resonators.

A four way dip switch is added to be able to select the transducer, especially to characterize their impedance response as presented in section 5.4.1.2. A BNC cable is added to connect the four transducer to the amplified signal generator.

A portable amplified signal generator is fabricated to drive the transducer at the half-wave thickness mode frequency. It is composed of an Arduino Uno coupled with a DDS module to generate the sinusoidal waves, and an inverted

AOP circuit with one of the resistance being a variable potentiometer allowing simple control over the amplifier gain.

6.3 Planar resonator characteristic

The conductance response to the planar resonators is investigated to establish the fabrication repeatability. Moreover this inform on the resonance frequencies expected. The C60 from cypher instruments is used to measure the conductance response for a frequency range going from 1.20 MHz to 1.80 MHz, for all four cavity. Cavities are isolated using the four-way switch. The results are shown in Figure 101

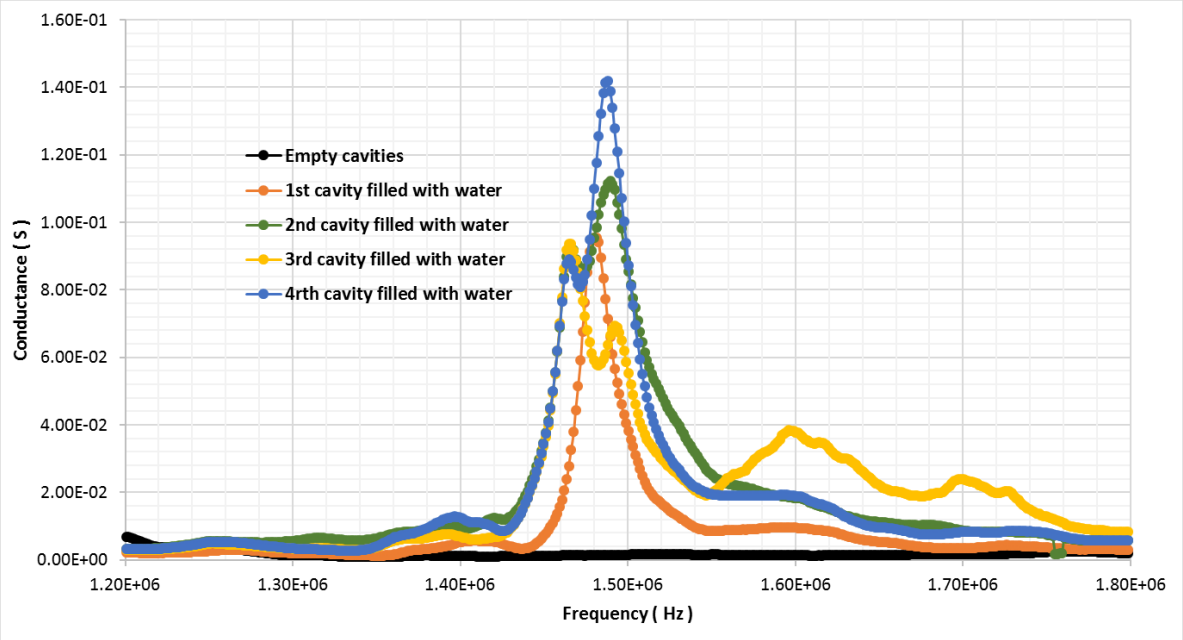

Figure 101 – Conductance response for all planar resonators in a bioreactor

The thickness resonance is associated to the peak of conductance for each cavity. All cavities have close resonance frequencies, from 1.46 MHz to 1.49 MHz. The value in conductance are related to the acoustic energy in the planar resonator. Cavities maximum related resonance at resonance frequencies vary from 95.10^{-2} S to 144.10^{-2} S. The planar resonators are similar but not identical.

In order to take into account this variability, transducer input is set a swept frequency from 1.44 MHz to 1.51 MHz at a rate of 20 Hz. A wider than necessary

range of frequencies is used as the resonance frequency can change over time because of material heating or dilatation. The driving amplitude is set to 7 Vpp for the whole investigation.

At this temperature, the temperature of the channel fluid can increase over-time, fluid temperature is a critical information for biomedical application, especially cell culture. The wire of a wire thermocouple is place in the middle of each cavity filled beforehand with water, the thermocouple is connected to a thermometer. The amplified swept frequency drive the transducer at an amplitude of 7 Vpp. The measurement are showed in a graph in Figure 102.

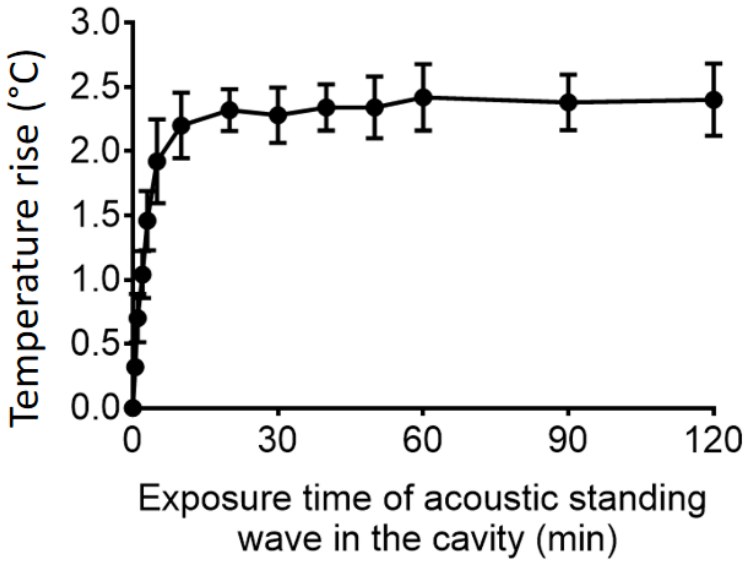

Figure 102 – Temperature rise over time in a planar resonator driven by a swept frequency from 1.44 MHz to 1.51 MHz with an amplitude of 7 Vpp

.

These measurement have been performed at room temperature, a temperature rise of 2.4 ± 0.3 ˚C. The temperature rise attains 80% of its maximum value in around five minutes. The temperature rise is significant be because the aggregation process in bioreactor will take place at room temperature, this will not have a significant effect on cell viability.

To measure the pressure field magnitude in the fluid cavities, the drop voltage method is used. It consist of reducing the voltage gradually and slowly, and report the voltage at which the particle fall to the bottom of the cavity, at this amplitude the weight of the particle pushing the particle downward is stronger than the acoustic radiation force pushing it upward. The drop amplitude for the four planar

resonator is 0.63 V ± 0.3 V. Which gives a maximum pressure at 7 Vpp of 380 ± 20 kPa.

6.4 Huh7 Hepatoma cell line discoid production

6.4.1 Huh7 culture

Huh7 hepatoma cell line was provided by Dr. A Ermre Savan from the Cancer sciences Academic Unit of the University of Southampton. The cells were culture in a mixture of Dylbecco Modiefied Eagle Medium, DMEM for short (Thermo Fisher, Inchinnan, UK), 10% heat-inactivated fetal bovine serum, FBS for short (Thermo Fisher), 100 U ml $^{-1}$ of penicillin, 100 µg ml^{-1} of streptomycin, and 250 ng ml^{-1} of Gibco Amphotericin B. Cells were maintained at 37°C in an incubator with 5% CO_2, medium is changed every 3 days.

6.4.2 Discoids production

To produce the huh7 discoids, cells are injected in the cavity open-side using a gel-loading flexible pipette (end height 0.3mm). The discoids are kept in levitation for two-hours at room temperature. Experiments showed that was sufficient to cause the cells to form stable aggregates that did not break apart on removal. Cell aggregate are then sucked out gently using a larger pipette tip (10 ml) before being placed back in the incubator on tissue culture plastic.

6.4.3 Discoids geometry and arrangement

Glicklis et al [102] showed that viability and function are impacted by the size of cell aggregate, moreover creating repeatable sized aggregates is important for many appications such as drug screening.

To investigate the size and shape of aggregate, cell aggregation process is observed during the first 15 minutes in the levitation cavity. The cavity is filled with 78 µl of a mixture of medium and huh7, After this time the cells are already structure in 9 to 12 discoids as shown in Figure 103-a). The aggregates diameter

depends on the concentration in cells of the fluid injected in the cavity. At a density of 0.25 x 10^6 cell/ml, small Huh7 cell aggregates were formed with a mean diameter of 381.6 ± SD 113 µm, the diameter does not change for notably for a density of 0.5 x 10^6 cell/ml. the diameter increase clearly for a cell density of 1.25 x 10^6 cell/ml, with a mean diameter of 525.4 ± SD 118.7 µm. Finally larger discoids were constructed for densities of 2.5 x 10^6 and 5 x 10^6, with a mean diameter of 1021 ± SD 267.8 µm and 1382 ± SD 403.1 µm, as shown in Figure 103-b)

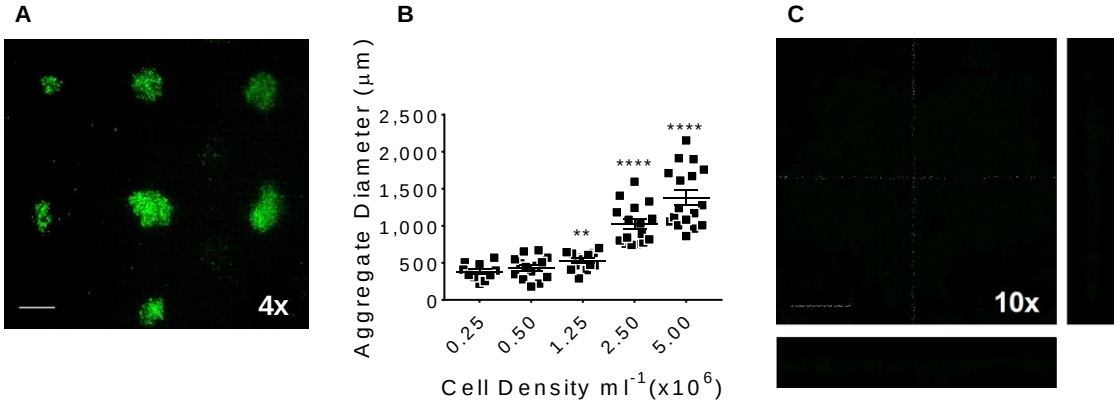

Figure 103 - Cells were pre-labelled with Calcein AM and loaded for 30 minutes in the AFB. (A) A representative image of discoids formed at density of 1.25 x10^6 cell ml^{-1}. Scale = 500 µm. (B) Discoid diameter (µm) was plotted against cell density. n = 3. *P* values shown in the graph are for comparison to cell density of 2.5 x 10^5 cell ml^{-1}. ** *P*<0.005, **** *P*<0.0001. Mean ± SEM. Multiple t-tests. (C) CellTracker™ Green CMFDA Dye (CTG) (Thermo Fisher) labelled Huh7 incubated in AFB for 1 hour at density of 10^6 cell ml^{-1}. Orthogonal projection of cell aggregate showed single layer of cells. Scale = 100 µm.

Aggregate thickness does not change with injected cell density. They always have the same structure, one to three cell layer in thickness unenvely arranged laterally, for a total thickness of 20 to 60 µm, as shown in Figure 103-c). As esxptected the resulting cell shape is a discoids. This is different from cell spheroids obtained with SAW device such as Chen. Et al one [77]

Aggregates formed with a concentration of 1.25 x 10^6 cell ml^{-1} showed high repeatability in shape, this concentration is chosen for later investigations.

6.5 E-cadherin

E-cadherin (Calcium dependent adhesion) is a cell adhesion molecule, it serves in the formation of adherens junctions that binds cells together. This molecule has been found to play a critical role in cell to cell adhesion, in the case where there is no matrix. Its expression is investigated using western blotting technique.

6.5.1 Method

In this sub-chapter, two types of cell aggregates are compared, the 2D monolayer, created using standard petri-dish, and the acoustofluidics bioreactor (AFB). They were cultured for 0.5, 1, 3, 6 and 16 hours. The protocol consist of lysing the cells using 1x TruPAGE™ LDS Sample Buffer [with 1mM ethylenediaminetetraacetate (EDTA), 1mM ethylene glycol-bis (β-aminoethyl ether)-N,N,N',N'-tetraacetic acid (EGTA) (Sigma). *and 0.5µg ml-1 Leupeptin] and run a TruPAGE® 10% precast gels (Sigma) under reducing conditions. Protein was loaded in a concentration of 30 µg as adjusted by the bicinchoninic acid (BCA) colorimetric protein assay kit (Sigma) in accordance with the manufacturer's instructions using a BSA standard. Molecular weights were determined using the PageRuler™ Plus Prestained Protein Ladder, 10 to 250 kDa (Thermo Fisher). Proteins were transferred to nitrocellulose membranes by a wet transfer method. Membranes were blocked for 1 hour in 5% non-fat blotting grade cow's milk (Bio-Rad) in 0.05 % Tris-buffered saline (TBS)–Tween® 20 solution. The membranes were then probed with 1 µg* ml^{-1} *mouse monoclonal anti-human E-cadherin IgG2B antibody Clone #180224 (R&D Systems, Oxfordshire, UK) overnight at 4˚C, followed by rabbit polyclonal anti-mouse-horseradish peroxidase (HRP) (DakoCytomation, Cambridgeshire, UK) at a dilution of 1:2000 for 45 minutes. Membranes were probed with mouse monoclonal anti β-actin-HRP conjugated (Sigma) for 1 hour at room temperature at dilution of 1:50000. Reactive bands were visualised using the Luminata Forte Western HRP substrate chemiluminescent substrate (Millipore UK Ltd., Hertfordshire, UK) in a ChemiDoc™ imaging system (Bio-Rad).*

6.5.2 Results

Huh7 cell in suspension before any aggregation or culture was found to have preserved E-cadherin molecules. When the cells are cultured in 2D monolayer or AFB, they lose their integrity, as shown in Figure 104-a). The intact E-cadherin have a lengh of 120 kDa, but they fragment into smaller parts mostly as C-terminal fragment 1, or CTF1 of 38 kDa, they also degrade at a lower degree to CTF4, of 23 kDa and CTF2 of 33 kDa, as shown in Figure 104-b). Nearly all E-cadherin degraded after 3 hours of cell aggregation in AFB. It is way quicker for 2D monolayer cell culture as shown in Figure 104-c), after 30 min they all have fragmented in smaller pieces. The AFB preserve huh7 E-cadherin for a longer time, but finally there is no notable difference between fragment size distributions after 6 hours.

This highlight the importance of E-cadherin in cell to cell interaction and adhesion for matrix-free cell culture. This molecule permit cell-cell adhesion using calcium related biochemical reaction. To confirm the importance of this molecule in the process of aggregation, 10 mM of EGTA (the selective calcium chelator) is added to the medium mix, this have been shown to completely inhibit any aggregation process in AFB which confirm the importance of E-cadherin, as shown in Figure 104-d).

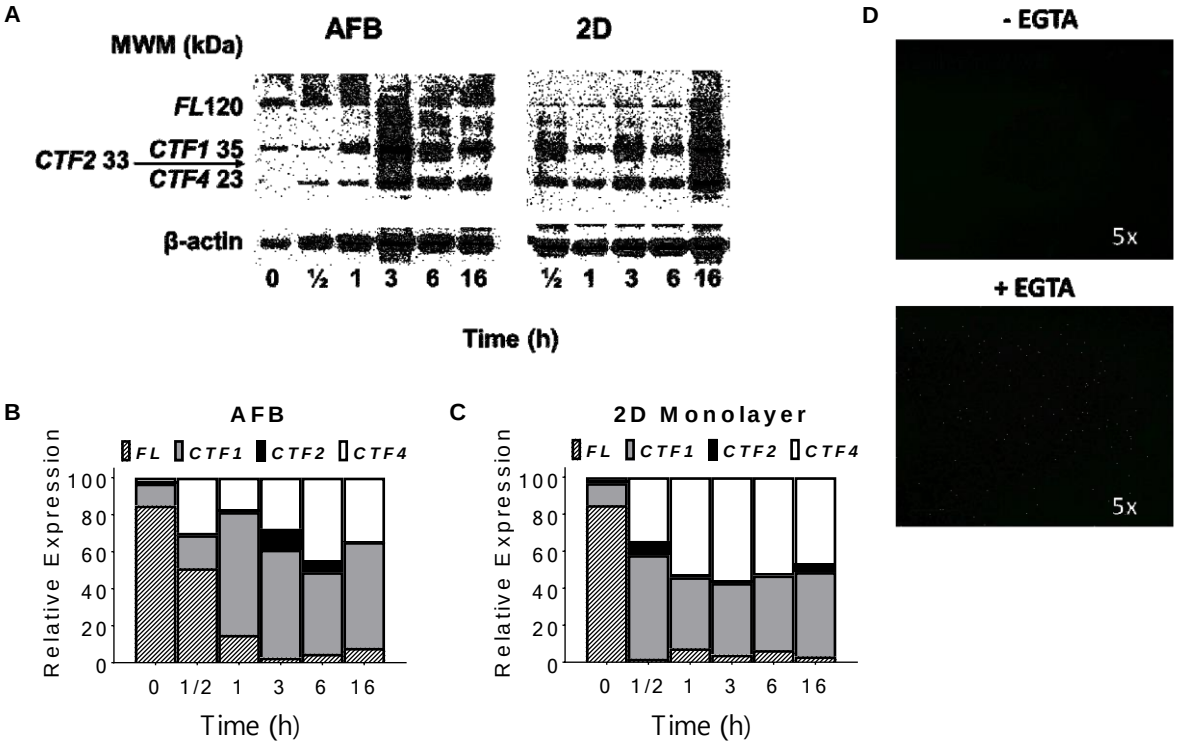

Figure 104 -(A) Representative blot for detection of E-cadherin protein expression in Huh7 grown as 2D monolayer or in AFB (0 time point, represents single cell suspension just before seeding). Molecular weight marker (MWM) is indicated. E-cadherin Full length, FL (120 kDa), C-terminal fragment 1, CTF1 (38 kDa), C-terminal fragment 2, CTF2 (33 kDa) and C-terminal fragment 4, CTF4 (23 kDa) are indicated. (B and C) Band density analysis (band intensity normalised to β-actin control) of E-cadherin fragments detected by western blotting in Huh7 cultured in AFB or 2D systems respectively. (D) EGTA (10 mM) prevented cells from aggregation following incubation for 3 hours in AFB. Cells were labelled with calcein-AM (green) before loading. Scale = 500 µm.

6.6 Viability

A lot of phenomenon can alter the viability of cells, in the case of acoustic manipulation an abrupt manipulation could pierce or disturb the huh7 membrane and alter its viability. A viability investigation is presented in this section.

6.6.1 Method

Staining technique was used to investigate the cell viability in the bioreactor, 2D monolayer aggregate were cultured using standard petri dish to compare viabilities of both techniques. Calcein-AM (Thermo Fisher) is a staining that becomes fluorescent upon hydrolysis, it is used as a marker for living cells. 1 µM is added to the medium before levitation in order to be able to take images during the levitation/aggregation process, as shown in Figure 103. Proidium Iodide, PI for short, is a staining that reacts to damaged plasma membranes, it is used as a dead cells marker, 3 µM was added to the medium.

The viability is expressed as a percentage, this value is obtained by imaging the particles using a Zeiss-microscope and process pictures using ImageJ, as shown in Figure 105-a). The living cells area showing in green is devided by the total area of both colour to have the viability percentage.

Viability was calculated in five different positions per condition in three different experiments.

6.6.2 Results

The viability of Huh7 has decreased sharply to an average of 43.3 and 47.0 % for 2D and AFB after 30 min of incubation, (following two hours of aggregation at room temperature). Then it decreased to respectively to 31.7 and 23.9 % for 3 hours, after 6 hours cell viability was at a low 3.46 and 8.72 % of viability, as shown in Figure 105-b).

HEPES (4-(2-hydroxyethyl)-1-piperazineethanesulfonic acid) is an organic chemical buffering agent, which helps maintaining the pH of a solution. HEPES is added to the DMEM culture medium before experiment. This additive resulted in greater viability results. Indeed, even after 6 hours of incubation (following aggregation) the 2D and AFB remained respectively at a 83.4 and 81.9 % viability. No marked difference is noticeable, the acoustic aggregation set up does not impact cell viability. The HEPES is kept as protocol for later investigation.

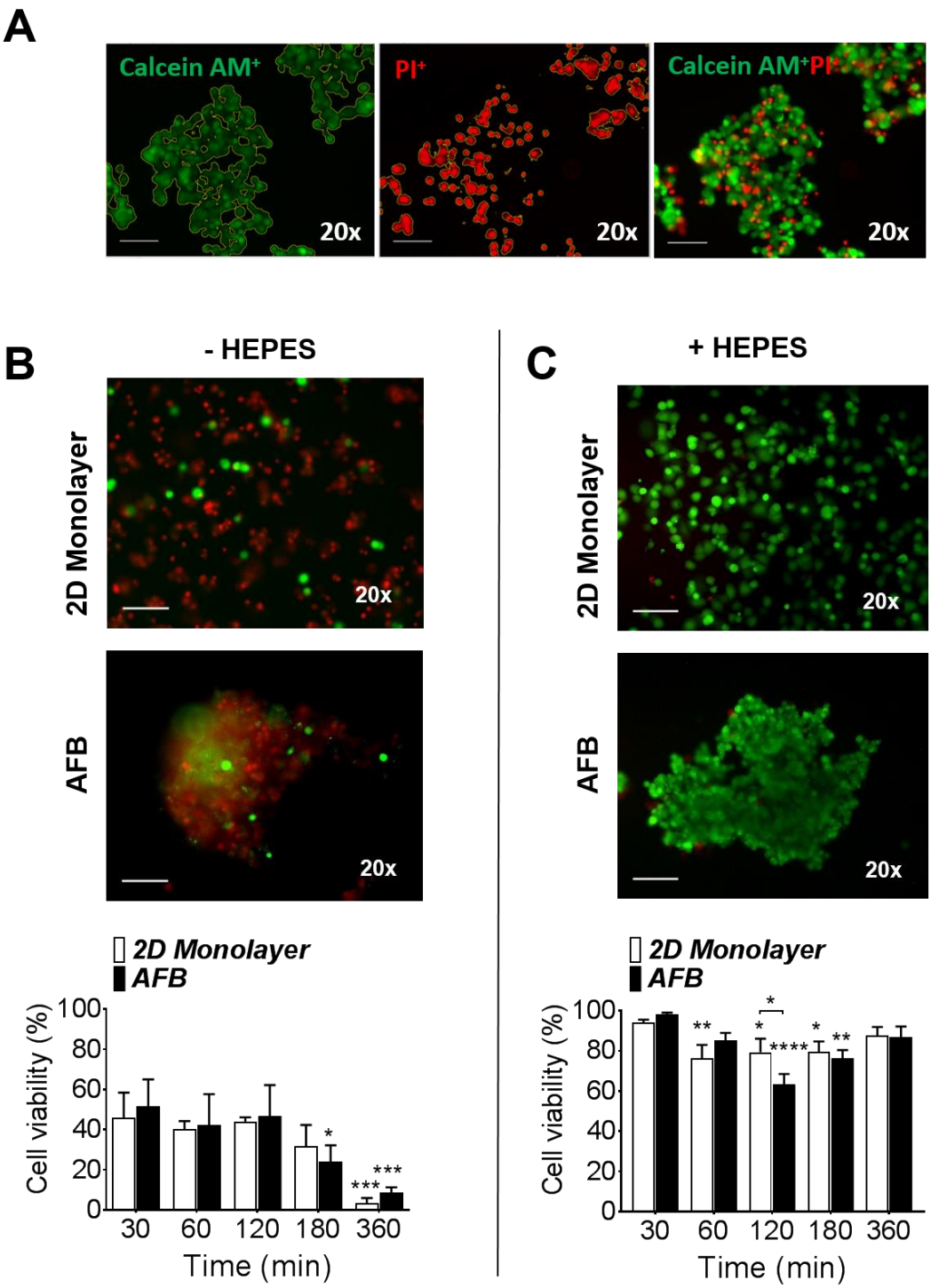

Figure 105 - Live cells were labelled with Calcein AM (green), and dead cells were labelled with Propidium Iodide (PI, red) in (A) absence or (B) presence of 25 mM (4-(2-hydroxyethyl)-1-piperazineethanesulfonic acid) (HEPES) in culture medium. Representative images of cells following 360 minutes incubation in 2D or AFB system were presented and percentage of live cells were plotted against time of cell incubation. Scale bar = 100 µm. n = 3. *P* values shown in the graph are for comparison to 30 minutes time point (on top of bars). * *P*<0.05, ** *P*<0.005, *** *P*<0.0005, **** *P*<0.0001. Mean ± SEM. Two-way ANOVA followed by Fisher's least significant difference (LSD) test.

6.6.3 Cell membrane disruption by sonoporation

Strong acoustic fields can create microbubble and strong streaming field, this can provoke disruption of the cell membrane. This effect is hypothesised to be the mechanism for sonoporation, the formation of transient pores in cells membranes under acoustic action. It can be useful for some application, or harm the cell viability and functionality. If the cell permeability is increased, various intracellular molecules are released.

In order to investigate the cell integrity/permeability in the AFB over time, Celcein-AM, this molecules become fluorescent in contact with intact cell membrane (31). The huh7 are preloaded with the dye then the fluorescent intensity is measured over time for the case of AFB cell aggregate and 2D monolayer standard Petri dish culture as shown in Figure 106-a).

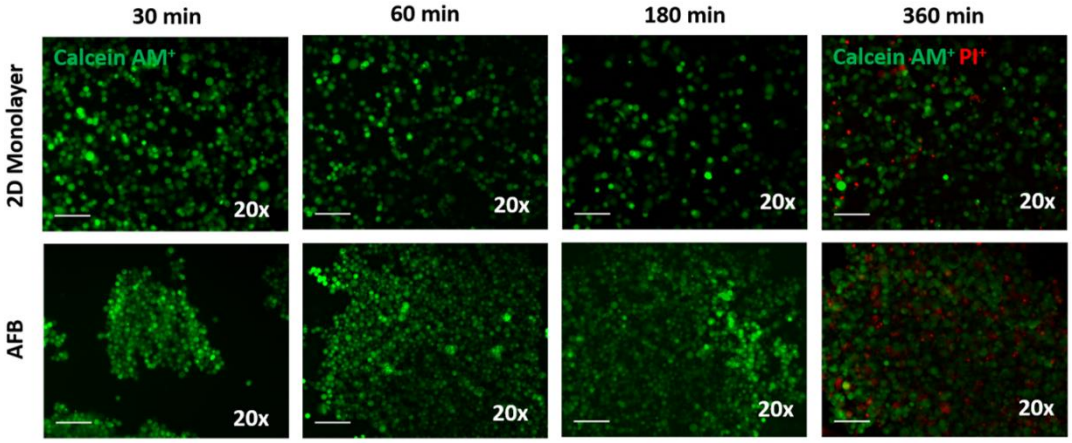

Figure 106 – (a) Permeability of Huh7 with time course in AFB compared to 2D monolayer culture with time course. Cells were preload with Calcein AM (1µM), scale = 100 µm

During the first 6 hours both cell culture technique did not disturb the cell membrane integrity noticeably. However in this test the PI dye showed a slightly higher death rate for cells grew in levitation.

The AFB driven at 7 Vpp and with a swept frequency from 1.44 MHz and 1.51 MHz do not generate microbubble by cavitation. The acoustofluidics environment seem to be good for cells, the manipulation seem to be gentle.

6.6.4 Huh7 apoptosis

Apoptosis is the natural form of cell death that occurs in multicellular organisms. In a human, billion cells die every day by apoptosis. This results in cell DNA fragmentation among other things.

An increase of apoptosis related to the culture technique studied in this thesis is investigated in the section.

6.6.4.1 Method

Cells were lysed using 20 µl TES lysis buffer [100 mM Tris, pH 8.0 + 20 mM EDTA + 0.8 % [w/v] sodium dodecyl Sulfate (SDS)] then incubated for 30-120 minutes at 37°C with 10 µl of RNase A at a concentration of 500 units ml^{-1}. DNA was extracted using proteinase K (20 µl of 10 mg ml^{-1}) overnight at 50°C in a heat block then ladder formation was explored by running DNA on a 1% agarose gel at 35 V for 4 hours. Quantification of bands was performed by Image Lab version 5.2.1 software using Bio-Rad's ChemiDoc™ Imaging Systems System (Bio-Rad Laboratories, Hercules, CA).

The same method will be used for in section 6.8 to investigate the effect of anti-cancer drug on Huh7 in AFB compared to other culture technique.

6.6.4.2 Results

Apoptosis are studied depending on 3 cell culture method and 4 time points, 2D monolayer in petri dish, 3D pellet using a conical tubes and a

centrifuge (200g). The DNA fragmentation of cells grew using these methods for 0.5, 1, 3 and 6 hours are reported below in Figure 107.

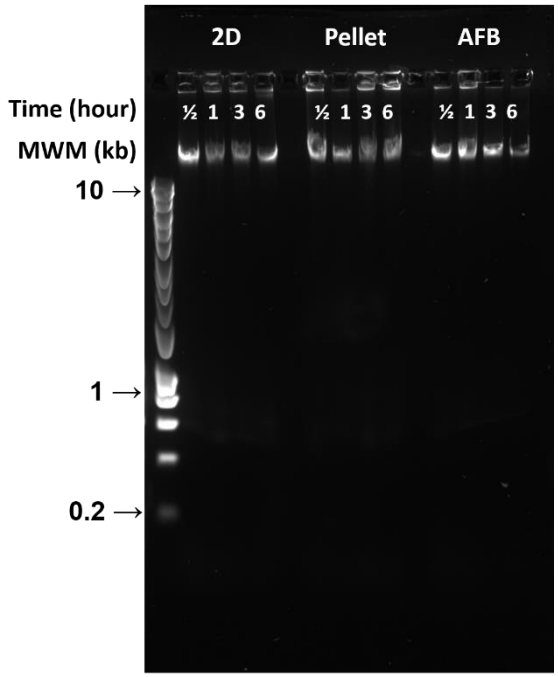

Figure 107 - DNA fragmentation assay of Huh7 DNA loaded in 1% agarose gel with different culture systems and time (representative image of 3 experiments). HyperLadder™ 1kb molecular weight marker (MWM) was indicated.

Huh7 DNA is intact for each trials, showing that the AFB, as the other technique does not remarkably show any apoptotic DNA degradation. This confirm again the AFB as a viable cell culture technique.

6.7 Hepatoma functions

Hepatocytes have a wide range of function in the body, they synthetize proteins, cholesterol and other molecule. They detoxify the blood stream. They do these tasks they generate a myriads of different molecule, all of them having their function.

The cell functionality is linked to its ability to create these molecules, the functionality of cell grew in levitation is investigate in this chapter and compared to the functionality resulting in other technique of cell culture.

6.7.1 Albumin and urea

Albumin is a water soluble protein generated by the liver and very common in the blood plasma. This proteins transport others molecules in the bloodstream such as fatty acids, hormones etc...

Urea serves an important role in the metabolism of compounds containing nitrogen.

6.7.1.1 Method

In this section, the AFB aggregates are compared to 2D technique cultured ones in petri dish and with pellet cultured ones in a conical tubes and by centrifuge them at 200g for five minutes.

The concentration of urea and albumin was quantified in the supernatant (the medium in which the cells grew) using the the ELISA DuoSET® kit for human albumin (R&D Systems, Oxfordshire, UK) according to the manufacturer's instructions. The urea method of measurement was taken from (20). Shortly, urea reagent mix with working concentrations of [100 mg L-1 o-phthalaldehyde, 513 mg L-1 primaquine bisphosphate, 2.5 mol.L-1 sulfuric acid, 2.5 g.L-1 boric acid, and 0.03% Brij-35] was prepared. In a volume of 200 µl freshly prepared reagent mix was added to 50 µl samples or standard (QuantiChrom, BioAssay Systems, Hayward, CA). Following 1 hour incubation at room temperature, absorbance at 430 nm was measured in a SpectraMax® Plus 384 Microplate Reader (Molecular Devices, Wokingham, UK). Concentration of urea of the sample against 5 mg.dL-1 standard was calculated in mg.dL-1.

6.7.1.2 Result on albumin

An increase in albumin production is measured in the supernatant of cell cultured in the acoustic bioreactor. Its concentration is 11.02 ± SEM 2.18 ng.ml^{-1} after 6 hours of levitation, which is close to double concentration after 30 minutes in the trap with a mean of 2.24 ± SEM 0.79 ng.ml^{-1}. The trend is similar for cells grew as 2D monolayer in standard petri dish, with a mean of 5.62 ± SEM 0.85 ng.ml^{-1} after 3 hours and 11.48 ± SEM 0.87 ng.ml^{-1} after 6 hours. The pellet cultured huh7 showed lower increase in albumin production, with a concentration of 4.67 ± SEM 0.91 ng.ml^{-1} after 3 hours and 6.74 ± SEM 0.434 ng.ml^{-1} after 6 hours.

Cell culture in AFB showed greater production in albumin compared to pelleted aggregates, and even greater production than 2D monolayer during the first hour, as shown in Figure 108.a). This shows that the synthetic functions of huh7 are not altered by the AFB, moreover they seem to be improved.

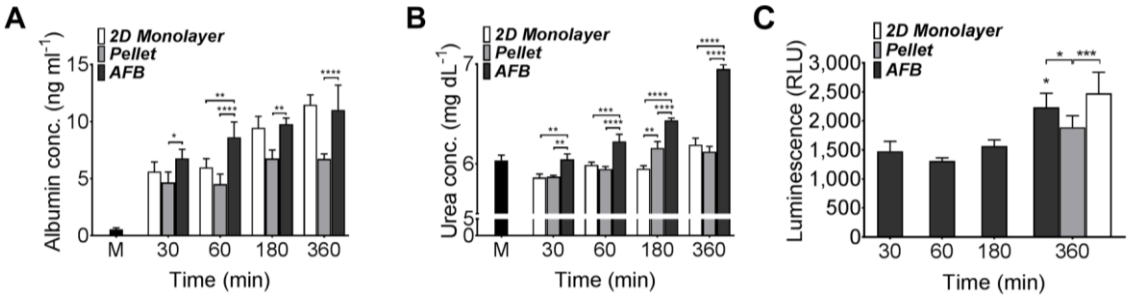

Figure 108-(A) Albumin concentrations (ng.ml^{-1}) and (B) Urea concentrations (mg dL$^{-1)}$ in supernatants from Huh7 cultured in 2D monolayer, pellet or AFB cultures with time course. n = 3. *P* values shown in the graph are for comparison to cells after 30 minutes between various cultures. (C) CYP3A4 activity in Huh7 cultured in AFB system with time course and following 6 h as 2D monolayer or pellet cultures. n = 3. *P* values shown in the graph are for comparison to cells after 30 minutes in AFB between various cultures. * *P*<0.05, ** *P*<0.005, *** *P*<0.0005, **** *P*<0.0001. Mean ± SEM. Two-way ANOVA followed by Fisher's LSD test. loaded in 1% agarose gel with different culture systems and time (representative image of 3 experiments). HyperLadder™ 1kb molecular weight marker (MWM) was indicated.

6.7.1.3 Results on urea

An comparatively important increase in urea concentration was measured in the supernatant of cells aggregated in AFB, indeed the secretion measured in the cell medium was 6.95 ± SEM 0.04 $mg.dL^{-1}$ following 6 hours compared to the measure after 30 minutes that was of 6.05 ± SEM 0.05 $mg.dL^{-1}$. In the case of 2D culture and pellet culture the increase in urea concentration were more limited, after 6 hours respectively a mean of 6.19 ± SEM 0.67 mg dL^{-1} and 6.12 ± SEM 0.05 mg dL^{-1} . All time concentration are given in Figure 108-b).

Urea production was found to be noticeably higher in cells cultured in AFB compared to 2D petri dish culture and pellet culture at all time, this prove the intactness of the metabolic function of the Huh7 under acoustic levitation condition.

6.7.2 CYP3A4

CYP3A4 is an important enzyme in the body produced by the liver. It oxidizes small foreign organic molecules, such as toxins or drugs, so that they can be removed from the body. It has the widest catalytic selectivity and responsible for the metabolism of about ~30 to 40 % of clinically used drugs [103].

Testing the production of huh7 is particularly interesting to validate AFB discoids as a model for drug toxicity.

6.7.2.1 Method

CYP3A4 activity in Huh7 in different cultures was measured using a P450-Glo(TM) CYP3A4 Assay (Luc-PFBE) Cell-Based/Biochemical luminescent assay (Promega UK Ltd, Southampton, UK) according to manufacturer's instructions. Briefly, Huh7 cells were cultured for various time periods in different culture

systems then basal CYP3A4 enzyme activity was assessed by incubating cells with luminogenic P450-Glo™ substrate (luciferin-PFBE, at final concentration of 50 µM) for 3 hours at room temperature. Produced luciferin was detected by incubating 25 µl of supernatant with an equal volume of Luciferin Detection in white opaque 96 well plate for 20 minutes at room temperature. Light was measured in a FLUOstar OPTIMA plate reader (BMG LABTECH, Ortenberg Germany).

6.7.2.2 Results on CYP3A4 investigation

The luminescence resulting from this method gives an insight on the concentration of CYP3Y4 for each of the culture method. The AFB, the 2D monolayer and the pellet culture. The luminescence are similar after six hours suggesting a comparable CYp3A4 activity in cells independently of the way they were cultured. After 6 hours of incubation the enzyme activity was markedly higher than after 30 minute of incubation, proving the enzyme vivid activity. As shown in Figure 108-c).

The AFB does not impact the CYP3A4 activity compared to other conventional cell culture method.

6.7.3 LDH

Lactate dehydrogenase (LDH or LD) is an enzyme found in nearly all living cells (animals, plants, and prokaryotes). LDH catalyzes the conversion of lactate to pyruvate in the liver.

6.7.3.1 Method

Equal volumes of 200mM Tris pH 8, 50 mM Lithium lactate, freshly prepared substrate solution [100µl P-Iodonitrotetrazolium Violet, INT (33mg ml^{-1} in DMSO) +

100µl, Phenazine methosulfate, PMS (9 mg ml^{-1}) + 2.3 ml β-NAD hydrate (3.74 mg ml^{-1})] and supernatants samples or positive control (5µg ml^{-1} L-Lactic Dehydrogenase from bovine heart) (Sigma) were loaded into an assay plate. The V_{max} was measured at 490nm for 10 min and LDH activity (U ml^{-1}) was calculated

This method will be used again in section 6.8, that investigate variousindicator of AFB cell aggregates reaction over 5FU anti-cancer cell.

6.7.3.2 Results

LDH activity are studied depending on 3 cell culture methods and 4 time points, 2D monolayer in petri dish, 3D pellet using a conical tubes and a centrifuge (200g). LDH activity in cells grew using these methods for 0.5, 1, 3 and 6 hours are reported below in Figure 109

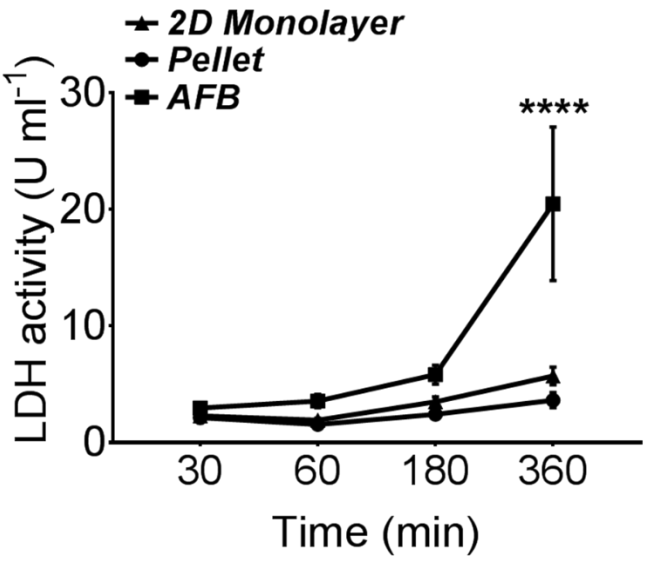

Figure 109 - Lactic Dehydrogenase (LDH) activity (U ml^{-1}) in supernatants from Huh7 cultures with time course. n = 3. *P* values shown in the graph are for comparison to between various cultures with time course (on top of bars). **** *P*<0.0001

The level of LDH activity is similar for all cell culture method up to 3 hours, at 6 hours the cells grew in levitation have significantly higher LDH activity. At 6 hours the 2D monolayer, the pellet and the AFB cell aggregate have respectively a mean of 5.71 ± SEM 0.75, 3.63 ± SEM 0.66 and 20.48 ± SEM 6.59 U ml^{-1} . This being the results of 3 experiment for each culture method.

This confirm the good function level of Huh7 grew in levitation using acoustic mode having lateral component.

6.8 Anti-cancer drug testing

Huh7 is a hepatocyte derived cellular carcinoma cell line. Carcinoma is a type of cancer that starts in organs cells, such as the liver. Like other types of cancer, carcinomas are abnormal cells that divide without control. They are able to spread to other parts of the body.

In the part, cell aggregated obtained with the 3 technique introduced earlier are treated with Fluorouracil, 5FU for short, it is a chemotherapy drug used to treat different cancers including liver carcinoma.

6.8.1 Cell Proliferation assay

Huh7 as other type of cancer cell, increase their number quickly, this is called cell proliferation, it is defined by the balance between cell divisions and cell loss through cell death or differentiation.

In order to study the Huh7 proliferation, the cells are grown in the 3 different culture systems and treated with 5FU (1, 10 and 100 µM) for 24, 48 and 72 h. Cell growth was determined using a colorimetric Quick Cell Proliferation Assay kit II (Abcam, Cambridge, UK) were used according to manufacturers' instructions. Briefly, lyophilized WST reagent was dissolved into 5 ml Electro Coupling Solution (ECS), aliquot the solution and store at -20°C. WST Solution in volume of 10 µl was

added to medium and cells were incubated in standard culture conditions for 3 hours. Absorbance was detected at 440 nm.

6.8.2 Results related to proliferation

5 Fluorouracil (5FU) is a cytostatic antimetabolite drug that has been reported to inhibit cell growth and induce apoptosis in Huh7 [104]. AFB generated Discoids were treated with varying concentrations of 5FU and compared to cells cultured as a 2D monolayer or pellet cultures.

In the first 24 hours of culture after anti-cancer treatment, the 2D monolayer pellet did not show viability decrease, however more than half of the active cells were lost when cultured in the AFB or as pellet. After this first day only small change in viability was noticeable using absorbance as shown in Figure 110-a)

The AFB aggregated cell showed a notable change in absorbance after 48 hours of 5FU treatment, with a decrease of a mean value of 7.90 ± SEM 2.20 % lower than untreated cells, as shown in Figure 110-d)

Pellet and 2D monolayer cultured aggregates showed higher lower level of absorbabce 48 hours of treatment, respectively a mean of 24.88 % ± SEM 4.76 and 14.71 % ± SEM 4.90 lower than untreated cells, as shown in Figure 110.b)&c).

After 72 hours of 5FU treatment at 100 µM, the aggregate resulted to acoustic levitation showed similar pattern of proliferation decline as aggregates obtained with 2D monolayer cell culture compared to untreated cells, with a respective mean of 8.86 % ± SEM 2.07 and 9.29% ± SEM 5.05. Pellet cell aggregates showed greater decrease in proliferation with a mean of 15.57% ± SEM 4.67 compared to untreated cells at the same conditions.

It is interesting to notice that after 48 hours of 5FU treatment the growth inhibition of Huh7 that grew in AFB was induced for lower concentration of anti-cancer drug compared to pellet's aggregate and higher compared to 2D monolayer's aggregates, respectively IC50 5.54, 19.79 and 1.96 µM, as shown in Figure 110-e)

At the opposite after 72 hours of 5FU treatment the growth inhibition of Huh7 that grew in AFB was induced for higher concentration of anti-cancer drug compared to pellet's aggregate and lower compared to 2D monolayer's aggregates, respectively IC50 4.29, 2.00 and 9.52 µM, Figure 110-f)

To determine whether the decreased in cell survival was caused by blunting of cell growth or cell death, further calcein-AM/PI viability and LDH activity assays were used and presented in section 6.8.3.

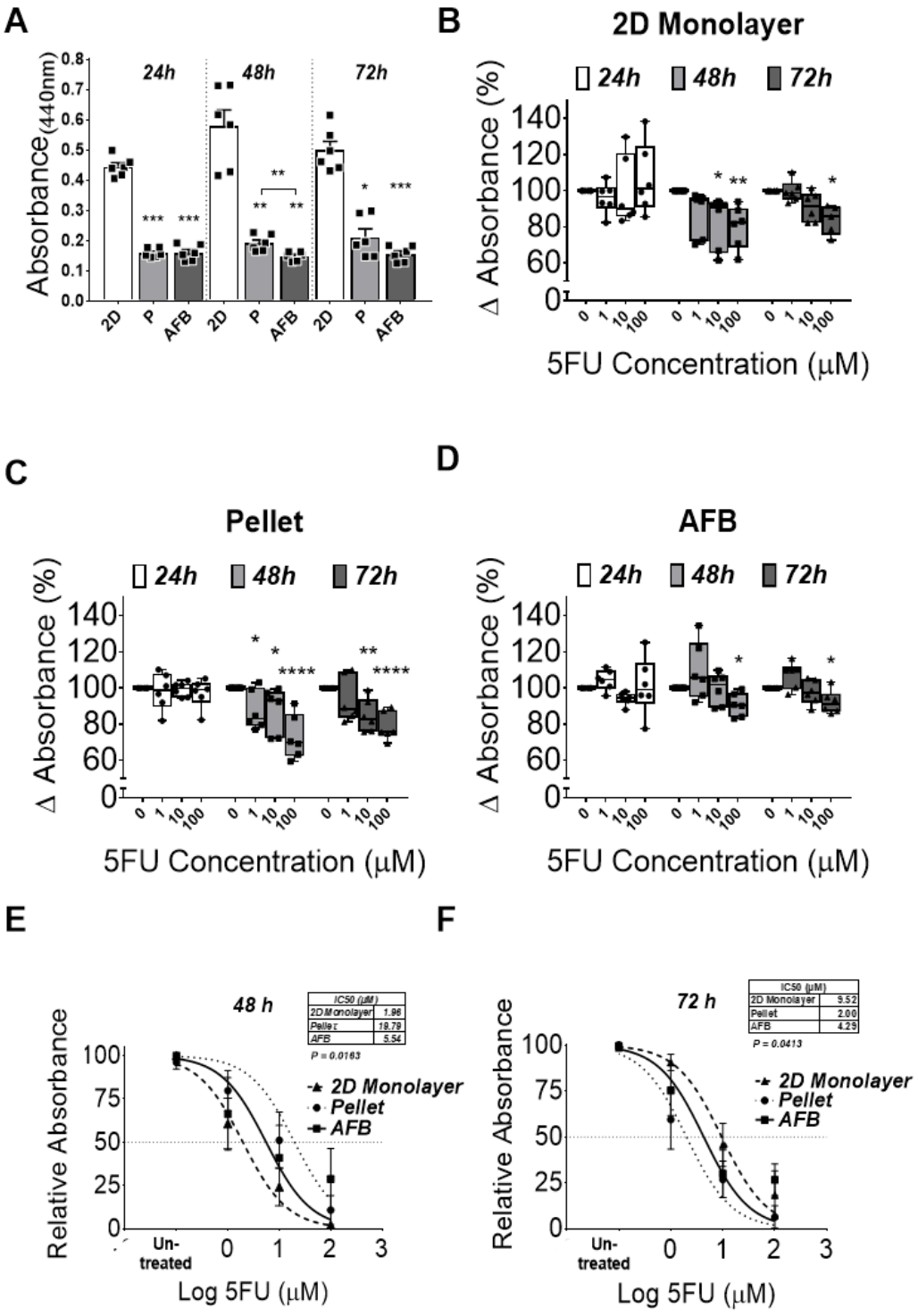

Figure 110 - Viability of Hhu-7 on various cell culutres (A) OR following treatment with various concentrations of 5 Fluorouracil (5FU) cultured in (B) 2D monolayer, (C) pellet or (D) AFB cultures with time course (expressed as difference from un-treated cells). n = 3. *P* values shown in the graph are for comparison to un-treated cells. (E and F) Inhibitory concentration 50 (IC50) of 5FU in various culture conditions following 4h or 72 h respectively. * *P*<0.05, ** *P*<0.005, *** *P*<0.0005, **** *P*<0.0001. Mean ± SEM. Two-way ANOVA followed by Fisher's LSD test.

6.8.3 Results related to viability, LDH activity and DNA fragmentation

To comprehend fully results of cell proliferation obtained in section 6.8.2, the viability, LDH activity and DNA fragmentation of cells aggregated using the different cell culture techniques are investigated in relation to 5FU drug treatment. The method used for viability test is introduced in 6.6.1, the LDH activity investigation is introduced in 6.7.3, the method for DNA fragmentation test was introduced in 6.6.4.

Cells aggregated treated with high concentration of 5FU during 72 hours showed visibly that aggregated cultured as 2D monolayer culture have a lesser death rate as the one cultured in discoids or pellet, as shown in Figure 111-a), meaning that as for the 2D monolayer the measurements in absorbance showed in Figure 110 were due to decrease in proliferation rate related to the drug treatment and not cell cytotoxicity.

The LDH activity measure in the supernatants englobing the cells demonstrated that for all level of 5FU treatment, the LDH activity of cell aggregated in AFB was greater than the ones cultured in 2D monolayer but lower than the one cultured in pellet, in the case of 100 µM of 5FU treatment, after 72 hours their respective level were 5.23 ± SEM 0.59, 4.39 ± SEM 0.47 and 6.40 ± SEM 0.97 $U.ml^{-1}$. This results suggest a difference in function of cells treated with 5FU depending on the cell culture technique.

Finally, apoptosis induction related to 5FU treatment in Huh7 was investigated by looking at their DNA fragmentation. The DNA of cell discoids obtained by AFB and cell 2D culture obtained in petri dish was observed after a concentration of 10^2 and 10^3 µM. The pellet's 3D aggregate showed stronger resistance against DNA fragmentation after treatment, it reacted only at high concentration (10^3 µM) of anti-cancer drug.

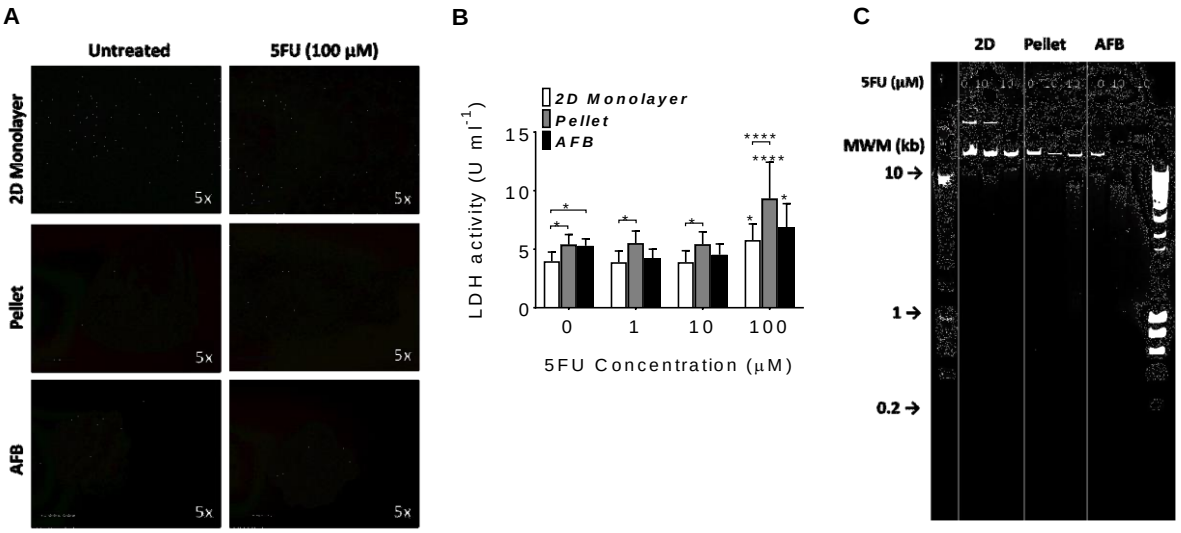

Figure 111-. (A) Live/dead staining of Huh7 cultured in 2D monolayer, pellet or AFB cultures 72 h following addition of 100 µM 5FU. Scale bar = 500 µm. (B) LDH (U ml^{-1}) release in supernatants from Huh7 cultured in various culture conditions 72 h following addition of 5FU. n = 3. *P* values shown in the graph are for comparison to untreated cells (on top of bars) or to cell in 2D monolayer culture. * *P*<0.05, ** *P*<0.005, *** *P*<0.0005, **** *P*<0.0001. Mean ± SEM. Two-way ANOVA followed by Fisher's LSD test. (C) DNA fragmentation assay of Huh7 DNA following treatment with 5FU loaded in 1% agarose gel with different culture systems (representative image of 3 experiments). HyperLadder™ 1kb molecular weight marker (MWM) was indicated.

6.9 Summary

A device was designed that levitated and agglomerated cells at an effective half-wave resonance excited by a frequency sweep centred close to 1.5 MHz. The device was designed to be thicker than many comparable structures, with a chamber height of 560 µm in order to allow for larger cell agglomerates.

The shape of the resulting cell discoids were found to depend primarily on seeding density, with typical dimensions 400x40 µm.

The influence of BAW cell aggregation technique on E-cadherin has been investigated. E-cadherin is an adhesion molecule driving the cell-cell aggregation

process, it is critical when aggregating particle without matrix. A substantial cleavage of E-cadherin following 3 hours of cell aggregation in levitation in the bioreactor. In 2D monolayer cell culture this cleavage happened earlier, just after 30 min. The E-cadherin promotes a calcium-dependent cell-cell adhesion. The importance of E-calherin was tested by adding EGTA (Calcium chelator) to the cell mix before injecting it in the cavity. This completely inhibit cell aggregation confirming the critical importance of E-cadherin for cell-cell aggregation without matrix.

The influence of this aggregation process on cell viability was investigated using Calcein AM and PI in both 2D monolayer and bioreactor. No marked difference in cell viability has been detected between the levitation culture and the more conventional 2D culture.

The synthetic and the metabolic functions of the Hu7 have been tested and compared to conventional petri dish 2D technique and 3D pellet cultures. Cell cultured in the bioreactor have shown a time dependent increase in albumin secretion, comparable to the one observed in 2D petri dish technique but distinctly higher than 3D pellet aggregate. As for Urea production in Huh7, cell aggregate obtained with acoustic levitation showed distinctively higher numbers as the ones obtained with other culture techniques. Finally, CYP3A4 activity measured in aggregate obtained with bioreactor and petri dish showed to be greater than in pellet cultured cells. The above functional characteristics showed that the levitated cells behaved in many ways closer to cells found in-vivo, supporting the technology as a basis for a screening and drug testing platform.

Finally, the reaction of the aggregate obtained using different cell culture method to fluorouracil (5FU), and anti-cancer drug, were investigated. Similar patterns of response were monitored between 2D monolayer and acoustic levitated aggregate, pellet culture showed to be responding to the drug only at high concentration of 5FU (1mM). This could be due to the morphology of aggregates in pellet culture which are spheroidal with relative high diameter (0.5mm) that could limit drug diffusion into the aggregate.

Finally, our findings demonstrate the system has the capacity to form viable, functional aggregates using BAW acoustic levitation, that are suitable as a model for drug toxicity screening

Chapter 7: Conclusion

7.1 Thesis review

The purpose of this project was to investigate, design, model, fabricate and test novel approaches for controlling lateral acoustic forces in the fluid cavity of BAW planar resonator.

Chapter 4 explored the sensitivity of acoustic modes to internal device parameters and geometry, including the sensitivity of the lateral energy gradient structure and magnitude. Using FEA multiphysics modelling, it showed that all the elements considered have a significant effect on the lateral force field. The complexity of the interdependent sensitivity made it difficult to draw clear conclusion or guidelines for a way to construct directly a planar resonator with strong (or weak) lateral force field. However, it showed that small changes in the structure can have large effects; it could be tentatively concluded that the transducer geometry seemed to be the most important element in relation of the lateral force field. This hypothesis was confirmed using PIV on fluorescent beads.

Chapter 5 investigated two novel strategies to control the lateral force field in a planar resonator excited at a half-wave frequency. Both techniques consist in adding an intermediate layer. The geometry of this layer directs the acoustic energy field in the cavity layer.

For static control, the first intermediate layer was composed of pillars of VeroClear a material 3D printed with high precision with air gaps between pillars and coupled to the manipulation cavity using glycerol. Modelling suggested optimum dimensions for layer thicknesses and pillar widths. Experimental results showed successful control. Strong acoustic streaming was also found that can disturb the agglomeration process, although agglomeration was achieved at higher acoustic energy.

For dynamic control, the second control layer consists of a channel containing a two-phase flow, composed of two acoustically different, immiscible fluids, driven by a syringe pump. Making this concept work was challenging because the channel design was constrained by both the acoustics (requiring a thick and wide channel), and the fluidic conditions for a stable two-phase flow (a thin and narrow channel produces better phase separation). Finally a balanced channel design was fabricated and particle transportation demonstrated using this method.

Finally in chapter 6, the knowledge acquired in chapter 4 was used to create a bioreactor with four identical planar resonators having strong lateral components. After process optimisation, the device was used to culture human liver cells (hu7) formed into multiple discoid shaped aggregates. The cells aggregate had this shape due to the balance between lateral and axial forces. Discoids obtained in this way were compared with cells cultured using conventional 2D monoculture and 3D spheroids from pellet culture. The investigation showed that the Bioreactor does not affect the cell viability, has a tendency to increase the cell functionality to be closer to in-vivo cells, and have comparable response to an anti-cancer drug. Thus this chapter demonstrates the suitability of the acoustic bioreactor for forming suitable cell structures for drug screening applications.

7.2 Main contribution

The main contributions that this research has achieved are listed below:

- I presented an in depth investigation into the complex relationship between design parameters and strength and structure of lateral components of acoustic modes in planar resonators. I used FEA to show that the even small changes in geometry can have large effect on the force magnitudes and structure of acoustic mode. This has been confirmed experimentally by changing transducer position and width and characterising the changed acoustic field over a range of positions and sizes. (Chapter 4)

• I came up with and investigated two novel strategies to control the acoustic radiation lateral force field in a planar resonator. Devices were designed, modelled, fabricated and characterized. In both case the principle is to introduce a structured layer between the transducer and the carrier. In the first one this structure is composed of static pillars, levitation occurs above the pillar. In the second one this layer is composed of a channel filled with two immiscible fluids, which when pumped through the channel, permits particle transport. (Chapter 5)

• I designed a bioreactor with modes having strong lateral components, to produce multiple huh7 discoids. The resulting discoids are compared to cell aggregates formed by 2D monoculture (petri dish) and pellet culture (centrifuge). Discoids formed in acoustic bioreactor showed to be suitable as a model for drug toxicity and screening. (Chapter 6)

7.3 Future work

Lateral forces in acoustic resonators will continue to be of interest and there are many avenues of research possible for better understanding, controlling and making use of them.

• By computational demands required to model 3D devices, more in depth modelling could extend the work of Chapter 3 and provide deeper insight into the importance of the geometric parameters and how they interact. In particular it would be useful to identify operating points in the parameter space (or other specific design features like the novel devices explored in this thesis), where there was less sensitivity to small variations to enable better control (either suppression, or intentional placement) of lateral forces.

• The thesis has demonstrated the feasibility of the device which used a static control layer to create multiple trapping locations in well-defined positions. Further work could explore the strong streaming patterns that are created, and seek to understand their origin, and either supress or control them. With this attended to a range of applications could be explored including more precisely controlled cell

trapping than that presented in Chapter 6. The streaming forces could also be harnessed to provide beneficial effects such as enhanced nutrient diffusion or cell stresses.

- Further characterization of the dynamically controlled planar resonator is necessary, with the potential to further enhance performance though more detailed design. Streaming flows in this device also need more investigation. With time, more detailed experiments could evaluate how quickly the trapped aggregates can follow the movement of droplets in the control channel. More complex channels shapes could also be investigated. Applications for this device might include bringing together cells of different types (e.g. liver cells and epithelial cells) for tissue engineering or more realistic tissue models, or using the shear stresses induced by the movement to induce cell differentiation or stimulate cartilage more effectively [82].

- The discoids of huh7 created by the bioreactor introduced in chapter 6 have been shown to be a promising drug testing model. To take this work forward, it would be necessary to address ways of scaling up the production of discoids, and ensuring that the automated process was reliable and uniform. More work could be done to explore factors affecting discoid shape, and the effect this has on viability, functionality and drug response.

Appendix A Acoustically modulated biomedical stimulation for human cartilage tissue engineering

Lab on a Chip

PAPER

View Article Online
View Journal | View Issue

Check for updates

Cite this: *Lab Chip*, 2018, **18**, 473

Acoustically modulated biomechanical stimulation for human cartilage tissue engineering†‡

Umesh S. Jonnalagadda, [a] Martyn Hill, [a] Walid Messaoudi,[a] Richard B. Cook,[a] Richard O. C. Oreffo, [b] Peter Glynne-Jones *[a] and Rahul S. Tare *[ab]

Received 9th November 2017,
Accepted 20th November 2017

DOI: 10.1039/c7lc01195d

rsc.li/loc

Bioacoustofluidics can be used to trap and levitate cells within a fluid channel, thereby facilitating scaffold-free tissue engineering in a 3D environment. In the present study, we have designed and characterised an acoustofluidic bioreactor platform, which applies acoustic forces to mechanically stimulate aggregates of human articular chondrocytes in long-term levitated culture. By varying the acoustic parameters (amplitude, frequency sweep, and sweep repetition rate), cells were stimulated by oscillatory fluid shear stresses, which were dynamically modulated at different sweep repetition rates (1–50 Hz). Furthermore, in combination with appropriate biochemical cues, the acoustic stimulation was tuned to engineer human cartilage constructs with structural and mechanical properties comparable to those of native human cartilage, as assessed by immunohistology and nano-indentation, respectively. The findings of this study demonstrate the capability of acoustofluidics to provide a tuneable biomechanical force for the culture and development of hyaline-like human cartilage constructs *in vitro*.

Open Access Article. Published on 04 January 2018. Downloaded on 12/18/2018 5:21:18 AM.
This article is licensed under a Creative Commons Attribution 3.0 Unported Licence.

Articular cartilage is a highly specialized form of hyaline cartilage that functions as a low-friction surface to allow for smooth articulation of the joints.[1] Given the avascular nature of the tissue and low mitotic activity of the resident chondrocytes, adult articular cartilage exhibits a limited capacity for self-repair. There are currently no effective pharmacological agents to promote comprehensive healing of articular cartilage defects and while surgical treatments, such as autologous chondrocyte implantation and microfracture, provide temporary relief to patients, these approaches are unable to restore the functionality of the damaged tissue over the long term.[2,3] To this end, tissue engineering has been employed to generate functionally relevant, hyaline-like cartilage grafts.

Tissue engineering aims to repair, replace, maintain, or enhance native host tissue.[4,5] These goals are typically accomplished through the *in vitro* culture of cells, supported by the application of appropriate biochemical/biomechanical cues, scaffolds/biomaterials, and bioreactor/culture systems to generate 3-dimensional (3D) tissue constructs for the eventual implantation into patients. To date, several groups have shown promising results in developing skeletal tissue structures, such as bone[6–11] and cartilage.[6,10,12–16] In the field of cartilage bioengineering, research has included the application of a variety of modalities, including pellet culture,[17] deposition printers,[10,18–20] micro-scale bioreactors[21] and stackable cell sheets.[22,23]

Literature has highlighted the importance of the physiochemical environment in promoting robust cartilage generation.[24,25] Mechanical stimulation using hydrostatic loads and cell stretching, among other forces, have been applied to activate mechanotransduction pathways and promote chondrogenesis in cells.[26,27] Dynamic stimulation (*e.g.* cyclic shear or dynamic compression) of the cells has been shown to result in the generation of more robust cartilage, compared to stimulation of cells with static forces.[26] Furthermore, mechanical stimulation of chondrocytes results in the secretion of parathyroid hormone-related protein (PTHrP), a chemical factor that has been found to aid chondrogenesis and reduce hypertrophy.[28–30] Thus, there is clear evidence that biomechanical stimulation of chondrocytes promotes chondrogenesis.

In recent years, cell-environment responses and phenotypic changes have been investigated in the field of bioacoustofluidics using ultrasonic standing wave fields. Ultrasonic standing wave fields, or acoustic traps, have been applied to induce patterning, alignment, and clustering of cells using either bulk acoustic waves (BAWs),[31–35] or surface

[a] *Mechanical Engineering, Faculty of Engineering and the Environment, University of Southampton, Southampton SO17 1 BJ, UK.*
E-mail: P.Glynne-Jones@soton.ac.uk; Tel: +44 (0)23 8059 5769
[b] *Centre for Human Development, Stem Cells and Regeneration, Institute of Developmental Sciences, Faculty of Medicine, University of Southampton, Southampton SO16 6YD, UK. E-mail: R.Tare@soton.ac.uk; Tel: +44 (0)23 8120 5257*

† **Data availability.** Data supporting this study are openly available from the University of Southampton repository (DOI: 10.5258/SOTON/D0002).

‡ Electronic supplementary information (ESI) available. See DOI: 10.1039/c7lc01195d

Open Access Article. Published on 04 January 2018. Downloaded on 12/18/2018 5:21:18 AM.
This article is licensed under a Creative Commons Attribution 3.0 Unported Licence.

acoustic waves (SAWs)[36,37] within micro-channels. Recent literature has described a number of configurations of both SAW[37,38] and BAW[14,32] based traps for cell manipulation, and preliminary findings have shown their ability to engineer functional hepatocyte and neuronal aggregates using scaffold-based and scaffold-free methodologies.[39,40]

BAW manipulation typically occurs within a layered resonator,[41] where a piezoelectric transducer is coupled to a chamber. The transducer creates a standing wave field within the fluid space of the chamber, within which an energy gradient subjects cells to acoustic radiation forces. As cells are introduced into the wave field, primary radiation forces direct the cells to a region of low acoustic potential energy, the pressure node. Variations of acoustic velocity amplitude within the pressure node,[42] along with intercellular attraction due to Bjerknes forces,[43] draw the cells into a levitated aggregate.

In the current study, we have used an acoustic trap to aggregate cells and by modifying the ultrasonic field we have generated time-varying radiation forces and drag forces on the cell aggregates. A number of groups have suggested that similar acoustically generated forces can affect cells and matrix proteins within the field.[14,31,44,45] The repeated displacement of the cells introduces mechanical stimulation in the form of fluid shear stress and this has the potential to alter the development of cartilage tissue within a scaffold-free environment. To date, however, investigation of scaffold-free tissue culture *via* bioacoustofluidics has been limited and little is known concerning the exploitation of the acoustic environment to maximise the potential of this approach.

Previously, we have demonstrated the potential of acoustic trapping for scaffold-free development of hyaline-like cartilage constructs,[14] by means of the long-term levitation of chondrocytes within an acoustofluidic bioreactor coupled with perfusion-based media exchange. The acoustic trap overcame some of the issues associated with conventional static pellet culture, specifically the lack of mechanical stimulation, inefficient oxygen diffusion and suboptimal metabolite mass transfer rates that adversely affect the scale-up, quality (*i.e.* formation of fibrous *versus* hyaline cartilage) and biomechanical properties of the cartilaginous constructs.[46] However, the contribution of different aspects of the acoustic environment to enhanced cartilage production remained unclear, and the closed fluidic loop had significant problems relating to bubble generation.

Here, we present a second-generation *open* design (*i.e.* a design with a free fluid surface adjacent to each resonant cavity) that has the advantages of immunity from bubble buildup, easy cell injection, parallelized throughput, and the potential for scaling to larger construct sizes. Crucially, we identify sources of mechanical stimulation created in our bioreactor, and demonstrate that these forces can be electronically modulated to produce human cartilage with improved physical properties. The combination of this acoustically induced mechanical stimulation and the growth factor PTHrP has been investigated and found to promote robust cartilage development.

Results

An open layered resonator configuration was adopted as shown in Fig. 1. The device comprises of a number of acoustically resonant cavities which are actuated by piezoelectric transducers situated below each one. Cells are introduced into the open-sided cavities using a gel-loading pipette. Acoustic levitation holds cells at the pressure node of the acoustic resonances and also brings the cells together laterally into a number of discrete aggregates within the resonator. Cells are drawn to the areas of high kinetic energy density modelled in Fig. 1C (more detailed information on the acoustic design can be found in the ESI†). The open design enables free exchange of gases to the environment (alleviating the problems with bubbles found in our previous work). Characterization of the resonators, including the reproducibility of their assembly, is discussed in the ESI† (S1).

The acousto-mechanical culture environment

Sweeping over a range of frequencies, as opposed to driving at a single frequency, has been used in acoustofluidics to create a time-averaged field containing contributions from a number of resonant modes,[47–49] to effect particle transport[50] or simply to ensure a mode was excited even if its precise centre frequency was unknown.[14] In this work however, frequency sweeping is found to modify the mechanical environment experienced by the cell constructs by dynamically moving them over the course of a sweep. It is shown that by making small variations to the electrical driving frequency around the acoustic resonance the acoustic force field changes, resulting in displacement of the aggregation positions of the cells laterally. Thus, by periodically varying this frequency (using a linear frequency sweep: variations of ±100 kHz at sweep repetition rates of up to 50 Hz), the aggregates vibrate backwards and forwards, inducing fluidic shear and deformational stress on the cell aggregates. In this manuscript, we use the term *sweep repetition rate* to denote how often the sequence of applied frequencies is cycled through, exploring a range of 1–50 Hz. This corresponds to the observable frequency of lateral vibration of the aggregates. It is important to note that the cells will be exposed to both the lateral, cyclic oscillations from the frequency sweep and to constant fluid flux as a result of acoustic streaming within the wave field, but the magnitude of the stresses due to the movement of the aggregate is found to be more than an order of magnitude higher than the streaming-induced stresses. As the cells are trapped at the pressure node of a standing wave, they do not experience pressure variations from the acoustic field, however as this is also the velocity antinode, density difference between the cells and the media leads to MHz frequency shear on the cells due to the acoustic excitation itself. This does not change significantly under the different driving conditions, hence is considered a constant throughout the different cell culture investigations. We also note that studies over shorter timescales have shown

 This journal is © The Royal Society of Chemistry 2018

Open Access Article. Published on 04 January 2018. Downloaded on 12/18/2018 5:21:18 AM.
This article is licensed under a Creative Commons Attribution 3.0 Unported Licence.

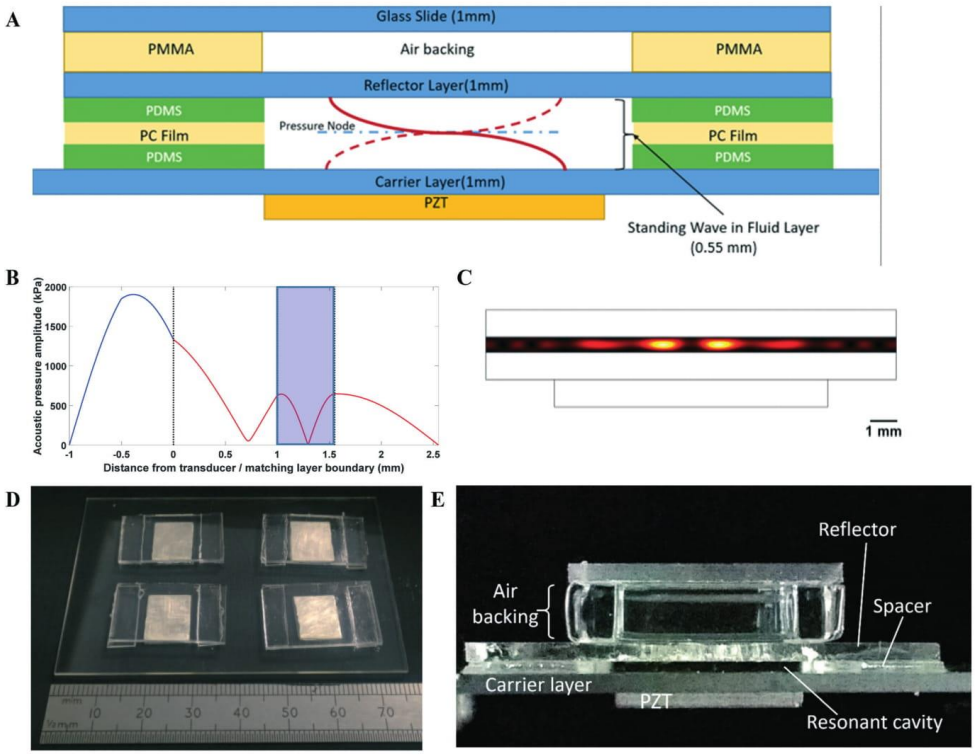

Fig. 1 Bioreactor design and modelling. (A) Schematic diagram detailing resonator design and the dimensions of each layer. (B) A 1-dimensional model was used to confirm cavity resonance frequency and the presence of a pressure node near the centre of the fluid cavity (blue region) for the desired resonator configuration. (C) The transfer impedance model was further validated with a FE model to determine the kinetic energy distribution at resonance, in order to better predict the energy distribution within the pressure node and where the cells are likely to levitate. (D) Angled top view of assembled plate to detail arrangement of multiple resonators on a single double-width glass slide. (E) Side view of assembled resonator, labelled to indicate position of PZT, spacers, carrier and reflector layers. The open sides of the resonant cavity allow for medium exchange within the cavity and alleviate problems with bubble formation experienced with previous closed resonator designs.

minimal bio-effect from the MHz shear stresses induced by levitation fields of comparable magnitude.[51]

As the frequency varies during each sweep, both the lateral acoustic forces and associated trapping positions change, so the relationship between the input frequency and the construct response would not be expected to be a linear one. Essentially, the aggregate is sequentially attracted to a number of trapping locations during the period of a sweep. Thus, it is observed that the construct movement and the associated mechanical stresses have frequency components of a higher order than the sweep repetition rate. The magnitude of the shear stresses on the cells varies with both the sweep repetition rate and the amplitude of the driving waveform as discussed below.

To assess the quality of the hyaline-like cartilage produced in the bioreactor, the chondrocytes were cultured for an extended period to allow for maturation of the cells and expression of key chondrogenic markers.[52,53] A culture period of 21 days under continuous acoustic excitation within the bioreactor was therefore used throughout the work. In the initial phase of cell culture within the bioreactor (typically around 14 days), aggregates were levitated with no contact with the resonator walls, and we hypothesize that the primary source of stress on the cells at this time is from the lateral oscillations. During the culture period beyond 14 days, the aggregates typically grew to a point at which the aggregates were in contact with the resonator walls and ceased to move freely. Throughout this phase the acoustic forces are more likely to induce deformational stresses, however we only quantify the fluid-shear derived forces in this paper.

Perfusion and acoustic streaming flows. Acoustic streaming is the mean flow induced in a fluid due to absorption of

Open Access Article. Published on 04 January 2018. Downloaded on 12/18/2018 5:21:18 AM.
This article is licensed under a Creative Commons Attribution 3.0 Unported Licence.

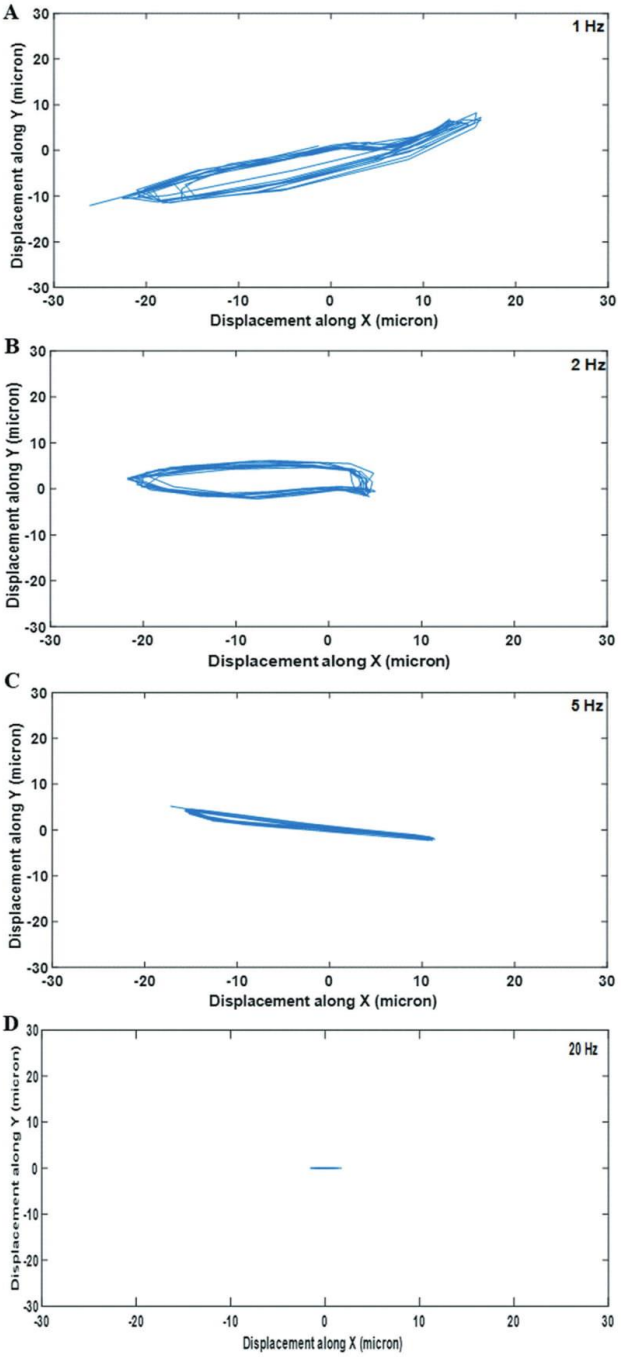

Fig. 2 Measuring cell displacement during acoustic stimulation to calculate induced stresses. Cell aggregates were subjected to varying cyclic stimulation regimes (A: 1 Hz; B: 2 Hz; C: 5 Hz; D: 20 Hz). The acoustic forces drag the aggregates through the fluid along the paths shown here. This data is later fed into a model to calculate the shear stresses experienced by the aggregates as they move. The displacement amplitude and path were found to vary with the sweep repetition rate (values inset in each graph). The sweep range was 200 kHz, voltage amplitude 10 V_{pp}.

 This journal is © The Royal Society of Chemistry 2018

Open Access Article. Published on 04 January 2018. Downloaded on 12/18/2018 5:21:18 AM.
This article is licensed under a Creative Commons Attribution 3.0 Unported Licence.

acoustic energy.[54,55] In the present study, boundary driven transducer-plane streaming is observed, which results from acoustic energy dissipated at the device walls.[56,57] Motion of the media due to acoustic streaming, coupled with block media changes, provide the perfusion for the cell aggregates in contrast to the previously reported system[14] which relied on the pumping of media. Streaming velocities are expected to be independent of the sweep repetition rate,[58] and in our system are measured to be of the order of 2 μm s^{-1}. The shear stresses on the cell aggregates resulting from these streaming flows are of the order of 13 μPa. These continuous stresses will be applied to the aggregates in addition to the larger time-varying stresses derived from the periodic lateral movement discussed below. It is important to note that the average acoustic energy entering the system is independent of the sweep repetition rate, hence other acoustic energy effects on cells (such as heating) will also be independent of this.

Quantifying and modulating aggregate displacement and fluidic shear stresses. To quantify how the acoustic driving parameters modulate fluidic shear stresses, the paths traced out by the cell aggregates in levitation were imaged. Fig. 2 shows example paths. It was observed that the sweep repetition rate affected the shape of the path followed by the cell aggregate (Fig. 2), and the size of the area traced out. Higher sweep repetition rates displayed reduced lateral displacement of the cells, with 20 Hz displaying virtually no measurable displacement. We deduce that for the parameters explored, the aggregates are in dynamic motion, limited by viscous drag. Essentially, at higher rates the aggregates have less time to move significantly before being redirected towards another location.

In the ESI† (S2), we describe a finite element model used to estimate the fluidic shear stresses induced by the experimentally observed aggregate motion. The time-varying shear stress is plotted in Fig. 3A, and presents a steady, periodic waveform. Given the cyclic nature of the stress and the complex two-dimensional pattern of the cell aggregate movement we choose to extract the peak-to-peak value of the stress waveform for subsequent comparison. The relationship between sweep repetition rate and shear stress is presented in Fig. 3B, which shows relatively high shear stresses between 2 and 10 Hz, but with significantly reduced stresses at the higher sweep repetition rates of 20 and 50 Hz. Further detailed examination of the role of driving voltage and repeatability (at 2 Hz) is shown in Fig. 3C – increased voltage leads to increased shear stresses, related to the expected squared dependence of acoustic forces on driving voltage.

As a result, control of both the sweep repetition rate and the driving voltage enable the system to be programmed to deliver a specific frequency and amplitude of mechanical stimulation to the cells over the course of the culture period. In order to investigate the effect of sweep repetition rate on cartilage formation, two frequencies were chosen. A lower frequency, high peak stress (example of 2 Hz), which is within the range of frequencies often chosen for conventional dynamic compression,[59,60] and a higher frequency, low peak stress (example of 50 Hz), which corresponds to the frequency used in our earlier study.[14]

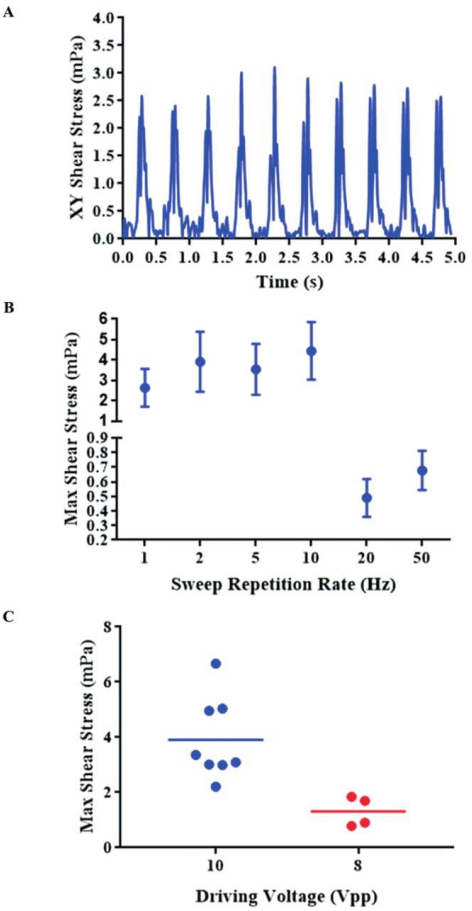

Fig. 3 Shear stress profiles of cells under different driving parameters: fluidic shear was calculated by applying measured aggregate displacements to an FE model. (A) The magnitude of the fluidic shear experienced by the aggregate shown in Fig. 2B (2 Hz sweep repetition rate). (B) Maximum shear stresses calculated for different sweep repetition rates and a driving voltage of 10 V_{pp} (n = 7–8, data shown as mean ± SD). (C) Maximum shear stress at different driving voltages (n = 4 for 8 V_{pp}, n = 8 for 10 V_{pp}) showing mean as a horizontal bar. The sweep frequency range is 200 kHz in all cases.

Biological response to physicochemical environment within acoustic trap

The role of the physicochemical environment within the acoustic trap in stimulating cartilage development was

Open Access Article. Published on 04 January 2018. Downloaded on 12/18/2018 5:21:18 AM.
This article is licensed under a Creative Commons Attribution 3.0 Unported Licence.

assessed at different sweep repetition rates at constant drive voltage. The mechanical stimulation regime that promoted cartilage formation was then supplemented with the growth factor, PTHrP, to examine whether this provided additional chemical cues in combination with mechanical stimulation for improved hyaline-like cartilage formation. Considering the qualitative nature of histochemical staining, semi-quantification of the staining of 50 Hz, 2 Hz, and 2 Hz + PTHrP constructs was performed by image segmentation (Fig. S7†) to approximate the matrix staining fraction relative to the total tissue section area. As the desired tissue is hyaline-like cartilage, the tissue quality was evaluated by the matrix composition of proteoglycans (Alcian blue staining) and collagen Type-II immunostaining. The relative staining fractions for these markers were then compared against collagen Type-I (marker for fibrocartilage) and collagen Type-X (marker for hypertrophic cartilage).

21 day culture of human articular chondrocyte (HAC) aggregates in presence of varying sweep repetition rates. HAC aggregates were cultured for 21 days in the acoustic traps using either a sweep repetition rate of 50 Hz (Fig. 4A, Fig. S2 and S8A†) or 2 Hz (Fig. 4B, Fig. S3 and S8B†) and the resulting 3-D tissue constructs were harvested for histological and immunohistochemical analyses to assess cartilage formation.

Day-21 constructs generated in the bioreactor in response to a sweep repetition rate of 50 Hz (Fig. 4A, Fig. S4 and S8A†) were compact in size (cross-sectional area of 0.343 mm^2 ±

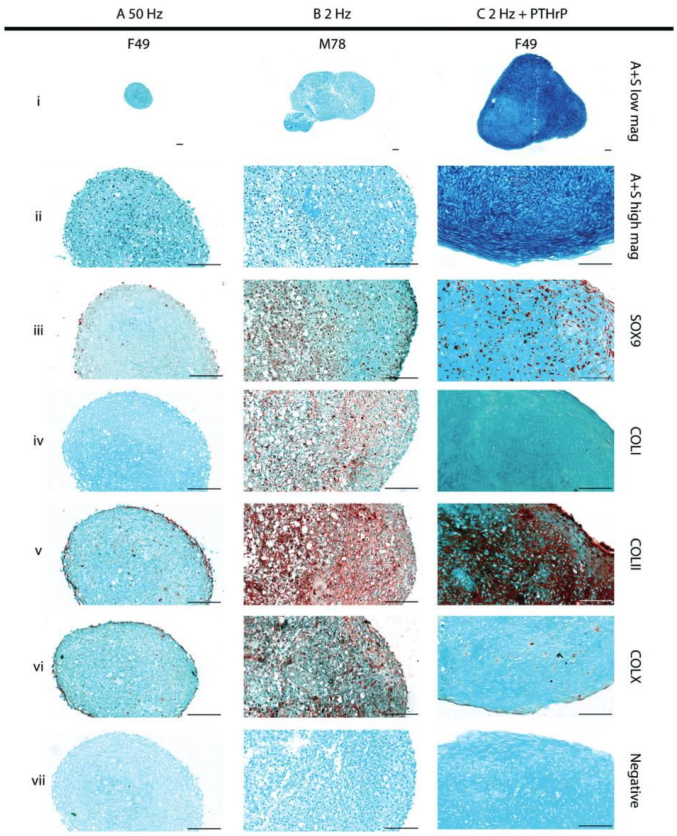

Fig. 4 Histological analyses of cartilage constructs engineered under different physicochemical environments. 21 day cartilage constructs engineered in resonators at (A) 50 Hz, (B) 2 Hz and (C) 2 Hz in combination with 10 ng ml^{-1} PTHrP supplementation. Alcian blue + Sirius red (A + S, i and ii) staining was performed on sections of the cartilage constructs to assess the histological structure, while formation of hyaline-like cartilage was confirmed by robust immunostaining for SOX-9 (iii) and Type II collagen (COLII, v), and negligible immunostaining for collagens Type I (COLI, iv) and Type X (COLX, vi). No staining was observed in the negative controls (omission of the primary antisera, vii) included in all immunostaining procedures. Tissue sections were selected from a representative set of (A) three patients and (B and C) four patients. Scale bars = 100 μm.

 This journal is © The Royal Society of Chemistry 2018

Open Access Article. Published on 04 January 2018. Downloaded on 12/18/2018 5:21:18 AM.
This article is licensed under a Creative Commons Attribution 3.0 Unported Licence.

0.235 across all patients) and appeared as aggregates of cells held together by extracellular matrix, composed largely of proteoglycans evidenced by Alcian blue staining (Fig. 4Ai and ii, Fig. S2i and ii and S8Ai†). The constructs exhibited minimal expression of the chondrogenic proteins, namely SOX-9 (Fig. 4Aiii, Fig. S2iii and S8Aii†) and Type-II collagen (COLII) (Fig. 4Av, Fig. S2v and S8Aiv†), coupled with minimal immunostaining for collagens Type-I (COLI) and Type-X (COL X) (Fig. 4Aiv and vi; Fig. S2iv and vi and S8Aiii and v,† respectively).

In contrast, day 21 constructs generated in the bioreactor in response to a sweep repetition rate of 2 Hz (Fig. 4B, Fig. S3 and S8B†) were consistently larger in size (cross-sectional area of 0.878 mm^2 ± 0.353 across all patients). Most cells in the cartilaginous constructs were located within distinct lacunae embedded in the Alcian blue-stained, proteoglycan-rich extracellular matrix (Fig. 4Bi and ii). Moreover, robust expression for SOX-9 and COLII were observed in the cells and the surrounding extracellular matrix, respectively (Fig. 4Biii and v; Fig. S3iii and v and S8Bii and iv†). However, it was possible to detect distinct immunostaining for COLI and COLX in the extracellular matrix of the cartilaginous constructs (Fig. 4Biv and vi; Fig. S3iv and vi and S8Biii and v†).

21 day culture of HAC aggregates in the bioreactor supplemented with PTHrP. To assess the possibility of further enhancing cartilage formation in the constructs, chondrocyte aggregates stimulated with a sweep repetition rate regime of 2 Hz for three weeks in the bioreactor were cultured in chondrogenic medium supplemented with PTHrP from day 10 to day 21 (*i.e.* 2 Hz + PTHrP regime). Day-21 constructs generated using these culture conditions (Fig. 4C, Fig. S4 and S8C†) were appreciably larger in size (cross-sectional area of 1.45 mm^2 ± 0.804 across all patients) compared to constructs generated in response to sweep repetition rates of 50 Hz and 2 Hz without the supplementation of PTHrP. The tissue generated within the constructs was reminiscent of native hyaline cartilage and was composed of numerous chondrocytes, characterized by the expression of SOX-9, located within distinct lacunae embedded in dense extracellular matrix constituted by Alcian blue-stained proteoglycans and abundant COLII (Fig. 4Ci–iii and v; Fig. S4i–iii and v and S8C i–ii and iv†). Furthermore, expression of COLI was markedly reduced in the cartilaginous constructs and restricted to the peripheral layer of the constructs (Fig. 4Civ; Fig. S4iv and S8Ciii†). Due to the inhibitory effect of PTHrP on chondrocyte hypertrophy, negligible expression of COLX was observed in the extracellular matrix of the cartilaginous constructs (Fig. 4Cvi; Fig. S4vi and S8Cv†). This, coupled with the marked absence of the two hypertrophic markers, namely osteopontin (OPN) and alkaline phosphatase (ALP), confirmed that the culture regime prevented terminal differentiation of the chondrocytes within the hyaline-like cartilage constructs (Fig. S5†). Nano-indentation showed that the mean (± SD) elastic modulus (187 ± 23 kPa) of the human cartilage constructs engineered using the 2 Hz + PTHrP regime was comparable to the average elastic modulus (200 ± 63 kPa) of native human articular cartilage (Fig. 5).

Discussion

In the present study, we have designed a novel acoustofluidic bioreactor system for the culture of HAC aggregates in levitation to generate 3D, hyaline-like cartilage. We have investigated and quantified how the fluidic shear stresses produced by the bioreactor could be modulated electronically, and assessed resulting differences in the quality of cartilage formation in the engineered constructs. We have shown that the ability to modulate the stresses provides the possibility of tuning the system to promote better cartilage formation.

The influence of the acoustically induced forces on cell and fluid displacement was quantified by particle tracking, following which computational modelling tools were used to estimate the magnitude of the fluid shear stress on the cells. Acoustic streaming allowed for nutrient exchange around the developing tissue in the place of bulk perfusion used in the first-generation acoustofluidic bioreactor.[14]

The stimulation created by oscillating the cell agglomerate laterally at a rate determined by the sweep repetition rate has a number of key advantages. Acoustic stimulation of cells has been reported to be complex and multifaceted, resulting in the repair, proliferation, and differentiation of numerous cell types.[61–63] It is a key feature of our method that the acoustic energy absorbed by the system (and hence any heating) is independent of the sweep repetition rate, providing a means to isolate the mechanical component of the resulting stimulation, as well as tailor it for specific goals. The contact-free nature of the stimulation is in contrast to contact-based methods which can reduce the surface area of the aggregate available for perfusion.[64] While it would be possible to design a bubble-resistant open system with shear induced by bulk perfusion, the current design allows for electronically controllable oscillatory shear at frequencies that would be more difficult to achieve in a bulk flow system. In addition, bulk perfusion requires that the levitated construct be held against

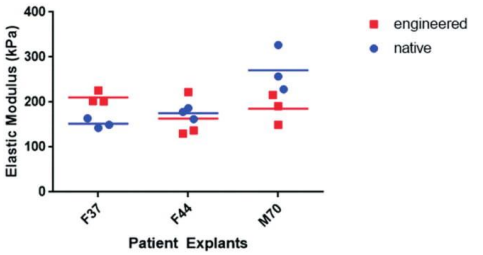

Fig. 5 Young's modulus of native human articular cartilage and 21 day cartilage constructs engineered in resonators at 2 Hz in combination with 10 ng ml^{-1} PTHrP. The elastic modulus of the engineered constructs was compared against native human articular cartilage using nano-indentation. Data acquired from three indentation points were used to determine the mean values for Young's/elastic moduli of engineered and native articular cartilage. Figure shows data distribution and the mean values as horizontal bars; n = 3 patients, namely F37, F44 and M70.

Open Access Article. Published on 04 January 2018. Downloaded on 12/18/2018 5:21:18 AM.
This article is licensed under a Creative Commons Attribution 3.0 Unported Licence.

the perfusion flow by the lateral acoustic radiation forces, limiting the magnitude of achievable flows.

The bio-effects of modulating the acoustic field on cartilage generation were determined by comprehensive immunohistological analyses of the cartilage constructs, generated as a result of 3-D, scaffold-free culture of HACs in the acoustofluidic bioreactor over a period of 21 days. This study found that a higher sweep rate (50 Hz), which produces lower shear stresses, resulted in sub-optimal formation of hyaline-like cartilage. In contrast, a 2 Hz regime resulted in the generation of cartilaginous constructs exhibiting regions of hyaline-like structure, characterized by robust SOX-9 and Type II collagen expression. However, the constructs were also characterized by the conspicuous presence of collagens Type I and Type X, normally expressed in fibrous and hypertrophic cartilage, respectively. This suggested that, although mechanical stimulation as a result of application of the sweep repetition rate of 2 Hz elicited a favorable chondrogenic response from the cells, further parameter optimization was necessary to promote the formation of robust hyaline-like cartilage and to minimize hypertrophy. Our previous study[14] demonstrated robust cell viability and negligible cell necrosis in day-21 cartilage constructs generated using the acoustofluidic bioreactor. Bazou *et al.*[51] also showed that the acoustic energy density required for levitation had no significant impact on hepatocyte viability over a period of hours, a conclusion supported by a separate study.[65] In this study, we have not assessed cell viability directly; it can be inferred that in constructs exhibiting robust cartilage production, cell viability will be good, however in constructs with suboptimal cartilage production we do not have data to point to the cause.

To improve cartilage formation, in addition to manipulating the mechanical environment, culture of the HAC aggregates within the acoustic field was investigated in the presence of PTHrP, a growth factor with defined roles in promoting chondrogenesis and inhibiting hypertrophy, especially in presence of mechanical stimulation.[28–30] Notably, 21 day constructs generated in the bioreactor in chondrogenic media supplemented with PTHrP, using a sweep repetition rate of 2 Hz were: i) appreciably larger in size, ii) exhibited distinct hyaline-like cartilage structure, iii) demonstrated robust expression of SOX-9 and Type II collagen, and, importantly, iv) displayed negligible expression of collagens Type I and Type X. Additionally, mechanical analysis of the cartilage tissue using nano-indentation showed the engineered human cartilage constructs to have stiffness similar to that of native human cartilage tissue.

With regard to literature concerning biomechanical stimulation, Schatti *et al.* implemented a parametric analysis study of compressive loading on chondrocytes and found that the rate of stimulation and magnitude of force affected the matrix composition of the tissue.[66] Correspondingly, we have examined and quantified the biomechanical stimulation applied by the acoustically derived periodic fluidic shear to aggregates, and shown how it can be modulated by varying the acoustic parameters. There are likely to be other interacting forces at play during the culture period, and further characterization of the interaction between the acoustic environment and the cells will be carried out in the future work, along with assessment of changes in chondrogenic gene expression in response to the acoustic environment. In summary our findings demonstrate the capability of acoustofluidics as a tuneable biomechanical force for the culture and development of hyaline-like human cartilage constructs *in vitro* and provide a new platform to investigate scaffold-free cartilage tissue engineering.

Materials and methods

All chemicals were purchased from Sigma-Aldrich UK and Invitrogen UK, unless stated otherwise.

Bioreactor design

A schematic of the resonator design is depicted in Fig. 1A. To fabricate the resonators, double-width glass slides (Corning, 75 × 50 × 1 mm) and standard microscope slides (Corning, 75 × 25 × 1 mm) were acid cleaned in a 6 M HCl solution for 3 hours. Double-width slides were washed in distilled water before adhesion to the piezoelectric transducers (Ferroperm PZ26, Kvistgaard, Denmark; 10 × 12 × 1 mm) with epoxy (Epoxy 353, Epotek, Billerica, MA, USA) at 80 °C for 1 hour. Four transducers were coupled to each double-width slide, which functioned as the carrier layer (Fig. 1D). Microscope slides were cut to 13 × 25 × 1 mm, which functioned as the reflector layer for the resonators. Polycarbonate film (500 micron Lexan, Cadillac Plastics) functioned as a spacer between the carrier and reflector and was coupled using PDMS (Dow Chemical Sylgard 182 1 : 10 curing agent : monomer). Fig. 1E depicts the assembled resonator. A laser cut poly(methyl methacrylate) (PMMA) spacer served to create an air cavity behind the reflector in conjunction with a second piece of glass of the same size as the reflector to maintain an air backing to the reflector layer. This air layer was important as it maintained the acoustic boundary conditions needed to excite the required half-wave resonance; without the seal provided by the spacer and the top glass layer, condensation of medium on top of the reflector was liable to change the boundary impedance. Polypropylene (5 mm, Aquarius Plastics) was cut to shape using a laser cutter and grooves were introduced into the top and bottom sheets using a micro-mill to fit the double-width glass slides and create a sealed environment to maintain a sterile culture environment (Fig. S6†).

Acoustic modelling and characterization

A 1D transfer impedance model[67] in MATLAB was used to guide the design and predict the acoustic pressure node configuration and resonant frequency of the system (Table 1 for summary of layer dimensions and sound velocities). The half-wave resonance was predicted at 1.49 MHz (Fig. 1B) and, experimentally, the resonant frequency of the various resonators was measured at 1.47–1.53 MHz from the electrical impedance spectra.

 This journal is © The Royal Society of Chemistry 2018

Open Access Article. Published on 04 January 2018. Downloaded on 12/18/2018 5:21:18 AM.
This article is licensed under a Creative Commons Attribution 3.0 Unported Licence.

Table 1 Table of parameters for 1D transfer impedance model and 2D FEM of resonator

Parameter name	Value/expression	Units
Transfer impedance model parameters		
Fluid layer thickness	550	μm
Carrier/reflector layer thickness	1000	μm
Piezoelectric transducer thickness	1000	μm
Adhesive layer thickness	1	μm
Density of carrier and reflector layer material	2500	kg m^{-3}
Density of fluid layer material	1000	kg m^{-3}
Density of adhesive layer	1080	kg m^{-3}
Speed of sound through adhesive layer	2640	m s^{-1}
Speed of sound through carrier and reflector layer	5872	m s^{-1}
Speed of sound through fluid layer	1540	m s^{-1}
Driving voltage	10	V_{pp}
Q-factor of layers	100	
COMSOL Model Parameters		
Fluid layer thickness	550	μm
Carrier/reflector/PZT dimensions (width × thickness)	10 × 1	mm
Speed of sound in fluid layer	1540	m s^{-1}

The voltage drop method was used to quantify the acoustic pressure generated within the resonators[68] (Fig. S1D†). A 2D finite element model based in "COMSOL multiphysics" was used to produce Fig. 1C. The model included piezoelectric coupling and pressure acoustics within the fluid layer, with sufficient mesh density that the fluid layer mesh was 16 elements thick (Table 1 for resonator model details). The acoustic radiation force was calculated using the Gor'kov equation[69] across a range of frequencies, enabling the resonant frequency to be identified.

An additional COMSOL finite element model was created to calculate the shear stress on a cell aggregate during levitation at a given sweep repetition rate. The lateral movement of cell aggregates was monitored using time lapse imaging at various driving voltages and sweep repetition rates. 16 frames were acquired for each frequency sweep, to ensure sufficient sampling (*i.e.* the frame rate for the 1 Hz sweep was 16 fps and 800 fps for 50 Hz). Sampling continued until 10 such cycles had been captured. The resulting time-lapse data was analyzed to track the path followed by the aggregates. For the lower frequency regimes, the displacement was estimated using image cross correlation. Pixel quantization error rendered this approach unreliable for the high frequency, low displacement frequency sweep rates of 20 and 50 Hz. In these cases velocities were estimated using particle image velocimetry. The observed aggregate lateral motion was then introduced into an FEM to simulate the shear stress on the cells (see ESI† S2 for full description of model and analysis).

Acoustic streaming characterization

Streaming flow velocities were measured using particle image velocimetry (PIV) as described in Zmijan *et al.*[70] 1 μm fluorescent polystyrene beads were used as tracers, imaging with a 10× objective at 400 ms frame intervals. Image data was analyzed *via* the MATLAB package MPIV[70] to quantify bead displacement and mean particle velocity between sequential frames. Following particle analysis, the median of each frame's particle velocities was established.

Isolation of human articular chondrocytes

HACs were isolated by sequential enzymatic digestion of deep-zone articular cartilage pieces dissected from the non-load-bearing region of the femoral heads.[71] Human femoral head samples were obtained from haematologically normal osteoarthritic patients (5 male, 7 female, mean age of 65) following routine total hip arthroplasty surgeries. Only tissue that would have been discarded was used in this study with approval of the Southampton and South West Hampshire Research Ethics Committee (Ref. 210/01). Pieces of deep-zone cartilage were dissected from the femoral heads and digested in 500 μg mL^{-1} trypsin-EDTA for 30 minutes at 37 °C and 5% CO_2. The tissue fragments were washed in PBS and incubated in 1 mg mL^{-1} hyaluronidase for 15 minutes at 37 °C and 5% CO_2. The resulting fragments were washed in PBS and then incubated in 10 mg mL^{-1} collagenase B (Roche Diagnostics 11088807001) overnight at 37 °C. The resulting cell suspension was filtered through a 70 μm sieve to remove undigested tissue/debris. Isolated chondrocytes were cultured to confluence in monolayer cultures in α-MEM supplemented with 10% (v/v) FBS, 100 unit per mL penicillin, 100 unit per mL streptomycin, and 100 μM ascorbate 2-phosphate. Cultures were maintained in humidified atmosphere at 37 °C, 5% CO_2 and 21% O_2. Passage 1 cells were utilized for the experiments.

ATDC5 cell culture

To probe the acoustic forces within the resonator (for the results shown in Fig. 2), immortalized murine chondrocytes, ATDC5 (Lonza), were used as a representative cell line. Monolayer cultures of murine chondrogenic ATDC5 cells were cultured in DMEM supplemented with 5% (v/v) FBS and 1× insulin-transferrin-selenium premix (ITS; insulin: 10 μg ml^{-1}; transferrin: 5.5 μg ml^{-1}; selenium: 5 ng ml^{-1}). Cultures were maintained in humidified atmosphere at 37 °C, 5% CO_2 and 21% O_2.

Bioreactor culture of human articular chondrocytes

The bioreactor was sterilized under UV light overnight prior to use. Monolayer cultured HACs were harvested at confluence and suspended in serum-free chondrogenic medium consisting of α-MEM supplemented with transforming growth factor-beta (10 ng mL^{-1}, TGF-β3, Peprotech 100-36E), 1× ITS, dexamethasone (10 nM, D4902), and L-ascorbate-2-phosphate (100 μM, A2P, A8960). Prior to cell insertion into the resonators, 9 mL of chondrogenic media was introduced into the bioreactor chamber, thereby fully immersing the resonators. Trapped air bubbles within the fluid layers of the

Open Access Article. Published on 04 January 2018. Downloaded on 12/18/2018 5:21:18 AM.
This article is licensed under a Creative Commons Attribution 3.0 Unported Licence.

resonators were removed and the function generator driving the bioreactor was enabled prior to any cell introduction into the resonators. Considering that the fluid layer dimensions are 10 mm × 12 mm × 0.55 mm (occluding volume then being 66 μL), 1.1×10^6 cells were suspended in 50 μl of chondrogenic media and introduced directly into the fluid layer of each resonator using a flexible gel-loading pipette tip, and cultured within the acoustic trap for 21 days under hypoxic conditions (37 °C, 5% CO_2 and 5% O_2). The media in the bioreactor was exchanged with fresh chondrogenic media every 2–3 days under sterile conditions in a tissue culture hood. To aid the transfer between the tissue culture hood and incubator, whilst continuously levitating the cells, the function generator was temporarily switched from a 12 V DC power supply to a battery as a portable power source.

The bioreactor was driven with a sweep range of 200 kHz (centered on the average experimentally derived cavity resonance for the bioreactor plate, approximately 1.5 MHz) and 10 V_{pp}, with a sweep rate of either 50 Hz or 2 Hz to investigate how the change in acoustic forces affects chondrogenesis. The 200 kHz bandwidth of the sweep was chosen as follows: It was found that there is a cluster of resonances close to the main levitation frequency, typically around 100 kHz in bandwidth. Beyond this little acoustic activity is typically observed. The wider 200 kHz bandwidth was chosen such that a similar cluster was visited in each device despite variations between devices. In some cultures, 10 ng mL^{-1} of parathyroid hormone-related protein (PTHrP[1–34], Bachem H-9095) and 30 mM of L-proline (P0380) were added to the chondrogenic medium, which was introduced into the bioreactor from days 10 to 21.

To minimize possible damage and conformational changes to the engineered tissue, the reflector layer was removed and the constructs were extracted from the active region of the resonators. Samples were then either prepared for histological analysis or introduced into an explant of native cartilage for mechanical testing. Preparation for histological staining was accomplished by chemically fixing the tissue overnight at 4 °C with either 90% ethanol or 4% paraformaldehyde (PFA).

Mechanical testing of cartilage explants

In order to assess the mechanical properties of the engineered tissue, the constructs were implanted into native cartilage and cultured for six weeks prior to nano-indentation. Full-thickness cartilage explants were harvested from the non-load bearing regions of osteoarthritic femoral heads and a defect was created in the explant using a 3 mm ball-drill bit. The engineered cartilage was positioned into the defect and the model was cultured on a transwell insert for six weeks at 37 °C and 5% CO_2.

Following the culture period, nanoindentation testing was performed using a NanoTest Vantage System (Micro Materials, Wrexham, UK), using a 400 μm diameter, diamond cono-spherical tip (E_i/Young's modulus = 1141 GPa, ν_i/Poisson's ratio = 0.07) in the liquid cell attachment to ensure the samples were submerged in PBS and stayed fully hydrated. The indentation points were manually selected on both the native cartilage and the engineered tissue. The indentations were run in load control to a maximum load of 0.05 mN at a rate of 0.005 mN s^{-1} with a dwell at peak load of 60 s to allow for creep run out. The average indentation depth was 2.5 μm ± 0.39 μm, which is less than 5% of the original material thickness of 2 mm to ensure the mechanics were reflective of the construct without any substrate influence.[62]

The data acquired from three indentation points was used to determine the mean reduced moduli (E_r) of the engineered and native cartilage and repeated for three patients. In order to obtain the Young's modulus (E_s) from the reduced modulus output by the nano-indentor, the Poisson's ratio (ν_s) of both the native and engineered cartilage was assumed to be 0.34.[49–51] The Young's modulus was then calculated by rearranging the terms from the general indenter equation[72] (eqn (1)).

$$E_s = \frac{(E_r E_i)(1-\nu_s^2)}{E_i - E_r(1-\nu_i^2)} \quad (1)$$

Histology

Paraffin embedding and sectioning. Fixed samples were washed in PBS before processing through graded ethanol (50–100%), followed by clearing with Histoclear (National Diagnostics HS-200). The tissue samples were then embedded in paraffin wax (Fisher 8002-74-2). Sequential sections were cut 7 μm thick on the microtome and mounted on glass slides.

For histological and immunohistochemical staining, paraffin sections were de-waxed and rehydrated through Histoclear, followed by graded ethanol (100–50%).

Alcian blue/Sirius red (A/S) staining. Sections were stained with Alcian blue 8GX (5 mg ml^{-1} in 1% (v/v) glacial acetic acid) and Sirius red F3B (10 mg ml^{-1} in saturated picric acid) following nuclear staining with Weigert's haematoxylin, as described previously.[73] Alcian blue stained the proteoglycan-rich cartilage matrix, while Sirius red stained the collagen-rich matrix.

Immunohistochemistry (IHC) staining. After de-paraffinization and rehydration, sections were quenched of endogenous peroxidase activity with 3% (v/v) H_2O_2 for five minutes at room temperature and blocked with 1% BSA in PBS for five minutes at 4 °C. Sections were incubated with relevant primary antiserum at 4 °C overnight. This was followed by three five minute washes in wash buffer (0.5% Tween 20 in PBS). Slides were then incubated for one hour with the appropriate biotinylated secondary antibody (dilution 1 : 100), washed three times for five minutes and then incubated for thirty minutes with ExtrAvidin–peroxidase (dilution 1 : 50). Visualisation of the immune complex involved the avidin-biotin method linked to peroxidase and AEC (3-amino-9-ethylcarbazole), resulting in a reddish brown reaction product following ten minute exposure to 30% peroxide. Negative controls (omission of the primary antisera) were included in all immunohistochemistry procedures. No staining

 This journal is © The Royal Society of Chemistry 2018

Open Access Article. Published on 04 January 2018. Downloaded on 12/18/2018 5:21:18 AM.
This article is licensed under a Creative Commons Attribution 3.0 Unported Licence.

was observed in any negative control sections. All sections were counter-stained with Alcian Blue 8GX. Glass coverslips were mounted with Hydromount (National Diagnostics) and allowed to dry for at least two hours.

The anti-SOX-9 antibody (rabbit polyclonal, IgG, Millipore, Watford, UK) was used at a dilution of 1 : 150 in 1% BSA in PBS following the antigen retrieval procedure, which involved treating sections in 0.01 M citrate buffer (pH 6.0) for thirty minutes at 75 °C before the application of the standard immunohistochemistry procedure.

For immunostaining using anti-collagen Type I, II and X antibodies as well as the anti-osteopontin (OPN) antibody, sections were treated with Hyaluronidase (0.8 mg ml^{-1}) at 37 °C for 20 minutes in order to unmask the epitopes and render them accessible for immunostaining. The LF68 anti-collagen Type I antibody (COLI rabbit IgG, gift from Dr Larry Fisher), anti-collagen Type II antibody (COLII rabbit IgG, Calbiochem, Watford, UK), anti-collagen Type X antibody (COLX rabbit IgG, Calbiochem, Watford, UK), and anti-OPN antibody (rabbit IgG, GeneTex Inc.) were used at a dilution of 1 : 1000, 1 : 500, 1 : 100, and 1 : 100, respectively.

Alkaline phosphatase staining. Sections, fixed using 90% ethanol, were immersed in activation buffer (Tris Maleate buffer, pH 7.4) overnight at room temperature. The slides were washed prior to interaction with Naphthol AS-B1 phosphate and the diazonium salt (fast red), which was precipitated at the site of the enzyme activity. The slides were mounted as described above.

Image analysis

Histology images were analysed for collagen and proteoglycan staining area by colour-segmentation using *k*-means cluster analysis. The source image was converted from RGB to L*a*b colour space. The colour information for the tissue section was then isolated from the image by focusing on the information in the a*b colour space. *K*-means clustering was then used to statistically analyse the mean pixel intensities and partition the pixel locations and values into three clusters ($k = 3$). This process was replicated three times to minimize cluster overlap.

The algorithm segmented the pixels values such that two clusters contained the pixel colour values on opposite ends of the A*B colour spectrum. For an immunohistochemistry image, the algorithm partitioned the counter-staining (*i.e.* Alcian blue) and target staining (*i.e.* AEC staining) into two clusters. A third cluster contained the intermediary values within the spectrum. Correspondingly, for A/S staining, the algorithm grouped the pixel values according to the Alcian blue target staining cluster, Sirius red staining cluster, and intermediate values cluster. The target staining area was isolated from the target and intermediate value clusters. The background, or whole section area, was segmented by global thresholding by Otsu and morphological filtering was applied to fill any holes within the subsequent binary image of the whole section.

The computed staining area was then normalized to the total section area to give an area fraction.

Microscopy

Histological sections were imaged using Olympus BX 51 dotSlide virtual slide microscope system (Olympus Microscopy). Fluorescence time-lapse images were obtained using an Olympus upright fluorescence microscope with FITC filter (excitation/emission wavelengths: 485 nm/515 nm, Carl Zeiss), Rhodamine filter (excitation/emission wavelengths: 546 nm/560 nm, Carl Zeiss), and Orca-Flash4.0 (Hammamatsu) with HCImage software.

Author contributions

USJ, PGJ, MH, ROCO, and RST conceived the work and designed the experiments. PGJ and RST co-supervised the project. USJ and WM contributed equally to designing the bioreactor system. USJ characterized the bioreactor assembly along with the acoustic environment, engineered the cartilage constructs using the bioreactor and performed histological analyses of the engineered constructs. RBC and USJ performed nano-indentation on the constructs to assess mechanical stiffness. USJ, PGJ, RBC, MH, ROCO, and RST analysed the data and wrote the manuscript.

Conflicts of interest

The authors declare no competing financial interests.

Acknowledgements

The authors gratefully acknowledge financial support for the work from the EPSRC Fellowship (EP/L025035/1) to PGJ and Wessex Medical Research innovation grant to RST. The authors would also like to acknowledge studentship support to USJ in the form of the Rayleigh PhD Scholarship from the Faculty of Engineering and the Environment. The authors would like to thank the orthopaedic surgeons at University Hospital Southampton for provision of femoral heads.

References

1 A. M. Bhosale and J. B. Richardson, *Br. Med. Bull.*, 2008, **87**, 77–95.
2 S. N. Redman, S. F. Oldfield and C. W. Archer, *Eur. Cells Mater.*, 2005, **9**, 23–32.
3 R. M. Schek, J. M. Taboas, S. J. Segvich, S. J. Hollister and P. H. Krebsbach, *Tissue Eng.*, 2004, **10**, 1376–1385.
4 A. Khademhosseini, R. Langer, J. Borenstein and J. P. Vacanti, *Proc. Natl. Acad. Sci. U. S. A.*, 2006, **103**, 2480–2487.
5 R. Langer and J. Vacanti, *Science*, 1993, **260**, 920–926.
6 H. Da, S. J. Jia, G. L. Meng, J. H. Cheng, W. Zhou, Z. Xiong, Y. J. Mu and J. Liu, *PLoS One*, 2013, **8**, e54838.
7 D. Tang, R. S. Tare, L. Y. Yang, D. F. Williams, K. L. Ou and R. O. Oreffo, *Biomaterials*, 2016, **83**, 363–382.

Appendix A

Open Access Article. Published on 04 January 2018. Downloaded on 12/18/2018 5:21:18 AM.
This article is licensed under a Creative Commons Attribution 3.0 Unported Licence.

8 D. M. Gibbs, C. R. Black, J. I. Dawson and R. O. Oreffo, *J. Tissue Eng. Regener. Med.*, 2016, **10**, 187–198.
9 C. R. Black, V. Goriainov, D. Gibbs, J. Kanczler, R. S. Tare and R. O. Oreffo, *Curr. Mol. Biol. Rep.*, 2015, **1**, 132–140.
10 H. W. Kang, S. J. Lee, I. K. Ko, C. Kengla, J. J. Yoo and A. Atala, *Nat. Biotechnol.*, 2016, **34**, 312–319.
11 D. M. Gibbs, C. R. Black, G. Hulsart-Billstrom, P. Shi, E. Scarpa, R. O. Oreffo and J. I. Dawson, *Biomaterials*, 2016, **99**, 16–23.
12 T. Xu, K. W. Binder, M. Z. Albanna, D. Dice, W. Zhao, J. J. Yoo and A. Atala, *Biofabrication*, 2013, **5**, 015001.
13 K. Y. Ching, O. G. Andriotis, S. Li, P. Basnett, B. Su, I. Roy, R. S. Tare, B. G. Sengers and M. Stolz, *J. Biomater. Appl.*, 2016, 0885328216639749.
14 S. Li, P. Glynne-Jones, O. G. Andriotis, K. Y. Ching, U. S. Jonnalagadda, R. O. Oreffo, M. Hill and R. S. Tare, *Lab Chip*, 2014, **14**, 4475–4485.
15 S. Li, B. G. Sengers, R. O. Oreffo and R. S. Tare, *J. Biomater. Appl.*, 2015, **29**, 824–836.
16 J. C. Babister, R. S. Tare, D. W. Green, S. Inglis, S. Mann and R. O. Oreffo, *Biomaterials*, 2008, **29**, 58–65.
17 R. S. Tare, D. Howard, J. C. Pound, H. I. Roach and R. O. Oreffo, *Biochem. Biophys. Res. Commun.*, 2005, **333**, 609–621.
18 I. T. Ozbolat and Y. Yu, *IEEE Trans. Biomed. Eng.*, 2013, **60**, 691–699.
19 K. C. Hribar, P. Soman, J. Warner, P. Chung and S. Chen, *Lab Chip*, 2014, **14**, 268–275.
20 M. Vaezi and S. Yang, *Int. J. Bioprint.*, 2015, **1**, 66–76.
21 M.-H. Wu, H.-Y. Wang, C.-L. Tai, Y.-H. Chang, Y.-M. Chen, S.-B. Huang, T.-K. Chiu, T.-C. Yang and S.-S. Wang, *Sens. Actuators, B*, 2013, **176**, 86–96.
22 B. Labbe, G. Marceau-Fortier and J. Fradette, *Methods Mol. Biol.*, 2011, **702**, 429–441.
23 M. Sato, M. Yamato, K. Hamahashi, T. Okano and J. Mochida, *Anat. Rec.*, 2014, **297**, 36–43.
24 S. P. Nukavarapu and D. L. Dorcemus, *Biotechnol. Adv.*, 2013, **31**, 706–721.
25 G. Vunjak-Novakovic, I. Martin, B. Obradovic, S. Treppo, A. J. Grodzinsky, R. Langer and L. E. Freed, *J. Orthop. Res.*, 2016, **17**, 130–138.
26 A. J. Grodzinsky, M. E. Levenston, M. Jin and E. H. Frank, *Annu. Rev. Biomed. Eng.*, 2003, **2**, 691–713.
27 H. Ogawa, E. Kozhemyakina, H.-H. Hung, A. J. Grodzinsky and A. B. Lassar, *Genes Dev.*, 2014, **28**, 127–139.
28 J. Fischer, A. Dickhut, M. Rickert and W. Richter, *Arthritis Rheum.*, 2010, **62**, 2696–2706.
29 Y. J. Kim, H. J. Kim and G. I. Im, *Biochem. Biophys. Res. Commun.*, 2008, **373**, 104–108.
30 T. Xu, K. Yang, H. You, A. Chen, J. Wang, K. Xu, C. Gong, J. Shao, Z. Ma and F. Guo, *Bone*, 2013, **56**, 304–311.
31 D. Bazou, A. Castro and M. Hoyos, *Ultrasonics*, 2012, **52**, 842–850.
32 K. A. Garvin, D. Dalecki, M. Yousefhussien, M. Helguera and D. C. Hocking, *J. Acoust. Soc. Am.*, 2013, **134**, 1483–1490.
33 K. A. Garvin, D. C. Hocking and D. Dalecki, *Ultrasound Med. Biol.*, 2010, **36**, 1919–1932.
34 K. A. Garvin, J. VanderBurgh, D. C. Hocking and D. Dalecki, *J. Acoust. Soc. Am.*, 2013, **134**, 1491–1502.
35 A. L. Bernassau, F. Gesellchen, P. G. A. MacPherson, M. Riehle and D. R. S. Cumming, *Biomed. Microdevices*, 2012, **14**, 559–564.
36 X. Ding, J. Shi, S.-C. S. Lin, S. Yazdi, B. Kiraly and T. J. Huang, *Lab Chip*, 2012, **12**, 2491–2497.
37 F. Guo, Z. Mao, Y. Chen, Z. Xie, J. P. Lata, P. Li, L. Ren, J. Liu, J. Yang, M. Dao, S. Suresh and T. J. Huang, *Proc. Natl. Acad. Sci. U. S. A.*, 2016, **113**, 1522–1527.
38 D. J. Collins, B. Morahan, J. Garcia-Bustos, C. Doerig, M. Plebanski and A. Neild, *Nat. Commun.*, 2015, **6**, 8686.
39 J. Liu, L. A. Kuznetsova, G. O. Edwards, J. Xu, M. Ma, W. M. Purcell, S. K. Jackson and W. T. Coakley, *J. Cell. Biochem.*, 2007, **102**, 1180–1189.
40 C. Bouyer, P. Chen, S. Guven, T. T. Demirtas, T. J. Nieland, F. Padilla and U. Demirci, *Adv. Mater.*, 2016, **28**, 161–167.
41 A. Lenshof, C. Magnusson and T. Laurell, *Lab Chip*, 2012, **12**, 1210–1223.
42 P. Glynne-Jones, C. Démoré, C. Ye, Y. Qiu, S. Cochran and M. Hill, *IEEE Trans. Ultrason. Ferroelectr. Freq. Control*, 2012, **59**, 1258–1266.
43 L. A. Crum, *J. Acoust. Soc. Am.*, 1975, **57**, 1363–1370.
44 G. O. Edwards, W. T. Coakley, J. R. Ralphs and C. W. Archer, *Eur. Cells Mater.*, 2010, **19**, 1–12.
45 A. Garbin, I. Leibacher, P. Hahn, H. Le Ferrand, A. Studart and J. Dual, *J. Acoust. Soc. Am.*, 2015, **138**, 2759–2769.
46 S. Li, R. O. Oreffo, B. G. Sengers and R. S. Tare, *Biotechnol. Bioeng.*, 2014, **111**, 1876–1885.
47 S. Oberti, A. Neild, R. Quach and J. Dual, *Ultrasonics*, 2009, **49**, 47–52.
48 M. Wiklund, A. Christakou, M. Ohlin, I. Iranmanesh, T. Frisk, B. Vanherberghen and B. Önfelt, *Micromachines*, 2014, **5**, 27–49.
49 A. E. Christakou, M. Ohlin, B. Onfelt and M. Wiklund, *Lab Chip*, 2015, **15**, 3222–3231.
50 O. Manneberg, B. Vanherberghen, B. Onfelt and M. Wiklund, *Lab Chip*, 2009, **9**, 833–837.
51 D. Bazou, R. Kearney, F. Mansergh, C. Bourdon, J. Farrar and M. Wride, *Ultrasound Med. Biol.*, 2011, **37**, 321–330.
52 S. J. Wang, D. Jiang, Z. Z. Zhang, A. B. Huang, Y. S. Qi, H. J. Wang, J. Y. Zhang and J. K. Yu, *Sci. Rep.*, 2016, **6**, 36400.
53 J. Fischer, A. Aulmann, V. Dexheimer, T. Grossner and W. Richter, *Stem Cells Dev.*, 2014, **23**, 2513–2523.
54 S. S. Sadhal, *Lab Chip*, 2012, **12**, 2292–2300.
55 M. Wiklund, R. Green and M. Ohlin, *Lab Chip*, 2012, **12**, 2438–2451.
56 J. Lei, P. Glynne-Jones and M. Hill, *Lab Chip*, 2013, **13**, 2133–2143.
57 J. Lei, P. Glynne-Jones and M. Hill, *Phys. Fluids*, 2016, **28**, 012004.
58 P. B. Muller and H. Bruus, *Phys. Rev. E: Stat., Nonlinear, Soft Matter Phys.*, 2015, **92**, 063018.
59 B. Khozoee, P. Mafi, R. Mafi and W. S. Khan, *Curr. Stem Cell Res. Ther.*, 2017, **12**, 260–270.

This journal is © The Royal Society of Chemistry 2018

Appendix B Investigation on function and response to 5FU to Huh7 discoid grew in levitation (being reviewed

Biomicrofluidics

Generation of functional hepatocyte 3D discoids in an acoustofluidic bioreactor

Cite as: Biomicrofluidics 13, 014112 (2019); https://doi.org/10.1063/1.5082603
Submitted: 22 November 2018 . Accepted: 31 January 2019 . Published Online: 12 February 2019

Mogibelrahman M. S. Khedr, Walid Messaoudi, Umesh S. Jonnalagadda, Ahmed M. Abdelmotelb, Peter Glynne-Jones, Martyn Hill, Salim I. Khakoo, and Mohammed Abu Hilal

View Online Export Citation CrossMark

ARTICLES YOU MAY BE INTERESTED IN

Reducing deposition of encrustation in ureteric stents by changing the stent architecture: A microfluidic-based investigation
Biomicrofluidics 13, 014101 (2019); https://doi.org/10.1063/1.5059370

Acoustofluidic particle steering
The Journal of the Acoustical Society of America 145, 945 (2019); https://doi.org/10.1121/1.5090499

Nuclear singlet relaxation by scalar relaxation of the second kind in the slow-fluctuation regime
The Journal of Chemical Physics 150, 064315 (2019); https://doi.org/10.1063/1.5074199

AIP Author Services
English Language Editing

AIP Publishing

© 2019 Author(s).

Biomicrofluidics ARTICLE scitation.org/journal/bmf

Generation of functional hepatocyte 3D discoids in an acoustofluidic bioreactor

Cite as: Biomicrofluidics 13, 014112 (2019); doi: 10.1063/1.5082603
Submitted: 22 November 2018 · Accepted: 31 January 2019 ·
Published Online: 12 February 2019

Mogibelrahman M. S. Khedr,[1,2,a)] Walid Messaoudi,[3] Umesh S. Jonnalagadda,[3] Ahmed M. Abdelmotelb,[1,4] Peter Glynne-Jones,[3] Martyn Hill,[3] Salim I. Khakoo,[1,5] and Mohammed Abu Hilal[1,5]

AFFILIATIONS

[1]Clinical and Experimental Sciences Academic Unit, Faculty of Medicine, University of Southampton, Southampton SO16 6YD, United Kingdom
[2]Faculty of Medicine, Suez Canal University, Ismailia 41111, Egypt
[3]Mechanical Engineering, Faculty of Engineering and Physical Sciences, University of Southampton, Southampton SO17 1BJ, United Kingdom
[4]Faculty of Medicine, Tanta University, Tanta 31527, Egypt
[5]Southampton University Hospitals NHS Trust, Southampton SO16 6YD, United Kingdom

[a)]**Author to whom correspondence should be addressed:** M.E.Khedr@soton.ac.uk. **Tel.:** +44 (0) 2381206153. **Mob:** +44 (0) 7961762098.

ABSTRACT

Ultrasonic standing wave systems have previously been used for the generation of 3D constructs for a range of cell types. In the present study, we cultured cells from the human hepatoma Huh7 cell line in a Bulk Acoustic Wave field and studied their viability, their functions, and their response to the anti-cancer drug, 5 Fluorouracil (5FU). We found that cells grown in the acoustofluidic bioreactor (AFB) expressed no reduction in viability up to 6 h of exposure compared to those cultured in a conventional 2D system. In addition, constructs created in the AFB and subsequently cultured outside of it had improved functionality including higher albumin and urea production than 2D or pellet cultures. The viability of Huh7 cells grown in the ultrasound field to 5FU anti-cancer drug was comparable to that of cells cultured in the 2D system, showing rapid diffusion into the aggregate core. We have shown that AFB formed 3D cell constructs have improved functionality over the conventional 2D monolayer and could be a promising model for anti-cancer drug testing.

Published under license by AIP Publishing. https://doi.org/10.1063/1.5082603

INTRODUCTION

Hepatocellular carcinoma cell (HCC) lines including Huh7, cultured in 2D systems, show substantial loss of their xenobiotic-metabolizing enzyme activity and liver cell markers in contrast to 3D-organized cells which significantly express higher levels of differentiation markers and exhibit function closer to mature liver cells.[1–3] In addition, the culturing of cancer cells in a 3D model has the advantage of mimicking the *in vivo* tumour cell architecture and reflecting the proliferation pattern, apoptosis, oxygen/nutrient distribution, and the cell cycle heterogeneity of a tumour mass.[4,5]

The production of cell aggregates to simulate *in vivo* cell structure has been a major focus for biology, especially for *in vitro* drug testing.[6] Studies suggest that acoustic wave traps open potential applications for cell tissue engineering. Two main types of technology are used for exciting acoustic waves: Surface Acoustic Wave (SAW) and Bulk Acoustic Wave (BAW), both allowing a scaffold free aggregation of cells in a 3D structure.[7] BAW manipulation device typically consists of a resonator,[8,9] where a transducer excites a planar resonance in a fluid chamber [Fig. 1(a-i)]. A thickness acoustic standing wave is created within the cavity, the resulting radiation force pushing cells toward the pressure node which is located in the middle of the fluid cavity, allowing levitation[8] [Fig. 1(a-ii)], and also inter-particle (or Bjerknes) forces, attracting cells together into aggregates [Fig. 1(a-iii)].[10]

Biomicrofluidics ARTICLE scitation.org/journal/bmf

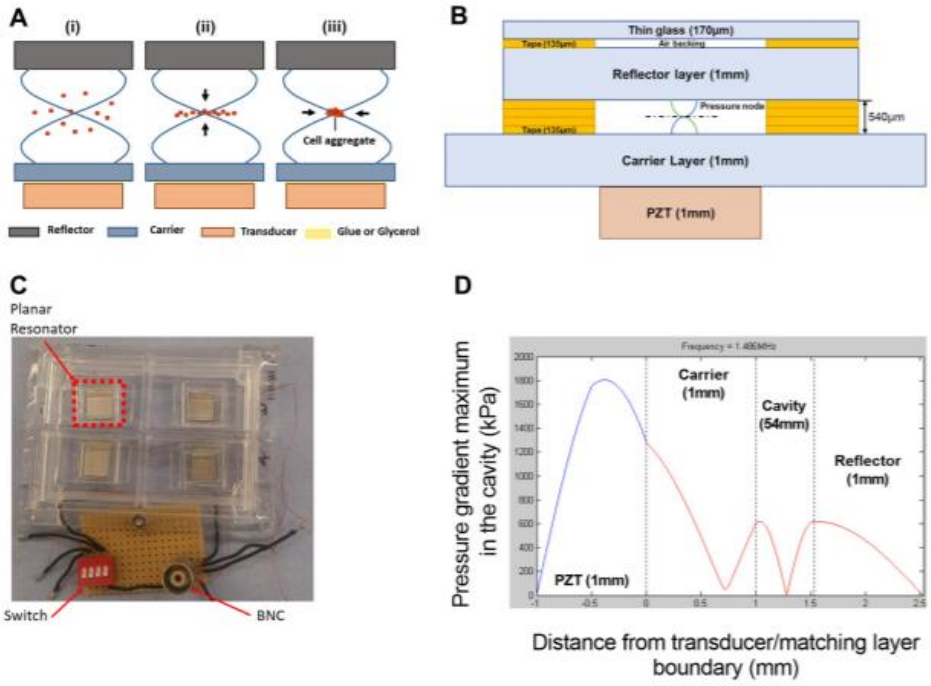

FIG. 1. Bioreactor design, fabrication, and modeling. (a) Planar resonator. (i) Acoustic standing wave in a planar resonator formed from reflections in the cavity of waves created by a transducer. (ii) This standing wave creates a time average acoustic energy gradient that "pushes" the particle to the pressure node (or kinetic energy maximum). (iii) Bjerknes forces aggregate the particles in a lump. (b) Schematic diagram detailing the planar resonator structure and dimensions. (c) Picture of the bioreactor showing the four resonator compartments and electrical connections. (d) Acoustic pressure amplitude in kPa in the layered resonator predicted by a transfer impedance model.

We describe the use of controllable cell aggregate formation in an acoustofluidic bioreactor (AFB) as a model for drug testing. The main benefits of contactless acoustic aggregation are the possibility of controlled mechanical stimulation induced by the force field;[11] the possibility of acoustic streaming to promote nutrient exchange with the surrounding media;[12] the ease of use; and finally, low energy and material costs.

In the present study, we have demonstrated the ability of a BAW mediated AFB system to form viable Huh7 cell aggregates in a short time. The Huh7 discoids we created possessed a substantial increase in the production of albumin and urea in addition to higher enzyme activity than the conventional 2D monolayer or pellet cultures. We have used 5 Fluorouracil (5FU), a cytostatic/cytotoxic anti-cancer agent that is commonly used for the treatment of solid tumours. 5FU resulted in a wide range of effects from the inhibition of cell proliferation to the induction of apoptosis and cell necrosis.[13,14] The AFB cell aggregates showed a robust susceptibility to the 5FU as compared to 2D controls.

MATERIALS AND METHODS

Bioreactor design, fabrication, and culture environment

The bioreactors used in the current study were fabricated according to the model that has been described by Jonnalagadda et al.[11] That bioreactor is a one-chamber device with a capacity of about 12 ml medium. We have used that model in investigating the Huh7 cell line viability and in performing the morphological studies. As seen in Figs. 1(b) and 1(c),

Published under license by AIP Publishing.

Biomicrofluidics ARTICLE scitation.org/journal/bmf

we have fabricated another four-chamber device, where every independent planar resonator has its own well (with a capacity of 1-2 ml medium) and that allowed running of four independent experiments in one device. The chamber spacer material was also changed to four layers of laser cut adhesive tape (3M 9731) to ease fabrication; however, the acoustic properties are not expected to differ as a result of this. This four-chamber model has been used for the rest of our studies.

Figure 1(d) shows the expected pressure distribution as modeled by a transfer impedance model[15] with a KLM transducer representation.[16] The bioreactor consists of four independently fabricated planar resonators (±5 μm in thickness and ±100 μm lateral arrangement) with each having its own fluidic well. Small manufacturing variations cause variability in the resonant frequency of each well. To hit the resonance frequency for each of them from a single source, a frequency sweep from 1.44 MHz to 1.51 MHz at a rate of 20 Hz is used. The voltage drop method was used to assess the acoustic pressure amplitude in the levitation cavity.[17] The acoustic pressure amplitude varies during the applied frequency sweep as the resonance is approached. By using the voltage drop method with the frequency sweep, we established that the mean force on particles (at the 7 Vpp driving amplitude, measured at the resonance frequency since the voltage varies across the sweep too) is equivalent to the force that would arise from a 380 kPa amplitude standing wave of constant amplitude. This is comparable to other acoustofluidic bioreactors.[18,19] Temperature rises within the chamber (caused by acoustic absorption) were measured by a thermocouple located inside and at the center of the planar resonator cavity and were found to be 2.4 ± 0.3 °C. The temperature rise attains 80% of its maximum value in around 5 min. The aggregation is not performed in an incubator, so the small rises in temperature above room temperature will not have a significant effect on viability.

Cell culture

The human hepatoma Huh7 cell line was a kind gift from Dr. A. Emre Sayan, Cancer Sciences Academic Unit, University of Southampton, UK. A Short Tandem Repeat (STR) analysis to verify the cell line identity was regularly performed. Cells were routinely cultured in Dulbecco's Modified Eagle Medium (DMEM) (Thermo Fisher, Inchinnan, UK) supplemented with 10% heat-inactivated fetal bovine serum (FBS) (Thermo Fisher), 100 U ml^{-1} of penicillin, 100 μg ml^{-1} of streptomycin, and 250 ng ml^{-1} of Gibco Amphotericin B. Cells were maintained at 37 °C in a humidified incubator with 5% CO_2 and the medium was changed every three days.

Cells were detached using non-enzymatic cell dissociation buffer (Sigma), washed once with complete medium and centrifuged at 250g for 5 min. Cell pellet was aliquoted into three populations; one cell aliquot was re-centrifuged as before and cell pellet was maintained in a 15 ml tube as the pellet culture. Another aliquot was seeded directly in a 12 well plate, and the third aliquot was loaded into AFB bioreactor. In anti-cancer drug testing, cells were loaded in the AFB for 2 h after which the generated discoids were transferred to 1% agarose coated 24 well plates. Following 24 h, AFB discoids or cells cultured in the 2D monolayer or as pellets were treated with serial 10-fold dilutions (1, 10, or 100 μM) of 5 Fluorouracil (5FU) (Sigma, Gillingham, UK) dissolved in dimethyl sulfoxide (DMSO) (Sigma). Negative control cells were treated with medium with DMSO alone. Supernatants were aspirated daily and replaced with new treatment medium for three subsequent days.

Viability and morphology of Huh7 in AFB

Cell viability was assessed by a live/dead staining technique. Calcein AM (Thermo Fisher) and Propidium Iodide (PI) (1-3 μM final concentrations of each) were added to medium following incubation of cells in the 2D monolayer or AFB cultures at room temperature. Imaging was performed in a Zeiss-microscope using AxioVision SE64 version 4.9.1 software. Viability was expressed as the percentage of viable cell area to the total cell area using Fiji version of ImageJ software for windows.[20] Viability was calculated in five different fields per condition in three independent experiments. For studying the aggregates' morphology, cells were incubated in medium with 5 μM CellTracker™ Green CMFDA Dye (Thermo Fisher) for 30 min and then loaded into the AFB at a density of 10^6 cells ml^{-1} for 1 h. Cell aggregates were recovered and imaged with a Leica TCS-SP8 Laser Scanning Confocal Microscope (Leica Biosystems, Wetzlar, Germany).

Detection of E-cadherin in Huh7 by western blotting

Huh7 were cultured as the 2D monolayer, pellet, or in AFB for 1/2, 1, 3, 6, and 16 h. Cells were lysed using 1× TruPAGE™ LDS Sample Buffer [with 1 mM ethylenediaminetetraacetate (EDTA), 1 mM ethylene glycol-bis (β-aminoethyl ether)-N,N,N′, N′-tetraacetic acid (EGTA) (Sigma), and 0.5 μg ml^{-1} Leupeptin] and run a TruPAGE® 10% precast gels (Sigma) with TruPAGE dithiothreitol (DTT) sample reducer buffer (Sigma) to disrupt the disulphide bridges in proteins which liberate small polypeptides. Protein was loaded in a concentration of 30 μg as adjusted by the bicinchoninic acid (BCA) colorimetric protein assay kit (Sigma) in accordance with the manufacturer's instructions using a BSA standard. Molecular weights were determined using the PageRuler™ Plus prestained protein ladder, 10-250 kDa (Thermo Fisher). Proteins were transferred to nitrocellulose membranes by a wet transfer method. Membranes were blocked for 1 h in 5% non-fat blotting grade cow's milk (Bio-Rad) in 0.05% Tris-buffered saline (TBS)–Tween® 20 solution. The membranes were then probed with 1 μg ml^{-1} mouse monoclonal anti-human E-cadherin IgG2B antibody Clone #180224 (R&D Systems, Oxfordshire, UK) overnight at 4 °C, followed by rabbit polyclonal anti-mouse-horseradish peroxidase (HRP) (DakoCytomation, Cambridgeshire, UK) at a dilution of 1:2000 for 45 min. Membranes were probed with mouse monoclonal anti-β-actin-HRP conjugated (Sigma) for 1 h at room temperature at a dilution of 1:50 000. Reactive bands were visualised using the Luminata Forte Western

Published under license by AIP Publishing.

Biomicrofluidics ARTICLE scitation.org/journal/bmf

HRP substrate chemiluminescent substrate (Millipore UK Ltd., Hertfordshire, UK) in a ChemiDoc™ imaging system (Bio-Rad).

Albumin ELISA and urea concentration assays

Albumin and urea concentrations in the supernatant of hepatocytes cultures were determined using the ELISA DuoSET® kit for human albumin (R&D Systems, Oxfordshire, UK) according to the manufacturer's instructions. Urea concentration was measured as described previously.[21] Briefly, the urea reagent mix working concentrations of 100 mg l^{-1} o-phthalaldehyde, 513 mg l^{-1} primaquine bisphosphate, 2.5 mol l^{-1} sulfuric acid, 2.5 g l^{-1} boric acid, and 0.03% Brij-35 were prepared. A volume of 200 μl freshly prepared reagent mix was added to 50 μl samples or standard (QuantiChrom, BioAssay Systems, Hayward, CA, USA). Following 1 h incubation at room temperature, absorbance at 430 nm was measured in a SpectraMax® Plus 384 Microplate Reader (Molecular Devices, Wokingham, UK). The concentration of urea of the sample against 5 mg dl^{-1} standard was calculated in mg dl^{-1}.

CYP3A4 activity assay

Cytochrome P450 3A4 (CYP3A4) activity in Huh7 in different cultures was measured using a P450-Glo™ CYP3A4 Assay (Luc-PFBE) Cell-Based/Biochemical luminescent assay (Promega UK Ltd, Southampton, UK) according to manufacturer's instructions. Briefly, Huh7 cells were cultured for various time periods in different culture systems then basal CYP3A4 enzyme activity was assessed by incubating cells with luminogenic P450-Glo substrate (luciferin-PFBE, at a final concentration of 50 μM) for 3 h at room temperature. The luciferin was detected by incubating 25 μl of supernatant with an equal volume of Luciferin Detection in a white opaque 96 well plate for 20 min at room temperature. Light was measured in a FLUOstar OPTIMA plate reader (BMG LABTECH, Ortenberg, Germany). Values have been corrected to the corresponding time course cell viability in various culture systems.

Analysis of apoptosis in Huh7 using a DNA fragmentation assay

Huh7 grown in various culture systems and those treated with 5FU (1, 10, and 100 μM) for various time points were investigated for possible induction of apoptosis using the DNA degradation assay as described.[22] Cells were lysed using 20 μl TES lysis buffer [100 mM Tris, pH 8.0 + 20 mM EDTA + 0.8% (w/v) sodium dodecyl Sulfate (SDS)] and then incubated for 30-120 min at 37 °C with 10 μl of RNase A at a concentration of 500 units ml^{-1}. DNA was extracted using proteinase K (20 μl of 10 mg ml^{-1}) overnight at 50 °C in a heat block and ladder formation was explored by running DNA on a 1% agarose gel at 35 V for 4 h. Quantification of bands was performed by Image Lab version 5.2.1 software using Bio-Rad's ChemiDoc Imaging Systems System (Bio-Rad Laboratories, Hercules, CA, USA).

Cell proliferation assay

Huh7 grown in various culture systems and treated with 5FU (1, 10, and 100 μM) for 24, 48, and 72 h. Cell growth was determined using a colourimetric Quick Cell Proliferation Assay kit II (Abcam, Cambridge, UK) according to manufacturers' instructions. Briefly, lyophilized water-soluble tetrazolium salt (WST-1) reagent was dissolved into 5 ml Electro Coupling Solution (ECS) and the solution stored at −20 °C. Ten microliters of WST-1 solution was added to the medium and cells were incubated in standard culture conditions for 3 h. Absorbance was detected at 440 nm.

Measurement of lactic dehydrogenase (LDH)

LDH levels in supernatants from Huh7 were grown in various culture systems and treated with 5FU (1, 10, and 100 μM) for 24, 48, and 72 h. Equal volumes of 200 mM Tris pH 8, 50 mM Lithium lactate, freshly prepared substrate solution [100 μl P-Iodonitrotetrazolium Violet, INT (33 mg ml^{-1} in DMSO) + 100 μl, Phenazine methosulfate, PMS (9 mg ml^{-1}) + 2.3 ml β-NAD hydrate (3.74 mg ml^{-1})] and supernatants samples or positive control (5 μg ml^{-1} L-Lactic Dehydrogenase from bovine heart) (Sigma) were loaded into an assay plate. The V_{max} was measured at 490 nm for 10 min and LDH activity (U ml^{-1}) was calculated.

Statistics

One-way or two-way ANOVA followed by Fisher's least significant difference (LSD) multiple comparisons tests and multiple or paired Student's t tests were performed using GraphPad Prism version 7.7.1 for Windows (GraphPad Software, La Jolla, CA, USA).

RESULTS

Generation of Huh7 discoids in an AFB

The size of cell aggregates has been shown to have a strong impact on cellular viability and function.[23] The uniformity of aggregates size is critical for the validity of chemotherapeutic drug screening. We investigated the size of discoids formed by injecting Huh7 cell suspensions of variable cell densities into the AFB. Huh7 cells were observed to aggregate over the course of 15 min following cell injection [Fig. 2(a) (Multimedia view)]. Typically, 9-12 discoids were formed corresponding to the acoustic trapping locations. At a density of 0.25×10^6 cells ml^{-1}, small Huh7 cell aggregates were formed (with a mean diameter of 381.6 ± SD 113 μm) and there was a little increase in discoid size at density of 0.5×10^6 cells ml^{-1} [Fig. 2(b)]. The size of discoids was markedly increased at a seeding density of 1.25×10^6 cells ml^{-1} (a mean diameter of 525.4 ± SD 118.7 μm, $P < 0.0001$) and larger discoids were generated at higher cell densities (a mean diameter of 1021 ± SD 267.8 μm, $P < 0.0001$ and 1382 ± SD 403.1 μm, $P < 0.0001$ at a cell density of 2.5×10^6 and 5×10^6 cells ml^{-1}, respectively). Up to 5×10^6 cells ml^{-1}, there was no marked change in size along the z (i.e., the sound propagation) axis.

Published under license by AIP Publishing.

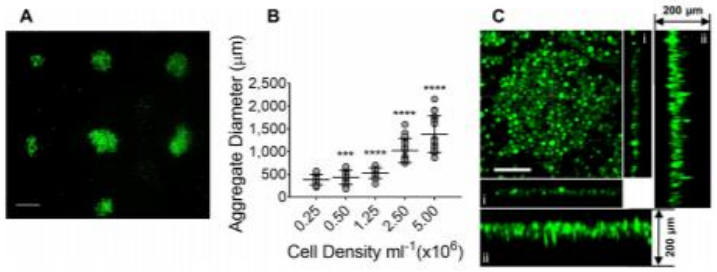

FIG. 2. Size of Huh7 discoids generated in acoustofluidic bioreactor (AFB). [(a) and (Multimedia view)] Huh7 discoids formed at a density of 1.25×10^6 cells ml^{-1} in AFB. Cells were pre-labeled with calcein AM and loaded for 30 min in the AFB. Scale bar = 500 μm. (b) Aggregate diameter (μm) was plotted against cell density (n = 3). *P* values shown in the graph are for the comparison to a cell density of 2.5×10^6 cells ml^{-1}. ***$P = 0.0001$, ****$P < 0.0001$. Mean ± SD. One-way ANOVA followed by Fisher's least significant difference (LSD) test. (c) Orthogonal projection of Huh7 showing a discoid shaped cell aggregate. A 200 μm z projection was demonstrated and showing x and y axes without (i) or with maximum projection (ii). Cells at a density of 10^6 cells ml^{-1} were labeled with CellTracker Green CMFDA Dye and incubated in the AFB for 1 h. Scale = 100 μm. Multimedia view: https://doi.org/10.1063/1.5011000000266

Cells were unevenly aggregated laterally, creating a multitude of discoids levitating in the same plane with thickness ranging from 20 to 60 μm [i.e., one to three cell layers, Fig. 2(c-i) and 2(c-ii)]. In a previous report, Chen *et al.* showed that the diameter of spheroids could depend on the density of cells in the medium and wavelength of standing wave.[24] Although the generated discoids in our system do not correspond to Chen's model, the overall volume of the discoids has altered with the change of density of cells in the medium while the thickness of the discoids does not change with density. The thickness of cell discoids was similar between the center and periphery of the cell aggregates. Cell discoids formed at a cell density of 1.25×10^6 cells ml^{-1} showed the least variability in size and therefore this cell density has been used in the subsequent experiments. The wavelength at the frequency used in our experiments was 1 mm in the filled cavity, which allowed the generation of large sized cell aggregates at high cell density.

In the absence of extracellular matrix, E-cadherin has been found to play a crucial role in cell-cell adhesion, maintenance of survival, and proliferation of cancer cell aggregates.[25] The role of E-cadherin adhesion molecules in AFB driven aggregate formation was investigated using western blotting. Huh7 single cell suspensions were found to express highly preserved E-cadherin molecules, while in the subsequent 2D monolayer or AFB cultures, E-cadherin was found to lose its integrity [Fig. 3(a)]. Seeding cells in an ultrasound field was observed to initiate a gradual cleavage of full length E-cadherin (120 kDa) into smaller fragments, mostly as C-terminal fragment 1, CTF1 (38 kDa) and to a lesser extent C-terminal fragment 4, CTF4 (23 kDa) and C-terminal fragment 2, CTF2 (33 kDa) [Fig. 3(b)]. Almost all E-cadherins underwent fragmentation following 3 h of cell aggregation in the AFB. On the other hand, E-cadherin was cleaved early in the course of the 2D monolayer cell culture [Fig. 3(c)]. Notably, cells in AFB cultures express more full length E-cadherin than those cultured as 2D monolayers, but there were no qualitative differences observed in fragments distribution in both cell cultures. These findings highlight the important role of E-cadherin in AFB induced cell-cell contact and aggregate formation. As E-cadherin promotes a calcium-dependent cell-cell adhesion,[26] the interference of E-cadherin assembly was tested by adding a selective calcium chelator (EGTA) to the culture medium. The presence of 10 mM EGTA in the culture medium was found to inhibit cell aggregation in the AFB [Fig. 3(d)], which suggests that calcium-dependent adhesion molecules contribute to discoid formation in the AFB.

Viability and functions of Huh7 in the AFB environment

The influence of the AFB on the viability and function of Huh7 was next investigated. The viability of Huh7 was detected by labeling cells with calcein AM and PI following incubation in the 2D monolayer or AFB cultures at room temperature [Fig. 4(a)]. It was found that the viability of Huh7 decreased to an average of 43.3% and 46.94% for 2D and AFB, respectively, at the previous conditions, and to 31.7%, $P = 0.1807$ and 23.92%, $P = 0.0111$ for 2D and AFB, respectively, at 3 h of incubation and was dramatically reduced to only 3.46%, $P = 0.0003$ and 8.72%, $P = 0.0002$ for 2D and AFB, respectively, after 6 h [Fig. 4(b)]. No marked differences were observed between the 2D monolayer and AFB cultures. Culture of Huh7 cells in DMEM culture medium buffered with [4-(2-hydroxyethyl)-1-piperazineethanesulfonic acid] (HEPES) (Thermo Fisher) showed an initial high cell viability of 94.11% and 98% following 30 min culture in 2D and AFB systems, respectively [Fig. 4(c)]. The viability of cells was found to be preserved at 83.35%, $P = 0.3438$ and 81.86%, $P = 0.1078$ for 2D and AFB, respectively, after 6 h of culture. No marked

Published under license by AIP Publishing.

Biomicrofluidics ARTICLE scitation.org/journal/bmf

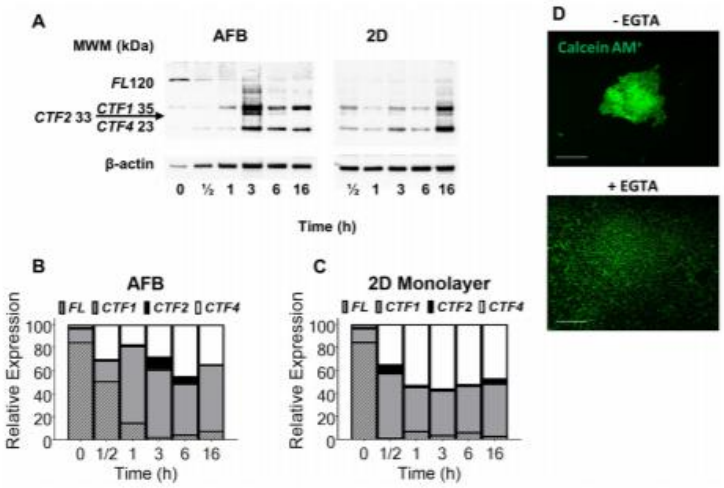

FIG. 3. Detection of E-cadherin expression in Huh7 using western blotting technique. (a) Representative blot for detection of E-cadherin protein expression in Huh7 grown as the 2D monolayer or in AFB (0 time point represents single cell suspension just before seeding). Molecular weight marker (MWM) is indicated. E-cadherin Full length, FL (120 kDa), C-terminal fragment 1, CTF1 (38 kDa), C-terminal fragment 2, CTF2 (33 kDa), and C-terminal fragment 4, CTF4 (23 kDa) are indicated. [(b) and (c)] Band density analysis (band intensity normalised to β-actin control) of E-cadherin fragments detected by western blotting in Huh7 cells cultured in AFB or 2D systems, respectively. (d) Effect of calcium chelation on AFB induced cell aggregates. Huh7 aggregate formation was observed using usual medium (without EGTA, –EGTA) or with 10 mM EGTA (+EGTA) in AFB for 3 h. Cells were labeled with calcein AM (green) before loading. Scale = 500 μm.

difference in cell viability was observed between the two culture methods.

The synthetic and metabolic functions of Huh7 cells were tested in the AFB with time course experiments and compared to the conventional 2D monolayer and 3D pellet cultures. Cells cultured in the AFB showed a time dependent increase in albumin secretion in the cell culture supernatant [Fig. 5(a)]. The albumin concentration rose to a mean of 11.02 ± SEM 2.18 ng ml^{-1} after 6 h in the AFB which is nearly double that after 30 min in the trap (a mean of 2.24 ± SEM 0.79 ng ml^{-1}, $P < 0.0001$). A similar pattern was observed with cells seeded as 2D monolayers (means of 5.62 ± SEM 0.85 ng ml^{-1}, $P = 0.0002$ and 11.48 ± SEM 0.87 ng ml^{-1}, $P < 0.0001$ at 3 and 6 h, respectively, compared to that after 30 min incubation). In contrast, pellet-cultured Huh7 did not show a marked increase in albumin levels (means of 4.67 ± SEM 0.91 ng ml^{-1}, $P = 0.0324$ and 6.74 ± SEM 0.434 ng ml^{-1}, $P = 0.0341$ at 3 and 6 h, respectively, compared to that after 30 min incubation). Albumin secretion from cells in both AFB and 2D cultures was markedly higher than that released from cells cultured as pellets. In addition, a noticeable increase in albumin levels was detected in the AFB system when compared to that observed in the 2D monolayer in the first hour of cell culture (means of 8.62 ± SEM 1.35 and 5.98 ± SEM 0.78 ng ml^{-1}, respectively, $P = 0.0078$).

Huh7 cells cultured in the AFB had a time dependent increase in urea secretion with a mean of 6.95 ± SEM 0.04 mg dl^{-1} following 6 h in culture from a baseline of 6.05 ± SEM 0.05 mg dl^{-1} at 30 min [Fig. 5(b)]. Similarly, cells in 2D culture were found to produce more urea following 6 h in culture (a mean of 6.19 ± SEM 0.67 mg dl^{-1}), while cells cultured as pellets showed high urea production after 3 h of incubation (a mean of 6.16 ± SEM 0.07 and 6.12 ± SEM 0.05 mg dl^{-1} at 3 and 6 h, respectively). Urea production was found to be higher in cells cultured in the AFB system when compared to other culture systems at all-time points.

Cytochrome P450 3A4 (CYP3A4) enzyme is the principal and abundant isoform of human CYP3A family.[27] It has the widest catalytic selectivity and is responsible for the metabolism of about ~30%–40% of clinically used drugs.[28,29] In this study, we measured basal CYP3A4 activity using a luminescent substrate based enzyme assay as an indicator of the metabolic status of Huh7 cells in used cultures. Huh7 cells subjected to ultrasound waves in AFB for 30 min express low CYP3A4 activity but following 6 h of incubation, cells retrieved high enzyme activity (a mean of 1431.386 ± SEM 139.66 and 2233.77 ± SEM 242.88 RLU, respectively, $P = 0.0397$) [Fig. 5(c)]. There is no distinct difference in CYP3A4 activity between cells cultured in AFB or 2D monolayer

Published under license by AIP Publishing.

Biomicrofluidics ARTICLE scitation.org/journal/bmf

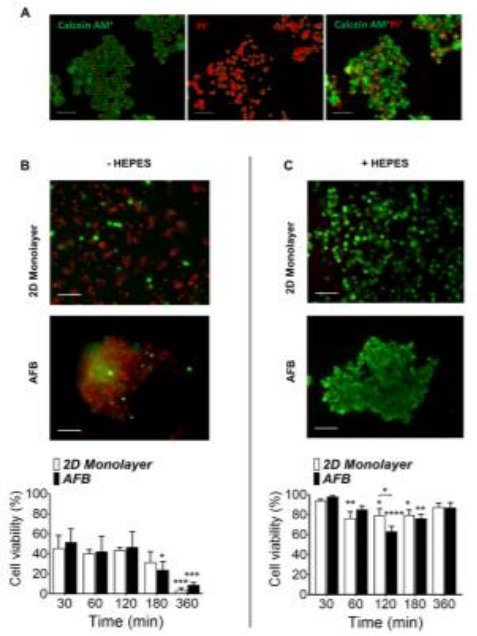

FIG. 4. Survival of Huh7 cells in the AFB. Live cells were labeled with calcein AM (green), and dead cells were labeled with Propidium Iodide (PI, red) in the (a) absence or (b) presence of 25 mM [4-(2-hydroxyethyl)-1-piperazineethanesulfonic acid] (HEPES) in culture medium. Representative images of cells following 360 min incubation in 2D or AFB system were presented and percentage of live cells were plotted against time of cell incubation. Scale bar = 100 μm. n = 3. *P* values shown in the graph are for comparison to 30 min time point (on top of bars). $^{*}P < 0.05$, $^{**}P < 0.005$, $^{***}P < 0.0005$, $^{****}P < 0.0001$. Mean ± SEM. Two-way ANOVA followed by Fisher's LSD test.

following 6 h and both cultures had higher enzyme activity compared to pelleted cells.

Acoustically driven microbubble cavitation and localised streaming are believed to play a role in ultrasound mediated cell membrane disruption (known as Sonoporation).[30,31] This results in an increase in cell membrane permeability and in the release of various intracellular molecules. Cell membrane permeability was tested using calcein AM. Calcein AM was readily taken up and converted by cytosolic esterase to calcein that gives an intense green florescence for viable cells with intact cell membrane.[32] We pre-loaded Huh7 cells with calcein AM dye and then monitored fluorescent intensity of calcein AM in cells at various time points in AFB [Fig. 5(d)]. Up to 6 h, cell exposure to ultrasound wave was not associated with any notable change of cell wall integrity as compared to cells cultured as 2D monolayers [Fig. 5(e)].

In the previous experiments, using the four-chamber device, with its limited volume capacity was associated with an impact on cell viability with time. Huh7 cells grown in AFB showed a higher percentage of dead cells (46.65% of total cells) at 6 h compared to cells grown in the 2D system (12.18% of total cells). A higher LDH activity was observed in Huh7 cells maintained for 6 h in the acoustic field (mean 20.48 ± SEM 6.59 U ml^{-1}) when compared to 2D or pellet cultures (mean of 5.71 ± SEM 0.75 and 3.63 ± SEM 0.66 U ml^{-1}, respectively) [Fig. 5(f)]. We found that medium levels in bioreactor wells were significantly decreased after 6 h and marked condensations were observed on the bioreactor lid. Loss of water from medium exposes cell to acute hyperosmolarity stress that may lead to cell apoptosis and death as describe before.[33,34] In contrast, we have shown previously that cell integrity has not been changed in the course of time when seeded in the one-chamber device, which accommodate larger volume of medium (see the Viability section). Potential stimulation of apoptosis in cultured Huh7 cells was investigated by DNA fragmentation. Cells did not show significant apoptotic DNA degradation in all three culture systems tested [Fig. 5(g)].

Anti-cancer drug testing

5 Fluorouracil (5FU) is a cytostatic antimetabolite drug that has been reported to inhibit cell growth and induce apoptosis in several HCC cell lines including Huh7.[13] AFB generated discoids were treated with various concentrations of 5FU and compared to cells cultured as 2D monolayers and pellet cultures. Drug dependent alteration of Huh7 viability was studied using a WST-1 salt cell proliferation assay. In the first 24 h of culture, more than half of the metabolically active cells died in the AFB and pellet cultures. However, deterioration of cell viability was not observed in cells grown as the 2D monolayer [Fig. 6(a)]. Interestingly, a dose dependent decrease in cell proliferation was observed after 48 h of 5FU treatment in cell aggregates formed in AFB (a mean of 7.90% ± SEM 2.20 lower than untreated cells) [Fig. 6(b)]. This decrease was higher in pellet cultures or 2D cultures (a mean of 24.88% ± SEM 4.76 and 14.71% ± SEM 4.90 lower than untreated cells, respectively) [Figs. 6(c) and 6(d)]. Following 72 h of anti-cancer treatment, Huh7 discoids generated in the AFB demonstrated a similar pattern of decline in their proliferation (a mean of 8.86% ± SEM 2.07 lower than untreated cells at 100 μM). At the same 5FU concentration, more growth inhibition was found in pelleted cells (a mean of 15.57% ± SEM 4.67 lower than untreated cells) but the decrease in cell growth in the conventional 2D culture was close to that noticed in AFB culture (a mean of 9.29% ± SEM 5.05 lower than untreated cells). Following 48 h culture, the growth inhibition of Huh7 was induced at lower concentrations of 5FU in 2D monolayers when compared to AFB [inhibitory concentration 50 (IC50) 1.96 and 5.54 μM, respectively], while the proliferation of cells cultured as pellets was inhibited at markedly higher concentrations (IC50 19.79 μM) [Fig. 6(e)]. The pattern of 5FU potency changed following 72 h as cell proliferation was inhibited at higher concentrations in 2D monolayers, while cells in the AFB did not

Published under license by AIP Publishing.

Biomicrofluidics ARTICLE scitation.org/journal/bmf

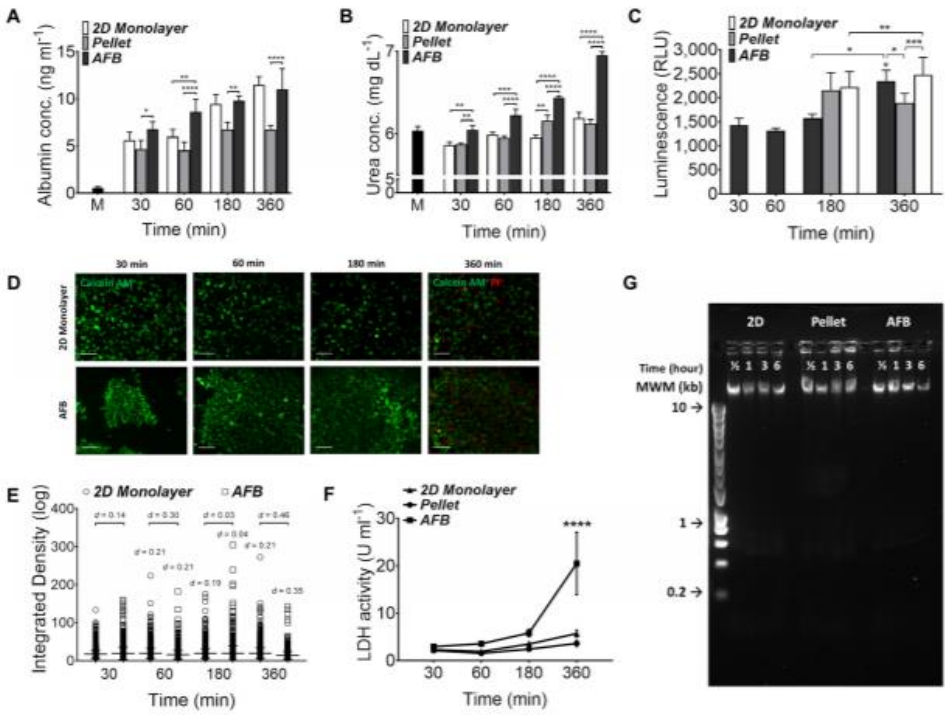

FIG. 5. Functions of Huh7 in the AFB. (a) Albumin concentrations (ng ml^{-1}) and (b) urea concentrations (mg dl^{-1}) in supernatants from Huh7 cultured in the 2D monolayer, pellet, or AFB cultures with time course. n = 3. *P* values shown in the graph are for comparison to cells after 30 min between various cultures. M, medium. (c) CYP3A4 activity in Huh7 cultured in the AFB system with time course and following 3 and 6 h as the 2D monolayer or pellet cultures. n = 3. *P* values shown in the graph are for comparison to cells after 30 min in AFB or between various cultures. *$P < 0.05$, ***$P < 0.0005$, ****$P < 0.0001$. Mean ± SEM. Paired Student *t* test. (d) Permeability of Huh7 with time course in AFB compared to the 2D monolayer culture with time course. Cells were preloaded with calcein AM (1 μM), scale = 100 μm and (e) quantification of change in cell fluorescence over time course, expressed as integrated density. Difference between means tested by Cohen's *d* effect size values were marked. Mean ± SD. $d = 0.2$ (small) and $d = 0.5$ (medium). (f) Lactic dehydrogenase (LDH) activity (U ml^{-1}) in supernatants from Huh7 cultures with time course. n = 3. *P* values shown in the graph are for comparison between various cultures with time course (on top of bars). ****$P < 0.0001$. Mean ± SEM. Two-way ANOVA followed by Fisher's LSD test. (G) DNA fragmentation assay of Huh7 DNA loaded in 1% agarose gel with different culture systems and time (representative image of 3 experiments). HyperLadder™ 1 kb molecular weight marker (MWM) was indicated.

show a significant change in their response to 5FU (IC50 9.52 and 4.29 μM, respectively). Conversely, the proliferation of cells cultured as pellets was inhibited at much lower concentration (IC50 2 μM) [Fig. 6(f)]. To determine whether the decreased in cell survival was caused by blunting of cell growth or cell death, further calcein AM/PI viability and LDH activity assays were used.

Numbers of dead cells were increased in the AFB or pelleted cultures following 72 h of incubation with high concentrations of 5FU [Fig. 7(a)], whereas few dead cells were observed in the 2D monolayer. The reaction of cells grown in 2D monolayers seems to appear as an inhibition of proliferation rather than cell cytotoxicity. LDH release in supernatants of cell aggregates from AFB or pellet cultures showed higher basal levels [Fig. 7(b)]. A marked increase in LDH activity was been found in cells grown after 72 h incubation with 5FU at 100 μM in all cell cultures. A limited increase in LDH release was observed in cells cultured in AFB as compared to a 2D monolayer (a mean of 5.23 ± SEM 0.59 and 4.39 ± SEM 0.47 U ml^{-1}, respectively). Pelleted cells did show a higher

Published under license by AIP Publishing.

Biomicrofluidics ARTICLE scitation.org/journal/bmf

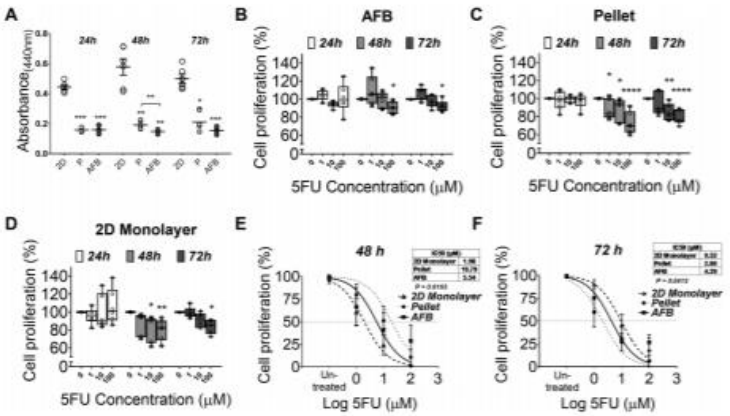

FIG. 6. Anticancer drug testing of Huh7 AFB generated discoids. Proliferation of Hhu-7 on various cell cultures (a) or following treatment with various concentrations of 5 Fluorouracil (5FU) cultured in (b) AFB, (c) pellet, or (d) 2D monolayer cultures with time course (expressed as percentage of un-treated cells). n = 3. *P* values shown in the graph are for comparison to un-treated cells. [(e) and (f)] Inhibitory concentration 50 (IC50) of 5FU in various culture conditions following 48 h or 72 h, respectively. $^{*}P < 0.05$, $^{**}P < 0.005$, $^{***}P < 0.0005$, $^{****}P < 0.0001$. Mean ± SEM. Two-way ANOVA followed by Fisher's LSD test.

LDH activity at all 5FU concentrations (a mean of 6.40 ± SEM 0.97 U ml^{-1}). Finally, the 5FU induction of apoptosis in Huh7 was explored by detecting the DNA fragmentation. DNA degradation in cell discoids generated in AFB was clear after 5FU treatment at concentrations of 10^2 and 10^3 μM [Fig. 7(c)]. The response of cells grown in the 2D monolayer was relatively less than that in AFB culture, but pellet culture showed responses only at a high concentration of 5FU (10^3 μM).

DISCUSSION

In the present study, we have investigated an acoustofluidic, matrix-free discoid aggregation system for Huh7 cells. In contrast to our previous work[18] with chondrocytes (which included 21 day levitated culture), the bioreactor was used only during an initial aggregate formation period of 6 h followed by the conventional culture in a well-plate. Following sonication, the Huh7 hepatoma cells have shown high viability and improved function in comparison to the conventional 2D monolayer culture. Moreover, exposure to ultrasound waves was associated with high levels of E-cadherin and an increase in proliferation in aggregated cells. The AFB fabricated cell aggregates were found to be suitable for anti-cancer drug testing and apoptosis assays.

The diameter of our disc-like aggregates was found to be dependent on cell density, while their thickness is relatively constant at a cell density up to 5×10^6 ml^{-1}. Bazou *et al.* have reported similar findings with the hepatoblastoma cell line, HepG2.[19] They noticed that at a density of 1×10^6 cells ml^{-1}, a 3D multilayer discoid cell aggregate formed which steadily increased in diameter with higher cell concentrations. In contrast to our results, they found an increase in aggregate thickness with higher cell densities and a tendency of cells to accumulate at the center of the discoid rather than its edges. However, the distribution of the lateral acoustic field of the Bazou device was significantly different, having a single kinetic energy density maximum, which attracted cells over an area many wavelengths in width, while in our device, multiple, smaller aggregates are formed, such that there is a different balance between axial and lateral components of the acoustic radiation force.

Cell-cell contact, spreading, and attachments were found to be initiated in the AFB, and these events cause stable aggregates. Huh7 cells express several adhesion molecules including E-cadherins,[3,35,36] which play a crucial role in hepatoma cell aggregate formation.[37] In the present study, we investigated the alteration of expression of E-cadherin in Huh7 in the AFB. Full length E-cadherin cell expression was higher in the AFB system than in the 2D monolayer culture that agrees with previous studies.[7,38] In these reports, ultrasound waves resulted in the accumulation of neural cell adhesion molecule (NCAM) and N-cadherin and induced re-organisation of F-actin accumulation of adhesion molecules markedly following 30 min of sonication. Initially, during the first 3 h of levitation in the AFB, cells appear to shift from cell suspension status where the preserved E-cadherin could potentially mediate cell aggregation to aggregates that may harbour proliferating cells, as evidenced by cleavage of E-cadherin. In fact, cleavage of E-cadherin is essential for tumour cell extrusion and proliferation.[39] In the case of 2D monolayers, limited cell contact could allow cells to

Published under license by AIP Publishing.

Biomicrofluidics ARTICLE scitation.org/journal/bmf

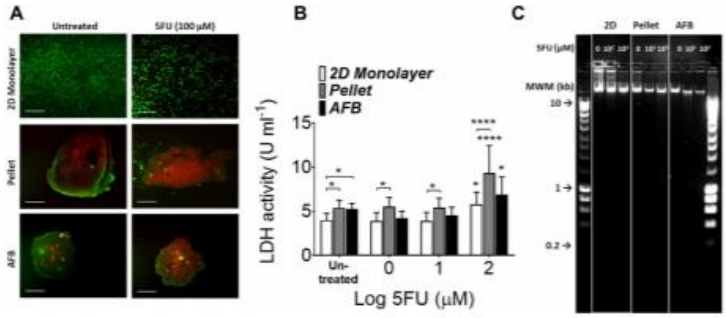

FIG. 7. 5FU induces cell death and apoptosis in Huh7 AFB generated discoids. (a) Live/dead staining of Huh7 cultured in the 2D monolayer, pellet, or AFB cultures 72 h following addition of 100 μM 5FU. Scale bar = 500 μm. (b) LDH (U ml^{-1}) release in supernatants from Huh7 cultured in various culture conditions 72 h following addition of 5FU. n = 3. *P* values shown in the graph are for comparison to untreated cells (on top of bars) or to the cell in the 2D monolayer culture. $^{*}P < 0.05$, $^{**}P < 0.005$, $^{***}P < 0.0005$, $^{****}P < 0.0001$. Mean ± SEM. Two-way ANOVA followed by Fisher's LSD test. (c) DNA fragmentation assay of Huh7 DNA following treatment with 5FU loaded in 1% agarose gel with different culture systems (representative image of 3 experiments). HyperLadder 1 kb molecular weight marker (MWM) was indicated.

proliferate early in their culture. AFB Huh7 cell aggregation is suggested to be E-cadherin dependent, which could make this system a good tool for studying cadherin mediated pathways.

Physical stresses resulted from exposure to acoustic radiation forces such as changes in temperature and cavitation effects could influence cell viability and may lead to cell damage.[40] Cell viability was assessed using calcein AM/PI live/dead dyes and DNA degradation assays. We did not find a marked effect of the AFB system on cell viability or the induction of apoptosis after 6 h in the bioreactor compared to the 2D culture system controls. This was in agreement with reports showing that cells that had been levitated in acoustofluidic systems maintained their integrity.[41–43] Moreover, a notable stability of the gene expression profile has been described in cells such as embryonic stem cells exposed to ultrasonic standing waves with a pressure amplitude up to 0.85 MPa.[44] The cavitation effect depends on the peak negative pressure (in MPa) as well as the frequency of acoustic wave. The ratio of these two factors determines the cavitation threshold that expressed as the mechanical index (MI). Risk of cavitation could be avoided by keeping the MI lower than 1.[40] Our system provided an exposure of Huh7 cells to a pressure amplitude (and peak negative pressure) of 0.38 MPa at a frequency of 1.5 MHz. These conditions reduced the risk of cavitation by keeping MI at about ~0.3. Moreover, the used pressure amplitude is far less than that reported before by Bazou *et al.*[18] (i.e., 1.96 MPa) which produce cavitation. Indeed, cells showed an intact cell membrane with the retention of calcein AM which exclude the occurrence of cavitation in our AFB.

In the present study, we have shown that the incubation of Huh7 cells in the AFB was associated with an improvement of their ability to produce albumin and urea. These results are in agreement with those previously reported with HepG2 cells.[7,19] In addition, we have observed increased CYP3A4 enzyme activity which was previously reported.[2] Culturing of Huh7 in a confluent state or in a 3D system could dampen their proliferative drive and promote their metabolic efficiency.[2,45,46] However, our results are more consistent with an advantageous effect of the AFB on Huh7 functions.

Our analysis of the 3D cultures has shown a decline of cell growth as compared to the 2D cultures, consistent with results reported previously with other cell types including Huh7.[5,47,48] Only Huh7 cells near the surface of a cell spheroid demonstrate a proliferation capacity, while quiescent cells are present at the center of the spheroid.[5] However, subconfluent cells in the 2D culture show unrestrained proliferative capacity. These differences in cell proliferation capacities in either 2D or 3D systems could explain differences in response to anti-cancer drugs between culture systems. We have demonstrated that 5FU could induce the deterioration of cell growth and apoptosis following 48 h of exposure to 5FU in agreement with previous reports.[14] Notably, after 48 h, the cytotoxic effect of 5FU was more pronounced on highly proliferative cells as 2D system while the potency of 5FU decreased when proliferation was limited as seen in AFB and pellet cultures. In addition, this resistance of the 3D cultures to 5FU might be a result of limited drug diffusion into the aggregates as reported before.[24,49]

According to the results of LDH and calcein AM/PI viability assay, pellet culture clearly showed a decrease in cell integrity early in culture which continued with the course of time. Although the predominate effect of 5FU is shown in proliferating cells, impaired DNA repair, mis-incorporation of 5FU, and subsequent RNA damage could have a large effect on cell survival and metabolism of other quiescent cells.[50] Cell necrosis and apoptosis are both induced by 5FU, but the predominance of one of them is dependent on the cell line

Published under license by AIP Publishing.

and the 5FU regime used.[14] The high potency of 5FU shown in pellet culture, following 72 h of treatment could not be due to the drug effect without the effect of the aggregation mechanism. The large size of pellets (>500 μm) could result in impaired cell viability, a phenomenon which has been consistently reported[51–53] that may cause a concurrent spontaneous cell death and eventually, decreased viable cell mass available for 5FU. On the other hand, the 2D monolayer had preserved cell mass and could increase the need for a higher concentration of 5FU to demonstrate the effect. Conversely, the discoid thickness of ~60 μm appears not to hinder oxygen/nutrient diffusion in AFB aggregates, and this might explain the relatively constant potency of 5FU in AFB aggregates during culture. We have noticed that the cytotoxicity effect of 5FU was well demonstrated in cells with limited proliferation capacities (as in the AFB or pellets) while its cytostatic effect was shown in highly proliferative cells such as in the 2D monolayer.

CONCLUSIONS

Our findings have demonstrated that AFB could be a good tool for the fabrication of size-controllable discoids. The AFB driven Huh7 cell aggregates showed high viability and their functions reflected their diversion toward differentiation. The hepatoma cell aggregates were found to express high levels of E-cadherin, and aggregate process could not be established without the presence of calcium in culture medium. Relatively short times were needed for the formation of stable aggregates. The AFB generated Huh7 aggregates were relatively uniform and due to rapid diffusion into the aggregate core, their response to anti-cancer was comparable to the standard 2D monolayer system, the factors which favour their use as a model for drug toxicity and screening.

ACKNOWLEDGMENTS

We are grateful to all colleagues in NK group, Faculty of Medicine, University of Southampton and Mechatronics Research group, Faculty of Engineering and Physical Sciences, University of Southampton for their assistance in development and their advice. This work was supported by grants from Liver and Pancreatic Cancer Research & Development Charity and University of Southampton, UK. The authors gratefully acknowledge the financial support for the work from the Engineering and Physical Sciences Research Council (EPSRC) Fellowship (No. EP/L025035/1) to P. Glynne-Jones.

Data supporting this study are openly available from the University of Southampton repository at https://doi.org/10.5258/SOTON/D0719.

REFERENCES

[1]S. C. Ramaiahgari, M. W. den Braver, B. Herpers, V. Terpstra, J. N. Commandeur, B. van de Water, and L. S. Price, Arch. Toxicol. **88**(5), 1083–1095 (2014).
[2]L. Sivertsson, M. Ek, M. Darnell, I. Edebert, M. Ingelman-Sundberg, and E. P. A. Neve, Drug Metab. Dispos. **38**(6), 995–1002 (2010).
[3]B. Sainz, Jr., V. TenCate, and S. L. Uprichard, Virol. J. **6**, 103 (2009).
[4]R. Edmondson, J. J. Broglie, A. F. Adcock, and L. J. Yang, Assay Drug Dev. Technol. **12**(4), 207–218 (2014).
[5]H. R. Jung, H. M. Kang, J. W. Ryu, D. S. Kim, K. H. Noh, E. S. Kim, H. J. Lee, K. S. Chung, H. S. Cho, N. S. Kim, D. S. Im, J. H. Lim, and C. R. Jung, Sci. Rep. **7**(1), 10499 (2017).
[6]R. J. W. Jen-Yin Goh and L. Dixon, "Development and use of in vitro alternatives to animal testing by the pharmaceutical industry 1980–2013," Toxicol. Res. **4**(5), 1297–1307 (2015).
[7]J. Liu, L. A. Kuznetsova, G. O. Edwards, J. Xu, M. Ma, W. M. Purcell, S. K. Jackson, and W. T. Coakley, J. Cell. Biochem. **102**(5), 1180–1189 (2007).
[8]P. Glynne-Jones, R. J. Boltryk, and M. Hill, Lab Chip **12**(8), 1417–1426 (2012).
[9]A. Lenshof, C. Magnusson, and T. Laurell, Lab Chip **12**(7), 1210–1223 (2012).
[10]L. A. Kuznetsova, D. Bazou, and W. T. Coakley, Langmuir **23**(6), 3009–3016 (2007).
[11]U. S. Jonnalagadda, M. Hill, W. Messaoudi, R. B. Cook, R. O. C. Oreffo, P. Glynne-Jones, and R. S. Tare, Lab Chip **18**(3), 473–485 (2018).
[12]J. J. Lei, P. Glynne-Jones, and M. Hill, Phys. Fluids **28**(1), 012004 (2016).
[13]M. Kondo, H. Nagano, H. Wada, B. Damdinsuren, H. Yamamoto, N. Hiraoka, H. Eguchi, A. Miyamoto, T. Yamamoto, H. Ota, M. Nakamura, S. Marubashi, K. Dono, K. Umeshita, S. Nakamori, M. Sakon, and M. Monden, Clin. Cancer Res. **11**(3), 1277–1286 (2005), see http://clincancerres.aacrjournals.org/content/11/3/1277.
[14]O. Brenes, F. Arce, O. Gatjens-Boniche, and C. Diaz, Biomed. Pharmacother. **61**(6), 347–355 (2007).
[15]M. Hill, Y. Shen, and J. J. Hawkes, Ultrasonics **40**(1–8), 385–392 (2002).
[16]R. Krimholtz, D. A. Leedom, and G. L. Matthaei, Electron. Lett. **6**(13), 398 (1970).
[17]S. P. Martin, R. J. Townsend, L. A. Kuznetsova, K. A. J. Borthwick, M. Hill, M. B. McDonnell, and W. T. Coakley, Biosens. Bioelectron. **21**(5), 758–767 (2005).
[18]D. Bazou, L. A. Kuznetsova, and W. T. Coakley, Ultrasound Med. Biol. **31**(3), 423–430 (2005).
[19]D. Bazou, W. T. Coakley, A. J. Hayes, and S. K. Jackson, Toxicol. In Vitro **22**(5), 1321–1331 (2008).
[20]J. Schindelin, I. Arganda-Carreras, E. Frise, V. Kaynig, M. Longair, T. Pietzsch, S. Preibisch, C. Rueden, S. Saalfeld, B. Schmid, J.-Y. Tinevez, D. J. White, V. Hartenstein, K. Eliceiri, P. Tomancak, and A. Cardona, Nat. Methods **9**, 676 (2012).
[21]R. J. Zawada, P. Kwan, K. L. Olszewski, M. Llinas, and S. G. Huang, Biochem. Cell Biol. **87**(3), 541–544 (2009).
[22]S. Kasibhatla, G. P. Amarante-Mendes, D. Finucane, T. Brunner, E. Bossy-Wetzel, and D. R. Green, CSH Protoc. **2006**, 1 (2006).
[23]R. Glicklis, J. C. Merchuk, and S. Cohen, Biotechnol. Bioeng. **86**(6), 672–680 (2004).
[24]K. Chen, M. Wu, F. Guo, P. Li, C. Y. Chan, Z. Mao, S. Li, L. Ren, R. Zhang, and T. J. Huang, Lab Chip **16**(14), 2636–2643 (2016).
[25]S. S. Kantak and R. H. Kramer, J. Biol. Chem. **273**(27), 16953–16961 (1998).
[26]M. Takeichi, Curr. Opin. Cell Biol. **7**(5), 619–627 (1995).
[27]T. Shimada, H. Yamazaki, M. Mimura, Y. Inui, and F. P. Guengerich, J. Pharmacol. Exp. Ther. **270**(1), 414–423 (1994), see http://jpet.aspetjournals.org/content/270/1/414.
[28]F. P. Guengerich, Annu. Rev. Pharmacol. Toxicol. **39**, 1–17 (1999).
[29]U. M. Zanger, M. Turpeinen, K. Klein, and M. Schwab, Anal. Bioanal. Chem. **392**(6), 1093–1108 (2008).
[30]Y. Zhou, K. Yang, J. Cui, J. Y. Ye, and C. X. Deng, J. Control. Release **157**(1), 103–111 (2012).
[31]D. Carugo, D. N. Ankrett, P. Glynne-Jones, L. Capretto, R. J. Boltryk, X. Zhang, P. A. Townsend, and M. Hill, Biomicrofluidics **5**(4), 044108–044115 (2011).
[32]D. Bratosin, L. Mitrofan, C. Palii, J. Estaquier, and J. Montreuil, Cytometry A **66a**(1), 78–84 (2005).
[33]R. Reinehr, S. Becker, A. Hongen, and D. Haussinger, J. Biol. Chem. **279**(23), 23977–23987 (2004).
[34]C. Leroy, C. Colmont, M. Pisam, and G. Rousselet, Eur. J. Cell Biol. **79**(12), 936–942 (2000).
[35]B. K. Straub, S. Rickelt, R. Zimbelmann, C. Grund, C. Kuhn, M. Iken, M. Ott, P. Schirmacher, and W. W. Franke, J. Cell Biol. **195**(5), 873–887 (2011).

Published under license by AIP Publishing.

[36]B. W. Wong, J. M. Luk, I. O. Ng, M. Y. Hu, K. D. Liu, and S. T. Fan, Biochem. Biophys. Res. Commun. **311**(3), 618–624 (2003).
[37]R.-Z. Lin, L.-F. Chou, C.-C. M. Chien, and H.-Y. Chang, Cell Tissue Res. **324**(3), 411–422 (2006).
[38]D. Bazou, G. A. Foster, J. R. Ralphs, and W. T. Coakley, Mol. Membr. Biol. **22**(3), 229–240 (2005).
[39]A. G. Grieve and C. Rabouille, J. Cell Sci. **127**(Pt 15), 3331–3346 (2014).
[40]M. Wiklund, Lab Chip **12**(11), 2018–2028 (2012).
[41]H. Bohm, P. Anthony, M. R. Davey, L. G. Briarty, J. B. Power, K. C. Lowe, E. Benes, and M. Groschl, Ultrasonics **38**(1–8), 629–632 (2000).
[42]S. Radel, L. Gherardini, A. J. McLoughlin, O. Doblhoff-Dier, and E. Benes, Bioseparation **9**(6), 369–377 (2000).
[43]S. Radel, A. J. McLoughlin, L. Gherardini, O. Doblhoff-Dier, and E. Benes, Ultrasonics **38**(1–8), 633–637 (2000).
[44]D. Bazou, R. Kearney, F. Mansergh, C. Bourdon, J. Farrar, and M. Wride, Ultrasound Med. Biol. **37**(2), 321–330 (2011).
[45]L. Sivertsson, I. Edebert, M. P. Palmertz, M. Ingelman-Sundberg, and E. P. A. Neve, Mol. Pharmacol. **83**(3), 659–670 (2013).
[46]M. Takagi, N. Fukuda, and T. Yoshida, Cytotechnology **24**(1), 39–45 (1997).
[47]W. A. Renner, M. Jordan, H. M. Eppenberger, and C. Leist, Biotechnol. Bioeng. **41**(2), 188–193 (1993).
[48]M. Haji-Karim and J. Carlsson, Cancer Res. **38**(5), 1457–1464 (1978), see http://cancerres.aacrjournals.org/content/38/5/1457.
[49]Y. C. Tung, A. Y. Hsiao, S. G. Allen, Y. S. Torisawa, M. Ho, and S. Takayama, Analyst **136**(3), 473–478 (2011).
[50]D. B. Longley, D. P. Harkin, and P. G. Johnston, Nat. Rev. Cancer **3**(5), 330–338 (2003).
[51]K. Groebe and W. MuellerKlieser, Int. J. Radiat. Oncol. Biol. Phys. **34**(2), 395–401 (1996).
[52]F. Hirschhaeuser, H. Menne, C. Dittfeld, J. West, W. Mueller-Klieser, and L. A. Kunz-Schughart, J. Biotechnol. **148**(1), 3–15 (2010).
[53]S. Y. Ong, H. Dai, and K. W. Leong, Biomaterials **27**(22), 4087–4097 (2006).

Published under license by AIP Publishing.

List of References

1. Hughes, M.P., R. Pethig, and X.-B. Wang, *Dielectrophoretic forces on particles in travelling electric fields.* Journal of Physics D: Applied Physics, 1996. **29**(2): p. 474.

2. Ashkin, A., J.M. Dziedzic, and T. Yamane, *Optical trapping and manipulation of single cells using infrared laser beams.* Nature, 1987. **330**(6150): p. 769.

3. Liu, C., et al., *Cell manipulation with magnetic particles toward microfluidic cytometry.* Journal of Applied Physics, 2009. **105**(10): p. 102014.

4. Torr, G., *The acoustic radiation force.* American Journal of Physics, 1984. **52**(5): p. 402-408.

5. Ding, X., et al., *On-chip manipulation of single microparticles, cells, and organisms using surface acoustic waves.* Proceedings of the National Academy of Sciences, 2012. **109**(28): p. 11105-11109.

6. Hartono, D., et al., *On-chip measurements of cell compressibility via acoustic radiation.* Lab on a Chip, 2011. **11**(23): p. 4072-4080.

7. Yamakoshi, Y., et al., *Effects of Bjerknes forces on gas-filled microbubble trapping by ultrasonic waves.* Japanese Journal of Applied Physics, 2001. **40**(5S): p. 3852.

8. Shields, C.W.t., C.D. Reyes, and G.P. Lopez, *Microfluidic cell sorting: a review of the advances in the separation of cells from debulking to rare cell isolation.* Lab Chip, 2015. **15**(5): p. 1230-49.

9. Nightingale, K.R., et al., *On the feasibility of remote palpation using acoustic radiation force.* The Journal of the Acoustical Society of America, 2001. **110**(1): p. 625-634.

10. Sarvazyan, A.P., O.V. Rudenko, and W.L. Nyborg, *Biomedical applications of radiation force of ultrasound: historical roots and physical basis.* Ultrasound in medicine & biology, 2010. **36**(9): p. 1379-1394.

11. Trinh, E.H., *Compact acoustic levitation device for studies in fluid dynamics and material science in the laboratory and microgravity.* Review of Scientific Instruments, 1985. **56**(11): p. 2059-2065.

12. Kundt, A., *Ueber eine neue Art akustischer Staubfiguren und über die Anwendung derselben zur Bestimmung der Schallgeschwindigkeit in festen Körpern und Gasen.* Annalen der Physik, 1866. **203**(4): p. 497-523.

13. Rayleigh, L., *XXXIV. On the pressure of vibrations.* The London, Edinburgh, and Dublin Philosophical Magazine and Journal of Science, 1902. **3**(15): p. 338-346.

14. King, L.V., *On the acoustic radiation pressure on spheres.* Proceedings of the Royal Society of London. Series A-Mathematical and Physical Sciences, 1934. **147**(861): p. 212-240.

15. Yosioka, K. and Y. Kawasima, *Acoustic radiation pressure on a compressible sphere.* Acta Acustica united with Acustica, 1955. **5**(3): p. 167-173.

16. Gor'Kov, L. *On the forces acting on a small particle in an acoustical field in an ideal fluid*. in *Sov. Phys. Dokl.* 1962.

17. Gor'kov, *On the forces acting on a small particle in an acoustical field in an ideal fluid.*

Soviet Physics Doklady, 1962. **Vol. 6**: p. p.773.

18. Doinikov, A., *Acoustic radiation pressure on a rigid sphere in a viscous fluid.* Proceedings of the Royal Society of London. Series A: Mathematical and Physical Sciences, 1994. **447**(1931): p. 447-466.

19. Laurell, T., F. Petersson, and A. Nilsson, *Chip integrated strategies for acoustic separation and manipulation of cells and particles.* Chemical Society Reviews, 2007. **36**(3): p. 492-506.

20. Aldrich, J.E., *Basic physics of ultrasound imaging.* Crit Care Med, 2007. **35**(5 Suppl): p. S131-7.

21. A. H. Weiser, M., R. E. Apfel, and E. A. Neppiras, *Interparticle Forces on Red Cells in a Standing Wave Field*. Vol. 56. 1984. 114-119.

22. Jiao, J., et al., *Experimental and theoretical analysis of secondary Bjerknes forces between two bubbles in a standing wave.* Ultrasonics, 2015. **58**: p. 35-42.

23. Boluriaan, S. and P.J. Morris, *Acoustic Streaming: From Rayleigh to Today.* International Journal of Aeroacoustics, 2003. **2**(3): p. 255-292.

24. Wiklund, M., R. Green, and M. Ohlin, *Acoustofluidics 14: Applications of acoustic streaming in microfluidic devices.* Lab Chip, 2012. **12**(14): p. 2438-51.

25. Eckart, C., *Vortices and Streams Caused by Sound Waves.* Physical Review, 1948. **73**(1): p. 68-76.

26. Rayleigh, L., *On the Circulation of Air Observed in Kundt's Tubes, and on Some Allied Acoustical Problems.* Philosophical Transactions of the Royal Society of London, 1884. **175**: p. 1-21.

27. Ingård, U. and S. Labate, *Acoustic circulation effects and the nonlinear impedance of orifices.* The Journal of the Acoustical Society of America, 1950. **22**(2): p. 211-218.

28. Sankaranarayanan, S.K.R.S., et al., *Flow induced by acoustic streaming on surface-acoustic-wave devices and its application in biofouling removal: A computational study and comparisons to experiment.* Physical Review E, 2008. **77**(6): p. 066308.

29. Qiu, L.M., et al., *Investigation on Gedeon Streaming in a Traveling Wave Thermoacoustic Engine.* AIP Conference Proceedings, 2006. **823**(1): p. 1115-1122.

30. Spengler, J.F., W.T. Coakley, and K.T. Christensen, *Microstreaming effects on particle concentration in an ultrasonic standing wave.* AIChE Journal, 2003. **49**(11): p. 2773-2782.

31. Wiklund, M., R. Green, and M. Ohlin, *Acoustofluidics 14: Applications of acoustic streaming in microfluidic devices.* Lab on a Chip, 2012. **12**(14): p. 2438-2451.

32. Leighton, T.G., *The Acoustic Bubble.* San Diego: Academic Press., 1994: p. 640.

33. Leighton, T.G., *Bubble population phenomena in acoustic cavitation.* Ultrasonics

Sonochemistry, 1995. **2**: p. 123.

34. Tajik, B., et al., *Heat transfer enhancement by acoustic streaming in a closed cylindrical enclosure filled with water.* International Journal of Heat and Mass Transfer, 2013. **60**: p. 230-235.

35. Liu, Y., H. Yang, and A. Sakanishi, *Ultrasound: mechanical gene transfer into plant cells by sonoporation.* Biotechnol Adv, 2006. **24**(1): p. 1-16.

36. Drinkwater, B.W., *Dynamic-field devices for the ultrasonic manipulation of microparticles.* Lab on a Chip, 2016. **16**(13): p. 2360-2375.

37. Nam, J., H. Lim, and S. Shin, *Manipulation of microparticles using surface acoustic wave in microfluidic systems: a brief review.* Korea-Australia Rheology Journal, 2011. **23**(4): p. 255-267.

38. Saito, M. and Y. Imanishi, *Host-guest composites containing ultrasonically arranged particles.* Journal of Materials Science, 2000. **35**(10): p. 2373-2377.

39. Llewellyn-Jones, T.M., B.W. Drinkwater, and R.S. Trask, *3D printed components with ultrasonically arranged microscale structure.* Smart Materials and Structures, 2016. **25**(2): p. 02LT01.

40. Lin, S.-C.S., X. Mao, and T.J. Huang, *Surface acoustic wave (SAW) acoustophoresis: now and beyond.* Lab on a Chip, 2012. **12**(16): p. 2766-2770.

41. Alghane, M., et al., *Experimental and numerical investigation of acoustic streaming excited by using a surface acoustic wave device on a 128° YX-LiNbO3substrate.* Journal of Micromechanics and Microengineering, 2010. **21**(1): p. 015005.

42. Wixforth, A., *Acoustically driven planar microfluidics.* Superlattices and Microstructures, 2003. **33**(5): p. 389-396.

43. Courtney, C.R.P., et al., *Manipulation of microparticles using phase-controllable ultrasonic standing waves.* The Journal of the Acoustical Society of America, 2010. **128**(4): p. EL195-EL199.

44. Orloff, N.D., et al., *Manipulating particle trajectories with phase-control in surface acoustic wave microfluidics.* Biomicrofluidics, 2011. **5**(4): p. 044107.

45. Ding, X., et al., *On-chip manipulation of single microparticles, cells, and organisms using surface acoustic waves.* Proceedings of the National Academy of Sciences, 2012. **109**(28): p. 11105.

46. Glynne-Jones, P., et al., *Mode-switching: a new technique for electronically varying the agglomeration position in an acoustic particle manipulator.* Ultrasonics, 2010. **50**(1): p. 68-75.

47. Glynne-Jones, P., R.J. Boltryk, and M. Hill, *Acoustofluidics 9: Modelling and applications of planar resonant devices for acoustic particle manipulation.* Lab Chip, 2012. **12**(8): p. 1417-26.

48. Qiu, Y., et al., *Screen-printed ultrasonic 2-D matrix array transducers for microparticle manipulation.* Ultrasonics, 2015. **62**: p. 136-46.

49. Kozuka, T., et al. *Acoustic micromanipulation using a multi-electrode transducer*. in *MHS'96 Proceedings of the Seventh International Symposium on Micro Machine and Human Science*. 1996.

50. Glynne-Jones, P., et al., *Array-controlled ultrasonic manipulation of particles in planar acoustic resonator.* IEEE Trans Ultrason Ferroelectr Freq Control, 2012. **59**(6): p. 1258-66.

51. Courtney, C.R.P., et al., *Manipulation of particles in two dimensions using phase controllable ultrasonic standing waves.* Proceedings of the Royal Society A: Mathematical, Physical and Engineering Sciences, 2012. **468**(2138): p. 337-360.

52. Courtney, C.R.P., et al., *Dexterous manipulation of microparticles using Bessel-function acoustic pressure fields.* Applied Physics Letters, 2013. **102**(12): p. 123508.

53. Grinenko, A., et al., *Acoustic radiation force analysis using finite difference time domain method.* J Acoust Soc Am, 2012. **131**(5): p. 3664-70.

54. Bernassau, A.L., et al., *Two-dimensional manipulation of micro particles by acoustic radiation pressure in a heptagon cell.* IEEE transactions on ultrasonics, ferroelectrics, and frequency control, 2011. **58**(10): p. 2132-2138.

55. Wiklund, M., *Acoustofluidics 12: Biocompatibility and cell viability in microfluidic acoustic resonators.* Lab on a Chip, 2012. **12**(11): p. 2018-2028.

56. Vanherberghen, B., et al., *Ultrasound-controlled cell aggregation in a multi-well chip.* Lab on a Chip, 2010. **10**(20): p. 2727-2732.

57. Rayleigh, L., *On Waves Propagated along the Plane Surface of an Elastic Solid.* Proceedings of the London Mathematical Society, 1885. **s1-17**(1): p. 4-11.

58. Takeuchi, M., H. Abe, and K. Yamanouchi. *Ultrasonic micromanipulation of small particles in liquid using VHF-range leaky wave transducers*. in *1994 Proceedings of IEEE Ultrasonics Symposium*. 1994.

59. Saito, M., S.-y. Izumida, and J. Hirota, *Ultrasonic trapping of paramecia and estimation of their locomotive force.* Applied Physics Letters, 1997. **71**(14): p. 1909-1911.

60. Saito, M., N. Kitamura, and M. Terauchi, *Ultrasonic manipulation of locomotive microorganisms and evaluation of their activity.* Journal of Applied Physics, 2002. **92**(12): p. 7581-7586.

61. Meng, L., et al., *Transportation of single cell and microbubbles by phase-shift introduced to standing leaky surface acoustic waves.* Biomicrofluidics, 2011. **5**(4): p. 44104-4410410.

62. Orloff, N.D., et al., *Manipulating particle trajectories with phase-control in surface acoustic wave microfluidics.* Biomicrofluidics, 2011. **5**(4): p. 44107-441079.

63. Wu, J. and G. Du, *Acoustic radiation force on a small compressible sphere in a focused beam.* The Journal of the Acoustical Society of America, 1990. **87**(3): p. 997-1003.

64. Wu, J.R., *Acoustical tweezers.* J Acoust Soc Am, 1991. **89**(5): p. 2140-3.

65. Hwang, J.Y., et al., *Cell membrane deformation induced by a fibronectin-coated polystyrene microbead in a 200-MHz acoustic trap.* IEEE Trans Ultrason Ferroelectr Freq Control, 2014. **61**(3): p. 399-406.

66. Zheng, F., et al., *Acoustic trapping with a high frequency linear phased array.* Applied Physics Letters, 2012. **101**(21): p. 214104.

67. Ravi, M., et al., *3D Cell Culture Systems: Advantages and Applications.* Journal of Cellular Physiology, 2015. **230**(1): p. 16-26.

68. Erickson, I.E., et al., *Differential Maturation and Structure–Function Relationships in Mesenchymal Stem Cell- and Chondrocyte-Seeded Hydrogels.* Tissue Engineering Part A, 2008. **15**(5): p. 1041-1052.

69. Fraley, S.I., et al., *A distinctive role for focal adhesion proteins in three-dimensional cell motility.* Nat Cell Biol, 2010. **12**(6): p. 598-604.

70. Liu, H. and K. Roy, *Biomimetic three-dimensional cultures significantly increase hematopoietic differentiation efficacy of embryonic stem cells.* Tissue Eng, 2005. **11**(1-2): p. 319-30.

71. Loessner, D., et al., *Bioengineered 3D platform to explore cell–ECM interactions and drug resistance of epithelial ovarian cancer cells.* Biomaterials, 2010. **31**(32): p. 8494-8506.

72. Mazzoleni, G., D. Di Lorenzo, and N. Steimberg, *Modelling tissues in 3D: the next future of pharmaco-toxicology and food research?* Genes & Nutrition, 2008. **4**(1): p. 13.

73. Breslin, S. and L. O'Driscoll, *Three-dimensional cell culture: the missing link in drug discovery.* Drug Discovery Today, 2013. **18**(5): p. 240-249.

74. Ivascu, A. and M. Kubbies, *Rapid Generation of Single-Tumor Spheroids for High-Throughput Cell Function and Toxicity Analysis.* Journal of Biomolecular Screening, 2006. **11**(8): p. 922-932.

75. Goodwin, T.J., et al., *Reduced shear stress: A major component in the ability of mammalian tissues to form three-dimensional assemblies in simulated microgravity.* Journal of Cellular Biochemistry, 1993. **51**(3): p. 301-311.

76. Souza, G.R., et al., *Three-dimensional tissue culture based on magnetic cell levitation.* Nature Nanotechnology, 2010. **5**: p. 291.

77. Chen, K., et al., *Rapid formation of size-controllable multicellular spheroids via 3D acoustic tweezers.* Lab on a Chip, 2016. **16**(14): p. 2636-2643.

78. Ovsianikov, A., A. Khademhosseini, and V. Mironov, *The Synergy of Scaffold-Based and Scaffold-Free Tissue Engineering Strategies.* Trends in Biotechnology, 2018. **36**(4): p. 348-357.

79. Sachlos, E. and J. Czernuszka, *Making tissue engineering scaffolds work. Review: the application of solid freeform fabrication technology to the production of tissue engineering scaffolds.* Eur Cell Mater, 2003. **5**(29): p. 39-40.

80. Huisken, J. and E.H.K. Stelzer, *Optical levitation of absorbing particles with a nominally Gaussian laser beam.* Optics Letters, 2002. **27**(14): p. 1223-1225.

81. Shi, J., et al., *Three-dimensional continuous particle focusing in a microfluidic channelvia standing surface acoustic waves (SSAW).* Lab on a Chip, 2011. **11**(14): p. 2319-2324.

82. Jonnalagadda, U.S., et al., *Acoustically modulated biomechanical stimulation for human cartilage tissue engineering.* Lab on a Chip, 2018. **18**(3): p. 473-485.

83. Li, S., et al., *Application of an acoustofluidic perfusion bioreactor for cartilage tissue engineering.* Lab on a Chip, 2014. **14**(23): p. 4475-4485.

84. Hill, M. and R.J.K. Wood, *Modelling in the design of a flow-through ultrasonic separator.* Ultrasonics, 2000. **38**(1): p. 662-665.

85. Hill, M., Y. Shen, and J.J. Hawkes, *Modelling of layered resonators for ultrasonic separation.* Ultrasonics, 2002. **40**(1-8): p. 385-392.

86. Hill, M., Y. Shen, and J.J. Hawkes, *Modelling of layered resonators for ultrasonic separation.* Ultrasonics, 2002. **40**(1): p. 385-392.

87. Krimholtz, R., D.A. Leedom, and G.L. Matthaei, *New equivalent circuits for elementary piezoelectric transducers.* Electronics Letters, 1970. **6**(13): p. 398-399.

88. Castillo, M., P. Acevedo, and E. Moreno, *KLM model for lossy piezoelectric transducers.* Ultrasonics, 2003. **41**(8): p. 671-679.

89. Gröschl, M., *Ultrasonic separation of suspended particles-Part I: Fundamentals.* Acta Acustica united with Acustica, 1998. **84**(3): p. 432-447.

90. Glynne-Jones, P., et al., *Array-controlled ultrasonic manipulation of particles in planar acoustic resonator.* IEEE transactions on ultrasonics, ferroelectrics, and frequency control, 2012. **59**(6): p. 1258-1266.

91. Lei, J., M. Hill, and P. Glynne-Jones, *Numerical simulation of 3D boundary-driven acoustic streaming in microfluidic devices.* Lab on a Chip, 2014. **14**(3): p. 532-541.

92. Dunn, F., et al., *Springer handbook of acoustics*. 2015: Springer.

93. Chowdhury, I. and S. Dasgupta, *Computation of Rayleigh Damping Coefficients for Large Systems*. Vol. 43. 2003. 6855-6868.

94. Ashkin, A. and J.M. Dziedzic, *Damping of optically levitated particles by feedback and beam shaping*. 1978, Google Patents.

95. Dowell, E.H., G. Gorman III, and D. Smith, *Acoustoelasticity: general theory, acoustic natural modes and forced response to sinusoidal excitation, including comparisons with experiment.* Journal of Sound and vibration, 1977. **52**(4): p. 519-542.

96. Djojodihardjo, H., *Vibro-acoustic analysis of the acoustic-structure interaction of flexible structure due to acoustic excitation.* Acta Astronautica, 2015. **108**: p. 129-145.

97. al., M.H.e., *Modelling of layered resonators for ultrasonic separation.* Ultrasonics, 2002. **40**: p. 385-392.

98. al., L.e. 1999: North america.

99. al., W.T.e., *PIVlab–towards user-friendly, affordable and accurate digital particle image velocimetry in MATLAB.* Journal of Open Research Software, 2016. **2**(1).

100. Zmijan, R., et al., *High throughput imaging cytometer with acoustic focussing.* RSC advances, 2015. **5**(101): p. 83206-83216.

101. Chen, Y., et al., *Standing surface acoustic wave (SSAW)-based microfluidic cytometer.* Lab on a Chip, 2014. **14**(5): p. 916-923.

102. Glicklis, R., J.C. Merchuk, and S. Cohen, *Modeling mass transfer in hepatocyte spheroids via cell viability, spheroid size, and hepatocellular functions.* Biotechnology and bioengineering, 2004. **86**(6): p. 672-680.

103. Zanger, U.M., et al., *Functional pharmacogenetics/genomics of human cytochromes P450 involved in drug biotransformation.* Analytical and bioanalytical chemistry, 2008. **392**(6): p. 1093-1108.

104. Kondo, M., et al., *Combination of IFN-α and 5-fluorouracil induces apoptosis through IFN-α/β receptor in human hepatocellular carcinoma cells.* Clinical cancer research, 2005. **11**(3): p. 1277-1286.